AN ANALYSIS OF INTERLAMINAR STRESSES IN UNSYMMETRICALLY LAMINATED PLATES

by

Donald Scott Norwood

Dissertation submitted to the Faculty of the
Virginia Polytechnic Institute and State University
in partial fulfillment of the requirements for the degree of

DOCTOR OF PHILOSOPHY

in

Engineering Mechanics

Approved:

C. T. Herakovich, Chairman

J. N. Reddy

M. J. Stuart

O. H. Griffin, Jr.

E. R. Johnson

June, 1990
Blacksburg, Virginia

AN ANALYSIS OF INTERLAMINAR STRESSES IN UNSYMMETRICALLY LAMINATED PLATES

by

Donald Scott Norwood

(ABSTRACT)

The results of a numerical study of interlaminar stresses within unsymmetrically laminated plates is presented. The focus of the study is upon the linear thermoelastic response of thin square laminated composite plates subjected to extensional, compressive, or thermal loading. Symmetric and unsymmetric 0/90, +45/–45, and 0/+45 laminate stacking sequences are examined to determine the effects of mismatch between adjacent layers in Poisson's ratio, coefficient of mutual influence, and coefficients of thermal expansion. Since the out-of-plane (transverse) deflections of unsymmetric laminates are typically large, a geometrically nonlinear kinematic description is used to account for the large displacements and rotations. The geometrically nonlinear three-dimensional boundary value problems are formulated from nonlinear elasticity theory and approximate solutions are determined using the finite element method. A total Lagrangian, displacement-based, incremental finite element formulation is implemented using Newton's method. Geometrically nonlinear global/local finite element analysis is used to obtain improved free edge stress predictions.

For laminates subjected to external loading, the mismatch in material properties between adjacent layers causes interlaminar stresses to arise near the free edges. For unsymmetric laminates under external loading, the mismatch in material properties about the geometric midplane causes out-of-plane deflections. For the laminates and loading conditions considered, the results of this study show that the out-of-plane deflections of unsymmetric laminates reduce interlaminar shear stresses. In addition, the out-of-plane deflections reduce interlaminar normal stresses for some laminates and increase these stresses for others. For the two-layer unsymmetric

laminates considered, the effect of out-of-plane deflections upon interlaminar normal stress was shown to be dependent upon the type of in-plane strain mismatch (i.e., normal and/or shear) caused by the dissimilar material properties. The results also show that as the out-of-plane deflections become large, the effects of geometric nonlinearity upon this stress-deformational response become important. These conclusions apply to extensional, compressive (prior to a change in mode shape), and thermal loading. The numerical results include interlaminar stresses for laminated plates which have buckled as a wide column under compressive loading.

ACKNOWLEDGEMENTS

This study was sponsored by the NASA-Virginia Tech Composites Program under NASA Grant NAG-1-343. The author wishes to express his gratitude to the following organizations which have provided the opportunity and support to conduct this study:

- Aircraft Structures Branch, NASA Langley Research Center
- ESM Department, Virginia Tech
- Structures Division, LTV Aerospace and Defense

The author wishes to thank the members of his graduate advisory committee for their participation and assistance. The author also wishes to thank Dr. Daniel Frederick and Dr. Michael Hyer for their support and assistance. The author is especially grateful to Dr. James H. Starnes and Dr. Mark J. Shuart for the opportunity to work on this project and to Dr. Carl T. Herakovich for his guidance as committee chairman.

The author wishes to thank Jim Smith, John Darnell, Al Curry, and John Pimm at LTV Aerospace for the opportunity to participate in his graduate program. Many thanks to the personnel of the Aircraft Structures Branch at NASA Langley Research Center for their support and for the generous use of their facilities. Special thanks to Kathleen Warnaar for all her computational assistance and helpful advice, Jeanie Kurtz for her illustrating assistance, and to Dr. Gene Poole and Andrea Overman for their valuable assistance in optimizing the fortran code. The author wishes to express his gratitude to Dr. J. N. Reddy, Dr. Gaylen Thurston, Dr. Manuel Stein, Dr. Walter Haisler, and Dr. Richard Schapery, for their valuable guidance and instruction. The author wishes to give special thanks to two instructors whose friendship, encouragement, and enlightenment are greatly appreciated: Professors Walter J. Horn and Stan H. Lowy.

The author wishes to express his gratitude to his friends and family for all their encouragement and support over the years. Many thanks to those acknowledged below and to the many others who could always be counted upon: the gang here at Langley, the Hinnants, the Warnaars, Dr. Dinesh Naik, Dr. David Whitaker, Juan Cruz, Ed Moas, Dan Sydow, and Dr. Michael Nemeth; the gang back at Tech, Danniella Thompson, Gina Novak-Ley, Andrea Ogden, Fred Stoll, and Dr. Michael Starbuck; the gang back in Texas, B.C., Richard DeWald, Dr. Richard Lumpkin, Steve Derdeyn, Bill Tillotson, Kevin Blake, Richard Benson, Alex Bielawski, Mark Tohlen, Linda Green, Richard Silvey, Richard Zapata, Paul Wood, Dr. Samit and Mabel Roy, Shankar Kalyanasandarum, Dr. Duane Sanders, Dr. Paul Peters and the wonderful folks at Parkland, and the McDonald, Corley, Benson, Dooghes, Tillotson, Wade, Kilpatrick, and Wilkinson families.

The author is especially grateful to his pals back in "the Cliffs": James McDonald and Brian Corley for their friendship, faith, and loyalty over the years and to his fellow Ph.D. candidates, office mates, and friends: Robert Ley and Richard Young for their valuable help, timely advice, and companionship. Finally, the author wishes to thank his family for their love, support, and spiritual guidance. Special thanks to his cousins Mary Brown-Waters and Gloria Rauch, brother Mike and sister Susan, and ever-patient parents. The author wishes to dedicate this dissertation to his parents, Donald Loyd and Joan Evelyn Norwood, for all their love, guidance, and support; one could do no better.

TABLE OF CONTENTS

Page

ACKNOWLEDGEMENTS iv

LIST OF TABLES ix

LIST OF FIGURES xii

LIST OF SYMBOLS xxii

1.0 INTRODUCTION 1

1.1 Introductory Remarks 1

1.2 Objectives of the Study 4

2.0 REVIEW OF THE LITERATURE 6

2.1 Unsymmetrically Laminated Plates 6

2.2 Interlaminar Stresses in Laminated Plates 17

2.3 Discussion of the Present Approximate Analysis 24

2.4 Summary 26

3.0 STUDY PARAMETERS 28

3.1 Discussion of Study Parameters 28

3.2 Parameters for Comparisons with Previous Results 33

4.0 THEORETICAL FORMULATION 34

4.1 Basic Assumptions 35

4.2 Analysis of Finite Deformation 36

4.2.1 Geometric Relationships 36

4.2.2 Strain Measures 39

4.2.3 Geometric Interpretation of Green-Lagrange Strain 42

4.3 Measures of Stress 44

4.4 Numerical Examples of Stress and Strain 48

4.5 Constitutive Equations 52

4.6 Total Potential Energy 53

4.7 Governing Equations and Boundary Conditions 54

4.8 Uniqueness and Stability 56
5.0 FINITE ELEMENT FORMULATION 59
5.1 Finite Element Implementation 59
5.1.1 Element Geometry and Interpolation Functions 60
5.1.2 Finite Element Equations 62
5.1.3 Numerical Integration 65
5.2 Computational Aspects 67
5.2.1 Global/Local Finite Element Analysis 68
5.2.2 Nonlinear Solution Strategy 70
5.2.3 Interlaminar Stress Computations 73
5.3 Verification Test Cases 79
6.0 RESULTS AND DISCUSSION 83
6.1 Objective of Interlaminar Stress Comparisons 85
6.2 Comparisons with Previous Results 86
6.2.1 Out-of-Plane Displacements 87
6.2.2 Interlaminar Stresses for 0/90 Laminates 88
6.2.3 Interlaminar Stresses for +45/–45 Laminates 91
6.3 Extensional Loading 93
6.3.1 Out-of-Plane Displacements 93
6.3.2 Interlaminar Stresses for 0/90 Laminates 95
6.3.3 Interlaminar Stresses for +45/–45 Laminates 97
6.3.4 Interlaminar Stresses for 0/+45 Laminates 98
6.3.5 Summary 98
6.4 Compressive Loading 101
6.4.1 Out-of-Plane Displacements 101
6.4.2 Interlaminar Stresses for 0/90 Laminates 106
6.4.3 Interlaminar Stresses for +45/–45 Laminates 109
6.4.4 Interlaminar Stresses for 0/+45 Laminates 109

6.4.5 Summary 110
6.5 Thermal Loading 112
6.5.1 Out-of-Plane Displacements 113
6.5.2 Interlaminar Stresses for 0/90 Laminates 116
6.5.3 Interlaminar Stresses for +45/–45 Laminates 118
6.5.4 Interlaminar Stresses for 0/+45 Laminates 119
6.5.5 Summary 120
7.0 CONCLUSIONS AND RECOMMENDATIONS 123
7.1 Summary and Concluding Remarks 124
7.2 Recommendations for Future Studies 126
REFERENCES 128
APPENDICES 138
A. The Coupling Behavior of Laminated Anisotropic Plates 138
B. Constitutive Equations 143
C. Finite Element Equations 150
D. Finite Element Models 152
E. Geometrically Nonlinear Plate Analysis 155
F. Results Using Reduced 3D Nonlinear Strain 159
TABLES 161
FIGURES 200
VITA 327

LIST OF TABLES

TABLE		PAGE
3.1	Lamina material properties for T300/5208 graphite/epoxy	161
3.2	Square laminated plate geometry for comparisons between symmetric and unsymmetric laminates	162
3.3	Loading and boundary conditions	163
3.4	Material property mismatch between adjacent layers	164
3.5	Unsymmetrically laminated plate stiffnesses	165
3.6	Symmetrically laminated plate stiffnesses	166
3.7	Square unsymmetrically laminated plate geometry for preliminary analyses	167
3.8	Lamina material properties for a typical graphite/epoxy composite material system	168
3.9	Square laminated plate geometry for comparisons with previous results	169
5.1	Order of element interpolations	170
5.2	Comparison of tensorial and conventional notations	171
6.1	Effects of geometric nonlinearity upon the predicted out-of-plane w displacements for the unsymmetric laminates	172
6.2	Effects of laminate membrane-flexural coupling and geometric nonlinearity upon the predicted interlaminar stresses due to material property mismatch ($u/a = +0.01$)	173
6.3	Effects of laminate membrane-flexural coupling and geometric nonlinearity upon the predicted interlaminar stresses due to material property mismatch ($u/a = -0.0005$, before a change in mode shape occurs)	174

6.4 Effects of laminate membrane-flexural coupling and geometric nonlinearity upon the predicted interlaminar stresses due to material property mismatch ($\Delta T = -280°F$) 175

6.5 Midplane w/h displacement extrema for the thick 4.0 in. square unsymmetric laminates ($u/a = +0.01$) 176

6.6 Interlaminar stresses along $x = 0$ at the 0/90 interface for the thick 4.0 in. square $0_{50}/90_{50}$ laminates ($u/a = +0.01$) 177

6.7 Interlaminar stresses along $x = 0$ at the +45/–45 interface for the thick 4.0 in. square $+45_{50}/-45_{50}$ laminates ($u/a = +0.01$) 178

6.8 Midplane w/h displacement extrema for the 2.0, 4.0, and 6.0 in. square unsymmetric laminates ($u/a = +0.01$) 179

6.9 Interlaminar stresses along $x = 0$ at the 0/90 interface for the 2.0 in. square $0_4/90_4$ laminates ($u/a = +0.01$) 180

6.10 Interlaminar stresses along $x = 0$ at the +45/–45 interface for the 2.0 in. square $+45_4/-45_4$ laminates ($u/a = +0.01$) 181

6.11 Interlaminar stresses along $x = 0$ at the 0/+45 interface for the 2.0 in. square $0_4/+45_4$ laminates ($u/a = +0.01$) 182

6.12 Midplane w/h displacement extrema for the 2.0, 4.0, and 6.0 in. square symmetric and unsymmetric laminates ($u/a = -0.01$) 183

6.13 Critical compressive edge displacements at which a change in mode shape occurs for the 2.0 in. square symmetric and unsymmetric laminates 184

6.14 Interlaminar stresses at the 0/90 interface for the 2.0 in. square $0_4/90_4$ laminates ($u/a = -0.01$) 185

6.15 Interlaminar stresses at the +45/–45 interface for a 2.0 in. square unsymmetric $[+45_4/-45_4]_t$ laminate ($u/a = -0.01$) 186

6.16 Interlaminar stresses at the 0/+45 interface for a 2.0 in. square unsymmetric $[0_4/+45_4]_t$ laminate ($u/a = -0.01$) 187

6.17 Midplane w/h displacement extrema for the 2.0, 4.0, and

6.0 in. square unsymmetric laminates ($\Delta T = -280°F$) 188

6.18 Interlaminar stresses along $x = 0$ and $y = 0$ at the 0/90 interface for the 2.0 in. square $0_4/90_4$ laminates ($\Delta T = -280°F$) 189

6.19 Interlaminar stresses along $x = 0$ and $y = 0$ at the +45/–45 interface for the 2.0 in. square $+45_4/-45_4$ laminates ($\Delta T = -280°F$) 190

6.20 Interlaminar stresses along $x = 0$ and $y = 0$ at the 0/+45 interface for the 2.0 in. square $0_4/+45_4$ laminates ($\Delta T = -280°F$) 191

A.1 The coupling behavior of laminated anisotropic plates 192

D.1 Loading and boundary conditions for finite element models 193

D.2 Summary of global and local finite element models 194

D.3 Summary of finite element models for comparisons with previous results and preliminary analyses 195

E.1 Comparison of midplane w/h displacement extrema predictions for 2.0, 4.0, and 6.0 in. square unsymmetric $[0_4/90_4]_t$ laminates ($\Delta T = -280°F$) 196

E.2 Comparison of experimental and theoretical curvatures for several square unsymmetric laminates ($\Delta T = -280°F$) 197

F.1 Comparison of midplane w/h displacement extrema predictions between Green-Lagrange and reduced 3D nonlinear strain for a 2.0 in. square unsymmetric $[0_4/90_4]_t$ laminate 198

F.2 Comparison of interlaminar stresses predictions between Green-Lagrange and reduced 3D nonlinear strain for a 2.0 in. square unsymmetric $[0_4/90_4]_t$ laminate 199

LIST OF FIGURES

FIGURE		PAGE
1.1	The interlaminar components of stress ...	200
3.1	Lamina principal material coordinate system and angle of orientation	201
3.2	Unsymmetric and symmetric laminated plate geometry	202
3.3	Laminate stacking sequences	203
3.4	External loading conditions	204
4.1	Motion of a material particle	205
4.2	Relative displacements between two neighboring points	206
4.3	Traction vector acting upon the surface of the body	207
4.4	Two-dimensional components of second Piola-Kirchhoff stress ${}_0^t S_{ij}$ and Cauchy stress ${}^t\sigma_{ij}$	208
4.5	Finite deformation of an elastic body	209
4.6	Percent difference between ${}_0^t E_{11}$ and ${}^t\epsilon'_{11}$ $(= \epsilon)$ versus engineering strain ϵ for the elastic body shown in Figure 4.5	210
4.7	Percent difference between ${}_0^t S_{11}$ and ${}^t\sigma'_{11}$ versus engineering strain ϵ for the elastic body shown in Figure 4.5 ($\nu = 0.25$)	211
5.1	Element geometry	212
5.2	Quarter and inversion symmetry finite element models	213
5.3	Geometry of global/local finite element analysis	214
5.4	Comparison of interlaminar stresses for nonlinear analysis	215
5.5	Computation of a vector normal to the interfacial surface	216
5.6	Midplane w/h displacement along $x = 0$ for a 2.0 in.	

square unsymmetric $[0_4/90_4]_t$ laminate ($\Delta T = -280°F$) 217

5.7 Comparison of interlaminar normal stress predictions along $x = 0$ for a 2.0 in. square unsymmetric $[0_4/90_4]_t$ laminate ($\Delta T = -280°F$) 218

5.8 Comparison of interlaminar shear stress predictions along $x = 0$ for a 2.0 in. square unsymmetric $[0_4/90_4]_t$ laminate ($\Delta T = -280°F$) 219

5.9 Comparison of u/L displacement predictions for the uniaxial extension of an isotropic bar 220

5.10 Comparison of transverse end w/h displacement predictions for a cantilever beam subjected to a transverse end load 221

5.11 Comparison of transverse end w/h displacement predictions for a cantilever beam subjected to uniformly distributed loading 222

5.12 Comparison of transverse end w/h displacement predictions for the elastica (cantilever beam subjected to a compressive axial end load) 223

5.13 Comparison of linear midplane w/h displacement predictions along $y = 0$ for a 2.0 in. square unsymmetric $[0_4/90_4]_t$ laminate ($\Delta T = -280°F$) 224

5.14 Comparison of nonlinear midplane w/h displacement predictions along $y = 0$ for a 2.0 in. square unsymmetric $[0_4/90_4]_t$ laminate ($\Delta T = -280°F$) 225

6.1 Displacement response within the plane $x = 0$ of the cross-ply laminates subjected to extensional loading 226

6.2 Displacement response within the plane $x = 0$ of the angle-ply laminates subjected to extensional loading 227

6.3 Midplane w/h displacement for a 4.0 in. square unsymmetric $[0_{50}/90_{50}]_t$ laminate ($u/a = +0.01$) 228

6.4 Midplane w/h displacement for a 4.0 in. square unsymmetric

$[+45_{50}/-45_{50}]_t$ laminate ($u/a = +0.01$) 229

6.5 Comparison with previous results [78] for σ_{zz} stress at the 0/90 interface for the 4.0 in. square symmetric $0_{50}/90_{50}$ laminates ($u/a = +0.01$) 230

6.6 Comparison with previous results [78] for τ_{yz} stress at the 0/90 interface for the 4.0 in. square symmetric $0_{50}/90_{50}$ laminates ($u/a = +0.01$) 231

6.7 σ_{zz} and S_{zz} stress along $x = 0$ at the 0/90 interface for the 4.0 in. square $0_{50}/90_{50}$ laminates ($u/a = +0.01$) 232

6.8 τ_{yz} and S_{yz} stress along $x = 0$ at the 0/90 interface for the 4.0 in. square $0_{50}/90_{50}$ laminates ($u/a = +0.01$) 233

6.9 Comparison with previous results [89] for σ_{zz} stress at the +45/–45 interface for the 4.0 in. square symmetric $+45_{50}/-45_{50}$ laminates ($u/a = +0.01$) 234

6.10 Comparison with previous results [89] for τ_{yz} stress at the +45/–45 interface for the 4.0 in. square symmetric $+45_{50}/-45_{50}$ laminates ($u/a = +0.01$) 235

6.11 Comparison with previous results [89] for τ_{xz} stress at the +45/–45 interface for the 4.0 in. square symmetric $+45_{50}/-45_{50}$ laminates ($u/a = +0.01$) 236

6.12 σ_{zz} and S_{zz} stress along $x = 0$ at the +45/–45 interface for the 4.0 in. square $+45_{50}/-45_{50}$ laminates ($u/a = +0.01$) 237

6.13 τ_{yz} and S_{yz} stress along $x = 0$ at the +45/–45 interface for the 4.0 in. square $+45_{50}/-45_{50}$ laminates ($u/a = +0.01$) 238

6.14 τ_{xz} and S_{xz} stress along $x = 0$ at the +45/–45 interface for the 4.0 in. square $+45_{50}/-45_{50}$ laminates ($u/a = +0.01$) 239

6.15 Midplane w/h displacement for a 2.0 in. square unsymmetric $[0_4/90_4]_t$ laminate ($u/a = +0.01$) 240

6.16 Midplane w/h displacement along $x = 0$ and $y = 0$ for a 2.0 in. square unsymmetric $[0_4/90_4]_t$ laminate ($u/a = +0.01$) 241

6.17 Midplane w/h displacement for a 2.0 in. square unsymmetric $[+45_4/-45_4]_t$ laminate ($u/a = +0.01$) 242

6.18 Midplane w/h displacement along $y/b = 1$ for a 2.0 in. square unsymmetric $[+45_4/-45_4]_t$ laminate ($u/a = +0.01$) 243

6.19 Midplane w/h displacement for a 2.0 in. square unsymmetric $[0_4/+45_4]_t$ laminate ($u/a = +0.01$) 244

6.20 Midplane w/h displacement along $x = 0$ and $y = 0$ for a 2.0 in. square unsymmetric $[0_4/+45_4]_t$ laminate ($u/a = +0.01$) 245

6.21 S_{zz} stress at the 0/90 interface for a 2.0 in. square unsymmetric $[0_4/90_4]_t$ laminate ($u/a = +0.01$) 246

6.22 S_{yz} stress at the 0/90 interface for a 2.0 in. square unsymmetric $[0_4/90_4]_t$ laminate ($u/a = +0.01$) 247

6.23 S_{xz} stress at the 0/90 interface for a 2.0 in. square unsymmetric $[0_4/90_4]_t$ laminate ($u/a = +0.01$) 248

6.24 σ_{zz} and S_{zz} stress along $x = 0$ at the 0/90 interface for the 2.0 in. square $0_4/90_4$ laminates ($u/a = +0.01$, local analysis) 249

6.25 τ_{yz} and S_{yz} stress along $x = 0$ at the 0/90 interface for the 2.0 in. square $0_4/90_4$ laminates ($u/a = +0.01$, local analysis) 250

6.26 S_{zz} stress at the +45/–45 interface for a 2.0 in. square unsymmetric $[+45_4/-45_4]_t$ laminate ($u/a = +0.01$) 251

6.27 S_{yz} stress at the +45/–45 interface for a 2.0 in. square unsymmetric $[+45_4/-45_4]_t$ laminate ($u/a = +0.01$) 252

6.28 S_{xz} stress at the +45/–45 interface for a 2.0 in. square unsymmetric $[+45_4/-45_4]_t$ laminate ($u/a = +0.01$) 253

6.29 σ_{zz} and S_{zz} stress along $x = 0$ at the +45/–45 interface for the 2.0 in. square $+45_4/-45_4$ laminates ($u/a = +0.01$, local analysis) .. 254

6.30 τ_{yz} and S_{yz} stress along $x = 0$ at the +45/–45 interface for the 2.0 in. square $+45_4/-45_4$ laminates ($u/a = +0.01$, local analysis) .. 255

6.31 τ_{xz} and S_{xz} stress along $x = 0$ at the +45/–45 interface for the 2.0 in. square $+45_4/-45_4$ laminates ($u/a = +0.01$, local analysis) .. 256

6.32 S_{xz} stress at the 0/+45 interface for a 2.0 in. square unsymmetric $[0_4/+45_4]_t$ laminate ($u/a = +0.01$) 257

6.33 S_{yz} stress at the 0/+45 interface for a 2.0 in. square unsymmetric $[0_4/+45_4]_t$ laminate ($u/a = +0.01$) 258

6.34 S_{xz} stress at the 0/+45 interface for a 2.0 in. square unsymmetric $[0_4/+45_4]_t$ laminate ($u/a = +0.01$) 259

6.35 σ_{xz} and S_{xz} stress along $x = 0$ at the 0/+45 interface for the 2.0 in. square $0_4/+45_4$ laminates ($u/a = +0.01$, local analysis) 260

6.36 τ_{yz} and S_{yz} stress along $x = 0$ at the 0/+45 interface for the 2.0 in. square $0_4/+45_4$ laminates ($u/a = +0.01$, local analysis) 261

6.37 τ_{xz} and S_{xz} stress along $x = 0$ at the 0/+45 interface for the 2.0 in. square $0_4/+45_4$ laminates ($u/a = +0.01$, local analysis) 262

6.38 Midplane w/h displacement for the 2.0 in. square symmetric $[90_4/0_4]_s$ and $[0_4/90_4]_s$ laminates ($u/a = -0.01$) 263

6.39 Load-displacement plots for a 2.0 in. square unsymmetric $[0_4/90_4]_t$ laminate ($u/a = -0.01$) 264

6.40 Midplane w/h displacement for a 2.0 in. square unsymmetric $[0_4/90_4]_t$ laminate ($u/a = -0.01$) 265

6.41 Load-displacement plots for a 2.0 in. square unsymmetric $[+45_4/-45_4]_t$ laminate ($u/a = -0.01$) 266

6.42 Midplane w/h displacement for a 2.0 in. square unsymmetric $[+45_4/-45_4]_t$ laminate ($u/a = -0.01$) 267

6.43 Load-displacement plots for a 2.0 in. square unsymmetric $[0_4/+45_4]_t$ laminate ($u/a = -0.01$) 268

6.44 Midplane w/h displacement for a 2.0 in. square unsymmetric $[0_4/+45_4]_t$ laminate ($u/a = -0.01$) 269

6.45 S_{zz} stress at the 0/90 interfaces for a 2.0 in. square symmetric $[90_4/0_4]_s$ laminate $(u/a = -0.01)$ 270

6.46 S_{yz} stress at the 0/90 interfaces for a 2.0 in. square symmetric $[90_4/0_4]_s$ laminate $(u/a = -0.01)$ 271

6.47 S_{xz} stress at the 0/90 interfaces for a 2.0 in. square symmetric $[90_4/0_4]_s$ laminate $(u/a = -0.01)$ 272

6.48 S_{zz} stress at the 0/90 interfaces for a 2.0 in. square symmetric $[0_4/90_4]_s$ laminate $(u/a = -0.01)$ 273

6.49 S_{yz} stress at the 0/90 interfaces for a 2.0 in. square symmetric $[0_4/90_4]_s$ laminate $(u/a = -0.01)$ 274

6.50 S_{xz} stress at the 0/90 interfaces for a 2.0 in. square symmetric $[0_4/90_4]_s$ laminate $(u/a = -0.01)$ 275

6.51 σ_{zz} and S_{zz} stress at the 0/90 interface for a 2.0 in. square unsymmetric $[0_4/90_4]_t$ laminate $(u/a = -0.01)$ 276

6.52 τ_{yz} and S_{yz} stress at the 0/90 interface for a 2.0 in. square unsymmetric $[0_4/90_4]_t$ laminate $(u/a = -0.01)$ 277

6.53 τ_{xz} and S_{xz} stress at the 0/90 interface for a 2.0 in. square unsymmetric $[0_4/90_4]_t$ laminate $(u/a = -0.01)$ 278

6.54 σ_{zz} and S_{zz} stress at the +45/–45 interface for a 2.0 in. square unsymmetric $[+45_4/-45_4]_t$ laminate $(u/a = -0.01)$ 279

6.55 τ_{yz} and S_{yz} stress at the +45/–45 interface for a 2.0 in. square unsymmetric $[+45_4/-45_4]_t$ laminate $(u/a = -0.01)$ 280

6.56 τ_{xz} and S_{xz} stress at the +45/–45 interface for a 2.0 in. square unsymmetric $[+45_4/-45_4]_t$ laminate $(u/a = -0.01)$ 281

6.57 σ_{zz} and S_{zz} stress at the 0/+45 interface for a 2.0 in. square unsymmetric $[0_4/+45_4]_t$ laminate $(u/a = -0.01)$ 282

6.58 τ_{yz} and S_{yz} stress at the 0/+45 interface for a 2.0 in. square unsymmetric $[0_4/+45_4]_t$ laminate $(u/a = -0.01)$ 283

6.59 τ_{zz} and S_{zz} stress at the 0/+45 interface for a 2.0 in. square unsymmetric $[0_4/+45_4]_t$ laminate ($u/a = -0.01$) 284

6.60 Principal curvature versus L/h for square unsymmetric $[0_4/90_4]_t$ laminates ($\Delta T = -280°F$) 285

6.61 Midplane w/h displacement for a 2.0 in. square unsymmetric $[0_4/90_4]_t$ laminate ($\Delta T = -280°F$) 286

6.62 Principal curvature versus L/h for square unsymmetric $[+45_4/-45_4]_t$ laminates ($\Delta T = -280°F$) 287

6.63 Midplane w/h displacement for a 2.0 in. square unsymmetric $[+45_4/-45_4]_t$ laminate ($\Delta T = -280°F$) 288

6.64 Principal curvature versus L/h for square unsymmetric $[0_4/+45_4]_t$ laminates ($\Delta T = -280°F$) 289

6.65 Midplane w/h displacement for a 2.0 in. square unsymmetric $[0_4/+45_4]_t$ laminate ($\Delta T = -280°F$) 290

6.66 S_{zz} stress at the 0/90 interface for a 2.0 in. square unsymmetric $[0_4/90_4]_t$ laminate ($\Delta T = -280°F$) 291

6.67 S_{yz} stress at the 0/90 interface for a 2.0 in. square unsymmetric $[0_4/90_4]_t$ laminate ($\Delta T = -280°F$) 292

6.68 S_{xz} stress at the 0/90 interface for a 2.0 in. square unsymmetric $[0_4/90_4]_t$ laminate ($\Delta T = -280°F$) 293

6.69 σ_{xz} and S_{xz} stress along $x = 0$ at the 0/90 interface for the 2.0 in. square $0_4/90_4$ laminates ($\Delta T = -280°F$, local analysis) 294

6.70 σ_{xz} and S_{xz} stress along $y = 0$ at the 0/90 interface for the 2.0 in. square $0_4/90_4$ laminates ($\Delta T = -280°F$, local analysis) 295

6.71 τ_{yz} and S_{yz} stress along $x = 0$ at the 0/90 interface for the 2.0 in. square $0_4/90_4$ laminates ($\Delta T = -280°F$, local analysis) 296

6.72 τ_{zz} and S_{zz} stress along $y = 0$ at the 0/90 interface for the 2.0 in. square $0_4/90_4$ laminates ($\Delta T = -280°F$, local analysis) 297

6.73 S_{zz} stress at the +45/–45 interface for a 2.0 in. square unsymmetric $[+45_4/-45_4]_t$ laminate ($\Delta T = -280°F$) 298

6.74 S_{yz} stress at the +45/–45 interface for a 2.0 in. square unsymmetric $[+45_4/-45_4]_t$ laminate ($\Delta T = -280°F$) 299

6.75 S_{zz} stress at the +45/–45 interface for a 2.0 in. square unsymmetric $[+45_4/-45_4]_t$ laminate ($\Delta T = -280°F$) 300

6.76 σ_{zz} and S_{zz} stress along $x = 0$ at the +45/–45 interface for the 2.0 in. square $+45_4/-45_4$ laminates ($\Delta T = -280°F$, local analysis) 301

6.77 σ_{zz} and S_{zz} stress along $y = 0$ at the +45/–45 interface for the 2.0 in. square $+45_4/-45_4$ laminates ($\Delta T = -280°F$, local analysis) 302

6.78 τ_{yz} and S_{yz} stress along $x = 0$ at the +45/–45 interface for the 2.0 in. square $+45_4/-45_4$ laminates ($\Delta T = -280°F$, local analysis) 303

6.79 τ_{yz} and S_{yz} stress along $y = 0$ at the +45/–45 interface for the 2.0 in. square $+45_4/-45_4$ laminates ($\Delta T = -280°F$, local analysis) 304

6.80 τ_{xz} and S_{xz} stress along $x = 0$ at the +45/–45 interface for the 2.0 in. square $+45_4/-45_4$ laminates ($\Delta T = -280°F$, local analysis) 305

6.81 τ_{xz} and S_{xz} stress along $y = 0$ at the +45/–45 interface for the 2.0 in. square $+45_4/-45_4$ laminates ($\Delta T = -280°F$, local analysis) 306

6.82 S_{zz} stress at the 0/+45 interface for a 2.0 in. square unsymmetric $[0_4/+45_4]_t$ laminate ($\Delta T = -280°F$) 307

6.83 S_{yz} stress at the 0/+45 interface for a 2.0 in. square

unsymmetric $[0_4/+45_4]_t$ laminate ($\Delta T = -280°F$) 308

6.84 S_{zz} stress at the 0/+45 interface for a 2.0 in. square unsymmetric $[0_4/+45_4]_t$ laminate ($\Delta T = -280°F$) 309

6.85 σ_{zz} and S_{zz} stress along $x = 0$ at the 0/+45 interface for the 2.0 in. square $0_4/+45_4$ laminates ($\Delta T = -280°F$, local analysis) 310

6.86 σ_{zz} and S_{zz} stress along $y = 0$ at the 0/+45 interface for the 2.0 in. square $0_4/+45_4$ laminates ($\Delta T = -280°F$, local analysis) 311

6.87 τ_{yz} and S_{yz} stress along $x = 0$ at the 0/+45 interface for the 2.0 in. square $0_4/+45_4$ laminates ($\Delta T = -280°F$, local analysis) 312

6.88 τ_{yz} and S_{yz} stress along $y = 0$ at the 0/+45 interface for the 2.0 in. square $0_4/+45_4$ laminates ($\Delta T = -280°F$, local analysis) 313

6.89 τ_{xz} and S_{xz} stress along $x = 0$ at the 0/+45 interface for the 2.0 in. square $0_4/+45_4$ laminates ($\Delta T = -280°F$, local analysis) 314

6.90 τ_{xz} and S_{xz} stress along $y = 0$ at the 0/+45 interface for the 2.0 in. square $0_4/+45_4$ laminates ($\Delta T = -280°F$, local analysis) 315

A.1 The deformational coupling relationships of laminated anisotropic plates 316

D.1 Global finite element model used for the analysis of 2.0 in. square symmetric and unsymmetric laminates 317

D.2 Global finite element model used for the geometrically nonlinear analysis of 2.0 in. square symmetric laminates subjected to compressive loading 318

D.3 Local finite element model used for the analysis of 2.0 in. square symmetric and unsymmetric laminates 319

D.4 Global finite element model used for comparisons with previous results for 4.0 in. square symmetric and unsymmetric laminates....320

D.5 Global finite element model used for the preliminary analysis of 2.0 in. square unsymmetric laminates....321

D.6 Global finite element model used for the preliminary analysis of 4.0 in. square unsymmetric laminates....322

D.7 Global finite element model used for the preliminary analysis of 6.0 in. square unsymmetric laminates....323

E.1 Midplane w/h displacement along $x = 0$ and $y = 0$ for a 2.0 in. square unsymmetric $[0_4/90_4]_t$ laminate ($\Delta T = -280°F$)....324

E.2 Midplane w/h displacement along $x = 0$ and $y = 0$ for a 4.0 in. square unsymmetric $[0_4/90_4]_t$ laminate ($\Delta T = -280°F$)....325

E.3 Midplane w/h displacement along $x = 0$ and $y = 0$ for a 6.0 in. square unsymmetric $[0_4/90_4]_t$ laminate ($\Delta T = -280°F$)....326

LIST OF SYMBOLS

SYMBOLS	DESCRIPTION
a, b	rectangular plate half-lengths in the x and y directions
A	cross-sectional area of a beam
A_{ij}	membrane stiffnesses for a laminated plate
B_{ij}	membrane-flexural stiffnesses for a laminated plate
$[{}_0^t B_{L0}]$	first component of linear strain-displacement matrix
$[{}_0^t B_{L1}]$	second component of linear strain-displacement matrix
$[{}_0^t B_L]$	linear strain-displacement matrix, $[{}_0^t B_{L0}] + [{}_0^t B_{L1}]$
$[{}_0^t B_{NL}]$	nonlinear strain-displacement matrix
$[{}_0^t \tilde{B}_{NL}]$	nonlinear strain-displacement submatrix
c	center of Mohr's circle of curvature, $\frac{1}{2}(\kappa_x + \kappa_y)$
${}_0^t C_{ij}$	right Cauchy-Green deformation tensor
${}_0 C_{ijkl}$	linear elastic constitutive coefficients
$[{}_0 C]$	linear elastic constitutive matrix
d	single layer or lamina thickness
D_{ij}	flexural stiffnesses for a laminated plate
D_{ij}^*	reduced flexural stiffnesses for a laminated plate
${}_0 e_{ij}$	linear strain tensor
E	Young's modulus for an isotropic material
E_1, E_2, E_3	Young's moduli for an orthotropic material

${}^{t}_{0}E_{ij}$	Green-Lagrange nonlinear strain tensor
E_{xx}, E_{yy}, E_{zz}	normal components of Green-Lagrange strain
E_{yz}, E_{xz}, E_{xy}	shear components of Green-Lagrange strain
${}^{t}_{0}E^{R}_{ij}$	reduced three-dimensional nonlinear strain
${}^{t}_{0}E^{T}_{ij}$	thermal strain due to free thermal expansion
${}^{t}_{0}f_{i}$	body force per unit volume in x_i direction
F	concentrated force
${}^{t}F_{i}$	force in x_i direction
${}^{t}_{0}\tilde{F}_{i}$	pseudo force in x_i direction, ${}^{0}_{t}x_{i,j}{}^{t}F_{i}$
$\{{}^{t}_{0}F\}$	global residual force vector
G	shear modulus for an isotropic material
G_{23}, G_{13}, G_{12}	shear moduli for an orthotropic material
h	laminated plate thickness
I	flexural moment of inertia for an isotropic beam
J	Jacobian of a coordinate transformation
J^{*}	inverse of the Jacobian
$[{}^{t}_{0}K]$	global stiffness matrix
$[{}^{t}_{0}K_{L}]$	linear stiffness matrix
$[{}^{t}_{0}K_{NL}]$	nonlinear stiffness matrix
L	square laminated plate length ($L = 2a = 2b$)
M_x, M_y, M_{xy}	flexural stress resultants

M_x^T, M_y^T, M_{xy}^T	thermal flexural stress resultants
n_i	components of unit normal vector
n_x, n_y, n_z	components of unit normal vector
N_x, N_y, N_{xy}	membrane stress resultants
N_x^T, N_y^T, N_{xy}^T	thermal membrane stress resultants
P, Q	material points within an elastic body
q_i	generalized coordinates for an elastic body
Q_{ij}	reduced lamina stiffnesses w.r.t. X_1, X_2, X_3 axes
$\bar{Q}_{ij}$	transformed reduced lamina stiffnesses w.r.t. x, y, z axes
r	radius of Mohr's circle of curvature, $\frac{1}{2}\sqrt{(\kappa_x - \kappa_y)^2 + \kappa_{xy}^2}$
$\{^{t+\Delta t}R\}$	global external force vector
s, ds	arc length, differential arc length
S, dS	surface area, differential surface area
S_1	surface on which ${}^t\bar{u}_i$ are prescribed
S_2	surface on which ${}^t_0\bar{t}_i$ are prescribed
${}^t_0S_{ij}$	second Piola-Kirchhoff stress tensor
S_{xx}, S_{yy}, S_{zz}	normal components of second Piola-Kirchhoff stresses
S_{yz}, S_{zz}, S_{xy}	shear components of second Piola-Kirchhoff stresses
$[{}^t_0S]$	second Piola-Kirchhoff stress matrix
$[{}^t_0\tilde{S}]$	second Piola-Kirchhoff stress submatrix
$\{{}^t_0\hat{S}\}$	second Piola-Kirchhoff stress vector

t	time
${}^t_0 t_i$	traction vector
${}^t_0 \bar{t}_i$	prescribed traction in x_i direction on surface S_2
t_x, t_y, t_z	components of stress acting upon an interfacial surface
t_N, t_S, t_T	normal, shear, and total components of interfacial stresses
T	Temperature
ΔT	change in temperature
T_g	glass transition temperature
${}^t_0 T_{ij}$	first Piola-Kirchhoff stress tensor
u, v, w	displacements in the x, y, and z directions, respectively
$u^\circ, v^\circ, w^\circ$	plate reference surface displacements
u_i	displacements in x_i coordinate directions
${}^t\bar{u}_i$	prescribed displacement in x_i direction on surface S_1
u_i^k	u_i element displacement at the kth node
$u_{i,j}$	displacement gradient
$\{u\}$	incremental nodal displacement vector
$\|\|u\|\|$	Euclidean norm of the nodal displacement vector
U_e	elastic strain energy of the body
V, dV	volume, infinitesimal volume
V_e	potential energy due to external forces
W^i	Gauss-Legendre quadrature weights

x, y, z	global laminated plate coordinates
x_i	coordinates
X_1, X_2, X_3	principal material coordinates
x_i^k	global coordinates of the kth node
${}_0^t x_{i,j}$	deformation gradient tensor
${}_t^0 x_{i,j}$	spatial deformation gradient tensor
α_{ij}	coefficients of thermal expansion
$\alpha_x, \alpha_y, \alpha_{xy}$	coefficients of thermal expansion
$\alpha_1, \alpha_2, \alpha_3$	coefficients of thermal expansion for an orthotropic material
β	angle
$\gamma_{yz}, \gamma_{zx}, \gamma_{xy}$	shear components of engineering strain
δ	variational operator
δ_{ij}	Kronecker delta
ϵ	engineering strain
$\epsilon_{xx}, \epsilon_{yy}, \epsilon_{zz}$	normal components of engineering strain
$\epsilon_x^\circ, \epsilon_y^\circ, \gamma_{xy}^\circ$	plate reference surface strains
ϵ_{ijk}	permutation symbol
${}_0\eta_{ij}$	nonlinear components of Green-Lagrange strain
$\eta_{xy,x}$	coefficient of mutual influence
θ	lamina angle of orientation
θ_x	orientation angle for interfacial surface

θ_y	orientation angle for interfacial surface
$\kappa_x, \kappa_y, \kappa_{xy}$	plate reference surface curvatures
κ_1, κ_2	plate reference surface principal curvatures
λ	stretch
ν	Poisson's ratio for an isotropic material
$\nu_{23}, \nu_{13}, \nu_{12}$	Poisson's ratios for an orthotropic material
ν_{xy}	Poisson's ratio for single layer or lamina
ξ_i	natural element coordinates
Π	total potential energy of the elastic body
${}^0\rho$	density in the initial (undeformed) configuration
${}^t\rho$	density in the current (deformed) configuration
${}^t\sigma_{ij}$	Cauchy stress tensor
${}^t\sigma'_{ij}$	transformed Cauchy stress tensor
$\sigma_{xx}, \sigma_{yy}, \sigma_{zz}$	normal components of Cauchy stresses
$\tau_{yz}, \tau_{zx}, \tau_{xy}$	shear components of Cauchy stresses
τ_{zn}	interlaminar shear stress acting normal to the free edge
τ_{zt}	interlaminar shear stress acting parallel to the free edge
ϕ	orientation angle for directions of principle curvature
ψ^k	element interpolation (shape) function for the kth node
${}_0\omega_{ij}$	linear rotation tensor

Chapter 1
INTRODUCTION

1.1 Introductory Remarks

During the past twenty-five years, composite materials have played a leading role in the advancement of aerospace structures technology. The significant gains in developing lighter, more efficient load-carrying structures can be attributed to the inherent advantages that composite materials have over conventional metallic materials. These advantages include:

- higher stiffness-to-weight ratio (specific stiffness)
- higher strength-to-weight ratio (specific strength)
- directionally dependent material properties (tailorability)

A minimum weight design is a primary objective in aerospace structures; therefore, the high specific stiffness and strength properties of composite materials are ideal for aerospace applications. The directionally dependent material properties can also be used to produce more efficient load-carrying structures. Beyond efficiency considerations, the directional properties of composite materials can be used to produce structures with unique coupling characteristics in the deformational response. This coupling behavior is referred to as laminate, mechanical, elastic, or thermoelastic coupling and it is unique to composite materials. Since this coupling behavior may be present in the mechanical, thermal, or hygroscopic response, it will be referred to herein as *laminate coupling* to distinguish it from *geometric coupling* which will be discussed near the end of this chapter. For the linear thermoelastic response of laminated anisotropic plates, laminate coupling is a linear coupling effect which may be present in the membrane response, flexural response, or in a combination of both membrane and flexural response. The level of coupling which exists within a given laminate is dependent upon the material properties, laminate

stacking sequence, layer thickness, and plate geometry. (For a brief review of the coupling behavior of laminated anisotropic plates, refer to appendix A).

Unsymmetric laminates exhibit laminate membrane-flexural coupling; that is, coupling between in-plane deformation and out-of-plane (transverse) deflections. This coupling is caused by a mismatch in material properties about the geometric midplane of the laminate. Such coupling can cause an unsymmetric laminate to deflect out-of-plane when subjected to in-plane loading. The membrane-flexural coupling of unsymmetric laminates can be used to design a composite structure which will deform into a favorable configuration in response to an anticipated external load condition. This coupling ability can be beneficial in the following applications:

- geometric (such as in achieving a desired shape)
- structural (such as redirecting the load path)
- aerodynamic (as in aeroelastic tailoring)

Unsymmetric laminates may not only be used specifically for their unique coupling characteristics, but these laminates can also arise in other applications. Locally unsymmetric laminates sometimes arise in the design of stiffened panels. Ply drop-offs, which occur frequently in practical design applications, often result in locally unsymmetric laminates. Finally, damage incurred during service, such as from impact or delamination, can result in an unsymmetric laminate.

A key factor to the success of any structural design is the accurate prediction of the structural response to the service environment. A major concern to designers and analysts of composite structures is the presence of interlaminar stresses. The interlaminar components of stress are those stresses which act upon planes parallel to the interfacial surfaces between the layers of the laminate (Figure 1.1). For fiber-reinforced composite laminates, these stresses are transferred between layers through the resin which holds the laminate together. The resin or matrix material possesses relatively low stiffness and strength properties in comparison to that of

the fibers. The weak link in this structural system is typically the bond between the fiber and the matrix. If interlaminar stresses become large, they can initiate failure at a fiber/matrix interface which can propagate into delamination; therefore interlaminar stresses are critical because such delaminations can propagate through the laminate and bring about the ultimate failure of the structure.

A lot of what is known about interlaminar stresses has been acquired through the study of what is known as the *free edge problem*. The free edge problem considers the response of a flat, finite-width symmetric composite laminate subjected to in-plane mechanical and/or hygrothermal loading. The symmetric laminate is idealized to be constructed of bonded layers of material in which the material properties vary from layer to layer. Away from the edges of the laminate, a state of plane stress and plane strain exists. This is consistent with the Kirchhoff-Love assumptions of classical plate theory. However, near the free edges of the laminate, the stress field is three-dimensional. Interlaminar stresses are known to occur near these free edges in a boundary layer region with an approximate width of one laminate thickness.

These interlaminar stresses are caused by the difference or mismatch in material properties between adjacent layers in the presence of a free edge. As external loading is applied to the composite laminate, each layer attempts to react in accordance with its characteristic material properties. However, since these layers are bonded together, continuity of displacements and stress equilibrium must be maintained across each interface. Along the free edges of the laminate, the surface is traction free. With these traction free conditions, each layer must react with adjacent layers in order to establish local equilibrium. These reactions take the form of interlaminar stresses.

Although significant progress has been made in the study of interlaminar stresses in symmetric laminates, little is known about those which occur in unsymmetric laminates. As mentioned previously, the laminate membrane-flexural

coupling of an unsymmetrically laminated plate will cause the plate to deflect out-of-plane when subjected to external loading. As the out-of-plane deflections become large, i.e., on the order of the laminate thickness, geometrically nonlinear strain-displacement relationships are required to accurately predict these large displacements and large rotations. This introduces an additional nonlinear coupling effect between the membrane and flexural response. This coupling will be referred to as *geometric coupling* and it is accounted for by the geometrically nonlinear kinematic description. Due to the existence of both laminate and geometric coupling, the mechanics of deformation in unsymmetric laminates, particularly near free edges, can be considerably more complex than for symmetric laminates.

1.2 Objectives of the Study

The purpose of this study is to investigate the interlaminar stress fields within unsymmetrically laminated plates and to determine the effects upon the stress-deformational response of laminate membrane-flexural coupling and geometric nonlinearity. The study focuses upon the linear thermoelastic response of thin square laminated composite plates subjected to extensional, compressive, and thermal loading. The nonlinear three-dimensional boundary value problems are formulated from the theory of nonlinear elasticity. Approximate solutions to the nonlinear boundary value problems are determined using the finite element method and Newton's method.

The main objectives of this study are as follows:

(1) Compare and contrast the interlaminar stress fields between comparable symmetric and unsymmetric laminates to determine the effects of laminate membrane-flexural coupling upon the interlaminar stress fields in unsymmetric laminates.

(2) Compare the predictions of geometrically linear and nonlinear theory to determine the effects of geometric nonlinearity upon the stress-deformational response.

(3) Develop a geometrically nonlinear analysis capability for predicting the three-dimensional, linear thermoelastic, finite deformational response of laminated anisotropic materials subjected to mechanical, thermal, and/or hygroscopic loading.

A review of the literature is presented in Chapter 2 which focuses upon the behavior of unsymmetrically laminated plates and the interlaminar stresses which occur in laminated plates. A brief discussion of the approximate analysis developed for this study is provided at the end of Chapter 2. Chapter 3 outlines the study parameters which include material properties, plate geometry, laminate stacking sequences, loading conditions, and boundary conditions. Chapter 4 presents the theoretical formulation of the governing equations and boundary conditions for the nonlinear three-dimensional boundary value problem. Chapter 5 provides a discussion of the finite element formulation of the nonlinear boundary value problem, computational aspects of the approximate solution, and results from numerical examples designed to evaluate the analytical approach. Chapter 6 contains the presentation and discussion of the numerical results for the investigation. Chapter 7 closes with the conclusions of the investigation and recommendations for future studies.

Chapter 2
REVIEW OF THE LITERATURE

The existing literature which pertains to this investigation may be grouped into two main areas of interest:

(1) Unsymmetrically laminated plates

(2) Interlaminar stresses in laminated plates

A review of the more significant contributions to each area of interest is provided in Sections 2.1 and 2.2. A discussion of the present approximate analysis is provided in Section 2.3. A summary of the review is found at the end of the chapter in Section 2.4.

2.1 Unsymmetrically Laminated Plates

Early Investigations

One of the first theoretical investigations of unsymmetric laminates was conducted by Timoshenko in 1925 [1]. Timoshenko considered the analysis of bimetallic thermostats subjected to a uniform change in temperature. The analysis was based upon the assumptions of Euler-Bernoulli beam theory and included calculations of stresses, deflections, and buckling temperatures. The stress calculations included axial and bending stresses with a brief discussion of the existence and approximate magnitudes of interlaminar normal and shear stresses located near the ends of the laminate.

An analysis of unsymmetrically laminated plates was proposed by Smith [2] in 1953. This study examined thin laminated plates composed of orthotropic layers with arbitrary orientations. The proposed analysis was a two-dimensional plate theory based upon the Kirchhoff-Love assumptions of classical plate theory. Smith concluded that the laminate behaved as a *homogeneous* orthotropic plate and

failed to account for the laminate membrane-flexural coupling of unsymmetrically laminated plates.

Classical Laminated Plate Theory

In 1961, Reissner and Stavsky [3] presented a two-dimensional plate theory that correctly accounted for the laminate membrane-flexural coupling of unsymmetrically laminated plates. The proposed plate theory was based upon the Kirchhoff-Love kinematic assumptions of classical plate theory and incorporated the heterogeneity of the plate into the analysis. This investigation proposed the foundation for what is known as classical laminated plate (CLP) theory. Reissner and Stavsky formulated several solutions using Airy stress functions to examine the effects of membrane-flexural coupling. They presented solutions for $[+\theta/-\theta]_t$ laminated plates subjected to (a) uniform membrane force N_x, (b) uniform bending moment M_x, and (c) sinusoidal transverse load. Numerical examples compared solutions using: (1) the theory proposed by Smith [2], (2) CLP theory neglecting the membrane-flexural coupling terms ($B_{ij} = 0$), and (3) CLP theory with no terms neglected. The considerable differences between the results clearly emphasized the importance of accounting for laminate membrane-flexural coupling. Reissner and Stavsky also presented the governing equations for the finite deflection of generally laminated plates which included the von Karman nonlinear strain-displacement equations [4]. The governing equations characterized the combined membrane-flexural coupling between the linear laminate coupling effect caused by the unsymmetric construction and the nonlinear geometric coupling effect caused by the nonlinear kinematic description. This nonlinear geometric coupling effect in laminated plates is the same type of coupling effect which was well known in the finite deflection theory of homogeneous isotropic plates. Stavsky expanded upon this work in several additional studies [5-9].

Dong, et al [10] used the Airy stress function formulation to find the solutions for more general laminates subjected to several types of mechanical loading conditions, including the cylindrical bending of a thin narrow laminate. They also presented equations for the calculation of interlaminar shear stresses based upon equilibrium considerations. A two-dimensional shell theory for the membrane and flexural behavior of thin generally laminated anisotropic shells was presented by Dong, Pister, and Taylor [11] in 1962. The small deflection theory accounted for the heterogeneity of the the shell and laminate membrane-flexural coupling effects.

In 1969, Whitney and Leissa [12] presented the governing equations of CLP theory which included inertia terms, thermal stresses, and the von Karman nonlinear strain-displacement equations for finite deflections. A Lagrangian kinematic description was used in which all tensorial quantities are referenced to the initial, undeformed configuration of the plate. The governing equations in terms of displacements are three coupled nonlinear partial differential equations and these equations possess the combined linear laminate and nonlinear geometric membrane-flexural coupling effects described by Reissner and Stavsky [3].

Early Studies Using Linear CLP Theory

Whitney conducted a number of investigations into the behavior of unsymmetrically laminated plates [12-18]. Using linear CLP theory, Whitney studied the effects of laminate membrane-flexural coupling upon the response of unsymmetrically laminated plates. He derived closed-form solutions for the bending, buckling, and vibration of unsymmetrically laminated plates using double Fourier series. Whitney's work focused upon the response of antisymmetrically laminated cross-ply and angle-ply rectangular plates. His solutions considered a variety of mechanical loading conditions and edge boundary conditions. His results showed that, in general, laminate membrane-flexural coupling led to an increase in transverse deflections, a decrease in fundamental vibrational frequencies, and a decrease in buckling loads. Thus the effect of laminate membrane-flexural coupling is to reduce the effective

stiffness of the plate. In addition, as the membrane-flexural coupling decreases, $B_{ij} \rightarrow 0$, and the level of lamina orthotropy decreases, $E_{11}/E_{22} \rightarrow 1$, the analytical results approach those of a homogeneous orthotropic plate.

Jones [19] and Jones, et al [20] studied the buckling and vibration of unsymmetrically laminated cross-ply and angle-ply plates. Using linear CLP theory, closed form solutions were derived for the buckling loads and vibration frequencies of simply-supported rectangular laminated plates. Like Whitney, Jones also found that laminate membrane-flexural coupling substantially decreases buckling loads and fundamental vibrational frequencies. For antisymmetric laminates of a given laminate thickness, he found that the effect of coupling dies out rapidly as the number of layers is increased. However, he also determined that for generally unsymmetric laminates of a given laminate thickness, the effect of coupling dies out slowly as the number of layers is increased. He concluded that, in general, laminate membrane-flexural coupling should not be neglected in the analysis of unsymmetric laminates.

Ashton [21] proposed an approximate method of analysis for the bending of unsymmetrically laminated plates subjected to transverse loading. Using the constitutive relationship for the laminated plate, he derived an approximate solution in which the membrane-flexural behavior becomes uncoupled and the flexural stiffness matrix of the laminate $[D]$ is replaced with a reduced flexural stiffness matrix $[D^*] = [D] - [B][A]^{-1}[B]$. Deflection calculations using the reduced flexural stiffness approach were compared with exact results obtained from Whitney [14]. Ashton's approximate solution for simply-supported unsymmetric cross-ply and angle-ply laminates compared well with Whitney's results. A more detailed discussion of the results from linear CLP theory may be found in references [22] and [23]. The remainder of this section focuses upon the results for studies investigating the bending, extensional, buckling, postbuckling, and thermal response of unsymmetrically laminated plates.

Bending and Extensional Loading

Experimental and analytical studies of the finite deflections of unsymmetric laminates subjected to bending and extension have been conducted by several investigators [24-27]. Numerical studies have been conducted using CLP theory with the von Karman nonlinear strain-displacement equations. Pao [24] presented results for the large deflection of unsymmetric laminates subjected to simple bending. Chia [25] presented results for the large deflection of unsymmetric laminates subjected to uniform transverse loading. Zagloul and Kennedy [26] presented both experimental and numerical results for the deflection of unsymmetric laminates subjected to transverse loading. The predicted nonlinear deflections of Zagloul and Kennedy compared fairly well with the experimental results. Sun and Chin [27] presented numerical results for antisymmetric laminates subjected to in-plane and/or uniform transverse loading. The results of the studies [25-27] for extensional and/or uniform transverse loading demonstrated the stiffening effect of geometric nonlinearity which led to an overprediction of out-of-plane deflections by linear theory as compared to nonlinear theory.

Buckling Behavior

In addition to the studies discussed previously [12-13,15-20], a number of experimental and analytical investigations have been conducted into the buckling behavior of unsymmetrically laminated plates [28-34]. Results have been obtained for unsymmetric laminates subjected to uniaxial compression with a variety of edge conditions:

(a) cccc - all edges clamped [29,32-33];

(b) cscs - loaded edges clamped, unloaded edges simply-supported [29,32-33];

(c) cfcf - loaded edges clamped, unloaded edges free [32];

(d) ssss - all edges simply supported [30-31,34]; and

(e) sfsf - loaded edges simply-supported, unloaded edges free [28-30,34].

The initial curvature of the unsymmetric laminates was usually eliminated by constructing the panels using a room-temperature bonding procedure [29-33]. Linear CLP theory was used to predict the critical buckling loads with the following assumptions:

(a) membrane-flexural terms neglected, $B_{ij} = 0$ [28-31];

(b) reduced flexural stiffness approximation [28-31]; and

(c) membrane-flexural terms present [32-33].

The results of these and earlier studies have shown that neglecting the membrane-flexural coupling terms substantially overpredicts the critical buckling load, in some cases by a factor of two or more. The results have also shown that although the reduced flexural stiffness approximation yields good results for some cases, the use of this approximate method can lead to erroneous predictions.

Although critical buckling loads can be calculated for unsymmetric laminates using linear CLP plate theory, as shown by Leissa [35], an unsymmetric laminate will deform immediately out-of-plane under in-plane loading unless additional forces in the form of edge moments, transverse shearing forces, and/or transverse pressure are provided. Since initially flat unsymmetric laminates deflect immediately out-of-plane upon loading, the classical bifurcation buckling behavior observed in symmetric laminates does not occur for compression-loaded unsymmetric laminates and the experimental buckling loads are difficult to determine. The load-deflection behavior of unsymmetric laminates is similar to that of eccentrically loaded plates or plates with initial curvature. Due to this similar load-deflection behavior, the method of Southwell [36] has been used successfully by a number of researchers [29-34] to determine experimental buckling loads for unsymmetric laminates.

Postbuckling Behavior

A number of analytical studies of the postbuckling behavior of unsymmetrically laminated plates have been conducted. The numerical results discussed in this subsection were determined using CLP theory and the von Karman nonlinear strain-displacement equations. Numerical postbuckling results have been obtained for a variety of unsymmetric laminates with ssss and cccc edge conditions.

Monforton [37] used the finite element method to determine the postbuckling response of unsymmetric laminates. Monforton's numerical results compared quite well with the experimental buckling loads presented by Mandel [30] and the numerical buckling loads predicted by Chamis [28]. Turvey and Wittrick [38] presented numerical results for unsymmetric angle-ply laminates with ssss edge conditions subjected to uniform transverse loading or uniaxial compression loading. Turvey and Wittrick studied the effects of laminate membrane-flexural coupling upon the response of these laminates. They determined that laminate membrane-flexural coupling reduced the critical buckling load, but had a small effect upon the postbuckled stiffness of unsymmetric angle-ply laminates. Harris [39] also studied the postbuckling behavior of unsymmetric angle-ply laminates with ssss edge conditions subjected to a variety of load conditions. Harris concluded that laminate membrane-flexural coupling effected not only the buckling loads and also the shapes of the buckling modes.

Chia and Prabhakara [40] presented numerical results for unsymmetric cross-ply and angle-ply laminates with cccc edge conditions subjected to uniform uniaxial and biaxial edge compression. Chia and Prabhakara also presented results for unsymmetric angle-ply laminates with ssss edge conditions subjected to uniform uniaxial compression. Chia and Prabhakara provided a variety of numerical results which include the effects of material properties and plate aspect ratio. In a later study, Prabhakara [41] provided results for unsymmetric cross-ply laminates with ssss edge conditions. Prabhakara found that the out-of-plane deflections at the

plate center were predicted by linear theory to be much higher than those predicted by nonlinear theory. Prabhakara also found that the membrane force at the center of the plate in the direction of loading increases until the buckling load is reached and then decreases as the in-plane compression is further increased. He also determined that the maximum membrane force is compressive, acts in the direction of loading, and occurs at the midpoint along the unloaded edges.

Chan [42] presented numerical results for unsymmetric cross-ply, angle-ply, and $[0/15/0/15]_t$ laminates with cccc and ssss edge conditions subjected to uniaxial compression. Chan reported that for the plates which bifurcate (the angle-ply and 0/15 laminates), there is considerably more load-carrying capability beyond the initial buckling load. Zhang and Matthews [43] presented numerical results for unsymmetric cross-ply laminates with ssss edge conditions subjected to uniaxial compression and unsymmetric angle-ply laminates with ssss edge conditions subjected to shear loading. They reported that both of these laminates exhibited nonbifurcational buckling behavior.

Jenson and Lagace [33] conducted an experimental and analytical investigation of the buckling and postbuckling behavior of both symmetric and unsymmetric laminates. Jenson and Lagace presented results for a variety of unsymmetric laminates with cccc and cscs edge conditions subjected to uniaxial compression. Buckling loads were predicted using linear CLP theory with membrane-flexural terms, B_{ij}, present. A nonlinear Ritz analysis, based upon CLP theory and the von Karman strain-displacement equations, was used to predict the finite deflections of the unsymmetric laminates.

Jenson and Lagace concluded that extensional-bending coupling can cause unsymmetric laminates to buckle into secondary mode shapes. The postbuckling behavior of a symmetric $[0/+45/0/+45/0]_s$ laminate which possesses extensional-shear and bending-twisting coupling was observed to be nearly identical to that of an unsymmetric $[0/+45/0/-45/0]_t$ laminate which possesses extensional-twist

coupling. This was especially true at higher load levels and was attributed to the geometric membrane-flexural coupling effects which become quite strong for large deflections. The authors also speculated that the more restrictive the side boundary conditions, the stronger the effect of laminate coupling, since these conditions give rise to addition stresses which increase the coupling effects. Finally, the authors concluded that the laminate coupling of an unsymmetric laminate has a strong effect on the buckling and postbuckling behavior of the laminate and that a geometrically nonlinear analysis is required to fully quantify the behavior of unsymmetrically laminated plates.

An excellent discussion of previous analytical results for the finite deflections of elastic plates may be found in [44]. This reference [44] includes a detailed discussion of results for the buckling and postbuckling behavior of unsymmetrically laminated plates. An excellent review of the many buckling and postbuckling studies which have been conducted for composite plates may be found in [45].

Thermal Loading

Several investigations have been conducted into the prediction of out-of-plane deflections and residual stresses in unsymmetric laminates as a result of the curing process. Pagano and Hahn [46] conducted an experimental and analytical study of the residual thermal stresses due to curing within composite laminates. Linear CLP plate theory was used to predict stresses and deflections in laminates taken from cure to room-temperature. The out-of-plane deflections of unsymmetric angle-ply laminates at room-temperature were measured experimentally and determined using linear CLP theory. All predicted deflections were within 15 percent of the measured values, with most of the predictions being less than the observed value. These calculations were based upon an assumed stress-free temperature of 250 °F.

Pagano and Hahn also carried out calculations to study the impact of residual stresses on laminate strength. Based upon their calculations (linear CLP), they speculated that residual curing stresses may initiate first-ply failure at as much as

one-half the in-plane load level. They were careful to point out that interlaminar stresses (not accounted for in linear CLP) near the free edges of the laminate may cause an initiation of failure at an even lower load level. They also point out that moisture absorption will tend to relieve residual thermal stresses.

Hyer has investigated the cured shapes of unsymmetric laminates at room-temperature both experimentally and analytically [47–50]. Hyer used a geometrically nonlinear two-dimensional plate theory to predict the shapes of unsymmetric cross-ply laminates at room temperature. The nonlinear plate analysis was based upon CLP theory and the von Karman nonlinear strain-displacement equations. An approximate solution to the governing equations was obtained using the Ritz method. The analysis idealized the laminate as a linear thermoelastic material subjected to a uniform decrease in temperature. Hyer's results demonstrated the importance of incorporating a geometrically nonlinear kinematic description into the thermal analysis of unsymmetric laminates. The out-of-plane deflections are overpredicted by linear theory as compared to those predicted by nonlinear theory. The results showed that the shapes predicted by geometrically nonlinear theory were quite different than those predicted by linear CLP theory. Some of the thinner unsymmetric cross-ply laminates were shown to have multiple shapes at room temperature. The second variation of the total potential was used to evaluate the stability of the nonlinear solutions and two of the shapes were determined to be stable at room-temperature. This result is consistent with the snap-through buckling behavior observed experimentally in certain thin unsymmetric laminates at room temperature [47]. Hyer's investigations also studied the effects of laminate material properties, stacking sequence, thickness, and aspect ratio upon the predicted shape at room temperature. An excellent summary of Hyer's work may be found in reference [50].

Hahn [51] conducted an experimental study of the room-temperature shapes of unsymmetric cross-ply laminates. He studied the effect of laminate geometry,

moisture absorption, and relaxation of residual stresses (time-dependent material behavior) upon the out-of-plane deflections. For thin $[0_4/90_4]_t$ graphite/epoxy laminates, several post-cure shapes were observed at room temperature. For laminates with a small span-to-depth or thickness ratio, a pure saddle shape or anticlastic shape is observed. For plates with large thickness ratios, two stable cylindrical shapes are possible at room temperature. A change from one mode shape to the other could be achieved by applying external force. These experimental observations were in agreement with the analytical predictions of Hyer [48-50]. The warping of the laminates appeared to be very dependent upon moisture content. As the moisture absorption increased, the residual stresses and thus the measured curvatures decreased. This is consistent with the observations of Pagano and Hahn [46]. The relaxation of residual stresses appeared to be negligible during a 220-day test period.

Wong [52] also investigated the shapes of unsymmetric laminates at room temperature experimentally and analytically. His investigation focused upon the cured shapes of thin square $[0_n/\theta_n]_t$ laminates, where $\theta = 15, 30, 45, 60, 75, 90$ degrees and $n = 1, 5, 10$. The effects of laminate thickness, moisture content, and mold curvature were examined. He reported that the $[0_n/\theta_n]_t$ laminates exhibited two stable cylindrical shapes at room temperature which exhibit the same snap-through buckling behavior discussed above [47–51]. As the laminate thickness was increased, the curvatures approached the prediction of linear CLP theory. His experimental results also showed that an increase in moisture content reduced the curvatures of the laminate.

2.2 Interlaminar Stresses in Laminated Plates

This section provides a brief discussion of previous investigations into the mechanics of interlaminar stresses in laminated plates. The discussion includes a review of the more significant results and a brief summary of the methods of analysis which have been used.

Early Investigations

Interlaminar stresses are known to exist near the free edges of laminated plates composed of dissimilar laminae. These stresses can arise in composite laminates subjected to mechanical, thermal, and/or hygroscopic loading. These stresses are caused by a difference or mismatch in material properties between adjacent layers in the presence of a traction free edge. These stresses arise in boundary layer regions near free edges in which the transition occurs between the interior stress field and the traction free edge condition. Interlaminar stress studies have been conducted for laminates composed of both isotropic and anisotropic materials.

One of the first investigations of the interlaminar stresses within laminated plates composed of anisotropic materials was conducted by Pipes and Pagano [53] in 1970. The study examined the elastic response of a $[+45/-45]_s$ finite-width symmetric composite laminate subjected to uniform axial extension. Under the assumption of uniform axial extension, the axial strain ϵ_{xx} is considered constant, the stress components are assumed independent of the axial coordinate x, and the general form of the displacement field reduces to:

$$u(x,y,z) = x\epsilon_{xx} + U(y,z) \tag{2.1}$$

$$v(x,y,z) = V(y,z) \tag{2.2}$$

$$w(x,y,z) = W(y,z) \tag{2.3}$$

The governing equations formulated from elasticity theory are a system of three coupled, second-order partial differential equations in terms of displacements u, v, and

w. Pipes and Pagano used the finite difference method to obtain an approximate solution to the linear three-dimensional boundary value problem.

The predicted stress field within most of the laminate was shown to be in agreement with the predictions of CLP theory. In a boundary layer region in which the transition occurs between the CLP theory solution and the traction free edge condition, the stress field was shown to be three-dimensional. The calculated stress results predicted the the existence of all three components of interlaminar stresses ($\sigma_{zz}, \tau_{yz}, \tau_{xz}$) at the interface between the $+45$ and -45 layers within this boundary layer region. The interlaminar components of stress decayed rapidly with increasing distance from the free edge. The in-plane components of stress predicted by CLP theory are also perturbed within this free edge region. The disturbance in the stress field was limited to a region approximately one laminate thickness wide; thus the disturbance was concluded to be a boundary layer or edge effect.

Pipes and Pagano found the τ_{xz} shear stress to be much larger than the σ_{zz} and τ_{yz} stresses. They also observed that as the finite difference mesh was refined, the τ_{xz} stress increased with no apparent bound. Citing the previous work of Bogy [54] and Hess [55,56], they suggested that the τ_{xz} stress might possibly be singular at the intersection of the interface with the free edge. Pipes and Daniels [57] used the Moire technique to examine the γ_{xz} shearing near the free edges of symmetric angle-ply laminates under uniform axial extension. Their experimental observations confirmed the analytical predictions. Pipes and Pagano expanded upon this work in subsequent investigations [58–60].

Puppo and Evenson [61] also proposed an approximate solution for a symmetric composite laminate subjected to extensional loading at about the same time as Pipes and Pagano [53]. Puppo and Evenson modeled the laminate as constructed of anisotropic elastic layers separated by thin layers of isotropic elastic adhesive. They presented results for a $[+45/-45]_s$ laminate under uniform axial extension.

Although the analysis neglected the normal component of interlaminar stress σ_{zz}, the analysis predicted a finite value of shear at the intersection between the interface and the free edge.

Isakson and Levy [62] used the finite element method to obtain an approximate solution for a symmetric composite laminate subjected to extension loading. Isakson and Levy's displacement-based analysis was similar to that of Puppo and Evenson [61] in that they modeled the laminate as consisting of anisotropic layers separated by layers of isotropic adhesive. The fiber-bearing anisotropic layers were modeled with a membrane element and the isotropic layers were modeled with a shear element; thus neglecting the existence of interlaminar normal stress. They analyzed the response of the $[+45/-45]_s$ laminate and their predictions of the τ_{zx} shear stress compared quite well with the predictions of Pipes and Pagano [53].

Rybicki [63] also used the finite element method to obtain an approximate three-dimensional solution for a symmetric composite laminate subjected to extensional loading. Rybicki used three-dimensional Maxwell stress functions expressed in terms of Hermite interpolation polynomials in a complementary energy formulation. Rybicki examined a variety of stacking sequences, including $[0/90]_s$, $[90/0]_s$, $[+45/-45]_s$, and $[-45/+45]_s$ laminates. His formulation accounted for all three components of interlaminar stresses and the results compared more favorably to the results of Pipes and Pagano [53] than with the results of Puppo and Evenson [61]. Because his assumed stress field did not contain singularities, he was unable to comment upon the singularity of the stress field, although his analysis predicted large interlaminar normal and shear stresses at the free edge.

Effects Upon Laminate Strength

Based upon the results of these early investigations, researchers began to study the influence of interlaminar stresses upon free edge delamination. Delaminations at the free edges of composite laminates are of great concern because they can lead to laminate failures at load levels well below those predicted for in-plane failures.

Foye and Baker [64] first suggested that interlaminar stresses may influence the strength of finite-width composite laminates. Their experimental data for composite laminates subjected to constant amplitude, cyclic loading showed that the fatigue strength of composite laminates depended upon laminate stacking sequence. Other experimental studies [60,65] which soon followed showed that both the static and fatigue strength of composite laminates depended upon laminate stacking sequence. Pagano and Pipes [59,60] conducted experimental and analytical studies to determine the influence of laminate stacking sequence upon the static strength of composite laminates. Pagano and Pipes showed how based upon the consideration of interlaminar stresses the layers of specific orientation could be arranged through the thickness to provide optimum laminate strength. Herakovich [66] demonstrated how the consideration of mismatch between adjacent layers in Poisson's ratio, coefficients of mutual influence, and coefficients of thermal expansion could be used in the design phase to minimize free edge stresses in composite laminates. Herakovich [67] also studied the influence of layer thickness upon the failure of angle-ply laminates.

Environmental Effects and Material Nonlinearity

Environmental effects upon the interlaminar stresses in laminated plates have been considered by a number of investigations. Herakovich [68] studied thermal free edge effects using the finite element method. He concluded that thermally induced free edge stresses could have a significant influence upon laminate strength. Additional numerical studies of thermal free edge effects were conducted by Wang and Crossman [69] and Griffin and Roberts [70]. The free edge response of composite laminates subjected to moisture absorption has been investigated by Farley and Herakovich [71] and by Crossman and Wang [72]. The effect of nonlinear material behavior upon the free edge response of laminated composites has been studied by Renieri and Herakovich [73], Nagarkar and Herakovich [74], and Griffin

[75]. A displacement-based finite element formulation was used in each of these investigations.

Thermoelastic Stresses in Unsymmetrically Laminated Strips

As mentioned in section 2.1, Timoshenko [1] commented upon the existence and approximate magnitudes of interlaminar thermoelastic stresses in bi-metallic thermostats composed of dissimilar isotropic materials in 1925. In 1969, Hess [55,56] presented a plane elasticity solution for the thermoelastic stress field within a bimaterial laminated strip. Hess found that for laminates whose length was greater than two laminate thicknesses, the stress field within most of the laminate agreed with the strength of materials solution given by Timoshenko [1]. His solution predicted the pertubation in the stress field near the ends of the laminate where the transition occurs between the Timoshenko distribution and the traction free end condition. In accordance with Saint Venant's principle, this region of pertubation was determined to be comparable in length to the laminate thickness. Hess determined that interlaminar normal and shear stresses exist within this region at the end of the laminate. The predicted interlaminar normal and shear stress distributions are similar to those predicted in the free edge problem of laminated plates.

Hess determined the solution to the two-dimensional boundary value problem using the method of eigenfunction expansion. The normal and shear stresses both appeared to be singular at the intersection of the interface and the free edge. He was unable to show this explicitly owing to the truncation of his eigenfunction series at 30 terms. Citing the work of Bogy [54] and Hein [76] in which it was shown that there exists a singularity in the stress field at the bonded interface between two quarter-planes of dissimilar materials, Hess proposed that both the normal and shear components of interlaminar stress are indeed singular at the intersection.

Yaniv and Ishai [77] conducted an experimental and analytical investigation of the interlaminar stresses in an unsymmetrically laminated strip consisting of a

graphite/epoxy lamina bonded to a thin sheet of aluminum. Their interest was in studying the effects of curing, thermal history, and material characteristics on the interlaminar stress field. A closed form solution was derived to predict the axial stresses within the adherend and a two-dimensional displacement-based finite element analysis was used to predict the interlaminar stresses near the ends of the beam. The closed-form solution based upon Euler-Bernoulli beam theory compared quite well with the overall deflections and axial strains within the adherends that were observed experimentally. The characteristics of the adhesive had an insignificant effect upon the predictions of the closed-form solution. In the regions near the ends, the interlaminar shear and normal stresses reached their maximum. The authors speculated that the stresses would eventually cause an interlaminar failure mode due to thermal loading. Experimental data suggested that the relationship between the deflections and temperature within the working range of the adhesive (below the glass transition temperature T_g) was approximately linear. The experimental deflection versus temperature data fell slightly below the linear theoretical curve which may possibly have been due to not accounting for geometric nonlinearity. The authors also concluded that the effect of stress relaxation within the adherends had an insignificant effect upon the response of the laminate.

Methods of Analysis

A number of methods have been used to obtain approximate solutions for interlaminar stresses in laminated plates. The method of finite differences has been used by Pipes and Pagano [53] and Pipes [58] to determine approximate solutions to the displacement-based formulations for uniform axial extension. The finite element method has been widely used by a number of researchers to obtain approximate solutions to free edge problems. Two-dimensional finite element formulations based upon uniform axial extension have been used by Herakovich, et al [78], Wang and Crossman [79], and others. Three-dimensional finite element formulations [63,80,81] have also been used for free edge analysis, including a 3D

formulation using cubic isoparametric elements [81]. Complementary energy [63] and assumed stress hybrid finite element formulations [82,83] have been used in an effort to exactly satisfy the traction free edge boundary conditions. Global/local finite element analysis has also been used for free edge studies [84,85,86]. The results of a numerical study investigating the reliability of the displacement-based finite element method for free edge analysis may be found in [87].

An analytical solution based upon the theory of anisotropic elasticity was proposed by Wang and Choi [88,89]. Assuming generalized plane deformation, Wang and Choi used Lekhnitskii's complex stress potentials [90] to derive a set of two linear coupled governing partial differential equations with constant coefficients. An eigenfunction expansion method was used to determine the homogeneous solution to the governing partial differential equations. The homogeneous solution yields the strength of the stress singularities at the intersection of the interface with the free edge. The remaining terms in the assumed form of the particular solution are then solved using a collocation method. Wang and Yaun [83] implemented this solution into an assumed stress hybrid finite element formulation.

Many other solutions have been proposed by a number of researchers. Tang [91] and Tang and Levy [92] used an approach in which a boundary layer solution based upon plane strain and torsion was matched with the interior solution from linear CLP theory. A pertubation method approach was used by Hsu and Herakovich [93] to obtain an approximate solution for uniform axial extension. Pagano [94,95] proposed an approximate analysis to predict the stress fields within laminated plates including the interlaminar stresses at free edges. Pagano's analysis was based upon an extension of Reissner's variational principle to laminated elastic plates. Pagano and Soni [96] proposed using this solution in a global/local formulation to obtain results for laminates with a large number of layers. Johnson and Kemp [97] proposed a similar approach in which the number of dependent variables per layer was reduced. Kassapoglou and Lagace [98] developed a simple approximate

analysis to predict interlaminar stresses at a free edge. The analysis was based upon overall force and moment equilibrium and the principle of minimum complementary energy. The method is considerably more efficient computationally than previous methods and is able to analyze thick laminates with a large number of layers. A more complete review, through 1980, of the literature on interlaminar stresses in composite laminates may be found in reference [99]. A detailed discussion of the mechanics of free edge stresses may be found in reference [100].

2.3 Discussion of the Present Approximate Analysis

As discussed at the end of Section 2.2, a number of methods have been used to determine the interlaminar stresses within laminated plates. The purpose of the present study is to investigate the interlaminar stresses within unsymmetrically laminated plates. The membrane-flexural coupling of unsymmetric laminates causes the laminate to deflect out of plane under the action of external loading. The membrane-flexural coupling eliminates from consideration many of the methods discussed in Section 2.2, since these methods are based upon simplifying assumptions such as uniform axial extension or generalized plane deformation. In addition to this, the finite deflections of unsymmetric laminates require that a geometrically nonlinear kinematic description be included in the analysis. Based upon these considerations, the boundary value problems of the present study are formulated from nonlinear three-dimensional elasticity theory. A Lagrangian kinematic description is used to derive the displacement-based formulation. Due to the complex nature of the nonlinear boundary value problem, the finite element method has been selected to determine an approximate solution.

There has been a great deal of discussion in the literature with regard to the ability of displacement-based finite element formulations to predict stresses near the free edge. The problem lies in the singularity of the interlaminar stress field at the intersection between the interface and the free edge. Tong and Pian [95] have

shown that the rate of convergence of displacement-based finite element solutions for problems with singularity are independent of the order of the approximation. Therefore, for problems with a mathematical singularity, the convergence of the finite element solution is not improved by using a higher order element or a refined mesh.

One alternative is to incorporate the singularity into the formulation of the element. However this implies that the strength of the singularity is known a priori. Swedlow [96] has suggested incorporating the strength of the singularity as an unknown in the finite element formulation. Wang and Yuan [91] incorporated the predicted singularity from their analytical solution into an assumed stress hybrid finite element formulation. However, as shown by Zwiers, Ting, and Spilker [97], for certain combinations of adjacent layers more than one singularity, each of different strength, may be present. The drawback of incorporating the singularities into the finite element formulation, even as an unknown, is that the functional form and number of singularities must be determined a priori and this is usually a very difficult and lengthy analytical task. Finally, even if the mathematical singularity could be predicted, its practical application may be questionable since in a real material this mathematical singularity in the stress field does not actually exist.

Fortunately the complex issue of determining these mathematical singularities in the stress field at free edges does not present a problem for the present investigation. Displacement-based finite element formulations have been widely used in many analytical investigations. The results of these investigations have shown that the displacement-based finite element method can provide an accurate prediction of the interlaminar stress field except for the region very near the free edge [98]. Furthermore, the interest of this study does not lie in the quantitative prediction of the interlaminar stress state at the free edge, but rather it is in the qualitative comparison of the entire interlaminar stress field distributions between symmetric and unsymmetric laminates. These qualitative comparisons can reveal insight into the

mechanics of the stress-deformational response of these laminates without having to explicitly determine the strength and nature of the mathematical singularities.

2.4 Summary

A number of experimental and analytical investigations have been conducted into the behavior of unsymmetrically laminated plates. These studies have focused upon investigating the laminate membrane-flexural coupling effects upon the response of unsymmetric laminates. These studies have examined the deflectional, buckling, and vibrational responses of unsymmetric laminates subjected to mechanical, thermal, and/or hygroscopic loading. The major conclusions of these studies are:

(1) The effects of laminate membrane-flexural coupling are important and should not be neglected in the analysis of unsymmetric laminates. In general, laminate membrane-flexural coupling results in a reduction in the stiffness of the plate; bending deflections are increased, buckling loads are decreased, and fundamental vibrational frequencies are decreased.

(2) Experimental and analytical studies have shown that the out-of-plane deflections of unsymmetric laminates are typically large. For finite deflections such as this, the effects of geometric membrane-flexural coupling are important and a geometrically nonlinear kinematic description should be included in the analysis of unsymmetric laminates.

A number of experimental and analytical studies have been conducted investigating the mechanics of interlaminar stresses in laminated plates. These investigations have included results for symmetric laminates subjected to mechanical, thermal and/or hygroscopic loading. Although a great number of investigations have been conducted, the studies of interlaminar stresses within unsymmetric laminates have been limited to thermally induced stresses for unsymmetrically laminated strips. In addition, although there have been a number of studies which have

considered the interlaminar stresses within laminated plates undergoing finite deflections [104,105], an investigation of free edge effects in such plates has apparently never been conducted.

In summary, the effects of laminate membrane-flexural coupling in unsymmetrically laminated plates are important and should not be neglected. The importance of including geometric nonlinearity into the analysis of unsymmetrically laminated plates has been clearly demonstrated. Studies of interlaminar stresses in unsymmetric laminates have been limited to the geometrically linear analysis of unsymmetrically laminated strips subjected to thermal loading. A comprehensive study of the interlaminar stress fields within unsymmetrically laminated anisotropic plates including the effects of laminate membrane-flexural coupling and geometric nonlinearity has not yet been accomplished.

Chapter 3
STUDY PARAMETERS

This chapter discusses the parameters for the problems considered in this study. This discussion includes material properties, plate geometry, laminate stacking sequences, loading conditions, and boundary conditions. The problems are divided into two groups:

(1) thin laminates subjected to extensional, compressive, or thermal loading.

(2) thick laminates subjected to extensional loading [53,78,89].

The first set of problems are the main focus of this study. These problem parameters are summarized in Tables 3.1, 3.2, and 3.3 and are discussed in detail in Section 3.1. The second set of problems are considered to provide numerical results which are compared with well-known previous results [78,89] for symmetric composite laminates subjected to extensional loading. The parameters for the second set of problems are discussed in Section 3.2.

3.1 Discussion of Study Parameters

The focus of this study is upon the linear thermoelastic response of thin square laminated composite plates subjected to extensional, compressive, and thermal loading. The laminated composite plates are composed of T300/5208 graphite/epoxy. The material properties for this fiber-reinforced composite material are given in Table 3.1. The composite material is assumed to be a linear thermoelastic, transversely isotropic solid with material properties that are independent of temperature. The principal material axes (X_1,X_2,X_3) for a single layer or lamina are shown in Figure 3.1, where the X_1 direction is aligned with the fiber direction. The angle of orientation θ of the principal material axes with respect to the global axes (x,y,z) of the plate is also shown in Figure 3.1. The geometry and global axes of the laminated plates are illustrated in Figure 3.2. A transversely isotropic solid is

characterized by five independent elastic constants and two independent coefficients of thermal expansion, for example:

$$E_1, E_2, \nu_{12}, \nu_{23}, G_{12} \tag{3.1a}$$

$$\alpha_{11}, \alpha_{22} \tag{3.1b}$$

where:

$E_3 = E_2$, $\nu_{13} = \nu_{12}$, $G_{13} = G_{12}$, $G_{23} = \frac{E_2}{2(1+\nu_{23})}$

$\alpha_{33} = \alpha_{22}$, $\alpha_{23} = \alpha_{13} = \alpha_{12} = 0$

The in-plane elastic properties, E_1, E_2, ν_{12}, and G_{12}, for T300/5208 graphite/epoxy are identical to those given in [50].

The stacking sequences and plate geometry for the symmetric and unsymmetric laminates are summarized in Table 3.2. The loading and boundary conditions for the laminated plates are summarized in Table 3.3. The geometry of each laminated plate is square in planform, $L = 2a = 2b$, with a length of $L = 2.0$ in. (Figure 3.2). The layer thickness for both unsymmetric and symmetric laminates is $d = 0.02$ in. The total laminate thickness for the unsymmetric laminates is $h = 0.04$ in. (2 layers) for a laminate thickness ratio of $L/h = 50$. The total laminate thickness for the symmetric laminates is $h = 0.08$ in. (4 layers) for a laminate thickness ratio of $L/h = 25$. The moderately large laminate thickness ratio for the unsymmetric laminates results in larger out-of-plane (transverse) deflections; thereby increasing the effects of geometric nonlinearity.

The selection of the laminated plate geometry is motivated by the focus upon interlaminar stresses. Interlaminar stresses are dependent upon the difference or mismatch in material properties between adjacent layers. The same layer or lamina thickness is used for both unsymmetric and symmetric laminates in order to achieve the same level of material property mismatch between adjacent layers. The layer thickness is equivalent to 4 plies of 0.005 in. thickness which is a typical layer thickness used in aerospace structural applications. The in-plane dimensions

of the laminated plate are limited by the size of numerical model (computational limit) and the minimum 3D finite element aspect ratio which is required for accurate displacement and stress predictions. The choice of a 2.0 in. plate length provides a moderately large thickness ratio for the unsymmetric laminates, $L/h = 50$, and yet still allows for a detailed finite element mesh refinement which leads to more accurate interlaminar stress predictions.

The stacking sequences for the symmetric and unsymmetric laminates are summarized in Figure 3.3. Symmetric and unsymmetric 0/90 cross-ply, +45/−45 angle-ply, and 0/+45 laminate stacking sequences are examined to determine the effects of mismatch in a variety of material properties between adjacent layers. The mismatch in mechanical and thermal properties between adjacent layers is summarized in Table 3.4. For example, the mismatch in Poisson's ratio ν_{xy} between adjacent 0 and 90 degree layers is given by [66]:

$$\nu_{xy}^{0} - \nu_{xy}^{90} \tag{3.2}$$

The unsymmetric and symmetric 0/90 cross-ply laminates possess a mismatch in Poisson's ratio ν_{xy} and coefficients of thermal expansion α_x and α_y between adjacent 0 degree and 90 degree layers. The unsymmetric and symmetric +45/−45 angle-ply laminates possess a mismatch in coefficient of mutual influence $\eta_{xy,x}$ and coefficient of thermal expansion α_{xy} between adjacent +45 degree and −45 degree layers. The unsymmetric and symmetric 0/+45 laminates possess a mismatch in each of these material properties between adjacent 0 degree and +45 degree layers.

The laminate stiffnesses for the unsymmetric and symmetric laminate stacking sequences are given in Table 3.5 and 3.6, respectively. The laminate membrane-flexural coupling of the unsymmetric laminates causes the initial geometric midplane of the laminate to deflect out of plane under the action of external loading. The initial geometric midplane of the symmetric laminates remains plane unless the laminate buckles under the action of compressive loading. The stacking sequences and

non-zero membrane-flexural coupling terms for the three unsymmetric laminates are given below:

(1) $[0_4/90_4]_t \rightarrow B_{11}, B_{22} \neq 0.$

(2) $[+45_4/-45_4]_t \rightarrow B_{16}, B_{26} \neq 0.$

(3) $[0_4/+45_4]_t \rightarrow B_{11}, B_{22}, B_{12}, B_{66}, B_{16}, B_{26} \neq 0.$

A summary of the laminate membrane-flexural coupling terms for unsymmetrically laminated plates is given below (for more details, refer to Appendix A):

$B_{11}, B_{22}, B_{12} \rightarrow$ extensional-bending coupling.

$B_{16}, B_{26} \rightarrow$ extensional-twisting coupling, shear-bending coupling.

$B_{66} \rightarrow$ shear-twisting coupling.

The reduced flexural stiffness approximations [21] for the unsymmetric laminates are also listed in Table 3.5. These reduced flexural stiffness terms are used with wide-column theory to predict linear buckling loads for the unsymmetric laminates.

The external loading conditions examined in this study are summarized below (Table 3.3, Figure 3.4):

(1) uniform extensional edge displacement, $u/a = +0.01$;

(2) uniform compressive edge displacement, $u/a = -0.01$; and

(3) uniform change in temperature, $\Delta T = -280°F$.

For geometrically nonlinear analysis, the external loading is applied incrementally from an initial unloaded state to the final loading state given above. The extensional loading condition is modeled after the free edge problem of a symmetric composite laminate subjected to uniform axial extension [53]. The displacement boundary conditions for the plate are clamped along the loaded edges and free along the unloaded edges. A loosely clamped condition is prescribed along the loaded edges in which the plate is free to undergo Poisson deformation in the y and z directions (the present approximate analysis is a full three-dimensional analysis). Both symmetric and unsymmetric laminates are restrained from warping out of plane along the loaded edges at the geometric midplane of the laminate

$w(\pm a, y, 0) = 0$. The loosely clamped, loaded edge boundary condition with out-of-plane restraint idealizes the conditions for a typical clamped test fixture. The displacement boundary conditions for the compressive loading condition are identical to the extensional loading condition except for a reversal in the direction of the applied edge displacement. The edge displacement was chosen to be quite large in an effort to produce large out-of-plane displacements; thereby increasing the effect of geometric nonlinearity.

The thermal loading condition models a laminate which has been cooled from an assumed stress-free state at an elevated cure temperature to a residual stress state at room temperature. This process is modeled analytically as an uniform decrease in temperature during which the constitutive behavior of the laminate is assumed to be linear thermoelastic. For the thermal loading condition, all surfaces of laminates are assumed traction free and each laminate is free to warp out of plane.

Finite element analysis results for the laminated plates and loading conditions discussed in this section are provided in Chapter 6. This includes numerical results for out-of-plane (transverse) displacements and interlaminar stresses for the symmetric and unsymmetric laminates listed in Table 3.2. The selection of the laminate geometry given in this section was based upon preliminary analyses which were conducted upon the unsymmetrically laminated plates listed in Table 3.7. The out-of-plane displacement results for these preliminary analyses are also provided in Chapter 6.

3.2 Parameters for Comparisons with Previous Results

As discussed at the beginning of this chapter, a second set of problems were considered to provide numerical results which are compared with well-known previous results [78,89]. The lamina material properties for these laminates are identical to those given in [53] and are listed in Table 3.8. The laminated plate geometry and stacking sequences are summarized in Table 3.9. The geometry of each laminated plate is square in planform, $L = 2a = 2b$, with a length of $L = 4.0$ in (Figure 3.2). The layer thickness for both unsymmetrically and symmetrically laminated plates is $d = 0.25$ in. The total laminate thickness for the unsymmetric laminates is $h = 0.5$ in. (2 layers) for a laminate thickness ratio of $L/h = 8$. The total laminate thickness for the symmetric laminates is $h = 1.0$ in. (4 layers) for a laminate thickness ratio of $L/h = 4$. The geometry for these thick laminates is based upon the plate geometry for the symmetric laminates given in [53]. The unsymmetric and symmetric stacking sequences are:

(1) $[0_{50}/90_{50}]_t, [90_{50}/0_{50}]_s, [0_{50}/90_{50}]_s$

(2) $[+45_{50}/-45_{50}]_t, [-45_{50}/+45_{50}]_s, [+45_{50}/-45_{50}]_s$

The extensional loading and boundary conditions are given in Table 3.4. Numerical results predicted by linear and nonlinear theory for the unsymmetric and symmetric laminates listed above are given in Chapter 6. In Section 6.2, the interlaminar stresses predicted by linear theory for the symmetric laminates are compared with previous results [78,89] for extensional loading.

Chapter 4
THEORETICAL FORMULATION

The mathematical boundary value problem of determining the three-dimensional stress-deformational response of an anisotropic elastic body is formulated in this chapter. The elastic body is assumed to undergo large displacements, large rotations, and small strains. A geometrically nonlinear kinematic description is incorporated into the analysis to account for the finite deflections of the elastic body. The geometrically nonlinear strain-displacement equations result in a set of nonlinear governing equations. These governing equations with boundary conditions constitute the nonlinear boundary value problem.

The nonlinear boundary value problem is derived from the basic principles of continuum mechanics and nonlinear anisotropic elasticity [90,106,107]. A displacement formulation is derived using a Lagrangian kinematic description in which all physical quantities are referred back to the initial (undeformed) configuration of the elastic body. The governing equations and boundary conditions are derived using the principle of minimum potential energy [108]. The boundary value problem formulated in this chapter is used to develop the model equations for the finite element formulation described in Chapter 5. Additional details for the theory outlined in this chapter may be found in references [109-111].

Tensorial or index notation is used for the formulations derived in Chapters 4 and 5. The range of free indices and implied summations is 3, unless it is stated otherwise. The notational convention used in this chapter for subscripts and superscripts is adopted from reference 110. An example illustrating this notation is provided below:

$$ {}^{t}_{0}u_{i,j} = {}^{t}_{0}u_{i,j}({}^{0}x_1, {}^{0}x_2, {}^{0}x_3) \tag{4.1} $$

The left superscript refers to the equilibrium configuration of the body. The left subscript refers to the equilibrium configuration with respect to which the quantity

is measured. The right subscript refers to the coordinate axes. The comma and the index j denote differentiation of the physical quantity ${}^t u_i$ with respect to coordinate ${}^0 x_j$. For the discussion of numerical results in Chapter 6, the more standard notation used for the mechanics of composite materials is adopted [22,23].

4.1 Basic Assumptions

The motion of a material particle within an elastic body is shown in Figure 4.1. At time $t = 0$, the elastic body is in its initial (undeformed) configuration. In this initial configuration, the body is assumed to be in its natural, unloaded state, free from all initial stresses and strains. At time t, the body is in its current (deformed) configuration under the action of external loading. The reference frame x_i is a right-handed Cartesian coordinate system. The initial coordinates of a material point ${}^0 P$ within the undeformed elastic body are given by:

$$ {}^0 x_i = {}^0 x_i({}^t x_1, {}^t x_2, {}^t x_3) \tag{4.2} $$

The current coordinates of the same material point ${}^t P$ within the deformed elastic body are given by:

$$ {}^t x_i = {}^t x_i({}^0 x_1, {}^0 x_2, {}^0 x_3) \tag{4.3} $$

The initial coordinates are related to the current coordinates by the displacement vector ${}^t u_i$:

$$ {}^t x_i = {}^0 x_i + {}^t u_i \tag{4.4} $$

Motion in which all particles are tracked in terms of the initial coordinates is referred to as a Lagrangian kinematic description [109]. In a Lagrangian kinematic description, all relevant tensorial quantities are referred to the undeformed configuration of the body and are functions of the initial coordinates. Motion in which all particles are tracked in terms of the current coordinates is referred to as an Eulerian kinematic description [109]. In an Eulerian kinematic description, all relevant tensorial quantities are referred to the deformed configuration of the body and are

functions of the current coordinates. Since it is assumed that the initial configuration of the body is the natural, unloaded state, the initial configuration of the body will be chosen as the reference state, to which all tensorial quantities in the statement of total potential energy will be referred. Thus a Lagrangian kinematic description is adopted for this analysis.

4.2 Analysis of Finite Deformation

This section begins with defining several geometric relationships between the initial (undeformed) configuration and the current (deformed) configuration. Specifically, geometric relationships for the following quantities are discussed:

(a) differential line segments ${}^0dx_i$ and ${}^tdx_i$;

(b) differential surfaces ${}^0dS$ and ${}^tdS$; and

(c) differential volumes ${}^0dV$ and ${}^tdV$.

The relationship for differential line segments is required in defining the Green-Lagrange nonlinear strain tensor. The relationships for differential volumes and surfaces are required in defining the measures of stress.

4.2.1 Geometric Relationships

Relationship between differential line segments ${}^0dx_i$ and ${}^tdx_i$

The relative displacement of two material points within an elastic body is shown in Figure 4.2. The differential vector ${}^0dx_i$ is a position vector which connects the two points ${}^0P$ and ${}^0Q$ in the undeformed configuration. The two material particles are assumed to be within the infinitesimal neighborhood of one another. As the elastic body undergoes loading, the material particles at ${}^0P$ and ${}^0Q$ move to new positions at ${}^tP$ and ${}^tQ$, respectively, in the deformed configuration of the body at time t. The initial vector ${}^0dx_i$ is displaced, stretched, and rotated to become the current vector ${}^tdx_i$ which connects points ${}^tP$ and ${}^tQ$. Although both material particles have been displaced, they are still considered within the infinitesimal

neighborhood of one another. The relationship between the initial and current differential line segments is given by:

$$ {}^{0}dx_i = {}^{0}_{t}x_{i,j}\,{}^{t}dx_j \tag{4.5} $$

and inversely:

$$ {}^{t}dx_i = {}^{t}_{0}x_{i,j}\,{}^{0}dx_j \tag{4.6} $$

The nine quantities ${}^{t}_{0}x_{i,j}$ are elements of the deformation gradient tensor. The second order tensor may be unsymmetric and is referred to initial coordinates in the undeformed configuration. The nine quantities ${}^{0}_{t}x_{i,j}$ are components of the spatial deformation gradient tensor which is referred to current coordinates in the deformed configuration at time t. This second order tensor may also be unsymmetric. The spatial deformation gradient tensor is the inverse of the deformation gradient tensor:

$$ {}^{t}_{0}x_{i,k}\,{}^{0}_{t}x_{k,j} = \delta_{ij} \tag{4.7} $$

$$ {}^{0}_{t}x_{i,k}\,{}^{t}_{0}x_{k,j} = \delta_{ij} \tag{4.8} $$

where the symbol δ_{ij} is the Kronecker delta.

Relationship between differential surfaces ${}^{0}dS$ and ${}^{t}dS$

The differential surface ${}^{0}dS$ in the initial configuration can be related to the same differential surface ${}^{t}dS$ in the current configuration through Nanson's formula [107]:

$$ \frac{{}^{0}\rho}{{}^{t}\rho}\,{}^{0}_{t}x_{i,r}\,{}^{0}n_i\,{}^{0}dS = {}^{t}n_r\,{}^{t}dS \tag{4.9} $$

and inversely:

$$ \frac{{}^{t}\rho}{{}^{0}\rho}\,{}^{t}_{0}x_{i,r}\,{}^{t}n_i\,{}^{t}dS = {}^{0}n_r\,{}^{0}dS \tag{4.10} $$

The quantities ${}^{0}\rho$ and ${}^{t}\rho$ are the densities at a point in the initial and current configurations, respectively. The quantities ${}^{0}n_i$ and ${}^{t}n_i$ are components of unit surface normals to the differential surfaces ${}^{0}dS$ and ${}^{t}dS$, respectively. Equations

(4.9) and (4.10) are used in Section 4.3 to relate stresses measured with respect to initial and current configurations.

Relationship between differential volumes ${}^0dV$ and ${}^tdV$

The principle of conservation of mass for a differential volume element may be expressed:

$$\int_{{}^0V} {}^0\rho \, {}^0dV = \int_{{}^tV} {}^t\rho \, {}^tdV \tag{4.11}$$

The initial coordinates ${}^0x_i$ can be regarded as a set of curvilinear coordinates in the deformed configuration. That is, initially straight lines parallel to the coordinate axes are now curves in the deformed configuration. Therefore, the transformation between ${}^0x_i$ and ${}^tx_i$ coordinates may be thought of as a transformation between curvilinear and right-handed Cartesian coordinates. Transforming the integral on the right-hand side of equation (4.11) to an integral over the undeformed configuration:

$$\int_{{}^tV} {}^t\rho \, {}^tdV = \int_{{}^0V} {}^t\rho |J| \, {}^0dV \tag{4.12}$$

and:

$$|J| = det|{}^t_0x_{i,j}| \tag{4.13}$$

$|J|$ is the determinant of the Jacobian of the transformation from initial to current coordinates. If the deformation is continuous, the determinant will always be positive and the absolute value sign may be dropped. Therefore, for an arbitrary volume:

$$\frac{{}^tdV}{{}^0dV} = \frac{{}^0\rho}{{}^t\rho} = J \tag{4.14}$$

and inversely:

$$\frac{{}^0dV}{{}^tdV} = \frac{{}^t\rho}{{}^0\rho} = J^{-1} \tag{4.15}$$

4.2.2 Strain Measures

The typical notion of normal strain is the engineering normal strain ϵ defined as the change in length divided by the initial length:

$$\epsilon = ({}^{t}L - {}^{0}L)/{}^{0}L \tag{4.16}$$

Equation (4.16) can be rewritten in a more general form:

$$\epsilon = ({}^{t}ds - {}^{0}ds)/{}^{0}ds \tag{4.17}$$

where:

$${}^{0}ds = \sqrt{{}^{0}dx_1\,{}^{0}dx_1 + {}^{0}dx_2\,{}^{0}dx_2 + {}^{0}dx_3\,{}^{0}dx_3} \tag{4.18}$$

$${}^{t}ds = \sqrt{{}^{t}dx_1\,{}^{t}dx_1 + {}^{t}dx_2\,{}^{t}dx_2 + {}^{t}dx_3\,{}^{t}dx_3} \tag{4.19}$$

${}^{0}ds$ and ${}^{t}ds$ are the respective lengths of the differential line segments ${}^{0}dx_i$ and ${}^{t}dx_i$ in the undeformed and deformed configurations, respectively. The engineering strain ϵ can be rewritten:

$$\epsilon = {}^{t}ds/{}^{0}ds - 1 = \lambda - 1 \tag{4.20}$$

where λ is the stretch or elongation of a differential element lying initially along ${}^{0}dx_i$. A more mathematically convenient form of strain is obtained by computing the difference of the squares of the differential lengths:

$$({}^{t}ds)^2 - ({}^{0}ds)^2 = {}^{t}dx_i\,{}^{t}dx_i - {}^{0}dx_i\,{}^{0}dx_i \tag{4.21}$$

The deformation gradient tensor is used to obtain:

$$({}^{t}ds)^2 - ({}^{0}ds)^2 = [{}^{t}_{0}x_{k,i}\,{}^{t}_{0}x_{k,j} - \delta_{ij}]\,{}^{0}dx_i\,{}^{0}dx_j \tag{4.22}$$

Equation (4.22) can be rewritten:

$$({}^{t}ds)^2 - ({}^{0}ds)^2 = [{}^{t}_{0}C_{ij} - \delta_{ij}]\,{}^{0}dx_i\,{}^{0}dx_j \tag{4.23}$$

where ${}^t_0C_{ij}$ is the right Cauchy-Green deformation tensor. The right Cauchy-Green deformation tensor is obtained from the product of the transpose of the deformation gradient tensor with the deformation gradient tensor itself. Finally, introducing the following notation:

$$({}^t ds)^2 - ({}^0 ds)^2 = 2\,{}^t_0E_{ij}\,{}^0dx_i\,{}^0dx_j \tag{4.24}$$

${}^t_0E_{ij}$ is known as the Lagrangian strain tensor, Green's strain tensor, or as the Green-Lagrange nonlinear strain tensor and is referred to herein as the Green-Lagrange strain tensor. The Green-Lagrange strain tensor is a function of initial coordinates and is referred to the initial (undeformed) configuration of the body. The Green-Lagrange strain tensor is used to formulate elastic strain energy of the body. An important feature of this measure of strain is that it remains invariant under rigid body translation or rotation. That is, the Green-Lagrange strain tensor will not predict straining of the body due to pure rigid body motion. The Green-Lagrange strain tensor can be rewritten in more convenient forms. From equations (4.23) and (4.24), the Green-Lagrange strain tensor can be rewritten:

$${}^t_0E_{ij} = \frac{1}{2}[{}^t_0C_{ij} - \delta_{ij}] \tag{4.25}$$

Using equation (4.4), the deformation gradient becomes:

$${}^t_0x_{k,i} = \delta_{ki} + {}^t_0u_{k,i} \tag{4.26}$$

Substituting this result into equation (4.25):

$${}^t_0E_{ij} = \frac{1}{2}[(\delta_{ki} + {}^t_0u_{k,i})(\delta_{kj} + {}^t_0u_{k,j}) - \delta_{ij}] \tag{4.27}$$

Rearranging, the more familiar form of the Green-Lagrange strain tensor is obtained:

$${}^t_0E_{ij} = \frac{1}{2}({}^t_0u_{i,j} + {}^t_0u_{j,i} + {}^t_0u_{k,i}\,{}^t_0u_{k,j}) \tag{4.28}$$

This is an exact expression of the finite Green-Lagrange strain and not a second order approximation of the strain. The linear strain tensor, linear rotation tensor, and the nonlinear strain components are defined as:

$$ {}_0e_{ij} = \frac{1}{2}({}^t_0u_{i,j} + {}^t_0u_{j,i}) \tag{4.29} $$

$$ {}_0\omega_{ij} = \frac{1}{2}({}^t_0u_{j,i} - {}^t_0u_{i,j}) \tag{4.30} $$

$$ {}_0\eta_{ij} = \frac{1}{2}({}^t_0u_{k,i}{}^t_0u_{k,j}) \tag{4.31} $$

where:

${}_0e_{ij}$ = linear strain tensor

${}_0\omega_{ij}$ = linear rotation tensor

${}_0\eta_{ij}$ = nonlinear component of the Green-Lagrange strain

The Green-Lagrange strain may be decomposed into linear and nonlinear components:

$$ {}^t_0E_{ij} = \frac{1}{2}({}_0e_{ij} + {}_0\eta_{ij}) \tag{4.32} $$

Combining equations (4.29) and (4.30), the displacement gradient tensor becomes:

$$ {}^t_0u_{j,i} = {}_0e_{ij} + {}_0\omega_{ij} \tag{4.33} $$

Using equations (4.28), (4.29), and (4.30), the Green-Lagrange strain tensor may be written:

$$ {}^t_0E_{ij} = {}_0e_{ij} + \frac{1}{2}({}_0e_{ki} + {}_0\omega_{ki})({}_0e_{kj} + {}_0\omega_{kj}) \tag{4.34} $$

In the case in which the components of the displacement gradient are small, the quadratic terms in the nonlinear strain tensor may be neglected. In this case of infinitesimal deformation, ${}_0e_{ij}$ are the engineering strains and ${}_0\omega_{kj}$ are the rotations.

4.2.3 Geometric Interpretation of Green-Lagrange Strain

In this section, a relationship is determined between Green-Lagrange strain and the engineering definition of strain. Suppose that the differential line element ${}^0dx_i$ is initially aligned in direction ${}^0n_i$. The square of the stretch of the line element is given by:

$$\lambda^2({}^0n_i) = \frac{{}^t ds^2}{{}^0 ds^2} \tag{4.35}$$

The components of the unit normal are given by:

$${}^0n_i = \frac{{}^0dx_i}{{}^0ds} \tag{4.36}$$

Rewriting equation (4.35) in view of equations (4.23) and (4.36):

$$\lambda^2({}^0n_i) = \frac{{}^0dx_i {}^t_0C_{ij} {}^0dx_j}{{}^0ds\,{}^0ds} \tag{4.37}$$

As an example, consider the stretch or elongation of the element lying initially parallel to the ${}^0x_1$ axis:

$${}^0n_i \rightarrow (1,0,0) \tag{4.38}$$

For this case, the stretch of the element becomes:

$$\lambda = \sqrt{{}^t_0C_{11}} = \sqrt{1 + 2{}^t_0E_{11}} \tag{4.39}$$

Returning to the engineering definition of strain given in equation (4.20):

$$\epsilon = \lambda - 1 = \sqrt{1 + 2{}^t_0E_{11}} - 1 \tag{4.40}$$

Solving for ${}^t_0E_{11}$:

$${}^t_0E_{11} = \epsilon + \frac{1}{2}\epsilon^2 \tag{4.41}$$

Equation (4.41) represents the relationship between the engineering strain and the Green-Lagrange strain for an element lying initially parallel to the ${}^0x_1$ axis. For small deformation, in which the square of the engineering strain is small, the Green-Lagrange strain is approximately equal to the engineering strain.

A similar relationship can be derived between the engineering shear strain and the Green-Lagrange strain. The engineering shear strain is defined as the change in angle between two lines which are initially perpendicular to one another. As an example, consider the case of two initially perpendicular differential line segments ${}^0dx'_i$ and ${}^0dx''_i$ which are oriented in the directions given by ${}^0n'_i$ and ${}^0n''_i$. In the deformed configuration, these differential line segments are oriented in the new directions ${}^tn'_i$ and ${}^tn''_i$. The cosine of the angle between these differential line segments in the current configuration is given by:

$$\cos({}^tn', {}^tn'') = \frac{{}^tdx'_i {}^tdx''_i}{\sqrt{{}^tdx'_m {}^tdx'_m}\sqrt{{}^tdx''_n {}^tdx''_n}} \tag{4.42}$$

Using the right Cauchy-Green deformation tensor, equation (4.42) can be rewritten:

$$\cos({}^tn', {}^tn'') = \frac{{}^t_0C_{ij} {}^0dx'_i {}^0dx''_j}{\sqrt{{}^t_0C_{mr} {}^0dx'_m {}^0dx'_r}\sqrt{{}^t_0C_{ns} {}^0dx''_n {}^0dx''_s}} \tag{4.43}$$

For the case in which the differential line segments are initially parallel to the x_1 and the x_2 axes, equation (4.43) becomes:

$$\cos(\theta_{12}) = \frac{{}^t_0C_{12}}{\sqrt{{}^t_0C_{11} {}^t_0C_{22}}} \tag{4.44}$$

Rewriting in terms of Green-Lagrange strain:

$$\cos(\theta_{12}) = \frac{2{}^t_0E_{12}}{\sqrt{(1 + 2{}^t_0E_{11})(1 + 2{}^t_0E_{22})}} \tag{4.45}$$

where the engineering strain γ is given by:

$$\gamma = \frac{\pi}{2} - \theta_{12} \approx \sin(\frac{\pi}{2} - \theta_{12}) = \cos(\theta_{12}) \tag{4.46}$$

For the case of infinitesimal deformation, the shearing component of the Green-Lagrange strain reduces to the definition of engineering shear strain:

$$\gamma \approx \cos(\theta_{12}) \approx 2{}^t_0E_{12} \tag{4.47}$$

4.3 Measures of Stress

The following measures of stress are defined this section:

(a) Cauchy stress, ${}^t\sigma_{ij}$

(b) First Piola-Kirchhoff stress, ${}^t_0T_{ij}$

(c) Second Piola-Kirchhoff stress, ${}^t_0S_{ij}$

In addition, equations relating these stress measures are also given. The purpose of this section is to define a measure of stress, namely the second Piola-Kirchhoff stress, which is a function of the initial coordinates and is referred to the initial (undeformed) configuration of the body. This measure of stress must be invariant under pure rigid body motion and energetically conjugate to the the Green-Lagrange strain tensor defined in Section 4.2. Together, the stress and strain tensors are used to define the elastic strain energy of the body.

A stress vector t_i acting upon the surface of the elastic body (Figure 4.3) is defined:

$$t_i = Limit_{\Delta S \to 0} \frac{\Delta F_i}{\Delta S} = \frac{dF_i}{dS} \tag{4.48}$$

The stress vector t_i may be related to the stress tensor σ_{ij} at that point through Cauchy's formula [108]:

$$t_i = \sigma_{ji} n_j \tag{4.49}$$

The elastic body is shown in Figure 4.4 in its initial (undeformed) and current (deformed) configurations at time 0 and t, respectively. In the initial configuration at time 0, the elastic body is assumed to be in its natural unloaded stress-free state. In the current configuration at time t, the elastic body is assumed to be under the action of external loading. ${}^0n_i$ is a unit vector which is normal to the differential surface ${}^0dS$ at point ${}^0P$ in the initial configuration. In the current configuration, the initial surface point ${}^0P$ has been displaced to surface point ${}^tP$. ${}^tn_i$ is a unit vector which is normal to the differential surface ${}^tdS$ at point ${}^tP$. The differential

force acting at point ${}^tP$ in the current configuration is denoted by ${}^tdF_i$. The quantity ${}^t_0d\tilde{F}_i$ is defined by the following expression:

$$ {}^t_0d\tilde{F}_i = {}^0_t x_{i,j}\, {}^tdF_j \tag{4.50} $$

The quantity ${}^t_0d\tilde{F}_i$ is a 'pseudo' force which is defined in order to refer the actual force ${}^tdF_i$ back to the initial (undeformed) configuration. The differential force components ${}^t_0d\tilde{F}_i$ are related to ${}^tdF_i$ in the same manner that a differential line segment ${}^0dx_i$ in the initial configuration is related to ${}^tdx_i$ in the current configuration. That is, ${}^t_0d\tilde{F}_i$ is the result of the actual force ${}^tdF_i$ undergoing the same stretch and rotation that ${}^tdx_i$ in the deformed configuration would have to undergo in order to return to its initial undeformed configuration ${}^0dx_i$. ${}^t_0d\tilde{F}_i$ has the same orientation with respect to the unit surface normal ${}^0n_i$ that ${}^tdF_i$ has with respect to the unit surface normal ${}^tn_i$. Using the differential forces ${}^t_0d\tilde{F}_i$ and ${}^tdF_i$, the following stress vectors can be defined:

$$ {}^tt_i = \frac{{}^tdF_i}{{}^tdS} \tag{4.51} $$

$$ {}^t_0t_i = \frac{{}^tdF_i}{{}^0dS} \tag{4.52} $$

$$ {}^t_0\tilde{t}_i = \frac{{}^t_0d\tilde{F}_i}{{}^0dS} \tag{4.53} $$

Using Cauchy's formula, the following stress tensors are defined:

$$ {}^tdF_i = {}^t\sigma_{ji}\, {}^tn_j\, {}^tdS \tag{4.54} $$

$$ {}^tdF_i = {}^t_0T_{ji}\, {}^0n_j\, {}^0dS \tag{4.55} $$

$$ {}^0d\tilde{F}_i = {}^t_0S_{ji}\, {}^0n_j\, {}^0dS \tag{4.56} $$

where:

${}^t\sigma_{ij}$ = Cauchy stress tensor

${}^t_0T_{ij}$ = first Piola-Kirchhoff stress tensor

${}_0^tS_{ij}$ = second Piola-Kirchhoff stress tensor

The Cauchy stress tensor is defined as a function of current coordinates and is referred to the current (deformed) configuration of the body. Cauchy stress is the measure of the actual force per unit deformed area acting at a point within the deformed body. Cauchy stress is a practical measure of stress in an engineering sense which should be used in the analysis of failure. In the absence of body moments or couple stresses, the Cauchy stress tensor is symmetric.

The first Piola-Kirchhoff stress tensor is defined as a function of initial coordinates and is referred to the initial (undeformed) configuration of the body. First Piola-Kirchhoff stress is the measure of the actual force per unit undeformed area. Although this measure of stress is referred to the initial configuration, the first Piola-Kirchhoff stress tensor, as will soon be shown, is not necessarily symmetric and is therefore difficult to use.

The second Piola-Kirchhoff stress tensor is also defined as a function of initial coordinates and is referred to the initial (undeformed) configuration of the body. Second Piola-Kirchhoff stress is the measure of the pseudo force per unit undeformed area. This measure of stress, although more complex than the first Piola-Kirchhoff stress tensor, is both symmetric and referred to the initial configuration. Like the Green-Lagrange strain tensor, the second Piola-Kirchhoff stress tensor is invariant under pure rigid body motion. Second Piola-Kirchhoff stress is energetically conjugate to the Green-Lagrange strain tensor and will be used in defining the elastic strain energy within the body.

Equations (4.9) and (4.10) can be used to obtain relationships between Cauchy, first Piola-Kirchhoff, and second Piola-Kirchhoff stress tensors. Equating the right-hand sides of equations (4.54) and (4.55):

$$ {}^t\sigma_{ji}\,{}^tn_j\,{}^tdS = {}_0^tT_{ji}\,{}^0n_j\,{}^0dS \tag{4.57}$$

Substituting equation (4.9) into equation (4.57):

$$ {}^{t}\sigma_{ki}\frac{{}^{0}\rho}{{}^{t}\rho}{}_{t}^{0}x_{j,k}\,{}^{0}n_{j}\,{}^{0}dS = {}_{0}^{t}T_{ji}\,{}^{0}n_{j}\,{}^{0}dS \tag{4.58} $$

For any arbitrary ${}^{0}n_{j}$:

$$ {}^{t}\sigma_{ki}\frac{{}^{0}\rho}{{}^{t}\rho}{}_{t}^{0}x_{j,k} = {}_{0}^{t}T_{ji} \tag{4.59} $$

and inversely:

$$ {}^{t}\sigma_{ji} = \frac{{}^{t}\rho}{{}^{0}\rho}{}_{0}^{t}x_{j,k}\,{}_{0}^{t}T_{ki} \tag{4.60} $$

Equations (4.59) and (4.60) show that although the Cauchy stress tensor is symmetric, the first Piola-Kirchhoff stress tensor is not necessarily symmetric. From equations (4.55) and (4.56), the relationship between the first and second Piola-Kirchhoff stress tensors is given by:

$$ {}_{0}^{t}S_{ij} = {}_{t}^{0}x_{j,k}\,{}_{0}^{t}T_{ik} \tag{4.61} $$

and inversely:

$$ {}_{0}^{t}T_{ik} = {}_{0}^{t}x_{k,j}\,{}_{0}^{t}S_{ij} \tag{4.62} $$

Substituting these results into equations (4.59) and (4.60), the relationship between the Cauchy and second Piola-Kirchhoff stress tensors is obtained:

$$ {}^{t}\sigma_{mn} = \frac{{}^{t}\rho}{{}^{0}\rho}{}_{0}^{t}x_{m,i}\,{}_{0}^{t}S_{ij}\,{}_{0}^{t}x_{n,j} \tag{4.63} $$

and inversely:

$$ {}_{0}^{t}S_{ij} = \frac{{}^{0}\rho}{{}^{t}\rho}{}_{t}^{0}x_{i,m}\,{}^{t}\sigma_{mn}\,{}_{t}^{0}x_{j,n} \tag{4.64} $$

In summary, both the second Piola-Kirchhoff stress tensor and Green-Lagrange strain tensor are functions of initial coordinates and are referenced to the initial (undeformed) configuration of the body. These quantities are used to formulate the elastic strain energy which is used for the expression of the total potential energy. The principle of minimum potential energy is used to derive the equations

of motion for the elastic body. These equations of motion with boundary conditions constitute the nonlinear boundary value problem. In the next section, a numerical example is provided which illustrates the differences between the measures of stress and strain defined in Sections 4.2 and 4.3.

4.4 Numerical Examples of Stress and Strain

The finite deformation of a linear elastic, isotropic cube of initial dimension ${}^0L$ is illustrated in Figure 4.5. The prime coordinate system shown is a body attached Cartesian coordinate system. At time 0, the elastic body is in its initial (undeformed) configuration. At time t, the elastic body is in its current (deformed) configuration. In reaching its current configuration at time t, the elastic body has undergone a rigid body translation in the 1-2 plane, a rigid body rotation of angle $+\theta$ about the x'_3 axis, and uniaxial extension along the x'_1 axis. The elastic cube has been stretched along the x'_1 axis by a uniform extensional loading on the x'_1 face and has undergone Poisson contraction in the x'_2 and x'_3 directions. The resultant of the extensional loading is denoted by force F.

The stretch in the x'_1 direction is given by:

$$\lambda_1 = \frac{{}^tL}{{}^0L} = 1 + \epsilon \tag{4.65}$$

The stretch in the x'_2 and x'_3 directions is given by:

$$\lambda_2 = \lambda_3 = 1 - \nu\epsilon \tag{4.66}$$

The components of the deformation gradient tensor are given by:

$${}^t_0x_{i,j} \Rightarrow \begin{bmatrix} (1+\epsilon)\cos(\theta) & -(1-\nu\epsilon)\sin(\theta) & 0 \\ (1+\epsilon)\sin(\theta) & (1-\nu\epsilon)\cos(\theta) & 0 \\ 0 & 0 & (1-\nu\epsilon) \end{bmatrix} \tag{4.67}$$

The components of the deformation gradient tensor include both the stretch and rotation of the elastic body. The Jacobian of the deformation gradient tensor is given by:

$$\frac{{}^0\rho}{{}^t\rho} = J = (1+\epsilon)(1-\nu\epsilon)(1-\nu\epsilon) \tag{4.68}$$

Using equation (4.26), the components of the displacement gradient tensor are given by:

$${}^t_0u_{i,j} \Rightarrow \begin{bmatrix} (1+\epsilon)\cos(\theta)-1 & -(1-\nu\epsilon)\sin(\theta) & 0 \\ (1+\epsilon)\sin(\theta) & (1-\nu\epsilon)\cos(\theta)-1 & 0 \\ 0 & 0 & (1-\nu\epsilon)-1 \end{bmatrix} \tag{4.69}$$

The components of the rotation tensor are given by:

$${}_0\omega_{ij} \Rightarrow \begin{bmatrix} 0 & [1+\frac{1}{2}(1+\nu)\epsilon]\sin(\theta) & 0 \\ -[1+\frac{1}{2}(1+\nu)\epsilon]\sin(\theta) & 0 & 0 \\ 0 & 0 & 0 \end{bmatrix} \tag{4.70}$$

The terms of the rotation tensor are dependent upon not only the rotation, as in the case of small deformations, but also upon the stretch as well. Using the components of the displacement gradient tensor, the components of the linear strain tensor are given by:

$${}_0e_{ij} \Rightarrow \begin{bmatrix} (1+\epsilon)\cos(\theta)-1 & \frac{1}{2}(1+\nu)\epsilon\sin(\theta) & 0 \\ \frac{1}{2}(1+\nu)\epsilon\sin(\theta) & (1-\nu\epsilon)\cos(\theta)-1 & 0 \\ 0 & 0 & -\nu\epsilon \end{bmatrix} \tag{4.71}$$

The strain ${}_0e_{ij}$ is not invariant under rigid body motion and is dependent upon the angle of rigid body rotation θ. The components of the Green-Lagrange strain tensor are given by:

$${}^t_0E_{ij} \Rightarrow \begin{bmatrix} \epsilon+\frac{1}{2}\epsilon^2 & 0 & 0 \\ 0 & -\nu\epsilon+\frac{1}{2}\nu^2\epsilon^2 & 0 \\ 0 & 0 & -\nu\epsilon+\frac{1}{2}\nu^2\epsilon^2 \end{bmatrix} \tag{4.72}$$

The Green-Lagrange strain is invariant under the rigid body motion. The components of strain are referred to the initial (undeformed) configuration of the elastic body. For example, ${}^t_0E_{11}$ gives the strain along fibers initially parallel to the ${}^0x_1$ axis.

As seen from equation (4.72), if the engineering strain ϵ is small, the Green-Lagrange strain is approximately given by:

$$ {}^{t}_{0}E_{ij} \Rightarrow \begin{bmatrix} \epsilon & 0 & 0 \\ 0 & -\nu\epsilon & 0 \\ 0 & 0 & -\nu\epsilon \end{bmatrix} \tag{4.73} $$

The components of engineering strain with respect to prime coordinates may be evaluated by inspection:

$$ {}^{t}\epsilon'_{ij} \Rightarrow \begin{bmatrix} \epsilon & 0 & 0 \\ 0 & -\nu\epsilon & 0 \\ 0 & 0 & -\nu\epsilon \end{bmatrix} \tag{4.74} $$

Thus for large displacements, large rotations, and small strains, the Green-Lagrange strain is approximately equal to the engineering strain.

On the basis of inspection, the components of the second Piola-Kirchhoff stresses are given by:

$$ {}^{t}_{0}S_{ij} \Rightarrow \begin{bmatrix} \frac{F}{{}^{0}L^{2}(1+\epsilon)^{2}} & 0 & 0 \\ 0 & 0 & 0 \\ 0 & 0 & 0 \end{bmatrix} \tag{4.75} $$

The components of second Piola-Kirchhoff stress are also invariant under rigid body motion and are referred to the initial (undeformed) configuration of the elastic body. Using these components and equation (4.63), the components of the Cauchy stress tensor are given by:

$$ {}^{t}\sigma_{ij} \Rightarrow \begin{bmatrix} \frac{F}{{}^{0}L^{2}(1-\nu\epsilon)^{2}}\cos^{2}(\theta) & \frac{F}{{}^{0}L^{2}(1-\nu\epsilon)^{2}}\sin(\theta)\cos(\theta) & 0 \\ \frac{F}{{}^{0}L^{2}(1-\nu\epsilon)^{2}}\sin(\theta)\cos(\theta) & \frac{F}{{}^{0}L^{2}(1-\nu\epsilon)^{2}}\sin^{2}(\theta) & 0 \\ 0 & 0 & 0 \end{bmatrix} \tag{4.76} $$

Transforming these components to the prime coordinate system, the Cauchy stresses become:

$$ {}^{t}\sigma'_{ij} \Rightarrow \begin{bmatrix} \frac{F}{{}^{0}L^{2}(1-\nu\epsilon)^{2}} & 0 & 0 \\ 0 & 0 & 0 \\ 0 & 0 & 0 \end{bmatrix} \tag{4.77} $$

The ratio of ${}^{t}_{0}S_{11}$ to ${}^{t}\sigma'_{11}$ is given by:

$$ \frac{{}^{t}_{0}S_{11}}{{}^{t}\sigma'_{11}} = \frac{(1-\nu\epsilon)^{2}}{(1+\epsilon)} \tag{4.78} $$

If the strain ϵ is small, then the second Piola-Kirchhoff stress is approximately equal to the rotated Cauchy stresses:

$$ {}^{t}_{0}S_{11} \approx {}^{t}\sigma'_{11} \tag{4.79} $$

As a numerical example, the percent difference between Green-Lagrange strain ${}^{t}_{0}E_{11}$ given by equation (4.72) and engineering strain ϵ is plotted as a function of engineering strain ϵ in Figure 4.6. The percent difference between second Piola-Kirchhoff stress ${}^{t}_{0}S_{11}$ given by equation (4.75) and Cauchy stress ${}^{t}\sigma'_{11}$ given by equation (4.77) is plotted as a function of engineering strain ϵ in Figure 4.7 ($\nu = 0.25$). In the present study, numerical results are determined for laminated plates subjected to an applied extensional edge displacement of $u/a = +0.01$. For an assumed engineering strain of the same magnitude, $\epsilon = +0.01$, the percent difference between ${}^{t}_{0}E_{11}$ and ϵ shown in Figure 4.6 is one-half percent. The percent difference for $\epsilon = +0.01$ between ${}^{t}_{0}S_{11}$ and ${}^{t}\sigma'_{11}$ shown in Figure 4.7 is one and one-half percent. For this numerical example, the results show that for moderately large strains, $\epsilon = +0.01$, the second Piola-Kirchhoff stresses and Green-Lagrange strains are good approximations of the Cauchy stresses and engineering strains.

In summary, for deformation which is large displacement, large rotation, and small strain, the Green-Lagrange strain is approximately equal to the engineering strain. Similarly, the second Piola-Kirchhoff stress is approximately equal to the Cauchy stress. Details concerning the computation of interlaminar stresses are discussed in Section 5.2.3. The constitutive equations relating stress and strain are discussed in the next section.

4.5 Constitutive Equations

Elastic behavior, in a classical sense, is understood to be the ability of a solid to recover its initial (undeformed) state after the external forces producing deformation have been removed. In mathematical terms, constitutive behavior may be considered to be thermoelastic if the material possesses a stress-free state and the functional relationship is such that stress is a single-valued function of strain and temperature [112]:

$$ {}^{t}_{0}S_{ij} = {}^{t}_{0}S_{ij}({}^{t}_{0}E_{ij}, T) \tag{4.80} $$

Furthermore, if the functional constitutive relationship satisfies the mathematical requirements of homogeneity and superposition, then the material behavior may be classified as linear.

In the present investigation, the constitutive behavior of the continuum is assumed to be to be linear thermoelastic. All material properties are assumed independent of temperature. The continuum is considered to be at most an orthotropic medium whose principal material axes may be arbitrarily oriented with respect to the global coordinate system. The constitutive relationship for a linear elastic (Hookean) anisotropic solid is given by [107]:

$$ {}^{t}\sigma_{ij} = {}_{0}C_{ijkl}({}_{0}e_{kl} - {}^{t}_{0}E^{T}_{kl}) \tag{4.81} $$

$$ {}^{t}_{0}S_{ij} = {}_{0}C_{ijkl}({}^{t}_{0}E_{kl} - {}^{t}_{0}E^{T}_{kl}) \tag{4.82} $$

where for small strains, the same constitutive relationships are used for both small and large deformation. The term ${}^{t}_{0}E^{T}_{kl}$ is the strain due to the free thermal expansion of the material. The linear thermoelastic strain-temperature relationship is given by:

$$ {}^{t}_{0}E^{T}_{ij} = \alpha_{ij}\Delta T \tag{4.83} $$

where:

α_{ij} = coefficients of thermal expansion

ΔT = change in temperature

For the purposes of this study, a coordinate transformation of the constitutive equations is given in Appendix B for a single rotation about an axis normal to the geometric midplane of the plate (Figures 3.1 and 3.2). The equations transform the lamina constitutive behavior from orthotropic to monoclinic material behavior.

Once the solution to the nonlinear boundary value has been determined, the Green-Lagrange strains are calculated using equations (4.28). The second Piola-Kirchhoff stresses are then calculated from the Green-Lagrange strains using equations (4.82). As the strains become large, the constitutive relationships may no longer be linear elastic and nonlinear material behavior must be accounted for. However, for the boundary value problems considered in the present study, the deformation is assumed to be large displacement, large rotation, and small strain. The second Piola-Kirchhoff stress and Green-Lagrange strain are invariant under rigid body motion, and the linear elastic constitutive relationships given by equations (4.82) are used.

4.6 Total Potential Energy

In this section, an expression is given for the total potential energy of a linear thermoelastic anisotropic body under the action of external loading. The expression for the total potential energy in the current (deformed) configuration at time t is referenced to the initial (undeformed) configuration at time 0 and all integrations are with respect to the initial (undeformed) geometry of the elastic body. Displacement boundary conditions ${}^t\bar{u}_i$ are prescribed along the surface S_1. External tractions ${}^t_0\bar{t}_i$ are prescribed along the surface S_2. The total potential energy Π for the elastic body is given by [108]:

$$\Pi = U_e + V_e \tag{4.84}$$

where:

U_e = elastic strain energy for the body

V_e = potential energy of the externally applied loading

The elastic strain energy for the body is given by:

$$U = \frac{1}{2}\int_{{}_0V} {}^t_0S_{ij}({}^t_0E_{ij} - {}^t_0E^T_{ij})\,{}^0dV \tag{4.85}$$

where:

${}^t_0S_{ij} = {}_0C_{ijkl}({}^t_0E_{kl} - {}^t_0E^T_{kl})$

${}^t_0E^T_{kl}$ = strain due to free thermal expansion

The potential energy for the externally applied loading is given by:

$$V_e = -\int_{{}_0V} {}^t_0f_i\,{}^tu_i\,{}^0dV - \int_{{}_0S_2} {}^t_0\bar{t}_i\,{}^tu_i\,{}^0dS \tag{4.86}$$

where:

${}^t_0f_i$ = body force per unit volume

${}^t_0\bar{t}_i$ = prescribed tractions on the surface S_2

Substituting equations (4.86) and (4.87) into equation (4.84), the total potential energy for the elastic body becomes:

$$\Pi = \frac{1}{2}\int_{{}_0V} {}^t_0S_{ij}({}^t_0E_{ij} - {}^t_0E^T_{ij})\,{}^0dV - \int_{{}_0V} {}^t_0f_i\,{}^tu_i\,{}^0dV - \int_{{}_0S_2} {}^t_0\bar{t}_i\,{}^tu_i\,{}^0dS \tag{4.87}$$

and displacements are prescribed along the surface S_1:

$${}^tu_i = {}^t\bar{u}_i \qquad on \quad S_1 \tag{4.88}$$

4.7 Governing Equations and Boundary Conditions

For the present analysis, the principle of minimum potential energy is used to derive the equations of equilibrium and the natural boundary conditions for the problem. The principle of minimum potential energy states that of all possible kinematically admissable displacement fields, the displacements which correspond

to a stable equilibrium configuration also make the total potential energy a relative minimum [108,112]:

$$\delta\Pi = (\delta U_e + \delta V_e) = 0 \tag{4.89}$$

Taking the first variation of the total potential energy of the body with respect to ${}^t u_i$:

$$\delta\Pi = \frac{\partial \Pi}{\partial {}^t u_i}\delta {}^t u_i = 0 \tag{4.90}$$

For an arbitrary variation of $\delta {}^t u_i$:

$$\frac{\partial \Pi}{\partial {}^t u_i} = 0 \tag{4.91}$$

Applying this principle to the total potential derived in the previous section yields:

$$\delta\Pi = \int_{{}^0V} {}^t_0 S_{ij}\delta {}^t_0 E_{ij}\, {}^0dV - \int_{{}^0V} {}^t_0 f_i \delta {}^t u_i\, {}^0dV - \int_{{}^0S_2} {}^t_0 \bar{t}_i \delta {}^t u_i\, {}^0dS \tag{4.92}$$

The first term in equation (4.92) may be expanded using (4.28):

$$\int_{{}^0V} {}^t_0 S_{ij}\delta {}^t_0 E_{ij}\, {}^0dV = \int_{{}^0V} {}^t_0 S_{kj}(\delta_{ik} + {}^t_0 u_{i,k})\delta {}^t_0 u_{i,j}\, {}^0dV \tag{4.93}$$

Integrating by parts:

$$\int_{{}^0V} {}^t_0 S_{kj}(\delta_{ik} + {}^t_0 u_{i,k})\delta {}^t_0 u_{i,j}\, {}^0dV = \int_{S_2} {}^t_0 S_{kj}\, {}_0n_j(\delta_{ik} + {}^t_0 u_{i,k})\delta {}^t_0 u_i\, {}^0dS - \int_{{}^0V} \left[{}^t_0 S_{kj}(\delta_{ik} + {}^t_0 u_{i,k})\right]_{,j} \delta {}^t u_i\, {}^0dV \tag{4.94}$$

where ${}_0n_i$ are components of a unit vector which is normal to the surface of the body. Substituting this result into equation (4.92):

$$-\int_{{}^0V} \{[{}^t_0 S_{kj}(\delta_{ik} + {}^t_0 u_{i,k})]_{,j} + {}^t_0 f_i\}\delta {}^t u_i\, {}^0dV + \int_{S_2} \left[{}^t_0 S_{kj}\, {}_0n_j(\delta_{ik} + {}^t_0 u_{i,k}) - {}^t_0 \bar{t}_i\right] \delta {}^t u_i\, {}^0dS = 0 \tag{4.95}$$

For an arbitrary variation of $\delta {}^t u_i$, the three equations of equilibrium are obtained:

$$\left[{}^t_0 S_{kj}(\delta_{ik} + {}^t_0 u_{i,k})\right]_{,j} + {}^t_0 f_i = 0 \qquad in \quad V \tag{4.96}$$

and the natural boundary conditions are:

$$ {}_0n_j {}^t_0S_{kj}(\delta_{ik} + {}^t_0u_{i,k}) - {}^t_0\bar{t}_i = 0 \qquad on \quad S_2 \tag{4.97} $$

where the assumed displacement field ${}^tu_i$ must satisfy the essential boundary conditions:

$$ {}^tu_i = {}^t\bar{u}_i \qquad on \quad S_1 \tag{4.98} $$

Substituting the constitutive equations (4.82) into equations (4.96) and (4.97) yields:

$$ [{}_0C_{kjmn}({}^t_0u_{m,n} + \frac{1}{2}{}^t_0u_{p,m}{}^t_0u_{p,n} - {}^t_0E^T_{mn})(\delta_{ik} + {}^t_0u_{i,k})]_{,j} + {}^t_0f_i = 0 \tag{4.99a} $$

$$ {}_0n_j{}_0C_{kjmn}({}^t_0u_{m,n} + \frac{1}{2}{}^t_0u_{p,m}{}^t_0u_{p,n} - {}^t_0E^T_{mn}) - {}^t_0\bar{t}_i = 0 \qquad on \quad S_2 \tag{4.99b} $$

$$ {}^tu_i = {}^t\bar{u}_i \qquad on \quad S_1 \tag{4.99c} $$

Equations (4.99) constitute the three-dimensional nonlinear boundary value problem in dependent variables u_1, u_2, and u_3. Equations (4.99a) are three coupled nonlinear partial differential equations. Equations (4.99b) are the natural boundary conditions and equations (4.99c) are the essential boundary conditions for the problem. Equations (4.99) are used in the next chapter to develop the model equations for the finite element formulation. The model equations are used to formulate the global nonlinear boundary value problem of a laminated anisotropic composite plate subjected to external loading.

4.8 Uniqueness and Stability

The mathematical requirements for the linearity of a given set of governing equations are homogeneity and superposition. For linear boundary value problems formulated from the theory of elasticity, the linearity of the governing equations can be used to establish the existence and uniqueness of a solution [108]. However, for nonlinear boundary value problems, the uniqueness of a solution cannot be

established. Multiple solutions may exist to the governing equations for the same set of boundary conditions.

The boundary value problems considered in this study are nonlinear and therefore multiple solutions may be obtained for the same set of external loading conditions. These solutions may be either stable or unstable equilibrium configurations. The physical possibility of multiple stable solutions for unsymmetric laminates under the action of external loading has been verified experimentally. For a given external load condition, multiple stable equilibrium configurations have been observed in thin unsymmetrically laminated plates subjected to compressive [33] and thermal [47,51,52] loading.

The study of elastic bodies possessing multiple equilibrium configurations under the same set of external loads is called the theory of elastic stability. The stability of a solution to the equations of equilibrium may be determined by examining the matrix formed by the second variation of the total potential energy [112,113]:

$$K_{ij} = \frac{\partial^2 \Pi}{\partial q_i \partial q_j} \tag{4.100}$$

where: K_{ij} = Stiffness coefficients for the stiffness matrix $[K]$

Π = Total potential energy of the elastic body

q_i, q_j = Generalized coordinates for the elastic body

If the stiffness matrix $[K]$ is positive definite, then the solution is stable and the total potential energy Π is a relative minimum. If the stiffness matrix $[K]$ is negative definite, negative indefinite, or indefinite, then the solution is unstable. If the stiffness matrix $[K]$ is positive semidefinite, then the stiffness matrix is singular and higher order derivatives of the total potential energy must be considered to determine the stability of the equilibrium configuration. Thus the stability of a solution may be determined by evaluating the determinant or eigenvalues of the stiffness matrix $[K]$.

The finite element method is used in the next chapter to obtain an approximate solution to the nonlinear boundary value problem. The formulation uses the linear form of Newton's method to solve the nonlinear boundary value problem. In the finite element formulation of Newton's method, the global tangent stiffness matrix evaluated at the equilibrium state corresponds to the second variation of the total potential energy. For the case in which the stiffness matrix is positive semidefinite, the load parameter embedded in the matrix reaches a critical level for which the load parameter is an eigenvalue of the homogeneous form of the governing equations. The global stiffness matrix becomes singular at this point and the Newton algorithm breaks down. The solution of the nonlinear governing equations is discussed further in Section 5.2.2.

Chapter 5
FINITE ELEMENT FORMULATION

This chapter discusses the approximate solution of the nonlinear boundary value problem by the finite element method. The chapter begins with the formulation of the nonlinear finite element equations and their solution using Newton's method. A total Lagrangian incremental approach is used to derive the displacement-based geometrically nonlinear finite element equations. The chapter also describes the computational aspects of the finite element analysis which include a discussion of global/local finite element analysis, nonlinear solution strategy, and interlaminar stress computations. The chapter concludes with a discussion of results for the verification test cases which were selected to evaluate the analytical approach.

5.1 Finite Element Implementation

The governing equations and boundary conditions derived in Chapter 4 are referenced to the initial (undeformed) configuration of the elastic body; thus a Lagrangian kinematic approach was used. The implementation of Newton's method results in an incremental formulation of the problem. If the incremental form of the equations is referred back to the initial (undeformed) configuration, the approach is referred to as a total Lagrangian formulation. If the incremental form of the equations is referred back to the most recently calculated current (deformed) configuration, then the approach is referred to as an updated Lagrangian formulation. If, in each fomulation, energetically consistent measures of stress and strain are used and the appropriate constitutive relationships are employed, then both formulations will yield identical results [110] and either approach may be used.

5.1.1 Element Geometry and Interpolation Functions

Four types of three-dimensional isoparametric hexahedral "brick" elements are included in the present finite element formulation. The four elements are illustrated in Figure 5.1. The coordinates x_i and the components of the displacement field u_i are interpolated within the element using the following equations:

$$x_i = \sum_{k=1}^{n} \psi^k x_i^k \tag{5.1}$$

$$u_i = \sum_{k=1}^{n} \psi^k u_i^k \tag{5.2}$$

where:

$\psi^k = \psi^k(\xi_1, \xi_2, \xi_3)$

n = nodes per element

The values of the coordinate x_i and displacement u_i at node number k are given by x_i^k and u_i^k, respectively. ψ^k are the interpolation or shape functions which are dependent upon the natural element coordinates ξ_i, $-1 \leq \xi_i \leq +1$. The element nodes are located along the element boundary (Figure 5.1). The element geometry and displacement field are dependent upon the nodal values, x_i^k and u_i^k, respectively. Such elements are referred to as Serendipity elements. If the element geometry and displacement field are interpolated by the same interpolation, then the elements are called isoparametric. The element shape functions for each of the isoparametric elements are given by [114]:

Corner nodes in the 16-node element ($\xi_1^k = \pm 1$, $\xi_2^k = \pm 1$, $\xi_3^k = \pm 1$):

$$\psi^k = \frac{1}{8}(1 + \xi_1^k \xi_1)(1 + \xi_2^k \xi_2)(1 + \xi_3^k \xi_3)(\xi_1^k \xi_1 + \xi_2^k \xi_2 - 1) \tag{5.3}$$

Typical side node in the 16-node element ($\xi_1^k = 0$, $\xi_2^k = \pm 1$, $\xi_3^k = \pm 1$):

$$\psi^k = \frac{1}{4}(1 - \xi_1{}^2)(1 + \xi_2^k \xi_2)(1 + \xi_3^k \xi_3) \tag{5.4}$$

Corner nodes in the 20-node element ($\xi_1^k = \pm 1$, $\xi_2^k = \pm 1$, $\xi_3^k = \pm 1$):

$$\psi^k = \frac{1}{8}(1 + \xi_1^k\xi_1)(1 + \xi_2^k\xi_2)(1 + \xi_3^k\xi_3)(\xi_1^k\xi_1 + \xi_2^k\xi_2 + \xi_3^k\xi_3 - 2) \tag{5.5}$$

Typical side node in the 20-node element ($\xi_1^k = 0$, $\xi_2^k = \pm 1$, $\xi_3^k = \pm 1$):

$$\psi^k = \frac{1}{4}(1 - \xi_1{}^2)(1 + \xi_2^k\xi_2)(1 + \xi_3^k\xi_3) \tag{5.6}$$

Corner nodes in the 24-node element ($\xi_1^k = \pm 1$, $\xi_2^k = \pm 1$, $\xi_3^k = \pm 1$):

$$\psi^k = \frac{1}{64}(1 + \xi_1^k\xi_1)(1 + \xi_2^k\xi_2)(1 + \xi_3^k\xi_3)[9(\xi_1{}^2 + \xi_2{}^2) - 10] \tag{5.7}$$

Typical side node in the 24-node element ($\xi_1^k = \pm\frac{1}{3}$, $\xi_2^k = \pm 1$, $\xi_3^k = \pm 1$):

$$\psi^k = \frac{9}{64}(1 - \xi_1{}^2)(1 + 9\xi_1^k\xi_1)(1 + \xi_2^k\xi_2)(1 + \xi_3^k\xi_3) \tag{5.8}$$

Corner nodes in the 32-node element ($\xi_1^k = \pm 1$, $\xi_2^k = \pm 1$, $\xi_3^k = \pm 1$):

$$\psi^k = \frac{1}{64}(1 + \xi_1^k\xi_1)(1 + \xi_2^k\xi_2)(1 + \xi_3^k\xi_3)[9(\xi_1{}^2 + \xi_2{}^2 + \xi_3{}^2) - 19] \tag{5.9}$$

Typical side node in the 32-node element ($\xi_1^k = \pm\frac{1}{3}$, $\xi_2^k = \pm 1$, $\xi_3^k = \pm 1$):

$$\psi^k = \frac{9}{64}(1 - \xi_1{}^2)(1 + 9\xi_1^k\xi_1)(1 + \xi_2^k\xi_2)(1 + \xi_3^k\xi_3) \tag{5.10}$$

where:

ξ_i^k = the value of natural coordinate ξ_i at node k

The order of element interpolation in each natural coordinate direction is summarized in Table 5.1. The 16-node and 24-node elements are often used in the analysis of laminated plates because of their higher order of interpolation of the in-plane displacement field. The 20-node and 32-node elements give an equal order interpolation in all three coordinate directions. The 20-node and 32-node elements were used exclusively in the present investigation. For any analysis in which stresses were required, the 32-node element was used.

5.1.2 Finite Element Equations

The nonlinear three-dimensional boundary value problem was derived in Section 4.7 using the principle of minimum total potential energy. Assuming that an equilibrium configuration exists at time $= t + \Delta t$, equation (4.92) may be rewritten [110]:

$$\int_{{}_0V} {}_0^{t+\Delta t}S_{ij}\delta {}_0^{t+\Delta t}E_{ij}\,{}^0dV = {}^{t+\Delta t}R \tag{5.11}$$

where:

$${}^{t+\Delta t}R = \int_{{}_0V} {}_0^{t+\Delta t}f_i\delta {}^{t+\Delta t}u_i\,{}^0dV + \int_{{}_0S_2} {}_0^{t+\Delta t}\bar{t}_i\delta {}^{t+\Delta t}u_i\,{}^0dS$$

Introducing the following incremental decompositions:

$${}_0^{t+\Delta t}S_{ij} = {}_0^tS_{ij} + {}_0S_{ij} \tag{5.12}$$

$${}_0^{t+\Delta t}E_{ij} = {}_0^tE_{ij} + {}_0E_{ij} \tag{5.13}$$

The first variation of the Green-Lagrange strain at time $t + \Delta t$ is given by:

$$\delta_0^{t+\Delta t}E_{ij} = \delta_0E_{ij} = \delta_0e_{ij} + \delta_0\eta_{ij} \tag{5.14}$$

Rewriting equation (5.11):

$$\int_{{}_0V} {}_0^tS_{ij}(\delta_0e_{ij} + \delta_0\eta_{ij})\,{}^0dV + \int_{{}_0V} {}_0S_{ij}(\delta_0e_{ij} + \delta_0\eta_{ij})\,{}^0dV = {}^{t+\Delta t}R \tag{5.15}$$

where:

$${}_0^tS_{ij} = {}_0C_{ijkl}({}_0^te_{kl} + {}_0^t\eta_{kl} - {}_0^tE_{kl}^T)$$

$${}_0S_{ij} = {}_0C_{ijkl}({}_0e_{kl} + {}_0\eta_{kl} - {}_0E_{kl}^T)$$

Equation (5.15) may be linearized by introducing the following approximations:

$${}_0S_{ij} = {}_0C_{ijkl}({}_0e_{kl} - {}_0E_{kl}^T) \tag{5.16}$$

$$\int_{{}_0V} {}_0S_{ij}\delta_0\eta_{ij}\,{}^0dV = 0 \tag{5.17}$$

Equation (5.15) can be rewritten:

$$\int_{{}_0V} {}_0C_{ijkl}({}_0e_{kl} - {}_0E^T_{kl})\delta_0 e_{ij}\, {}^0dV + \int_{{}_0V} {}^t_0S_{ij}\delta_0\eta_{ij}\, {}^0dV =$$

$${}^{t+\Delta t}R - \int_{{}_0V} {}^t_0S_{ij}\delta_0 e_{ij}\, {}^0dV \tag{5.18}$$

Equation (5.18) is an approximate equation of motion which can be solved for the increment of displacement u_i, where:

$$u_i = {}^{t+\Delta t}u_i - {}^t u_i \tag{5.19}$$

Equation (5.18) is a total Lagrangian formulation of the incremental equations of motion. The incremental equations (5.18) and (5.19) are used in the formulation of the Newton solution procedure. The finite element approximation of the incremental equations of motion is formulated by substituting the displacement field given by equations (5.2) into equations (5.18). The resulting system of m finite element equations may be written (in matrix form):

$$[{}^t_0K]\{u\} = \{{}^{t+\Delta t}R\} - \{{}^t_0F\} \tag{5.20}$$

where:

$[{}^t_0K]$ = global stiffness matrix

$\{u\}$ = incremental nodal displacement vector

$\{{}^{t+\Delta t}R\}$ = external force vector

$\{{}^t_0F\}$ = initial stress vector

m = number of degrees of freedom per element

The transpose of the incremental nodal displacement vector is given by:

$$\{u\}^T = \{\, u_1^1 \quad u_2^1 \quad u_3^1 \quad u_1^2 \quad \dots \quad u_3^n \,\} \tag{5.21}$$

where:

u_i^k = increment of displacement u_i at node k

n = nodes per element

The global stiffness matrix $[{}^t_0K]$ is composed of the linear stiffness matrix $[{}^t_0K_L]$ and the nonlinear stiffness matrix $[{}^t_0K_{NL}]$:

$$[{}^t_0K] = [{}^t_0K_L] + [{}^t_0K_{NL}] \tag{5.22}$$

The nonlinear finite element equations may be summarized as follows [110]:

$$\int_{{}_0V} {}_0C_{ijkl}({}_0e_{kl} - {}_0E^T_{kl})\delta_0 e_{ij}\, {}^0dV = \{\delta u\}^T[{}^t_0K_L]\{u\} \tag{5.23}$$

$$\int_{{}_0V} {}^t_0S_{ij}\delta_0\eta_{ij}\, {}^0dV = \{\delta u\}^T[{}^t_0K_{NL}]\{u\} \tag{5.24}$$

$$\int_{{}_0V} {}^t_0S_{ij}\delta_0 e_{ij}{}^0dV = \{\delta u\}^T\{{}^t_0F\} \tag{5.25}$$

$$[{}^t_0K_L] = \int_{{}_0V} [{}^t_0B_L]^T[{}_0C][{}^t_0B_L]^0dV \tag{5.26}$$

$$[{}^t_0K_{NL}] = \int_{{}_0V} [{}^t_0B_{NL}]^T[{}^t_0S][{}^t_0B_{NL}]^0dV \tag{5.27}$$

$$\{{}^t_0F\} = \int_{{}_0V} [{}^t_0B_L]^T\{{}^t_0\hat{S}\}^0dV \tag{5.28}$$

The nonlinear stiffness matrix $[{}^t_0K_{NL}]$ and the initial stress vector $\{{}^t_0F\}$ are both dependent upon the stresses, ${}^t_0S_{ij}$, of the most recently calculated equilibrium configuration. $[{}^t_0B_L]$ is the linear strain-displacement matrix and $[{}^t_0B_{NL}]$ is the nonlinear strain-displacement transformation matrix. The $[{}^t_0B_L]$ matrix is dependent upon the nodal displacements, ${}^tu^k_i$, of the most recently calculated equilibrium configuration. $[{}^t_0S]$ and $\{{}^t_0\hat{S}\}$ are matrices which contain components of the second Piola Kirchhoff stresses ${}^t_0S_{ij}$ within the elastic body at time t. The components of the $[{}^t_0B_L]$, $[{}^t_0B_{NL}]$, $[{}^t_0S]$, and $\{{}^t_0\hat{S}\}$ matrices are given in Appendix C. $[{}_0C]$ is the linear elastic constitutive matrix which contains the quantities ${}_0C_{ijkl}$. The equations used for the Newton iteration are:

$$[{}^t_0K^{(i-1)}]\{u^{(i)}\} = \{{}^{t+\Delta t}R\} - \{{}^t_0F^{(i-1)}\} \tag{5.29}$$

$$\{^{t+\Delta t}u^{(i)}\} = \{^{t+\Delta t}u^{(i-1)}\} + \{u^{(i)}\} \tag{5.30}$$

The initial conditions for the procedure are:

$$\{^{t+\Delta t}u^{(0)}\} = \{^{t}u\} \tag{5.31}$$

$$\{^{t+\Delta t}_{0}F^{(0)}\} = \{^{t}_{0}F\} \tag{5.32}$$

The right-hand side of equation (5.19) is the correction to the error in the approximation of the previous iteration. The iterative procedure is conducted until the calculated increment of displacement is sufficiently small. The convergence criterion for this investigation is to conduct the iterative procedure until the following relationship is satisfied:

$$\frac{||u||}{||^{t}u||} \leq 0.0001 \tag{5.33}$$

where $||u||$ and $||^{t}u||$ are L_2 (or Euclidean) norms of the incremental and total displacement vectors, respectively. The selection of this criterion was based upon the results of a convergence study conducted early in the investigation.

5.1.3 Numerical Integration

Each of the finite element equations derived in section 5.1.2 must be integrated over the initial volume or surface of the element. Polynomial-based interpolation functions are used to interpolate the displacements $^{t}u_i$ and initial coordinates $^{0}x_i$. The integrals presented in the previous section are of the form:

$$I(^{0}x_1, ^{0}x_2, ^{0}x_3) = \int_{-a}^{+a}\int_{-b}^{+b}\int_{-c}^{+c} F(^{0}x_1, ^{0}x_2, ^{0}x_3)\,^{0}dx_1\,^{0}dx_2\,^{0}dx_3 \tag{5.34}$$

The integrands of these equations are difficult to evaluate by classical means, but can be efficiently evaluated numerically using Gauss-Legendre quadrature. The Gauss-Legendre quadrature formula is given by:

$$\int_{a}^{b} F(x)dx = \int_{-1}^{+1} f(\xi)J\,d\xi = \sum_{i=1}^{n} W^{i} f(\xi^{i}) \tag{5.35}$$

where:

J = the determinant of the Jacobian (transformation between x and ξ)

W^i = Gauss weight factors

ξ^i = Gauss points

n = number of Gauss points

Gauss-Legendre quadrature is capable of exactly integrating an integrand which is a polynomial of order n by using $(n+1)/2$ Gauss points [115]. The integral on the left hand side of equation (5.35) is transformed from the x coordinate system, with a domain $a \leq x \leq b$, to the ξ coordinate system, with a domain of $-1 \leq \xi \leq +1$. This is the same as the transformation which exists between the coordinates ${}^0x_i$ and the natural element coordinate ξ_i. This quadrature formula can therefore be readily applied to integrals of the form shown in equation (5.34). The Jacobian matrix $[J]$ which transforms the coordinates ${}^0x_i$ into natural element coordinates ξ_i is given by:

$$[J] = [\frac{\partial^0 x_i}{\partial \xi_j}]^T = \begin{bmatrix} \frac{\partial^0 x_1}{\partial \xi_1} & \frac{\partial^0 x_2}{\partial \xi_1} & \frac{\partial^0 x_3}{\partial \xi_1} \\ \frac{\partial^0 x_1}{\partial \xi_2} & \frac{\partial^0 x_2}{\partial \xi_2} & \frac{\partial^0 x_3}{\partial \xi_2} \\ \frac{\partial^0 x_1}{\partial \xi_3} & \frac{\partial^0 x_2}{\partial \xi_3} & \frac{\partial^0 x_3}{\partial \xi_3} \end{bmatrix} \tag{5.36}$$

where:

$$\frac{\partial^0 x_i}{\partial \xi_j} = \sum_{k=1}^{n} \frac{\partial \psi^k}{\partial \xi_j} {}^0x_i^k \tag{5.37}$$

The inverse of this transformation is given by:

$$[J^*] = [J]^{-1} \tag{5.38}$$

Using this transformation, the integrand of equation (5.34) may be transformed to natural element coordinates:

$$\int_{-a}^{+a} \int_{-b}^{+b} \int_{-c}^{+c} F({}^0x_1, {}^0x_2, {}^0x_3) {}^0dx_1 {}^0dx_2 {}^0dx_3 =$$

$$\int_{-1}^{+1} \int_{-1}^{+1} \int_{-1}^{+1} f(\xi_1, \xi_2, \xi_3) J d\xi_1 d\xi_2 d\xi_3 \tag{5.39}$$

The integral on the right-hand side of equation (5.39) is approximated using a three-dimensional form of the Gauss-Legendre quadrature:

$$\int_{-1}^{+1}\int_{-1}^{+1}\int_{-1}^{+1} f(\xi_1,\xi_2,\xi_3)J\,d\xi_1 d\xi_2 d\xi_3 =$$

$$\sum_{i=1}^{n1}\sum_{j=1}^{n2}\sum_{k=1}^{n3} W^i W^j W^k f(\xi_1^i,\xi_2^j,\xi_3^k) \tag{5.40}$$

where:

n_i = number of gauss points in the ξ_i direction

A 4 x 4 x 4 Gaussian quadrature was used for most of the test cases considered in this study. For initial test cases in which an approximate solution of a nonlinear displacement field was sought with a coarse finite element mesh, a reduced 3 x 3 x 3 integration was used in order to reduce the number of required computations.

5.2 Computational Aspects

This section addresses the following computational aspects of the finite element analysis:

(1) Global/local finite element analysis.

(2) Nonlinear solution strategy.

(3) Interlaminar stress computations.

Tensorial (or index) notation has been used up to this point in order to clarify the development of the theory. However, in discussing the numerical results, the more conventional notation from classical laminated plate theory [22,23] is adopted. A comparison of these two notations is given in Table 5.2. The conventional notation is used for the remainder of this discussion.

5.2.1 Global/Local Finite Element Analysis

This section provides a summary of the procedures used for geometrically linear and nonlinear global/local finite element analyses. The laminates considered in this study possess two types of symmetries in material properties, laminate geometry, and external loading. These two symmetries are:

(1) Quarter symmetry $\Rightarrow$ [0/90] laminates.

(2) Inversion symmetry [116] $\Rightarrow$ [+45/−45] and [0/+45] laminates.

These symmetries are used to reduce the size of the numerical models and reduce the number of required computations. The regions of the laminate which are modeled using quarter and inversion symmetry are shown in Figure 5.2.

Since the interlaminar stress fields possess steep gradients near the free edges of the laminate, global/local finite element analysis was utilized in order to obtain more accurate free edge stress predictions. The geometry of the global/local finite element analysis is illustrated in Figure 5.3. The method of global/local finite element analysis has been used by a number of researchers [84,85,86] to conduct geometrically linear analyses of laminated composite structures. Both geometrically linear and nonlinear global/local finite element analyses are conducted in the present study for the cases of extensional and thermal loading. For the nonlinear analysis of the compression cases, interlaminar stresses existed across the entire interfacial surface; thus a detailed global finite element analysis was required.

The global/local modeling scheme is summarized below:

(a) A global solution for the displacement field is obtained from a quarter or inversion symmetric global finite element analysis of the laminate.

(b) The nodal displacements from the global finite element solution are used in the expression for the element displacement field, given by equations (5.2), to calculate interpolated displacements for nodes within the local finite element model.

(c) Interpolated displacements from the global solution are used as displacement boundary conditions for the local finite element analysis.

The selection of the location for the global/local interface was based upon two requirements:

(1) The displacements along the global/local interface predicted by the global finite element model must be converged.

(2) The boundary layer in which the interlaminar stresses exist must be contained within the local region.

The first requirement listed above is extremely important, since the accuracy of the solution for the local analysis is only as accurate as the displacement boundary conditions obtained from the solution for the global analysis. Based upon these requirements, careful consideration was given to both the selection of the location for the global/local interface and in the design of the global and local finite element meshes. The final selection of the global/local interface was based upon the results of detailed displacement and stress convergence studies conducted during this investigation. The region modeled by the local finite element analysis is shown in Figure 5.3. The local model extends from $0.8 \leq y/b \leq 1.0$. For thermal loading, local finite element analyses were also conducted for a local model which extended from $0.8 \leq x/a \leq 1.0$. For the 2.0 in. unsymmetric laminates ($L/h = 50$), this region extended a distance of 5.0 laminate thicknesses in from the free edge. For the 2.0 in. symmetric laminates ($L/h = 25$), this region extended a distance of 2.5 laminate thicknesses in from the free edge. The finite element models used in this study are summarized in Appendix D.

The procedures for geometrically linear and nonlinear global/local finite element analyses are summarized below:

Geometrically linear analysis – The linear solution from the global finite element analysis may be interpolated at any location within a global element using the element displacement field given by equations (5.2). The linear solution from the

global analysis is interpolated at the nodes in the local finite element model which lie along the global/local interface. These interpolated nodal displacements along the global/local interfacial surface are used to prescribe displacement boundary conditions for the linear local finite element analysis.

Geometrically nonlinear analysis – Like the linear analysis, the nonlinear solution from the global finite element analysis may be interpolated at any location using the element displacement field given by equations (5.2). The nonlinear solution from the global analysis is interpolated at the nodes within the local finite element model. The interpolated nodal displacements which lie along the global/local interface are used to prescribe displacement boundary conditions for the nonlinear local finite element analysis. The interpolated nodal displacements at the remaining nodes in the local model are used as an initial approximation for the initiation of the Newton algorithm.

5.2.2 Nonlinear Solution Strategy

The approximate solution of the three-dimensional nonlinear boundary value problem is extremely computationally intensive. The three-dimensional aspect of the problem results in a large system of simultaneous linear algebraic equations. The nonlinear nature of the boundary value problem adds an additional level of difficulty in that an iterative solution scheme (Newton's method) is used in which the system of simultaneous equations must be formulated and solved multiple times. This nonlinear solution procedure is further complicated by the existence of bifurcation points, multiple solution paths, and the large number of iterations which may be required before a converged solution is obtained.

Newton's method is initiated by providing the iterative algorithm with an approximate solution which is assumed to be in the neighborhood of the solution. If the initial approximate solution is within the neighborhood of the solution, the

algorithm will converge quadratically to the solution. Because geometrically nonlinear three-dimensional analysis is so computationally intensive, it is desirable to provide an initial approximate solution which is very close to the actual solution in order to reduce the number of required iterations. In the present study, initial approximate solutions were obtained from either nonlinear two-dimensional plate theory or the present nonlinear three-dimensional finite element analysis using a coarse mesh with reduced integration. Once the nonlinear solution is obtained, the solution is interpolated to provide an initial approximate solution for the nonlinear analysis of the refined three-dimensional finite element mesh.

The existence of bifurcation points and multiple solution paths can make the determination of a nonlinear solution difficult. At a bifurcation point, the nonlinear solution branches into multiple nonlinear solution paths. From a stability standpoint, these paths may be stable or unstable. The stability of a solution may be determined by evaluating the second variation of the total potential energy, $\delta^2\pi$, for positive definiteness (refer to section 4.8). As a bifurcation point is reached, the load level reaches a critical value which is an eigenvalue for the linear system of homogenous equations. At this point, the linear differential operator or tangent stiffness matrix becomes singular and the linear system of equations are no longer consistent. The linear form of Newton's method breaks down at this point. A number of methods may be used to overcome these difficulties of determining solutions for nonlinear problems with bifurcation points and multiple solution paths. The two methods which were used in the present study are summarized below.

The first method consists of providing the Newton algorithm with an initial approximate solution which is based upon the anticipated response of the elastic body. Oftentimes, an approximate mode shape for the nonlinear equilibrium configuration of the elastic body can be estimated. This approximate mode shape may be based on a number of factors, such as previous experimental or analytical results. As stated above, Newton's method is initiated by providing the algorithm

with an initial approximate solution which is assumed to be in the neighborhood of the solution. Therefore, if the appoximate solution, based upon the anticipated mode shape, is close enough to the solution, convergence to the solution will occur. If the load level for the desired solution is very close to a bifurcation point, a large number of iterations may be required, if convergence occurs at all. For these cases, the nonlinear solution may be obtained at a slightly higher load level, and then the nonlinear solution can be obtained by unloading down the nonlinear path.

The second method is to apply a small force or set of forces to the numerical model to 'stabilize' the solution as it passes near the bifurcation point. Once the desired load level is reached, the pseudo-loading may be removed and the iterative scheme restarted. If the approximate solution is sufficiently close enough to the actual solution, then the Newton procedure will converge toward it. Physically, this may be visualized as providing additional external loading to perturb the elastic body away from the critical state to a more stable deformed configuration. Mathematically, the introduction of the pseudo load modifies the set of equations such that the system of equations remains consistent (nonsingular) as it passes near the bifurcation point.

In addition to these two methods, others have been proposed by a number of researchers. Thurston [117,118] has proposed an effective method of extending Newton's method through bifurcation points in which higher order terms in the Taylor series expansion about the initial approximate solution are used to extend the method through bifurcation points. Although Thurston's method is an effective approach, the two methods described above were used in the present investigation because they provided a practical means of obtaining a solution without requiring extensive modification to the existing analysis.

5.2.3 Interlaminar Stress Computations

This section provides a brief discussion of the computational details for the following:

(1) Calculation of interlaminar stresses.

(2) Cauchy and second Piola-Kirchhoff stresses.

(3) Interpolations for surface plots.

Calculation of Interlaminar Stresses

The finite element method provides an approximate solution for the u, v, and w displacements at every finite element node point throughout the elastic body. The displacement gradient at any point within an element is evaluated using the element interpolation functions and nodal displacements. The strains at a given point are calculated from the displacement gradient using the strain-displacement equations. The stresses are calculated directly from the strains using the constitutive equations.

It has been suggested that the most accurate locations to evaluate the stresses within an element are at the element Gauss point locations used for the Gauss-Legendre quadrature of the element matrices [119,120]. Therefore, in the present study, the stresses are evaluated at each of these element Gauss points. However, the focus of this study is upon the components of interlaminar stress at the interface between adjacent laminae. An accurate and efficient method of determining these interlaminar stresses is by averaging the interlaminar stress values at Gauss points located above and below the interfacial surface. For a given x and y Gauss location, this method averages the interlaminar stress values at the closest two Gauss points located directly above and below (same x and y location) the interfacial surface. Thus a linear interpolation of the through-the-thickness variation of the interlaminar stresses is used to determine the stresses acting upon the interfacial surfaces. The assumption of a linear variation is a good approximation since the

closest Gauss points are located quite near the interfacial surface. Plots of the through-the-thickness variation of the interlaminar stress field also supported this assumption. In the present study, the interlaminar stresses predicted from both linear and nonlinear theory, Cauchy and second Piola-Kirchhoff stress, respectively, are calculated using this stress averaging scheme.

Cauchy and Second Piola-Kirchhoff Stresses

For geometrically linear analysis, the displacements, rotations, and strains of the elastic body are considered small and the linear strain-displacement equations (4.29) are used to calculate the strain at any given point. Cauchy stresses are calculated directly from the linear strains using the constitutive equations (4.81). For small deformation, the linear strain and Cauchy stress calculated from linear theory are the same as the engineering definitions of stress and strain.

For geometrically nonlinear analysis, displacements and rotations of the elastic body may be large, but the strains are still considered small. The Green-Lagrange nonlinear strain-displacement equations (4.28) are used to calculate the strain at any given point. Second Piola-Kirchhoff stresses are calculated directly from the Green-Lagrange strains using the same constitutive relations (4.82) used in the linear analysis (4.81). The Green-Lagrange strains and second Piola-Kirchhoff stresses calculated from nonlinear theory are referred to the original configuration of the elastic body. For small strains, these stresses and strains are approximately equal to the engineering stresses and strains [121]. The deformation considered in this study is assumed to be that of large displacement, large rotation, and small strain. Therefore, the Green-Lagrange strains and second Piola-Kirchhoff stresses calculated from nonlinear theory may be compared directly to the linear strains and Cauchy stresses calculated from linear theory.

The assumption, that the second Piola-Kirchhoff stress for small strains is approximately equal to the engineering stress or Cauchy stress, can be evaluated

through the consideration of a numerical example taken from this study. The example considers the stress-deformation response of a 2.0 inch square, T300/5208 graphite/epoxy, unsymmetric $[0_4/90_4]_t$ laminate subjected to a uniform change in temperature, $\Delta T = -280°F$ (detailed results are given in section 6.5). The out-of-plane (transverse) deflections are large; that is, on the order of the laminate thickness.

Interlaminar stress results are obtained from both geometrically linear and nonlinear finite element analysis. A discussion of these results follows in which comparisons are made between:

(1) Cauchy stresses (linear theory);

(2) second Piola-Kirchhoff stresses (nonlinear theory);

(3) Cauchy stresses (nonlinear theory, from equation 4.63); and

(4) interfacial stresses, t_N and t_S (nonlinear theory).

The Cauchy stresses σ_{zz}, τ_{yz}, and τ_{xz} and second Piola-Kirchhoff stresses S_{zz}, S_{yz}, and S_{xz} are calculated as discussed above. The second Piola-Kirchhoff stresses are measured with respect to the initial (undeformed) configuration of the elastic body. Therefore, S_{zz}, S_{yz}, and S_{xz}, act truly normal and parallel to the interfacial surface between adjacent plies in the undeformed configuration (refer to Figure 5.4). For small strains, these stresses are approximately equal to the engineering or Cauchy stresses acting upon the interfacial surface.

The actual engineering stresses or Cauchy stresses can be calculated directly from the second Piola-Kirchhoff stresses through equation (4.63). These stresses are measured with respect to the current (deformed) configuration, but are oriented with respect to the initial (undeformed) coordinates of the elastic body (refer to Figure 5.4). Therefore, at locations in which a finite rotation of the original geometric midplane has occurred, the σ_{zz}, τ_{yz}, and τ_{xz} components of stress are no longer acting truly normal and parallel to the current (deformed) interfacial surface. The finite rotations of the plane tangent to the interfacial surface at that point must

be accounted for. The engineering stresses acting upon the interfacial surface can be calculated from the Cauchy stresses (from equation 4.63) by rotating the stress state. For the purposes of this example, the calculation of the approximate normal t_N and shear t_S stress components acting upon a plane tangent to the interfacial surface (refer to Figure 5.4) is summarized below:

(1) The Cauchy stress and displacement gradient tensors at the interfacial surface are approximately determined using the stress averaging method discussed at the beginning of this section.

(2) The approximate orientation of a normal to the plane tangent to the interfacial surface is calculated. Referring to Figure 5.5, the components of the normal are determined from the vector product of two unit vectors lying along:

   (a) intersection between the tangent plane and xz-plane; and

   (b) intersection between the tangent plane and yz-plane.

   The components of these two unit vectors are determined from the following components of the displacement gradient:

$$\theta_x = \frac{\partial w}{\partial y}, \quad \theta_y = -\frac{\partial w}{\partial x} \tag{5.41}$$

(3) Using the direction cosines for the orientation of the tangent plane, the x, y, and z components of the traction vector acting upon the interfacial surface are calculated using Cauchy's formula given by equation (4.49):

$$t_x = n_x\sigma_{xx} + n_y\tau_{xy} + n_z\tau_{xz} \tag{5.42a}$$

$$t_y = n_x\tau_{yx} + n_y\sigma_{yy} + n_z\tau_{yz} \tag{5.42b}$$

$$t_z = n_x\tau_{zx} + n_y\tau_{yz} + n_z\sigma_{zz} \tag{5.42c}$$

where:

$$n_x = \cos\theta_x \sin\theta_y \tag{5.43a}$$

$$n_y = -\sin\theta_x \cos\theta_y \tag{5.43b}$$

$$n_z = \cos\theta_x \cos\theta_y \tag{5.43c}$$

(4) The normal t_N and shear t_S components of the stress acting upon the interfacial plane are given by:.

$$t_N = n_x t_x + n_y t_y + n_z t_z \tag{5.44}$$

$$t_S = \sqrt{t_T^2 - t_N^2} \tag{5.45}$$

where:

$$t_T^2 = t_x^2 + t_y^2 + t_z^2 \tag{5.46}$$

The displacement and stress results for the $[0_4/90_4]_t$ laminate are shown in Figures 5.6, 5.7, and 5.8. Figure 5.6 shows the w/h displacement of the midplane along the line $x = 0$ predicted by linear and nonlinear theory. A greater out-of-plane w displacement is predicted by linear theory and the maximum w displacement predicted by either theory is on the order of the laminate thickness. The rotations along the interfacial surface between the 0 and 90 degree plies become quite large near the edges of the laminate.

The distribution of normal stress along $x = 0$ at the 0/90 interface is shown in Figure 5.7. The t_x component of the stress vector acting along $x = 0$ is zero and the normal t_N and shear t_S stress components lie completely within the yz plane. The second Piola-Kirchhoff stress S_{zz} compares quite well with the normal stress t_N. The maximum Cauchy stress σ_{zz} calculated from the nonlinear theory using equations 4.63 is slightly less than the predicted maximum t_N stress. This difference is the result of the finite rotation of the interfacial surface, but the effect of the finite rotation upon the normal stress is small. Finally, the maximum Cauchy stress σ_{zz} predicted by linear analysis is less than the maximum t_N and S_{zz} stresses predicted by nonlinear theory.

The distribution of shear stress along $x = 0$ at the 0/90 interface is shown in Figure 5.8. The second Piola-Kirchhoff stress S_{yz} compares quite well with the

shear stress t_S. The Cauchy stresses τ_{yz} calculated from the nonlinear theory using equations 4.63 are shown to be quite different than the t_S shear stresses. This large difference is the result of the finite rotation of the interfacial surface. The Cauchy stress τ_{yz} calculated from (4.63), is shown to vary linearly, as does the slope of the interfacial surface since the curvature of the surface, κ_y, is approximately constant along y. Finally, the maximum Cauchy stress τ_{yz} predicted by linear analysis is less than the maximum t_S and S_{yz} stresses predicted by nonlinear theory.

The main conclusions based upon the results of this numerical example are that:

(a) The assumption that for geometrically nonlinear analysis with small strains, the second Piola-Kirchhoff stress is approximately equal to the engineering stress or Cauchy stress is a valid assumption.

(b) For geometrically nonlinear analysis, the determination of Cauchy or engineering stresses acting upon an interfacial surface of a laminate requires a great deal of additional computations.

Interpolations for Surface Plots

A number of surface plots are presented in Chapter 6 to illustrate the variation of both displacement and interlaminar stress fields across the interfacial surface. A uniform grid of data values at equally spaced x and y locations is required to generate the three-dimensional projection of the surface. However, the values of displacement obtained from the analysis are given at the element node points and stress values are given at the element Gauss points. Therefore, the displacement and stress data at the interfacial surface must be interpolated into a uniform grid. The element interpolation functions for the 32-node (cubic) element are used to interpolate the displacements into the uniform grid points. Interlaminar stresses are interpolated using a more general polynomial interpolation scheme which would allow for irregularly spaced data points. The interpolation scheme fit a quadratic

surface to the closest nine data points (Gauss points). The stress value at the grid point was then interpolated using this quadratic interpolation scheme.

5.3 Verification Test Cases

A number of finite element test cases were conducted in order to verify the finite element implementation of the analysis and to evaluate the analytical approach. The test cases were conducted in two phases. The first phase of test cases was designed to verify the finite element implementation by running a large number of simple cases which could be verified by results from the principles of continuum mechanics and strength of materials. The second phase of test cases was designed to evaluate the analytical approach by comparing results from the present analysis with results from the current literature.

The numerical results from the first phase of test cases compared quite well with the theoretical results. These test cases consisted of single element models subjected to externally applied forces, externally applied displacements, and uniform change in temperature. These test cases focused upon verifying the following aspects of the finite element implementation:

(a) Gaussian quadrature;

(b) element formulation;

(c) constitutive equations for an anisotropic solid medium;

(d) implementation of force and displacement boundary conditions;

(e) thermal analysis; and

(f) implementation of inversion symmetry.

The results from this first phase of test cases are omitted for brevity. The second phase of test cases focused upon two analytical capabilities:

(a) three-dimensional boundary value problems; and

(b) geometric nonlinearity.

The results for the second phase of test cases are discussed below.

The three-dimensional capabilities of the finite element analysis were evaluated by comparing with previous results for the free edge problem of a symmetric, finite-width composite laminate subjected to uniform axial extension. Interlaminar stresses (predicted by linear theory) determined from the present analysis were compared with the results of Herakovich, et al [78] and Wang and Choi [89]. The prediction of the interlaminar stresses at the free edges compared very well with the previous results. The comparison of these results are presented in Section 6.2.

The geometrically nonlinear capabilities were evaluated by conducting the following test cases:

(1) Nonlinear extension of an isotropic solid.

(2) Nonlinear bending of a cantilever beam with a transverse tip load.

(3) Nonlinear bending of a cantilever beam with a distributed loading.

(4) The elastica (postbuckling of a cantilever beam in compression).

(5) Thermal deflections of an unsymmetric cross-ply laminate.

The geometrically nonlinear solution for the uniaxial loading of an isotropic linear elastic solid can be derived from the basic principles of nonlinear elasticity. Based upon the theory covered in Chapter 4, the governing equation for the engineering strain can be written:

$$\frac{F}{{}^0A(1+\epsilon)} - E[\epsilon + \frac{1}{2}\epsilon^2] = 0 \tag{5.47}$$

where:

F = the axial force applied

ϵ = engineering strain ($\Delta L/L$)

E = Young's modulus

Equation (5.47) may be solved exactly or by using Newton's method. A comparison of the present analysis with the numerical solution from nonlinear elasticity theory is shown in Figure 5.9. Figure 5.9 shows the variation of the nondimensionalized end extension u/L with the applied uniform pressure (actual force per

unit undeformed area, where msi = 10^6 psi). The agreement between the present analysis and the numerical solution is very good.

The geometrically nonlinear bending of an isotropic cantilever beam under transverse load was considered for the cases of:

(a) concentrated transverse tip load; and

(b) uniformly distributed transverse loading.

For case (a), the present analysis was compared to the numerical solution given in reference 122 which was based upon nonlinear beam theory. Figure 5.10 shows the variation of the nondimensionalized transverse tip displacement w/L with the load parameter alpha α:

$$\alpha = \frac{FL^2}{EI} \tag{5.48}$$

where:

F = applied transverse tip load

L = length of the beam

E = Young's modulus

I = moment of inertia in bending

The agreement between the present analysis and the numerical solution [122] for case (a) is very good. For case (b), the present analysis was compared to the numerical solution given in reference 123 which was based upon nonlinear beam theory. Figure 5.11 shows the variation of the nondimensionalized transverse tip displacement w/L with the uniformly distributed loading. The agreement between the present analysis and the numerical solution [123] for case (b) is very good.

The postbuckling behavior of an isotropic cantilever beam under a compressive axial tip load, also known as the elastica, was also considered. The present analysis was compared with a numerical solution based upon the theory found in reference 124. The nonlinear finite element solution in the postbuckling range was determined by using: (1) pseudo loading through the bifurcation point; and (2) providing an initial approximate solution (refer to section 5.2.2). Both methods

produced successful convergence to the postbuckled solution. Figure 5.12 shows the variation of the nondimensionalized transverse tip displacement w/L with the normalized axial load (normalized with respect to the Euler buckling load). The agreement between the present analysis and the numerical solution is very good.

The thermal deflections of an unsymmetric cross-ply laminate were considered to evaluate the thermal analysis capability to predict the geometrically nonlinear response of laminated composite plates. The laminate considered was a T300/5208 graphite/epoxy $[0_4/90_4]_t$ laminate (material properties are given in Table 5.1) subjected to a uniform temperature change of $\Delta T = -280°F$. The laminate is square in planform ($a = b$) with a length of $L = 2a = 2b = 2.0$ in. and a laminate thickness of $h = 0.04$ in. Both geometrically linear and nonlinear finite element analyses were conducted. The linear results from the present analysis were compared with the results from linear classical laminated plate theory. Figure 5.13 shows the variation of the midplane w/h displacement with x/a. The agreement between the present analysis for 50 and 200 element models and linear classical laminated plate theory is very good. The agreement between the predictions of the 50 and 200 element models is an indication of the rapid convergence of the finite element solution. The nonlinear results from the present analysis were compared with the results from the nonlinear laminated plate analysis discussed in Appendix E. Figure 5.14 shows the variation of the midplane w/h displacement with x/a. The agreement between the present analysis and nonlinear laminated plate theory is very good. Comparisons between the predictions of the nonlinear plate analysis and previous experimental results [46,47,51] may also be found in Appendix E.

Chapter 6
RESULTS AND DISCUSSION

This chapter begins with introductory remarks regarding the numerical results and a discussion of the objective of the interlaminar stress comparisons between symmetric and unsymmetric laminates. Finite element analysis results are then presented for thin square laminated composite plates subjected to extensional, compressive, and thermal loading. The extensional loading cases include numerical results for thick laminates which are compared with previous results [78,89] for symmetric composite laminates subjected to uniform axial extension. The results for extensional, compressive, and thermal loading are summarized at the end of Sections 6.3, 6.4, and 6.5, respectively. The main conclusions of these summaries may be found in Tables 6.1 through 6.4.

The discussion in this chapter focuses upon the results for cross-ply and angle-ply laminates since these laminates exhibit different types of material property mismatch between adjacent layers (Table 3.4). The results for the cross-ply laminates demonstrate the effects of mismatch in in-plane normal strain ϵ_{yy} between adjacent layers which may be due to either a mismatch in ν_{xy}, α_x, or α_y. The results for the angle-ply laminates demonstrate the effects of mismatch in in-plane shear strain γ_{xy} between adjacent layers which may be due to either a mismatch in $\eta_{xy,x}$ or α_{xy}.

Geometrically linear and nonlinear three-dimensional finite element analyses are conducted for both symmetric and unsymmetric laminates. The initial geometric midplane of the symmetric laminates remains plane during loading, unless buckling occurs under the action of compressive loading. The laminate membrane-flexural coupling of the unsymmetric laminates causes the laminate to immediately deflect out of plane under the action of external loading. For laminates which deflect out of plane, transverse w displacement results are given at the geometric

midplane of the laminate. The predictions from nonlinear theory are obtained using the Green-Lagrange nonlinear strain tensor (numerical results using a reduced form of 3D nonlinear strain may be found in Appendix F). The interlaminar stress results are Cauchy stresses, σ_{ij}, predicted by linear theory and second Piola-Kirchhoff stresses, S_{ij}, predicted by nonlinear theory (refer to Section 5.2.3). Quarter symmetry finite element models are used for the cross-ply laminates and inversion symmetry models are used for the angle-ply (+45/–45) and 0/+45 laminates. Global/local finite element analysis (refer to Section 5.2.1) is used for the extensional and thermal loading cases in order to provide a more accurate prediction of free edge stresses.

The interlaminar stress results for each laminate are given at the interfacial surfaces between adjacent layers. The interlaminar stress results for symmetric laminates are given at the $z/h = +0.25$ interface, unless stated otherwise. As discussed in Section 5.2.3, these stresses are average values calculated from element Gauss points located nearest to the interfacial surface. Although interlaminar stress comparisons are sometimes made between symmetric and unsymmetric laminates at Gauss points which are located closest to the free edge, emphasis is placed upon point-by-point stress comparisons along the entire interface, since the stresses closest to the free edge may not be as accurate as stresses away from the free edge (refer to Section 2.3). For each load condition, interlaminar stress results are given at the interfacial surface along the plane $x = 0$ (Figure 3.2). For thermal loading, interlaminar stress results are also given along the plane $y = 0$. For compressive loading, nonlinear theory predicts that each laminate undergoes a change in mode shape during loading. After the change in mode shape has occurred, interlaminar stresses exist not only in regions near the free edges, but across the entire interfacial surface of the laminate. For these compression cases, the interlaminar stress results are given for the entire interfacial surface.

6.1 Objective of Interlaminar Stress Comparisons

For laminated plates subjected to external loading, the mismatch in material properties between adjacent layers causes interlaminar stresses to arise near the free edges of the laminate. For unsymmetric laminates under external loading, the mismatch in material properties about the geometric midplane causes the laminate to deflect out of plane. The objective of the interlaminar stress comparisons between symmetric and unsymmetric laminates is to determine the effect of these out-of-plane (transverse) deflections on the interlaminar stresses in unsymmetric laminates. Two examples are discussed below in order to illustrate how this objective is accomplished.

The three cross-ply laminates considered in this study are shown in Figure 6.1. On the left-hand side of Figure 6.1, the laminates are shown in their initial (undeformed) state within the plane $x = 0$. On the right-hand side of Figure 6.1, the laminates are shown in their current (deformed) state within the plane $x = 0$ under the action of extensional loading in the x direction. As discussed in Chapter 3, the same layer thickness was chosen for all laminates in order to achieve the same level of material property mismatch between adjacent layers. This figure illustrates the effect of mismatch in in-plane normal strain, ϵ_{yy}, between the 0 and 90 degree layers which is caused by a mismatch in Poisson's ratio ν_{xy} between the layers.

The upper half of the symmetric $[90/0]_s$ laminate is the same as the unsymmetric $[0/90]_t$ laminate which has an out-of-plane restraint $w(x, y, -h/2) = 0$ applied to its lower surface (Figure 6.1). The lower half of the symmetric $[0/90]_s$ laminate is the same as the unsymmetric $[0/90]_t$ laminate which has an out-of-plane restraint $w(x, y, +h/2) = 0$ applied to its upper surface. The out-of-plane restraint in each case is due to the presence of the other half of the laminate. For extensional loading, the unsymmetric $[0/90]_t$ laminate is free from out-of-plane restraint and deflects out of plane with a positive κ_y curvature. The upper half of the symmetric $[90/0]_s$ laminate and the lower half of the symmetric $[0/90]_s$ laminate are prevented from

deflecting out of plane by the other half of the laminate. Therefore, by comparing the interlaminar stresses within these laminates, the effect of out-of-plane restraint upon the interlaminar stresses within the unsymmetric $[0/90]_t$ laminate can be determined. And conversely, by comparing the interlaminar stresses within these laminates, the effect of the out-of-plane deflections upon the interlaminar stresses within the unsymmetric $[0/90]_t$ laminate can also be determined.

The three angle-ply laminates considered in this study are shown in Figure 6.2. This figure illustrates the effect of mismatch in in-plane shear strain, γ_{xy}, between the +45 and –45 degree layers which is caused by a mismatch in coefficient of mutual influence $\eta_{xy,x}$. The mismatch in in-plane shear strain between adjacent layers causes the unsymmetric $[+45/-45]_t$ laminate to deflect out of plane with twisting κ_{xy} curvature, although as shown in Figure 6.2, the out-of-plane deflections are zero along the line $(0, y, 0)$. As with the cross-ply laminates, by comparing the interlaminar stresses within these angle-ply laminates, the effect of the out-of-plane deflections upon the interlaminar stresses within the unsymmetric $[+45/-45]_t$ laminate can be determined.

6.2 Comparisons with Previous Results

This section discusses the numerical results for thick square graphite-epoxy laminated composite plates subjected to extensional loading ($u/a = +0.01$). The numerical results are compared with previous results [78,89] for symmetric composite laminates under uniform axial extension. The lamina material properties for the graphite-epoxy material system are given in Table 3.8. The geometry for the thick laminated composite plates is summarized in Table 3.9. The material and geometric properties for the symmetrically laminated composite plates are the same as those used in [53,78,89]. The unsymmetric and symmetric laminate stacking sequences considered are:

(1) $[0_{50}/90_{50}]_t$, $[90_{50}/0_{50}]_s$, $[0_{50}/90_{50}]_s$

(2) $[+45_{50}/-45_{50}]_t$, $[-45_{50}/+45_{50}]_s$, $[+45_{50}/-45_{50}]_s$.

The boundary conditions for the case of extensional loading are given in Table 3.3.

6.2.1 Out-of-Plane Displacements

The midplane w/h displacement extrema predicted by linear and nonlinear theory for the unsymmetric laminates are given in Table 6.5. For the loading range considered ($u/a = +0.01$), a unique nonlinear equilibrium configuration is predicted for each laminate at all load levels. The out-of-plane deflections of the unsymmetric laminates are predicted to be quite small by both linear and nonlinear theory (less than one percent of the laminate thickness). Linear theory predicts slightly greater out-of-plane deflections as compared to nonlinear theory. The effect of geometric nonlinearity upon the predicted response is for the unsymmetric laminate to stiffen and align itself with the in-plane extensional loading.

Surface plots of the midplane w/h displacements for one quarter of a 4.0 in. square $[0/90]_t$ laminate are shown in Figure 6.3. The deflections predicted by linear theory (Figure 6.3a) are similar in shape to those predicted by nonlinear theory (Figure 6.3b). The largest w displacements are predicted by both linear and nonlinear theory to occur at the midlength along the free edges $(0, \pm b, 0)$. Linear theory overpredicts this displacement by approximately 12 percent. Linear theory also overpredicts the displacement at the plate center by approximately 18 percent. The extensional-bending coupling, due to the mismatch in ν_{xy} between adjacent layers, causes the positive κ_y curvature in the laminate. The out-of-plane constraint $w(\pm a, y, 0)$ causes the laminate to bow slightly in the direction of loading with positive κ_x curvature. The major effect of geometric nonlinearity is to reduce this κ_x curvature as the unsymmetric laminate aligns itself with the extensional loading.

Surface plots of the midplane w/h displacements for a 4.0 in. square $[+45/-45]_t$ laminate are shown in Figure 6.4. The deflections predicted by linear theory (Figure 6.4a) are quite similar to those predicted by nonlinear theory (Figure 6.4b). The largest w displacements are predicted by both linear and nonlinear theory to occur along the free edges near the loaded ends of the laminate. Linear theory overpredicts this displacement by only 3 percent. The w displacement is equal to zero along the lines $(x,0,0)$ and $(0,y,0)$. The extensional-twisting coupling, due to the mismatch in $\eta_{xy,x}$ between adjacent layers, causes the positive κ_{xy} twisting curvature in the laminate. The out-of-plane constraint $w(\pm a,y,0)$ causes the w displacement to return to zero at the loaded edges. The effect of geometric nonlinearity is to slightly reduce the out-of-plane κ_{xy} twisting curvature of the laminate.

6.2.2 Interlaminar Stresses for 0/90 Laminates

The interlaminar stress results for the thick cross-ply laminates under extensional loading are summarized in Table 6.6. Since the out-of-plane deflections of the unsymmetric laminates are small (less than one percent of the laminate thickness), the differences in the interlaminar stress predictions between linear theory (Cauchy stresses) and nonlinear theory (second Piola-Kirchhoff stresses) are also small (less than 2 percent). The interlaminar stress results predicted by linear theory for the symmetric cross-ply laminates are compared with the results of Herakovich, et al [78] in Figures 6.5 and 6.6. The interlaminar stress predictions for the σ_{zz} and τ_{yz} stresses compare very well with the previous results [78], differing mainly in the prediction of maximum stress at the free edge. The interlaminar τ_{xz} shear stress is predicted to be equal to zero by both the present and previous numerical analyses.

Interlaminar stress distributions along $x = 0$ for both the symmetric and unsymmetric cross-ply laminates are shown in Figures 6.7 and 6.8. The interlaminar stresses shown are those predicted by linear theory (Figures 6.7a and 6.8a) and nonlinear theory (Figures 6.7b and 6.8b). As is well known, the interlaminar normal

stresses in a symmetric cross-ply laminate are dependent upon the laminate stacking sequence (Figure 6.7). The interlaminar normal stresses, which arise in order to satisfy local moment equilibrium, are quite different in the symmetric $[90/0]_s$ laminate as compared to the symmetric $[0/90]_s$ laminate. The difference in the interlaminar normal stress distributions are due to the difference in sign of the moments that each react against [100].

Comparing the interlaminar normal stresses in the unsymmetric laminate with those in the symmetric laminates, the distribution of normal stresses in the unsymmetric $[0/90]_t$ laminate is more similar to that in the symmetric $[0/90]_s$ laminate (Figure 6.7). The interlaminar normal stresses are similar in that as the free edge is approached in both laminates, the normal stresses vary from small compressive values to larger tensile values. The maximum normal stresses for both laminates are tensile and occur at the free edge. On the other hand, as the free edge is approached in the symmetric $[90/0]_s$ laminate, the normal stresses vary from tensile values to compressive values, and then transition back to tensile values near the free edge. The largest compressive and tensile normal stresses in the symmetric $[90/0]_s$ laminate are of approximately the same magnitude with the largest tensile normal stress occurring at the free edge.

The σ_{zz} and S_{zz} interlaminar normal stresses are much larger in the unsymmetric $[0/90]_t$ laminate as compared to a symmetric $[90/0]_s$ laminate (Figure 6.7). The largest tensile stresses are predicted to be a factor of 3.7 times greater by linear theory and a factor of 3.5 times greater by nonlinear theory. When compared to the symmetric $[0/90]_s$ laminate, however, the σ_{zz} and S_{zz} stresses are smaller in the unsymmetric $[0/90]_t$ laminate (Figure 6.7). The largest tensile stresses are predicted to be 16 percent smaller by linear theory and 18 percent smaller by nonlinear theory. Therefore, depending upon the symmetric stacking sequence, the interlaminar normal stresses in the unsymmetric $[0/90]_t$ laminate may be either much larger or smaller than those occurring in comparable symmetric laminates. Based upon the

discussion in Section 6.2, if the unsymmetric $[0/90]_t$ laminate is free from out-of-plane restraint $w(0,0,-h/2)$, then the out-of-plane deflections significantly increase the interlaminar normal stresses. If the unsymmetric $[0/90]_t$ laminate is free from out-of-plane restraint $w(0,0,+h/2)$, then the out-of-plane deflections decrease the interlaminar normal stresses.

The τ_{yz} and S_{yz} interlaminar shear stresses which act in a direction normal to the free edge are shown in Figure 6.8. The interlaminar shear stress distribution in the unsymmetric laminate is similar to those in the symmetric laminates with the maximum shear stresses occurring near the free edges. The sign of the shear stresses in the unsymmetric $[0/90]_t$ laminate and symmetric $[90/0]_s$ laminate are opposite to those in the symmetric $[0/90]_s$ laminate. For all laminates, the τ_{yz} and S_{yz} stresses decrease at the free edge and approach approximate satisfaction of the traction free boundary condition. The τ_{yz} and S_{yz} stresses are smaller in the unsymmetric $[0/90]_t$ laminate as compared to the symmetric laminates. As compared to the symmetric $[90/0]_s$ laminate, the largest shear stresses in the unsymmetric laminate are predicted to be 22 percent smaller by both linear and nonlinear theory. As compared to the symmetric $[0/90]_s$ laminate, the largest shear stresses in the unsymmetric laminate are predicted to be 16 percent smaller by both linear and nonlinear theory. Therefore, the interlaminar shear stresses acting in a direction normal to the free edge in the unsymmetric $[0/90]_t$ laminate are smaller than those occurring in comparable symmetric laminates. Based upon the discussion in Section 6.2, if the unsymmetric $[0/90]_t$ laminate is free from out-of-plane restraint, the out-of-plane deflections decrease the interlaminar shear stresses.

Unlike the results for symmetric laminates, the τ_{zz} and S_{zz} stresses are nonzero at the free edges of the unsymmetric $[0/90]_t$ laminate. τ_{zz} and S_{zz} stresses vary from a large positive value at the plate corners to approximately zero at the intersection of the free edge with the line $(0,y,0)$. These stresses are discussed in

greater detail in Section 6.3.2 in which a surface plot of the variation of S_{zz} across the 0/90 interfacial surface is provided.

6.2.3 Interlaminar Stresses for +45/−45 Laminates

The interlaminar stress results for the thick angle-ply laminates under extensional loading are summarized in Table 6.7. Like the thick cross-ply laminates, the out-of-plane deflections of the unsymmetric laminates are small (less than one percent of the laminate thickness), and the differences in the interlaminar stress predictions between linear and nonlinear theory are also small (less than 2 percent). The interlaminar stress results predicted by linear theory for the symmetric angle-ply laminates are compared with the results of Wang and Choi [89] in Figures 6.9, 6.10, and 6.11. The interlaminar stress predictions for the σ_{zz} and τ_{xz} stresses compare very well with the previous results [89], differing mainly in the prediction of maximum stress at the free edge. There is a difference in the predicted τ_{yz} stresses, however these stresses are very small compared to the τ_{xz} and σ_{zz} stresses (less than 5 percent). The differences between the τ_{yz} stress predictions may be due to the differences in the formulations. The present analysis is a full three-dimensional analysis and the previous analysis [89] is based upon generalized plane deformation.

Interlaminar stress distributions along $x = 0$ for for both the symmetric and unsymmetric angle-ply laminates are shown in Figures 6.12 through 6.14. Except for the change in sign of the τ_{xz} shear stress, the interlaminar stresses within the symmetric laminates are identical to one another. Comparing the interlaminar normal stresses in the unsymmetric laminate with those in the symmetric laminates, the distribution of normal stresses are similar (Figure 6.12). As the free edge is approached in each laminate, the normal stresses vary from small tensile values to larger compressive values with the largest stresses occurring at the free edge. However, the σ_{zz} and S_{zz} stresses are larger in the unsymmetric $[+45/-45]_t$ laminate

as compared to the symmetric laminates. The largest compressive stresses are predicted to be 24 percent larger by linear theory and 23 percent larger by nonlinear theory. Therefore, the interlaminar normal stresses in the unsymmetric $[+45/-45]_t$ laminate are larger than those occurring in comparable symmetric laminates. If the unsymmetric $[+45/-45]_t$ laminate is free from out-of-plane restraint (Section 6.2), the out-of-plane deflections increase the interlaminar normal stresses.

The τ_{yz} and S_{yz} interlaminar shear stresses which act in a direction normal to the free edge are shown in Figure 6.13. The τ_{yz} and S_{yz} stresses in the symmetric laminates approach zero at the free edge and approximately satisfy the traction free boundary condition. In the unsymmetric laminate, the τ_{yz} and S_{yz} stresses are zero along $x = 0$. The τ_{yz} and S_{yz} stresses are zero along most of the length (in the x direction) in the unsymmetric laminate, becoming non-zero within regions near the loaded edges. Therefore, the τ_{yz} and S_{yz} interlaminar shear stresses are zero in the unsymmetric $[+45/-45]_t$ laminate, while these shear stresses are non-zero in comparable symmetric laminates. If the unsymmetric $[+45/-45]_t$ laminate is free from out-of-plane restraint (Section 6.2), the out-of-plane deflections completely relieve the interlaminar shear stresses acting normal to the free edge.

The τ_{xz} and S_{xz} interlaminar shear stresses which act in a direction parallel to the free edge are shown in Figure 6.14. The sign of the shear stresses in the unsymmetric $[+45/-45]_t$ laminate and symmetric $[-45/+45]_s$ laminate are opposite to those in the symmetric $[+45/-45]_s$ laminate. For each laminate, the largest τ_{xz} and S_{xz} stresses occur at the free edges of the laminate. The τ_{xz} and S_{xz} stresses are slightly smaller in the unsymmetric $[+45/-45]_t$ laminate as compared to the symmetric laminates. The largest shear stresses are predicted to be 6 percent smaller by both linear and nonlinear theory. Therefore, the interlaminar shear stresses acting parallel to the free edge in the unsymmetric $[+45/-45]_t$ laminate are slightly smaller than those occurring in comparable symmetric laminates. If the unsymmetric $[+45/-45]_t$ laminate is free from out-of-plane restraint (Section 6.2),

the out-of-plane deflections decrease the interlaminar shear stresses acting parallel to the free edge.

6.3 Extensional Loading

This section discusses the numerical results for thin square T300/5208 graphite-epoxy laminated composite plates subjected to extensional loading ($u/a = +0.01$). The lamina material properties for the T300/5208 graphite-epoxy material system are given in Table 3.1. The geometry for the thin laminated composite plates is summarized in Table 3.2. The unsymmetric and symmetric laminate stacking sequences considered are:

(1) $[0_4/90_4]_t$, $[90_4/0_4]_s$, $[0_4/90_4]_s$

(2) $[+45_4/-45_4]_t$, $[-45_4/+45_4]_s$, $[+45_4/-45_4]_s$

(3) $[0_4/+45_4]_t$, $[+45_4/0_4]_s$, $[0_4/+45_4]_s$

The boundary conditions for the case of extensional loading are given in Table 3.3.

6.3.1 Out-of-Plane Displacements

The midplane w/h displacement extrema predicted by linear theory and nonlinear theory for the unsymmetric laminates are given in Table 6.8. The midplane w/h displacement extrema are given for unsymmetric laminates with thickness ratios of $L/h = 50, 100, 150$. For the loading range considered ($u/a = +0.01$), a unique nonlinear equilibrium configuration is predicted for each laminate at all load levels. The out-of-plane deflections for the 2.0 in. ($L/h = 50$) unsymmetric laminates are predicted by both linear and nonlinear theory to be small (less than 25 percent of the laminate thickness). Like the results for the thicker laminates (Section 6.2.1), linear theory overpredicts the out-of-plane deflections and the effect of geometric nonlinearity is for the unsymmetric laminate to stiffen and align itself with the in-plane extensional load. Since the out-of-plane deflections are larger in

the thinner laminates, the effects of geometric nonlinearity are stronger than those observed in the thicker laminates.

Surface plots of the midplane w/h displacements for one quarter of a 2.0 in. square $[0/90]_t$ laminate are shown in Figure 6.15. There are noticeable differences in the displacement predictions between linear (Figure 6.15a) and nonlinear theory (Figure 6.15b). These differences can be more clearly seen in the plots along $x = 0$ and $y = 0$ provided in Figure 6.16. The largest w displacements are predicted by both linear and nonlinear theory to occur at the midlength along the free edges $(0, \pm b, 0)$. Linear theory overpredicts this displacement by a factor of 3. Linear theory also overpredicts the displacement at the plate center by a factor of 24. As discussed in Section 6.2.1, the extensional-bending coupling, due to the mismatch in ν_{xy} between adjacent layers, causes the positive κ_y curvature and the out-of-plane constraint $w(\pm a, y, 0)$ causes the slight positive κ_x curvature. The effects of geometric nonlinearity are quite strong as the laminate stiffens and aligns itself with the in-plane extensional loading.

Surface plots of the midplane w/h displacements for a 2.0 in. square $[+45/-45]_t$ laminate are shown in Figure 6.17. The deflected shape predicted by linear theory (Figure 6.17a) is similar to that predicted by nonlinear theory (Figure 6.17b). Midplane w/h displacements along the free edge $(y/b = 1)$ are shown in Figure 6.18. The largest w displacements are predicted by both linear and nonlinear theory to occur along the free edges near the loaded ends of the laminate. Linear theory overpredicts this displacement by approximately 15 percent. The w displacement is equal to zero along the lines $x = 0$ and $y = 0$. As discussed in Section 6.2.1, the extensional-twisting coupling, due to the mismatch in $\eta_{xy,x}$ between adjacent layers, causes the positive κ_{xy} twisting curvature and the out-of-plane constraint $w(\pm a, y, 0)$ causes the w displacement along the free edges to return to zero near the loaded edges. The effect of geometric nonlinearity is to reduce the κ_{xy} curvature in the laminate.

Surface plots of the midplane w/h displacements for a 2.0 in. square $[0/+45]_t$ laminate are shown in Figure 6.19. There are noticeable differences in the displacement predictions between linear (Figure 6.19a) and nonlinear theory (Figure 6.19b). These differences can be more clearly seen in the plots along $x = 0$ and $y = 0$ provided in Figure 6.20. The largest w displacements are predicted by both linear and nonlinear theory to occur along the free edges of the laminate. Linear theory overpredicts this displacement by a factor of $1\frac{1}{2}$. Linear theory also overpredicts the center displacement by a factor of over $3\frac{1}{2}$. The mismatch in ν_{xy} and $\eta_{xy,x}$ between adjacent layers causes full membrane-flexural coupling ($B_{ij} \neq 0$) in the unsymmetric laminate. The combined effect of the full membrane-flexural coupling and the out-of-plane constraint $w(\pm a, y, 0)$ causes the complex deflected shapes shown (Figures 6.19 and 6.20). The laminate has a negative κ_{xy} twisting curvature with negative κ_x and κ_y normal curvatures. The effect of geometric nonlinearity is quite strong as the laminate stiffens and aligns itself with the in-plane extensional loading.

6.3.2 Interlaminar Stresses for 0/90 Laminates

The interlaminar stress results for the thin cross-ply laminates subjected to extensional loading are summarized in Table 6.9. Since the out-of-plane deflections of the unsymmetric laminate are small (less than 25 percent of the laminate thickness), the differences in the interlaminar stress predictions between linear and nonlinear theory are also small (less than 2 percent). The interlaminar stress results for the thin cross-ply laminates agree quite well with the results of the thicker cross-ply laminates discussed in Section 6.2.2.

Surface plots of the interlaminar stress distributions predicted by nonlinear theory are provided in Figures 6.21 through 6.23. Stress concentrations are predicted at the plate corners where the traction free surface intersects with the surface upon which the edge displacements are prescribed. These stress concentrations arise in

order to satisfy local equilibrium at the plate corners. Interlaminar stress distributions along $x = 0$ for both the symmetric and unsymmetric cross-ply laminates are shown in Figures 6.24 and 6.25.

The σ_{zz} and S_{zz} interlaminar normal stresses are much larger in the unsymmetric $[0/90]_t$ laminate as compared to a symmetric $[90/0]_s$ laminate (Figure 6.24). The largest tensile stresses are predicted to be a factor of 3.2 times greater by both linear and nonlinear theory. When compared to the symmetric $[0/90]_s$ laminate, the σ_{zz} and S_{zz} stresses are smaller in the unsymmetric $[0/90]_t$ laminate (Figure 6.24). The largest tensile stresses are predicted to be only 8 percent smaller by linear theory and only 9 percent smaller by nonlinear theory. Like the thicker cross-ply laminates (Section 6.2.2), depending upon the symmetric stacking sequence, the interlaminar normal stresses in the unsymmetric $[0/90]_t$ laminate may be either much larger or smaller than those occurring in comparable symmetric laminates.

The τ_{yz} and S_{yz} interlaminar shear stresses which act in a direction normal to the free edge are shown in Figure 6.25. The τ_{yz} and S_{yz} stresses are smaller in the unsymmetric $[0/90]_t$ laminate as compared to the symmetric laminates. As compared to the symmetric $[90/0]_s$ laminate, the largest shear stresses in the unsymmetric laminate are predicted to be 29 percent smaller by both linear and nonlinear theory. As compared to the symmetric $[0/90]_s$ laminate, the largest shear stresses in the unsymmetric laminate are predicted to be 19 percent smaller by linear theory and 18 percent smaller by nonlinear theory. Like the thicker cross-ply laminates (Section 6.2.2), the interlaminar shear stresses acting in a direction normal to the free edge in the unsymmetric $[0/90]_t$ laminate are smaller than those occurring in comparable symmetric laminates.

Unlike the results for symmetric laminates, the τ_{xz} and S_{xz} stresses are nonzero at the free edges of the unsymmetric $[0/90]_t$ laminate. The shear stresses vary from a large positive value at the plate corners to approximately zero at the intersection of the free edge with the line $x = 0$ (for example, refer to Figure 6.23).

The large positive shear stress at the corner is caused by the intersection of the prescribed uniform u displacement with the free edge. The large τ_{zx} shear stress arises to counteract the rigid body rotation about the z-axis of the element of material above the midplane at the corner of the laminate.

6.3.3 Interlaminar Stresses for +45/−45 Laminates

The interlaminar stress results for the thin angle-ply laminates under extensional loading are summarized in Table 6.10. Since the out-of-plane deflections of the unsymmetric laminate are small (less than 2 percent of the laminate thickness), the differences in the interlaminar stress predictions between linear and nonlinear theory are also small (less than 4 percent). The interlaminar stress results for the thin angle-ply laminates agree quite well with the results of the thicker angle-ply laminates discussed in Section 6.2.3. Surface plots of the interlaminar stress distributions predicted by nonlinear theory are provided in Figures 6.26 through 6.28. Like the unsymmetric cross-ply laminates, stress concentrations are predicted at the plate corners. Interlaminar stress distributions along $x = 0$ for both symmetric and unsymmetric angle-ply laminates are shown in Figures 6.29 through 6.31.

The σ_{zz} and S_{zz} interlaminar stresses are larger in the unsymmetric $[+45/-45]_t$ laminate as compared to the symmetric laminates (Figure 6.29). The largest compressive stresses are predicted to be 26 percent larger by linear theory and 29 percent larger by nonlinear theory. Like the thicker angle-ply laminate (Section 6.2.3), the interlaminar normal stresses in the unsymmetric $[+45/-45]_t$ laminate are larger than those occurring in comparable symmetric laminates.

The τ_{yz} and S_{yz} interlaminar shear stresses which act in a direction normal to the free edge are shown in Figure 6.30. As shown in Figure 6.30, the τ_{yz} and S_{yz} stresses are zero along $x = 0$ in the unsymmetric laminate. The τ_{yz} and S_{yz} stresses are zero along most of the length of the free edge, becoming non-zero within regions near the loaded edges. Like the thicker angle-ply laminates, the τ_{yz} and

S_{yz} interlaminar shear stresses are zero in the unsymmetric $[+45/-45]_t$ laminate, while these shear stresses are non-zero in comparable symmetric laminates.

The τ_{zz} and S_{zz} interlaminar shear stresses which act in a direction parallel to the free edge are shown in Figure 6.31. The τ_{zz} and S_{zz} stresses are slightly smaller in the unsymmetric $[+45/-45]_t$ laminate as compared to the symmetric laminates. The largest shear stresses are predicted to be less than 1 percent smaller by both linear and nonlinear theory. Again, like the thicker angle-ply laminates, the interlaminar shear stresses acting parallel to the free edge in the unsymmetric $[+45/-45]_t$ laminate are slightly smaller than those occurring in comparable symmetric laminates.

6.3.4 Interlaminar Stresses for 0/+45 Laminates

The interlaminar stress results for the thin 0/+45 laminates under extensional loading are summarized in Table 6.11. Since the out-of-plane deflections of the unsymmetric laminate are small (less than 4 percent of the laminate thickness), the differences in the interlaminar stress predictions between linear and nonlinear theory are also small (less than 6 percent). Surface plots of the interlaminar stress distributions predicted by nonlinear theory are provided in Figures 6.32 through 6.34. Like the unsymmetric cross-ply and angle-ply laminates, stress concentrations are predicted at the plate corners. Interlaminar stress distributions along $x = 0$ for both symmetric and unsymmetric angle-ply laminates are shown in Figures 6.35 through 6.37.

6.3.5 Summary

The main conclusions based upon the numerical results for extensional loading are given below. These conclusions are summarized in Tables 6.1 and 6.2. Interlaminar shear stresses acting in a direction normal to the free edge are denoted as τ_{zn}. Interlaminar shear stresses acting in a direction parallel to the free edge are

denoted as τ_{zt}. For the laminated plates and boundary conditions considered, the main conclusions for extensional loading are:

(1) Out-of-plane displacements: For the unsymmetric laminates considered, the out-of-plane deflections caused by laminate membrane-flexural coupling are predicted to be larger in magnitude by linear theory as compared to nonlinear theory. The effect of geometric nonlinearity is to reduce the out-of-plane deflections (stiffening effect) of the unsymmetric laminates.

(2) Mismatch in in-plane normal strain: The following behavior is observed for the cross-ply laminates in which there exists a mismatch in Poisson's ratio ν_{xy} between adjacent layers. Interlaminar normal σ_{zz} and shear τ_{zn} stresses exist within the free edge regions of both symmetric and unsymmetric laminates. For the unsymmetric and symmetric cross-ply laminates, the maximum tensile normal stresses occur at the free edges. The following differences are observed in the predicted interlaminar stresses for the unsymmetric $[0/90]_t$ laminate as compared to the symmetric laminates:

- Interlaminar normal stresses σ_{zz} are either smaller or much larger.
- Interlaminar shear stresses τ_{zn} are smaller.

Depending upon the symmetric stacking sequence, the interlaminar normal σ_{zz} stresses may be either smaller or much larger in the unsymmetric laminate as compared to the symmetric laminates. The shear τ_{zn} stresses are relieved by the out-of-plane deflections of the unsymmetric laminate.

(3) Mismatch in in-plane shear strain: The following behavior is observed for the angle-ply laminates in which there exists a mismatch in the coefficient of mutual influence $\eta_{xy,x}$ between adjacent layers. Interlaminar normal σ_{zz} and shear τ_{zt} stresses exist within the free edge regions of both symmetric and unsymmetric laminates. Interlaminar shear stresses τ_{zn} are present within the symmetric laminates and are zero within the unsymmetric laminate. The maximum interlaminar normal stresses σ_{zz} are compressive and occur at the free edges.

The maximum interlaminar shear stresses τ_{zt} are very large and also occur at the free edges. The following differences are observed in the predicted interlaminar stresses for the unsymmetric $[+45/-45]_t$ laminate as compared to the symmetric laminates:

- Interlaminar normal stresses σ_{zz} are larger.
- Interlaminar shear stresses τ_{zn} vanish.
- Interlaminar shear stresses τ_{zt} are smaller.

The out-of-plane twisting deflections of the unsymmetric laminate increase the interlaminar normal stresses σ_{zz} and reduce the interlaminar shear τ_{zt} stresses. The interlaminar shear stresses τ_{zn} are completely relieved by the out-of-plane deflections of the unsymmetric laminate.

(4) Comparison of stress predictions between linear and nonlinear theory: For the symmetric and unsymmetric laminates, the difference between the interlaminar stresses predicted by linear theory (Cauchy stresses) and nonlinear theory (second Piola-Kirchhoff stresses) are small. The reason that the differences are small is that even though the differences in the predicted out-of-plane deflections between linear and nonlinear theory are large, the maximum deflection predicted by either theory is small (less than 25 percent of the laminate thickness).

(5) Comparison of results for thick and thin laminates: The trends observed in conclusions (1) through (4) apply to the numerical results for both the thick (Section 6.2) and thin (Section 6.3) laminates. Although the out-of-plane deflections were smaller for the thick laminates, the out-of-plane deflections of the unsymmetric laminates had an important effect on the interlaminar stresses for both the thick and thin laminates.

6.4 Compressive Loading

This section discusses the numerical results for thin square T300/5208 graphite-epoxy laminated composite plates subjected to compressive loading ($u/a = -0.01$). The lamina material properties for the T300/5208 graphite-epoxy composite material system are given in Table 3.1. The geometry for the thin laminated composite plates is summarized in Table 3.2. The unsymmetric and symmetric laminate stacking sequences considered are:

(1) $[0_4/90_4]_t$, $[90_4/0_4]_s$, $[0_4/90_4]_s$

(2) $[+45_4/-45_4]_t$

(3) $[0_4/+45_4]_t$

The boundary conditions for compressive loading given in Table 3.3 are identical to extensional loading (Sections 6.2 and 6.3) with the exception of a reversal in the direction of the applied edge displacement. The symmetric laminates buckle out of plane under compressive loading; therefore these laminates are modeled completely through the thickness. Inversion symmetric finite element analyses of the symmetric +45/–45 and 0/+45 laminates were not conducted due to the large number of degrees of freedom required (computational constraint).

6.4.1 Out-of-Plane Displacements

The midplane w/h displacement extrema predicted by linear and nonlinear theory for the symmetric ($L/h = 25$) and unsymmetric ($L/h = 50, 100, 150$) laminates are given in Table 6.12. The w displacements predicted by linear theory are consistent with the predictions of linear theory for extensional loading; the initial geometric midplane of the symmetric laminates remains plane throughout loading and the out-of-plane w displacements of the unsymmetric laminates are equal and opposite to those predicted for extensional loading.

The out-of-plane w displacements predicted by nonlinear theory are quite different in that each laminate undergoes a change in mode shape during loading. For

the symmetric laminates, the initial geometric midplane remains plane until the laminate buckles into a single half-wave equilibrium configuration in the loading x direction (Figure 6.38). In contrast to the symmetric laminates, the unsymmetric laminates deflect immediately out of plane under the compressive in-plane loading. During loading, the unsymmetric laminates also undergo a change in mode shape in which the laminate transitions into a single half-wave equilibrium configuration in the loading x direction. Before this change in mode shape occurs, the deflected shapes of the unsymmetric laminates are quite similar to those predicted by linear theory, except that greater out-of-plane deflections are predicted by nonlinear theory. Both symmetric and unsymmetric laminates buckle as wide-columns with a significant decrease in postbuckling stiffness after the change in mode shape has occurred. The transition to the single half-wave configuration occurs quite rapidly over a very small range of compressive loading. After the change in mode shape occurs, the out-of-plane deflections of the laminate become quite large for both symmetric and unsymmetric laminates; i.e., on the order of the laminate thickness.

The critical compressive loads at which a change in laminate mode shape occurs are given in Table 6.13. The table compares the buckling loads predicted by linear wide-column theory [124] with the buckling loads predicted by the present nonlinear three-dimensional finite element analysis. The critical average membrane stress resultants for the symmetric cross-ply laminates are predicted by treating the plates as wide orthotropic columns:

$$N_x = \frac{4\pi^2 D_{11}}{L^2} \tag{6.1}$$

where:

$L = 2a = 2b$ = length of the square plate

D_{11}= flexural stiffness in the loading x direction

The critical average membrane stress resultants for the unsymmetric laminates are predicted by idealizing the plates as wide orthotropic columns using the reduced flexural stiffness approximation proposed by Ashton [21]:

$$N_x = \frac{4\pi^2 D_{11}^*}{L^2} \tag{6.2}$$

where:

$$[D^*] = [B][A]^{-1}[B]$$

The buckling loads predicted by the nonlinear three-dimensional finite element analysis were determined by integrating the in-plane S_{xx} stresses over the surface $x = +a$ using Gauss-Legendre quadrature:

$$N_x = \frac{1}{2b}\int_{-b}^{+b}\int_{-h/2}^{+h/2} S_{xx}(+a, y, z)dydz \tag{6.3}$$

The method of Southwell [36], discussed in Chapter 2, was used to determine the buckling loads from the nonlinear finite element analysis results.

Wide-column theory overpredicts the critical loads as compared to the nonlinear 3D finite element analysis (Table 6.13). The greatest difference was predicted for the symmetric $[0/90]_s$ laminate for which wide-column theory overpredicted the buckling load by 19 percent. The differences between the predicted buckling loads may be due to the fact that the wide-column theory neglects both geometric nonlinearity and three-dimensional effects and only approximately accounts for the membrane-flexural coupling of unsymmetric laminates. Although the critical loads predicted by linear wide-column theory for the unsymmetric laminates compared quite well (up to 7 percent difference) with the nonlinear 3D finite element analysis, as discussed in Chapter 2, the reduced flexural stiffness approximation can sometimes lead to erroneous predictions.

Midplane w/h displacements predicted by nonlinear theory for the postbuckled 2.0 in. square symmetric $[90/0]_s$ and $[0/90]_s$ laminates are shown in Figure 6.38.

Both symmetric laminates exhibit bifurcation buckling behavior in which the laminate may buckle in either the $-z$ or $+z$ direction. The symmetric $[90/0]_s$ laminate buckles at a critical average membrane stress resultant of $N_x = -1857$ pounds per in. ($u/a = -0.00167$). The symmetric $[0/90]_s$ laminate buckles at a critical average membrane stress resultant of $N_x = -7912$ pounds per in. ($u/a = -0.00714$). Since the symmetric $[0/90]_s$ laminate has a higher D_{11} flexural stiffness, the laminate buckles at a higher buckling load (by factor a of over four) than the $[90/0]_s$ laminate. At $u/a = -0.01$, the symmetric $[0/90]_s$ laminate supports a compressive axial load of over four times the load supported by the symmetric $[90/0]_s$ laminate.

Load-displacement plots predicted by nonlinear theory for the 2.0 in. square unsymmetric $[0/90]_t$ laminate are shown in Figure 6.39. The unsymmetric $[0/90]_t$ laminate exhibits nonbifurcational buckling behavior. Although the magnitude of the displacement is small (Figure 6.39), the plate center deflects immediately out of plane upon loading. Midplane w/h displacements for the 2.0 in. square unsymmetric $[0/90]_t$ laminate are shown in Figure 6.40. The displacements shown are the predictions of linear theory (Figure 6.40a) and nonlinear theory (Figure 6.40b) for $u/a = -0.01$. For compressive loading up to $u/a = -0.0004$, the w displacements are underpredicted by linear theory as compared to nonlinear theory. For this loading range, nonlinear theory predicts that the center displacement $w(0,0,0)$ is negative and the displacement along the free edges $w(0,\pm b,0)$ is positive. During the loading range between -0.0004 and -0.0005, the center w displacement begins to decrease while the edge w displacements continue to increase. As the loading is increased beyond $u/a = -0.0005$, the center w displacement becomes positive and the laminate begins to deflect in the $+z$ direction. The critical average membrane stress resultant predicted by Southwell's method is $N_x = -291$ pounds per in. ($u/a = -0.00054$). As the loading is increased beyond the critical load, the center w displacement increases rapidly (Figure 6.39) and the plate transitions into a single half-wave equilibrium configuration (Figure 6.40b).

Load-displacement plots predicted by nonlinear theory for the 2.0 in. square unsymmetric $[+45/-45]_t$ laminate are shown in Figure 6.41. The unsymmetric $[+45/-45]_t$ laminate exhibits bifurcational buckling behavior. Midplane w/h displacements for the 2.0 in. square unsymmetric $[+45/-45]_t$ laminate are shown in Figure 6.42. The displacements shown are the predictions of linear theory (Figure 6.42a) and nonlinear theory (Figure 6.42b) for $u/a = -0.01$. For compressive loading up to $u/a = -0.0013$, the w displacements are slightly underpredicted by linear theory as compared to nonlinear theory. For this loading range, nonlinear theory predicts that the laminate twists out of plane and the w displacements along $(x,0,0)$ and $(0,y,0)$ remain zero. The center w displacement remains zero (Figure 6.41) until the average membrane stress resultant reaches the critical value of $N_x = -193$ pounds per in. $(u/a = -0.00134)$. At the critical load, the nonlinear solution bifurcates into two stable nonlinear solution paths (Figure 6.41). Since Poisson's ratio ν_{xy} does not vary through the thickness, there is no tendency for the laminate to deflect in either the $+z$ or $-z$ direction. For loading beyond the critical load, the center w displacement increases rapidly (Figure 6.41) and the plate transitions into a single half-wave equilibrium configuration (Figure 6.42b).

Load-displacement plots predicted by nonlinear theory for the 2.0 in. square unsymmetric $[0/+45]_t$ laminate are shown in Figure 6.43. The unsymmetric $[0/+45]_t$ laminate exhibits nonbifurcational buckling behavior. Although the magnitude of the displacement is small (Figure 6.43), the plate center deflects immediately out of plane upon loading. Midplane w/h displacements predicted for the 2.0 in. square unsymmetric $[0/+45]_t$ laminate are shown in Figure 6.44. The displacements shown are the predictions of linear theory (Figure 6.44a) and nonlinear theory (Figure 6.44b) for $u/a = -0.01$. For compressive loading up to $u/a = -0.0006$, w displacements are underpredicted by linear theory as compared to nonlinear theory. For the $[0/+45]_t$ laminate, the center w displacement of the laminate is positive throughout loading. The critical average membrane stress resultant predicted by

Southwell's method is $N_x = -422$ pounds per in. $(u/a = -0.00080)$. As the loading is increased beyond the critical load, the center w displacement increases rapidly (Figure 6.43) and the plate transitions into a single half-wave equilibrium configuration (Figure 6.44b).

6.4.2 Interlaminar Stresses for 0/90 Laminates

The interlaminar stress results for the cross-ply laminates are summarized in Table 6.14. The interlaminar stress results predicted by linear theory are consistent with the predictions by linear theory for extensional loading; the interlaminar stresses are equal and opposite to those predicted for extensional loading. Since the interlaminar stresses predicted by linear theory for extensional loading are discussed in detail in Sections 6.2 and 6.3, the focus of the remainder of Section 6.4 will be upon the interlaminar stresses predicted by nonlinear theory.

As discussed in Section 6.4.1, nonlinear theory predicts that both symmetric and unsymmetric laminates undergo a change in laminate mode shape during the compressive loading. Before this change in mode shape occurs, the interlaminar stresses predicted by nonlinear theory are similar to those predicted by linear theory; differing mainly in the overall magnitude. However, after the change in mode shape has occurred, the interlaminar stress fields within the laminate change dramatically. After the change in mode shape, the compressive axial load begins to be transferred between adjacent layers across the interfacial surface. This transfer of load results in the existence of interlaminar stresses which extend across the entire interfacial surface of the laminate. The axial load transfer results in compressive normal S_{zz} stresses and large S_{xz} shear stresses. Like the out-of-plane w displacements of the laminate, these interlaminar stresses vary with the x coordinate in the loading direction. The interlaminar stresses caused by the axial load transfer combine with the free edge stresses caused by the mismatch in material properties between adjacent layers. These interlaminar stresses combine to form a complex stress state

with the maximum interlaminar stresses occurring at the free edges of the laminate. The dominant component of interlaminar stress is typically the S_{zz} stress which is caused by the transfer of the compressive axial load across the interfacial surface.

The interlaminar stress extrema for the symmetric $[90/0]_s$ laminate are given in Table 6.14. For the symmetric $[90/0]_s$ laminate, linear theory predicts interlaminar σ_{zz} and τ_{yz} stresses for the $z/h = +0.25$ interface which are equal and opposite to those shown in Figures 6.24 and 6.25, respectively. The τ_{xz} stresses are predicted by linear theory to be equal to zero across the interface. Linear theory predicts that the σ_{zz} and τ_{yz} stresses are independent of the x coordinate in the loading direction. Surface plots of the interlaminar stresses predicted by nonlinear theory for the postbuckled symmetric $[90/0]_s$ laminate ($u/a = -0.01$) are shown in Figures 6.45 through 6.47. The interlaminar stresses for the 0/90 interfaces at $z/h = +0.25$ and $z/h = -0.25$ are shown in each figure.

The S_{zz} interlaminar normal stresses are compressive across most of the interface and vary with the x coordinate (Figure 6.45). The S_{zz} stresses vanish along the line $(\pm 0.5a, y, \pm 0.25h)$, except near the free edges of the laminate. Large S_{yz} interlaminar shear stresses exist near the free edges of the laminate and also vary with the x coordinate (Figure 6.46). The S_{xz} interlaminar shear stresses are very large and also extend across the entire interface (Figure 6.47). The S_{xz} stresses vary with the x coordinate and the maximum S_{xz} stress occurs at the free edge at $(\pm 0.5a, \pm b, \pm 0.25h)$ where the maximum slope in the x direction occurs. For each component of interlaminar stress, the largest stresses occur near the free edges of the laminate.

The interlaminar stress extrema for the symmetric $[0/90]_s$ laminate are given in Table 6.14. For the symmetric $[0/90]_s$ laminate, linear theory predicts interlaminar σ_{zz} and τ_{yz} stresses for the $z/h = +0.25$ interface which are equal and opposite to those shown in Figures 6.24 and 6.25, respectively. The τ_{xz} stresses are predicted by linear theory to be equal to zero across the interface. Like the symmetric $[90/0]_s$

laminate, linear theory predicts that the σ_{zz} and τ_{yz} stresses are independent of the x coordinate. Surface plots of the interlaminar stresses predicted by nonlinear theory for the postbuckled symmetric $[0/90]_s$ laminate ($u/a = -0.01$) are shown in Figures 6.48 through 6.50. The interlaminar stresses for the 0/90 interfaces at $z/h = +0.25$ and $z/h = -0.25$ are shown in each figure.

The interlaminar stresses for the symmetric $[0/90]_s$ laminate are quite similar to those predicted for the symmetric $[90/0]_s$ laminate, differing mainly in overall magnitude. The maximum S_{zz} interlaminar normal stress at the free edges of the symmetric $[0/90]_s$ laminate (Figure 6.45) is approximately 5.8 times greater than that in the symmetric $[90/0]_s$ laminate (Figure 6.48). The maximum S_{xz} interlaminar shear stress at the free edges of the symmetric $[0/90]_s$ laminate (Figure 6.47) is approximately 5.5 times greater than that in the symmetric $[90/0]_s$ laminate (Figure 6.50). The maximum S_{zz} and S_{xz} stresses are larger in the symmetric $[0/90]_s$ laminate because it has a higher D_{11} flexural stiffness and is supporting over 4 times the compressive axial load than the symmetric $[90/0]_s$ laminate.

Surface plots of the interlaminar stresses predicted by linear and nonlinear theory for the unsymmetric $[0_4/90_4]_t$ laminate ($L/h = 50$) are shown in Figures 6.51 through 6.53. After the change in mode shape has occurred, the S_{zz} and S_{xz} stresses are predicted by nonlinear theory to exist across most of the interfacial surface (Figures 6.51b and 6.53b). All three components of interlaminar stress are predicted to vary with the x coordinate. The S_{zz} interlaminar normal stresses are compressive (Figure 6.51b) with the maximum stresses occurring at $(0, \pm b, 0)$. The S_{xz} interlaminar shear stresses are very large (Figure 6.53b) with the maximum stresses occurring at $(\pm 0.5a, \pm b, 0)$ where the slope in the x direction reaches a maximum value (Figure 6.40b). For each component of interlaminar stress, the largest stresses occur near the free edges of the laminate.

6.4.3 Interlaminar Stresses for +45/−45 Laminates

The interlaminar stress results for the $[+45/-45]_t$ laminate are summarized in Table 6.15. Surface plots of the interlaminar stresses predicted by linear and nonlinear theory for the $[+45/-45]_t$ laminate ($L/h = 50$) are shown in Figures 6.54 through 6.56. After the change in mode shape has occurred, the S_{zz}, S_{yz}, and S_{xz} stresses are predicted by nonlinear theory to exist across most of the interfacial surface (Figures 6.54b, 6.55b, and 6.56b). Each component of interlaminar stress is predicted to vary with the x coordinate. Although these interlaminar stresses exist across most of the interface, they are relatively small compared to the interlaminar stresses near the free edges. For each component of interlaminar stress, the largest stresses occur near the free edges.

6.4.4 Interlaminar Stresses for 0/+45 Laminates

The interlaminar stress results for the unsymmetric $[0/+45]_t$ laminate are summarized in Table 6.16. Surface plots of the interlaminar stresses predicted by linear and nonlinear theory for the unsymmetric $[0/+45]_t$ laminate ($L/h = 50$) are shown in Figures 6.57 through 6.59. After the change in mode shape has occurred, the S_{zz}, S_{yz}, and S_{xz} stresses are predicted by nonlinear theory to exist across most of the interfacial surface (Figures 6.57b, 6.58b, and 6.59b). Each component of interlaminar stress is predicted to vary with the x coordinate. Like the unsymmetric $[+45/-45]_t$ laminate, the interlaminar stresses which exist across most of the interface are relatively small compared to the interlaminar stresses near the free edges. For each component of interlaminar stress, the largest stresses occur near the free edges.

6.4.5 Summary

The main conclusions based upon the numerical results for compressive loading are given below. These conclusions are summarized in Tables 6.1 and 6.3. The boundary conditions for compressive loading (Table 3.3) are equal and opposite to those prescribed for extensional loading. The conclusions listed in Table 6.3 only apply for load levels below that in which a change in mode shape occurs. The conclusions for load levels beyond that in which a change in mode shape occurs are provided below. For the laminated plates and boundary conditions considered, the main conclusions for compressive loading are:

(1) Out-of-plane displacements predicted by linear theory: The out-of-plane displacements predicted by linear theory for compressive loading are consistent with the predictions of linear theory for extensional loading; the initial geometric midplane of the symmetric laminates remains plane and the out-of-plane displacements of the unsymmetric laminates are equal and opposite to those predicted for extensional loading.

(2) Out-of-plane displacements predicted by nonlinear theory: Nonlinear theory predicts that both symmetric and unsymmetric laminates undergo a change in mode shape during loading. The geometric midplane of the symmetric laminates remains plane until the laminate buckles into a single half-wave equilibrium configuration in the loading x direction. For the unsymmetric laminates, the laminate membrane-flexural coupling causes the laminate to deflect immediately out of plane under the compressive in-plane loading. During loading, the unsymmetric laminates undergo a change in laminate mode shape in which the laminate transitions into a single half-wave equilibrium configuration in the x direction. The unsymmetric $[0/90]_t$ and $[0/+45]_t$ laminates exhibit nonbifurcational buckling behavior. The unsymmetric $[+45/-45]_t$ laminate passes through a bifurcation point in which the plate may buckle in either the

$+z$ or $-z$ direction. In summary, nonlinear theory predicts: (a) greater out-of-plane deflections (softening effect) for unsymmetric laminates and (b) that both symmetric and unsymmetric laminates undergo a change in mode shape during loading.

(3) Interlaminar stresses predicted by linear theory: The interlaminar stresses predicted by linear theory for compressive loading are also consistent with the predictions of linear theory for extensional loading; the interlaminar stresses for compressive loading are equal and opposite to those predicted for extensional loading.

(4) Interlaminar stresses predicted by nonlinear theory: Nonlinear theory predicts that both symmetric and unsymmetric laminates undergo a change in mode shape during loading:

   (a) Before the change in mode shape: The interlaminar stresses predicted by nonlinear theory are similar to those predicted by linear theory, differing mainly in overall magnitude. Before the change in mode shape occurs, the conclusions listed in Table 6.3 apply to these laminates.

   (b) After the change in mode shape: The compressive axial load begins to be transferred between adjacent layers across the interfacial surface. This transfer of compressive axial load results in interlaminar stresses existing across the entire interfacial surface of the laminate. The interlaminar stress fields for these single half-wave equilibrium configurations are characterized by compressive normal stresses and shear stresses acting in the direction of the axial load which exist across the entire interfacial surface of the laminate. These stresses due to axial load transfer combine with the free edge stresses caused by a mismatch in material properties between adjacent layers. The maximum interlaminar stresses occur near the free edges of the laminate.

(5) Predictions of critical buckling loads: For the boundary conditions of clamped loaded edges and free unloaded edges, the critical loads predicted for the unsymmetric laminates by linear wide-column theory using a reduced flexural stiffness approximation [21] compared quite well with the nonlinear 3D finite element analysis. Buckling loads for the unsymmetric $[0/90]_t$ and $[0/+45]_t$ laminates which exhibited nonbifurcational buckling were determined using Southwell's method [36] on the nonlinear finite element results. The stiffness of the unsymmetric laminates with free unloaded edges is significantly reduced after the change in mode shape has occurred.

6.5 Thermal Loading

This section discusses the numerical results for thin square T300/5208 graphite-epoxy laminated composite plates subjected to uniform thermal loading ($\Delta T = -280°F$). The lamina material properties for the T300/5208 graphite-epoxy material system are given in Table 3.1. The geometry for the thin laminated composite plates is summarized in Table 3.2. The unsymmetric and symmetric laminate stacking sequences considered are:

(1) $[0_4/90_4]_t$, $[90_4/0_4]_s$, $[0_4/90_4]_s$

(2) $[+45_4/-45_4]_t$, $[-45_4/+45_4]_s$, $[+45_4/-45_4]_s$

(3) $[0_4/+45_4]_t$, $[+45_4/0_4]_s$, $[0_4/+45_4]_s$

The boundary conditions for thermal loading are given in Table 3.3. The thermal loading condition idealizes a laminate which has been cooled from assumed stress-free state at an elevated temperature to a residual stress state at room temperature. Each laminate is free to deflect out of plane and all surfaces of the laminate are traction free.

6.5.1 Out-of-Plane Displacements

The midplane w/h displacement extrema predicted by linear and nonlinear theory for the unsymmetric laminates are given in Table 6.17. The midplane w/h displacement extrema are given for unsymmetric laminates with thickness ratios of $L/h = 50, 100, 150$. For the uniform temperature change prescribed ($\Delta T = -280°F$), a critical thickness ratio L/h is predicted by nonlinear theory for each unsymmetric laminate stacking sequence. For $L/h < L/h_{crit}$, the laminate has a unique stable equilibrium shape at room temperature. For $L/h > L/h_{crit}$, the laminate has two stable equilibrium shapes at room temperature. A stable mode shape can be reached from the alternate stable mode shape by a snap-through buckling action. The prediction of multiple stable shapes at room temperature is in agreement with previous experimental results [47,51,52] and with the numerical results of Hyer [48-50] for unsymmetric cross-ply laminates. A comparison of the present numerical results with previous results may be found in Appendix E. The out-of-plane deflections for the 2.0 in. square ($L/h = 50$) unsymmetric laminates predicted by both linear and nonlinear theory are large; on the order of the laminate thickness. Linear theory predicts greater out-of-plane deflections as compared to the predictions of nonlinear theory. In summary, nonlinear theory predicts smaller out-of-plane deflections (stiffening effect) and that multiple stable equilibrium configurations may exist for unsymmetric laminates at room temperature.

A geometrically nonlinear plate analysis was formulated for this study to predict the approximate thermoelastic response of unsymmetrically laminated plates. The plate analysis, described in Appendix E, is based upon classical laminated plate theory [23] and uses the von Karman nonlinear strain-displacement equations [4]. The plate analysis was used to provide an initial approximation to the nonlinear three-dimensional finite element analysis. The curvatures of the reference surface are approximately (small deformation) given by:

$$\kappa_x = -\frac{\partial^2 w}{\partial x^2} \tag{6.4a}$$

$$\kappa_y = -\frac{\partial^2 w}{\partial y^2} \tag{6.4b}$$

$$\kappa_{xy} = -2\frac{\partial^2 w}{\partial x \partial y} \tag{6.4c}$$

The approximate principal curvatures and orientation of the principal axes with respect to the global x-y axes are given by:

$$\kappa_1 = c + r \tag{6.5a}.$$

$$\kappa_2 = c - r \tag{6.5b}$$

$$\tan(2\phi) = \frac{\kappa_{xy}}{(\kappa_x - \kappa y)} \tag{6.5c}$$

where:

$2c = \kappa_x + \kappa_y$

$2r = \sqrt{(\kappa_x - \kappa_y)^2 + \kappa_{xy}^2}$

ϕ = orientation angle from x-y to 1-2 axes

Plots of midplane w/h displacement and principal curvatures for the unsymmetric $[0/90]_t$, $[+45/-45]_t$, and the $[0/+45]_t$ laminates are provided in Figures 6.60 through 6.65. For the three unsymmetric laminate stacking sequences considered, linear theory predicts that the principal curvatures are equal and opposite, $\kappa_1 = -\kappa_2$, and independent of laminate thickness ratio L/h (Figures 6.60, 6.62, 6.64). Nonlinear theory predicts a unique pair of principal surface curvatures (curve AB) for all L/h up to the critical thickness ratio (point B). At the critical thickness ratio, the nonlinear solution bifurcates into three nonlinear solution paths. The nonlinear solution path BD is an extension of the solution AB beyond the critical thickness ratio. The nonlinear solutions along the path BD are unstable equilibrium configurations and cannot be physically maintained. The nonlinear solutions along paths BC and BE are stable equilibrium configurations. A stable equilibrium configuration along BC can be snapped to from a stable equilibrium configuration along BE, and vice versa. As shown in Figures 6.60, 6.62 and 6.64,

as L/h increases beyond the critical thickness ratio, the curvature in one direction approaches the linear prediction, while the curvature in the other direction approaches zero.

For the unsymmetric $[0/90]_t$ laminate, the 1-2 directions of principal curvature are aligned with the global x-y directions; that is, $\phi = 0$, $\kappa_x = \kappa_1$, $\kappa_y = \kappa_2$. The critical thickness ratio for the $[0/90]_t$ laminate is approximately $L/h = 85$ (Figure 6.60). For a 2.0 in. square unsymmetric $[0/90]_t$ laminate ($L/h = 50$), a saddle shape is predicted by both linear (Figure 6.61a) and nonlinear (Figure 6.61b) theory in which $\kappa_x = -\kappa_y$. The largest w displacements are predicted by both linear and nonlinear theory to occur at $(\pm a, 0, 0)$ and $(0, \pm b, 0)$. Linear theory overpredicts this largest displacement by approximately 28 percent. The mismatch between adjacent layers in α_x and α_y causes the negative κ_x and positive κ_y curvatures, respectively. The effect of geometric nonlinearity reduces the out-of-plane displacements of the unsymmetric laminate (stiffening effect).

The unsymmetric $[+45/-45]_t$ laminate is the same as the unsymmetric $[0/90]_t$ laminate which has been rotated +45 degrees. Therefore, the principal angle of orientation is predicted to be $\phi = +45°$ by both linear and nonlinear theory. In addition, the principal curvatures predicted by linear theory for the unsymmetric $[0/90]_t$ and $[+45/-45]_t$ laminates are equal. The critical thickness ratio predicted by nonlinear theory for the unsymmetric $[+45/-45]_t$ laminate is approximately $L/h = 98$ (Figure 6.62). At the critical thickness ratio, the principal curvatures for the unsymmetric $[0/90]_t$ and $[+45/-45]_t$ laminates are equal. For a 2.0 in. square unsymmetric $[+45/-45]_t$ laminate ($L/h = 50$), a surface with negative κ_{xy} twisting curvature is predicted by both linear (Figure 6.63a) and nonlinear (Figure 6.63b) theory. The largest w displacements are predicted by both linear and nonlinear theory to occur at the plate corners $(\pm a, \pm b, 0)$ and $(\pm a, \mp b, 0)$. Linear theory overpredicts this largest displacement by approximately 16 percent. The negative κ_{xy} curvature is caused by the mismatch in α_{xy} between adjacent

layers. The effect of geometric nonlinearity reduces the out-of-plane displacements of the laminate (stiffening effect).

For the unsymmetric $[0/+45]_t$ laminate, the principal angle of orientation predicted by linear theory is $\phi = -22.5°$. The critical thickness ratio for the $[0/+45]_t$ laminate is approximately $L/h = 112$ (Figure 6.64). For the stable nonlinear path AC, the principal angle is $\phi = -22.5°$. The principal angle for the stable nonlinear paths BC and BE are $\phi = -22.5° + \beta$ and $\phi = -22.5° - \beta$, respectively, where β varies with L/h ($0 < \beta < 11.5°$). For a 2.0 in. square unsymmetric $[0/+45]_t$ laminate ($L/h = 50$), surfaces with negative κ_x, positive κ_y ($\kappa_x = -\kappa_y$), and positive κ_{xy} curvatures are predicted by both linear (Figure 6.65a) and nonlinear (Figure 6.65b) theory. The largest w displacements are predicted by both linear and nonlinear theory to occur at $(\pm a, \pm b, 0)$ and $(\pm a, \mp b, 0)$. Linear theory overpredicts this largest displacement by approximately 15 percent. The κ_x, κ_y, and κ_{xy} curvatures are caused by the mismatch between adjacent layers in α_x, α_y, and α_{xy}. The effect of geometric nonlinearity reduces the out-of-plane displacements of the laminate (stiffening effect).

6.5.2 Interlaminar Stresses for 0/90 Laminates

The interlaminar stress results for the thin cross-ply laminates subjected to uniform thermal loading are summarized in Table 6.18. Although the out-of-plane deflections of the unsymmetric laminate are large (on the order of the laminate thickness), the differences in the interlaminar stress predictions between linear and nonlinear theory are small (less than 4 percent). Surface plots of the interlaminar stress distributions predicted by nonlinear theory are provided in Figures 6.66 through 6.68. Stress concentrations are predicted at the plate corners for all three components of interlaminar stress. Interlaminar stress distributions along $x = 0$ and $y = 0$ for both the symmetric and unsymmetric cross-ply laminates are shown in Figures 6.69 through 6.72.

The mismatch in α_y for thermal loading and the mismatch in ν_{xy} for extensional loading cause a similar mismatch in in-plane normal strain between adjacent layers (Table 3.4). The interlaminar stress distributions along $x = 0$ are quite similar to those resulting from extensional loading (for example, compare Figures 6.24 and 6.69 or Figures 6.25 and 6.71). The σ_{zz} and S_{zz} interlaminar normal stresses along $x = 0$ are much larger in the unsymmetric $[0/90]_t$ laminate as compared to a symmetric $[90/0]_s$ laminate (Figure 6.69). The largest tensile stresses are predicted to be a factor of 3.3 times greater by both linear and nonlinear theory. When compared to the symmetric $[0/90]_s$ laminate, the σ_{zz} and S_{zz} stresses along $x = 0$ are smaller in the unsymmetric $[0/90]_t$ laminate (Figure 6.69). The largest tensile stresses are predicted to be only 5 percent smaller by linear theory and only 4 percent smaller by nonlinear theory. Along $y = 0$, the interlaminar normal stresses for the symmetric $[0/90]_s$ and $[90/0]_s$ laminates are equal to those along $x = 0$ for the symmetric $[90/0]_s$ and $[0/90]_s$ laminates, respectively (Figures 6.69 and 6.70). Like the cross-ply laminates under extensional loading (Sections 6.2.2 and 6.3.2), depending upon the symmetric stacking sequence, the interlaminar normal stresses in the unsymmetric $[0/90]_t$ laminate may be either much larger or smaller than those occurring in comparable symmetric laminates.

The τ_{yz} and S_{yz} interlaminar shear stresses which act in a direction normal to the free edge are shown in Figure 6.71. The τ_{yz} and S_{yz} stresses are smaller in the unsymmetric $[0/90]_t$ laminate as compared to the symmetric laminates. As compared to the symmetric $[90/0]_s$ laminate, the largest shear stresses in the unsymmetric laminate are predicted to be 30 percent smaller by linear theory and 28 percent smaller by nonlinear theory. As compared to the symmetric $[0/90]_s$ laminate, the largest shear stresses in the unsymmetric laminate are predicted to be 20 percent smaller by linear theory and 17 percent smaller by nonlinear theory. Along $y = 0$, the τ_{xz} and S_{xz} stresses for the symmetric $[0/90]_s$ and $[90/0]_s$ laminates are equal the τ_{yz} and S_{yz} stresses along $x = 0$ for the symmetric $[90/0]_s$ and $[0/90]_s$

laminates, respectively (Figures 6.71 and 6.72). Again, like the cross-ply laminates under extensional loading (Sections 6.2.2 and 6.3.2), the interlaminar shear stresses acting in a direction normal to the free edge in the unsymmetric $[0/90]_t$ laminate are smaller than those occurring in comparable symmetric laminates.

6.5.3 Interlaminar Stresses for +45/−45 Laminates

The interlaminar stress results for the thin angle-ply laminates under uniform thermal loading are summarized in Table 6.19. Since the out-of-plane deflections of the unsymmetric laminate are large (on the order of the laminate thickness), the differences in the interlaminar stress predictions between linear and nonlinear theory are also large (less than 29 percent). Surface plots of the interlaminar stress distributions predicted by nonlinear theory are provided in Figures 6.73 through 6.75. Stress concentrations are predicted at the plate corners for the interlaminar normal stresses. Interlaminar stress distributions along $x = 0$ and $y = 0$ for both symmetric and unsymmetric angle-ply laminates are shown in Figures 6.76 through 6.81.

Both the mismatch in α_{xy} for thermal loading and the mismatch in $\eta_{xy,x}$ for extensional loading cause a similar but opposite mismatch in in-plane shear strain *between* adjacent layers (Table 3.4). The σ_{zz} and S_{zz} interlaminar normal stresses along $x = 0$ are much larger in the unsymmetric $[+45/-45]_t$ laminate as compared to the symmetric laminates (Figure 6.76). The largest tensile stresses are predicted to be a factor of 5.5 greater by linear theory and a factor of 4.5 greater by nonlinear theory. For each laminate, the interlaminar normal stresses along $x = 0$ are equal to those along $y = 0$ (Figures 6.76 and 6.77). Like the angle-ply laminates under extensional loading (Sections 6.2.3 and 6.3.3), the interlaminar normal stresses in the unsymmetric $[+45/-45]_t$ laminate are larger than those occurring in comparable symmetric laminates.

The τ_{yz} and S_{yz} interlaminar shear stresses along $x = 0$, which act in a direction normal to the free edge, are shown in Figure 6.78. As shown in Figure 6.78, the τ_{yz} and S_{yz} stresses are zero along $x = 0$ in the unsymmetric laminate. The τ_{yz} and S_{yz} stresses are zero along most of the length of the free edge (along $y = \pm b$), becoming non-zero near the opposite edges (along $x = \pm a$). For each laminate, the τ_{yz} and S_{yz} stresses along $x = 0$ are equal to the τ_{xz} and S_{xz} stresses along $y = 0$ (Figures 6.78 and 6.81). Like the angle-ply laminates under extensional loading, the interlaminar shear stresses which act in a direction normal to the free edge are zero in an unsymmetric $[+45/-45]_t$ laminate, while these shear stresses are non-zero in comparable symmetric laminates.

The τ_{xz} and S_{xz} interlaminar shear stresses along $x = 0$, which act in a direction parallel to the free edge, are shown in Figure 6.79. The τ_{xz} and S_{xz} stresses are much smaller in the unsymmetric $[+45/-45]_t$ laminate as compared to the symmetric laminates. The largest shear stresses are predicted to be 28 percent smaller by linear theory and 49 percent smaller by nonlinear theory. For each laminate, the τ_{xz} and S_{xz} stresses along $x = 0$ are equal to the τ_{yz} and S_{yz} stresses along $y = 0$ (Figures 6.79 and 6.80). Again, like the angle-ply laminates under extensional loading, the interlaminar shear stresses acting parallel to the free edge in the unsymmetric $[+45/-45]_t$ laminate are smaller than those occurring in comparable symmetric laminates.

6.5.4 Interlaminar Stresses for 0/+45 Laminates

The interlaminar stress results for the thin 0/+45 laminates under uniform thermal loading are summarized in Table 6.20. Since the out-of-plane deflections of the unsymmetric laminate are large (on the order of the laminate thickness), the differences in the interlaminar stress predictions between linear and nonlinear theory are also large (up to 44 percent). Surface plots of interlaminar stress distributions predicted by nonlinear theory are provided in Figures 6.82 through 6.84. Like

the unsymmetric angle-ply laminates, stress concentrations are predicted for the interlaminar normal stresses at the plate corners. Interlaminar stress distributions along $x = 0$ and $y = 0$ for both symmetric and unsymmetric angle-ply laminates are shown in Figures 6.85 through 6.90.

6.5.5 Summary

The main conclusions based upon the numerical results for thermal loading are given below. These conclusions are summarized in Tables 6.1 and 6.4. For the laminated plates and boundary conditions considered, the main conclusions for thermal loading are:

(1) Out-of-Plane Displacements: For the unsymmetric laminates considered, the out-of-plane deflections caused by laminate membrane-flexural coupling are predicted to be larger in magnitude by linear theory as compared to nonlinear theory. Nonlinear theory predicts a critical thickness ratio L/h for each of the unsymmetric laminate stacking sequences in which:

   (a) For laminates with L/h less than the critical value, a unique stable shape exists for the laminate at room temperature.

   (b) For laminates with L/h greater than the critical value, multiple stable shapes are predicted at room temperature.

   The prediction of multiple stable shapes at room temperature is in agreement with previous experimental results [47,51,52] and with the numerical results of Hyer [48-50] for unsymmetric cross-ply laminates. In summary, nonlinear theory predicts: (a) smaller out-of-plane deflections (stiffening effect) for unsymmetric laminates and that (b) multiple stable shapes may exist for unsymmetric laminates at room temperature.

(2) Mismatch in in-plane normal strain: The following behavior is observed for the cross-ply laminates in which there exists a mismatch in α_x and α_y between adjacent layers. Interlaminar normal σ_{zz} and shear τ_{zn} stresses exist within

the free edge regions of both symmetric and unsymmetric laminates. The maximum tensile normal stresses occur at the free edges. The following differences are observed in the predicted interlaminar stresses for the unsymmetric laminate as compared to the symmetric laminates:

- Interlaminar normal stresses σ_{zz} are either smaller or much larger.
- Interlaminar shear stresses τ_{zn} are smaller.

Depending upon the symmetric laminate stacking sequence, the σ_{zz} normal stresses are either smaller or much larger in the unsymmetric laminate as compared to the symmetric laminates. The τ_{zn} shear stresses are relieved by the out-of-plane deflections of the unsymmetric laminate.

(3) Mismatch in in-plane shear strain: The following behavior is observed for the angle-ply laminates in which there exists a mismatch in α_{xy} between adjacent layers. Interlaminar normal σ_{zz} and shear τ_{zt} stresses exist within the free edge regions of both symmetric and unsymmetric laminates. Interlaminar shear stresses τ_{zn} are present within the symmetric laminates and are zero within the unsymmetric laminate. The maximum interlaminar normal stresses σ_{zz} are compressive and occur at the free edges. The maximum interlaminar shear stresses τ_{zt} are very large and also occur at the free edges. The following differences are observed in the predicted interlaminar stresses for the unsymmetric laminate as compared to the symmetric laminates:

- Interlaminar normal stresses σ_{zz} are larger.
- Interlaminar shear stresses τ_{zn} vanish.
- Interlaminar shear stresses τ_{zt} are smaller.

The out-of-plane twisting deflections of the unsymmetric laminate increase the interlaminar normal stresses σ_{zz} and reduce the interlaminar shear τ_{zt} stresses. The interlaminar shear stresses τ_{zn} are completely relieved by the out-of-plane deflections of the unsymmetric laminate.

(4) Comparison of stress predictions between linear and nonlinear theory: For the symmetric laminates, the difference in the interlaminar stress predictions of linear theory (Cauchy stresses) and nonlinear theory (second Piola-Kirchhoff stresses) are small. For the unsymmetric laminates, however, there are large differences in the stress predictions between linear and nonlinear theory. These large differences are due to the large out-of-plane deflections of the unsymmetric laminates.

(5) Comparison with results for extensional loading: For extensional loading, the differences in the interlaminar stress fields between symmetric and unsymmetric laminates were not as great as those predicted in the thermal loading cases. The reason that these differences were not as great is because the laminates for the extensional loading cases were restrained from deflecting out-of-plane along the loaded edges of the laminate. This edge restraint reduced the out-of-plane deflections in the unsymmetric laminates. The unsymmetric laminates for the thermal loading cases were allowed to freely deflect out of plane and consequently have larger transverse w deflections. This is also the reason that greater differences are observed in interlaminar stresses predicted by linear and nonlinear theory. The larger the out-of-plane deflections, the greater the difference in interlaminar stress predictions between linear and nonlinear theory.

(6) Comparison with results for compressive loading: The conclusions stated in (5) above also apply for compressive loading prior to a change in laminate mode shape. However, after the change in mode shape has occurred, additional interlaminar stresses arise as the axial load is transferred between adjacent layers and the interlaminar stress fields extend across the entire interfacial surface.

Chapter 7
CONCLUSIONS AND RECOMMENDATIONS

The purpose of this study was to investigate the interlaminar stress fields within unsymmetrically laminated plates and to determine the effects upon the stress-deformational response of laminate membrane-flexural coupling and geometric nonlinearity. The study focused upon the linear thermoelastic response of thin square laminated composite plates subjected to extensional, compressive, or thermal loading. Symmetric and unsymmetric 0/90, +45/–45, and 0/+45 laminate stacking sequences were considered to determine the effect of mismatch between adjacent layers in Poisson's ratio, coefficient of mutual influence, and coefficients of thermal expansion. The results for symmetric and unsymmetric laminates were compared to determine the effects of laminate membrane-flexural coupling upon the interlaminar stress fields in unsymmetric laminates. The predictions of geometrically linear and nonlinear theory were compared to determine the effects of geometric nonlinearity upon the stress-deformational response. Appoximate solutions to the nonlinear three-dimensional boundary value problems were determined using the finite element method and Newton's method.

For laminated plates subjected to external loading, the mismatch in material properties between adjacent layers causes interlaminar stresses to arise near the free edges of the laminate. For unsymmetric laminates, the mismatch in material properties about the geometric midplane causes out-of-plane (transverse) deflections. The results of this numerical study show that the out-of-plane deflections of unsymmetric laminates, caused by the laminate membrane-flexural coupling, have a strong effect upon the interlaminar stresses at the free edges of the laminate.

7.1 Summary and Concluding Remarks:

The main conclusions based upon the results of this investigation are:

(1) For the laminated plates, loading conditions, and boundary conditions considered, the results of this study show that the out-of-plane deflections of unsymmetric laminates relieve interlaminar shear stresses. In addition, the out-of-plane deflections reduce interlaminar normal stresses for some laminates and increase these stresses for others. Specifically, the following differences are observed in the predicted interlaminar stresses for the unsymmetric laminates as compared to the symmetric laminates:

   (a) For a mismatch in in-plane normal strain (mismatch in ν_{xy}, α_x, or α_y):

      - Interlaminar normal stresses are either smaller or much larger.
      - Interlaminar shear stresses τ_{zn} are smaller.

   (b) For a mismatch in in-plane shear strain (mismatch in $\eta_{xy,x}$ or α_{xy}):

      - Interlaminar normal stresses are larger.
      - Interlaminar shear stresses τ_{zn} vanish.
      - Interlaminar shear stresses τ_{zt} are smaller.

   where τ_{zn} is the component of interlaminar shear stress acting in a direction normal to the free edge and τ_{zt} is the component of interlaminar shear stress acting in a direction parallel to the free edge. For a mismatch in in-plane normal strain between adjacent layers, the differences observed in the interlaminar normal stresses between unsymmetric and symmetric laminates depends upon the stacking sequence of the symmetric laminate. These conclusions applied to extensional, compressive (prior to a change in mode shape), and thermal loading.

(2) As the out-of-plane deflections become large, i.e., on the order of the laminate thickness, the effects of geometric nonlinearity upon the stress-deformational

response become important; that is, the differences in the interlaminar stress predictions between linear and nonlinear theory can become quite large.

(3) For compressive loading, nonlinear theory predicts that both symmetric and unsymmetric laminates undergo a change in mode shape during loading:

   (a) Prior to the change in mode shape – The interlaminar stresses predicted by nonlinear theory are similar to those predicted by linear theory; that is, the interlaminar stresses are approximately equal and opposite to those predicted for extensional loading.

   (b) After the change in mode shape – The transfer of the compressive axial load between adjacent layers begins to take place across the interfacial surfaces. This transfer of axial load results in interlaminar stresses existing across the entire interfacial surfaces of the laminate. The interlaminar stresses due to this load transfer combine with the interlaminar free edge stresses caused by the mismatch in material properties between adjacent layers. The maximum interlaminar stresses resulting from this combined effect occur at the free edges of the laminate.

(4) For the compression-loaded laminates considered with boundary conditions of clamped loaded edges and free unloaded edges, the critical loads predicted for the unsymmetric laminates by linear wide-column theory using a reduced flexural stiffness approximation [21] compared quite well with the present nonlinear finite element analysis. Buckling loads for the $[0_4/90_4]_t$ and $[0_4/+45_4]_t$ laminates, which exhibited nonbifurcational buckling, were determined using Southwell's method [36] on the nonlinear finite element analysis results. The stiffness of the unsymmetric laminates with free unloaded edges is significantly reduced after the change in mode shape has occurred.

(5) For each of the unsymmetric laminate stacking sequences considered, a critical laminate thickness ratio $(L/h)_{crit}$ was predicted for the thermally-loaded unsymmetric laminates at room temperature. For $L/h < (L/h)_{crit}$, a unique

stable shape is predicted for the laminate at room temperature. For $L/h > (L/h)_{crit}$, multiple stable shapes are predicted for the laminate at room temperature. The prediction of multiple stable shapes at room temperature is in agreement with previous experimental results [47,51,52] and with the numerical results of Hyer [48-50] for unsymmetric cross-ply laminates.

(6) For large displacements, large rotations, and small strains, the interlaminar components of second Piola-Kirchhoff stress were determined to be a good approximation for the interlaminar components of Cauchy stress.

(7) An effective procedure has been demonstrated for a geometrically nonlinear three-dimensional global/local analysis of laminated composite plates.

7.2 Recommendations for future studies:

The recommendations for future studies can be grouped into three categories:

(a) Experimental verification – Experimental verification of the present analysis is needed. The displacement, strain, and stress results from the analysis could be compared to experimental results for composite laminates subjected to extensional, compressive, or thermal loading. The simplest of these comparisons could be with experimental measurements of the out-of-plane displacements of a cured unsymmetric laminate at room temperature. Further comparisons could be made with experimental results for extensional or compressive loading on unsymmetric laminates constructed using a room-temperature cure process; thereby eliminating initial out-of-plane deflections caused by residual (thermal or hygroscopic) strain.

(b) Applications of the present analysis – The present analysis is quite general and could be applied to a variety of laminates, loading conditions, structural geometries, and boundary conditions. The analysis could be used to study a number of related problems which are of interest to structural researchers. Several of these problems are listed below:

(1) Postbuckling of laminated plates under various edge conditions.

(2) Nonlinear bending of laminated beams and plates.

(3) Laminated plates subjected to combined hygrothermomechanical loading.

(4) Application to more complex structural geometries.

Examples of more complex structural geometries include: stiffeners attached to laminated panels, plates with holes, ply drop-offs, or hybrid laminates. The method of global/local finite element analysis described in Section 5.2.1 could be used to conduct a detailed analysis within the free edge regions of such structures. Boundary conditions for the local finite element analysis could be obtained by either nonlinear plate analysis or the present nonlinear three-dimensional analysis.

(c) Extensions of the present analysis – The present analysis could be extended to account additional effects such as material nonlinearity or time-dependent behavior. For example, the total Lagrangian incremental finite element formulation could be coupled with an incremental plasticity analysis to study the effects of large displacements, large rotations, and large strains. In addition, the constitutive model could be modified to account for temperature or time dependent material behavior. The incremental finite element formulation could also be modified to study the dynamic response of laminated composite structures.

REFERENCES

1. Timoshenko, S. P., "Analysis of Bi-metal Thermostats", *Journal of the Optical Society of America and Review of Scientific Instruments*, Vol. 11, 1925, pp. 233–255.

2. Smith, C. B., "Some New Types of Orthotropic Plates Laminated of Orthotropic Material", *Journal of Applied Mechanics*, Vol. 20, No. 2, 1953, pp. 286–288.

3. Reissner, E. and Stavsky, Y., "Bending and Stretching of Certain Types of Heterogeneous Aeolotropic Elastic Plates", *Journal of Applied Mechanics*, Vol. 28, 1961, pp. 402–408.

4. von Karman, T., "Festigkeitsprobleme in Maschinenbau", *Encykl. Math. Wiss.*, Vol. 4, No. 4, 1910, pp. 348–352.

5. Stavsky, Y., "On the Theory of Heterogeneous Anisotropic Plates", Ph.D. Thesis, Massachussetts Institute of Technology, Cambridge, MA., 1959.

6. Stavsky, Y., "Bending and Stretching of Laminated Aeolotropic Plates", *Proceedings of the ASCE, Journal of Engineering Mechanics*, No. EM6, 1961, pp. 31–56.

7. Stavsky, Y., "Thermoelasticity of Heterogeneous Aeolotropic Plates", *Proceedings of the ASCE, Journal of Engineering Mechanics*, No. EM2, 1963, pp. 89–105.

8. Stavsky, Y., "Finite Deformations of a Class of Aeolotropic Plates with Material Heterogeneity", *Israel Journal of Technology*, Vol. 1, 1963, pp. 69–74.

9. Stavsky, Y., "On the General Theory of Heterogeneous Aeolotropic Plates", *Aeronautical Quarterly*, Vol. 15, 1964, pp. 29–38.

10. Dong, S. B., Matthiesen, R. B., Pister, K. S., and Taylor, R. L.,"Analysis of Structural Laminates", ARL 76, Aeronautical Research Laboratory, Office of Aerospace Research, USAF, Wright-Patterson AFB, Sept. 1961.

11. Dong, S. B., Pister, K. S., and Taylor, R. L., "On the Theory of Laminated Anisotropic Shells and Plates", *Journal of Aerospace Sciences*, Vol. 29, 1962, pp. 969–975.

12. Whitney, J. M. and Leissa, A. W., "Analysis of Heterogeneous Anisotropic Plates", *Journal of Applied Mechanics*, Vol. 36, 1969, pp. 261–266.

13. Whitney, J. M., "A Study of the Effects of Coupling Between Bending and Stretching on the Mechanical Behavior of Layered Anisotropic Composite Materials", Ph.D. Dissertation, Ohio State University, Columbus, OH, 1968.

14. Whitney, J. M. and Leissa, A. W., "Analysis of a Simply Supported Laminated Anisotropic Rectangular Plate", *AIAA Journal*, Vol. 8, 1970, pp. 28–33.

15. Whitney, J. M., "The Effect of Boundary Conditions on the Response of Laminated Composites", *Journal of Composite Materials*, Vol. 4, 1970, pp. 192–203.

16. Whitney, J. M., "Bending-Extension Coupling in Laminated Plates Under Transverse Loading", *Journal of Composite Materials*, Vol. 3, 1969, pp. 20–28.

17. Whitney, J. M., "Shear Buckling of Unsymmetrical Cross-Ply Plates", *Journal of Composite Materials*, Vol. 3, 1969, pp. 359–363.

18. Whitney, J. M., "Cylindrical Bending of Unsymmetrically Laminated Plates", *Journal of Composite Materials*, Vol. 3, 1969, pp. 715–719.

19. Jones, R. M., "Buckling and Vibration of Unsymmetrically Laminated Cross-Ply Rectangular Plates", *AIAA Journal*, Vol. 11, 1973, pp. 1626–1632.

20. Jones, R. M., Morgan, H. S., and Whitney, J. M., "Buckling and Vibration of Antisymmetrically Laminated Angle-Ply Rectangular Plates", *Journal of Applied Mechanics*, Vol. 12, 1973, pp. 1143–1144.

21. Ashton, J. E., "Approximate Solutions for Unsymmetrically Laminated Plates", *Journal of Composite Materials*, Vol. 3, 1969, pp. 189–191.

22. Jones, R. M., *Mechanics Of Composite Materials*, McGraw-Hill, New York, 1975.

23. Whitney, J. M., *Structural Analysis of Laminated Anisotropic Plates*, Technomic Publishing Co., Lancaster, PA, 1987.

24. Pao, Y. C., "Simple Bending Analysis of Laminated Plates by Large Deflection Theory", *Journal of Composite Materials*, Vol. 4, 1970, pp. 380–389.

25. Chia, C. Y., "Large Deflections of Heterogeneous Anisotropic Rectangular Plates", *International Journal of Solids and Structures*, Vol. 10, 1974, pp. 965–976.

26. Zaghloul, S. A. and Kennedy, J. B., "Nonlinear Analysis of Unsymmetrically Laminated Plates", *Journal of Engineering Mechanics, Proc. of the ASCE*, No. EM3, 1975, pp. 169–186.

27. Sun, C. T. and Chin, H., "On the Analysis of Asymmetric Composite Laminates", *AIAA Journal*, Vol. 26, 1988, pp. 714–718.

28. Chamis, C. C., "Buckling of Anisotropic Composite Plates", *Proc. of the ASCE, Journal of Engineering Mechanics*, No. ST10, 1969, pp. 2119–2139.

29. Ashton, J. E. and Love, T. S., "Experimental Study of the Stability of Composite Plates", *Journal of Composite Materials*, Vol. 3, 1969, pp. 230–242.

30. Mandell, J. F., "An Experimental Study of the Buckling of Anisotropic Plates", M.S. Thesis, Case Western Reserve University, June 1968.

31. Kicher, T. P. and Mandell, J. F., "Experimental Study of the Stability of Composite Plates", *AIAA Journal*, Vol. 9, 1971 pp. 605–613.

32. Lagace, P. A., Jenson, D. W., and Finch, D. C., "Buckling of Unsymmetric Composite Laminates", *Composite Structures*, Vol. 5, 1986, pp. 101–123.

33. Jenson, D. W. and Lagace, P. A., "Influence of Mechanical Couplings on the Buckling and Postbuckling Behavior of Anisotropic Plates", *AIAA Journal*, Vol. 26, 1988, pp. 1269–1277.

34. Chailleux, A., Hans, Y., and Verchery, G., "Experimental Study of the Buckling of Laminated Composite Columns and Plates", *International Journal of Mechanical Sciences*, Vol. 17, 1975, pp. 489–498.

35. Leissa, A. W., "Conditions for Laminated Plates to Remain Flat Under Inplane Loading", *Composite Structures*, Vol. 6, 1986, pp. 261–270.

36. Southwell, R. V., "On the Analysis of Experimental Observations in Problems of Elastic Stability", Proc. of the Royal Society, London, Series A, Vol. 135, 1932, pp. 601–616.

37. Monforton, G. R., "Discrete Element Displacement Analysis of Anisotropic Sandwich Shells", Ph.D. Thesis, Case Western Reserve University, 1971.

38. Turvey, G. J. and Wittrick, W. H., "The Large Deflection and Post-Buckling Behaviour of Some Laminated Plates", *Aeronautical Quarterly*, Vol. 24, 1973, pp. 77–86.

39. Harris, G. Z., "The Buckling and Post-Buckling Behavior of Composite Plates Under Biaxial Loading", *International Journal of Mechanical Sciences*, Vol. 17, 1975, pp. 187–202.

40. Chia, C. Y. and Prabhakara, M. K., "Postbuckling Behavior of Unsymmetrically Layered Anisotropic Rectangular Plates", *Journal of Applied Mechanics*, Vol. 41, 1974, pp. 155–162.

41. Prabhakara, M. K., "Post-Buckling Behavior of Simple-Supported Cross-Ply Rectangular Plates", *Aeronautical Quarterly*, Vol. 27, 1976, pp. 309–316.

42. Chan, D. P., "An Analytical Study of the Post-Buckling of Laminated Anisotropic Plates", *Fiber Science and Technology*, Vol. 11, 1978, pp. 165–187.

43. Zhang, Y. and Matthews, F. L., "Large Deflection Behavior of Simply Supported Laminated Panels Under In-Plane Loading", *Journal of Applied Mechanics*, Vol. 52, 1985, pp. 553–558.

44. Chia, C. Y., *Nonlinear Analysis of Plates*, McGraw-Hill, New York, 1980.

45. Leissa, A. W., "Buckling of Laminated Composite Plates and Shell Panels", AFWAL-TR-85-3069, 1985.

46. Pagano, N. J. and Hahn, H. T., "Evaluation of Composite Curing Stresses", ASTM STP 617, *American Society for Testing and Materials*, 1977, pp. 317–329.

47. Hyer, M. W., "Some Observations on the Cured Shape of Thin Unsymmetric Laminates", *Journal of Composite Materials*, Vol. 15, 1981, pp. 175–194.

48. Hyer, M. W., "Calculations of the Room-Temperature Shapes of Unsymmetric Laminates", *Journal of Composite Materials*, Vol. 15, 1981, pp. 296–310.

49. Hyer, M. W., "The Room Temperature Shapes of Four-Layer Unsymmetric Cross-Ply Laminates", *Journal of Composite Materials*, Vol. 16, 1982, pp. 318–340.

50. Hyer, M. W., "Mechanics of Unsymmetric Laminates", in: *Handbook of Composites, Vol. 2 - Structures and Design*, C.T. Herakovich and Y.M. Tarnopol'skii, eds., Elsevier Science Publishers, 1988, pp. 85–114.

51. Hahn, H. T., "Warping of Unsymmetric Cross-Ply Graphite/Epoxy Laminates", *Composites Technology Review*, Vol. 3, 1981, pp. 114–117.

52. Wong, M., "The Effects of Fabrication and Moisture on the Curvatures of Thin Graphite/Epoxy Laminates", M.S. Thesis, Massachusetts Institute of Technology, 1981.

53. Pipes, R. B. and Pagano, N. J., " Interlaminar Stresses in Composite Laminates Under Uniform Axial Extension", *Journal of Composite Materials*, Vol. 4, 1970, pp. 538–548.

54. Bogy, D. B., "Edge Bonded Dissimilar Orthogonal Elastic Wedges Under Normal and Shear Loading", *Journal of Applied Mechanics*, Vol. 35, 1968, pp. 460–466.

55. Hess, M. S., "The End Problem for a Laminated Elastic Strip - I. The General Solution", *Journal of Composite Materials*, Vol. 3, 1969, pp. 262–280.

56. Hess, M. S., "The End Problem for a Laminated Elastic Strip - II. Differential Expansion Stresses", *Journal of Composite Materials*, Vol. 3, 1969, pp. 630–641.

57. Pipes, R. B. and Daniel, I. M., "Moire Analysis of the Interlaminar Shear Edge Effect in Laminated Composites", *Journal of Composite Materials*, Vol. 5, 1971, pp. 255–259.

58. Pipes, R. B., "Solution of Certain Problems in the Theory of Elasticity for Laminated Anisotropic Systems", Ph.D. Dissertation, University of Texas at Arlington, 1972.

59. Pagano, N. J. and Pipes, R. B., "The Influence of Stacking Sequence On Laminate Strength", *Journal of Composite Materials*, Vol. 5, 1971, pp. 50–57.

60. Pagano, N. J. and Pipes, R. B., "Some Observations on the Interlaminar Strength of Composite Laminates", *International Journal of Mechanical Sciences*, Vol. 15, 1973, pp. 679–688.

61. Puppo, A. H. and Evenson, H. A., "Interlaminar Shear in Laminated Composites Under Generalized Plane Stresses", *Journal of Composite Materials*, Vol. 4, 1970, pp. 204–220.

62. Isakson, G. and Levy, A., "Finite Element Analysis of Interlaminar Shear in Fibrous Composites", *Journal of Composite Materials*, Vol. 5, 1971, pp. 273–276.

63. Rybicki, E. F., "Approximate Three-Dimensional Solutions for Symmetric Laminates Under Inplane Loading", *Journal of Composite Materials*, Vol. 5, 1971, pp. 354–360.

64. Foye, R. L. and Baker, D. J., "Design of Orthotropic Laminates", presented at the 11th Annual AIAA Structures, Structural Dynamics, and Materials Conference, Denver, Colorado, April 1970.

65. Whitney, J. M. and Browning, C. E, "Free-Edge Delamination in Tensile Coupons", *Journal of Composite Materials*, Vol. 6, 1972, pp. 300–303.

66. Herakovich, C. T., "On the Relationship Between Engineering Properties and Delamination of Composite Materials", *Journal of Composite Materials*, Vol. 15, 1981, pp. 336–348.

67. Herakovich, C. T., "Influence of Layer Thickness on the Strength of Angle-Ply Laminates", *Journal of Composite Materials*, Vol. 16, 1982, pp. 216–227.

68. Herakovich, C. T., "On Thermal Edge Effects in Composite Laminates", *International Journal of Mechanical Sciences*, Vol. 18, 1976, pp. 129–134.

69. Wang, A. S. D. and Crossman, F. W., "Edge Effects on Thermally Induced Stresses in Composite Laminates", *Journal of Composite Materials*, Vol. 11, 1977, pp. 300–312.

70. Griffin, O. H., Jr. and Roberts, J. C., "Numerical/Experimental Correlation of Three-Dimensional Thermal Stress in Graphite/Epoxy Laminates", *Journal of Composite Materials*, Vol. 17, 1983, pp. 539–548.

71. Farley, G. L. and Herakovich, C. T., "Influence of Two-Dimensional Hygrothermal Gradients on Interlaminar Stresses Near Free Edges", *Environmental Effects on Advanced Composite Materials*, ASTM STP 658, Am. Soc. for Testing and Materials, p. 143–159.

72. Crossman, F. W. and Wang, A. S. D., "Stress Field Induced by Transient Moisture Sorption in Finite-Width Composite Laminates", *Journal of Composite Materials*, Vol. 12, 1978, pp. 2–18.

73. Renieri, G. D. and Herakovich, C. T., "Nonlinear Analysis of Fibrous Composites", VPI-E-76-10, Virginia Polytechnic Institute and State University Report also NASA CR-148317, 1976.

74. Nagarkar, A. P. and Herakovich, C. T., "Nonlinear Temperature Dependent Failure Analysis of Finite Width Composite Laminates", VPI-E-79-36, Virginia Polytechnic Institute and State University Report, 1979.

75. Griffin, O. H., Jr., "Three-Dimensional Inelastic Finite Element Analysis of Laminate Composites", Ph.D. Dissertation, Virginia Polytechnic Institute and State University, Blacksburg, Va., 1980.

76. Hein, V. L., "Residual Stresses in a Two-Material Wedge and a Finite Cylinder", Ph.D. Thesis, Lehigh University, 1968.

77. Yaniv, G., and Ishai, O., "Residual Thermal Stresses in Bonded Metal and Fiber-Reinforced Plastic Systems", *Composites Technology Review*, Vol. 3, 1981, pp. 131–137.

78. Herakovich, C. T., Nagarkar, A., and O'Brien, D. A., "Failure Analysis of Composite Laminates with Free Edges", *Modern Developments in Composite Materials and Structures* , J.R. Vinson, ed., ASME, New York, 1979, pp. 53–66.

79. Wang, A. S. D. and Crossman, F. W., "Some New Results on Edge Effect in Symmetric Composite Laminates", *Journal of Composite Materials*, Vol. 11, 1977, pp. 92–106.

80. Barker, R. M., Dana, J. R. and Pryor, C. W., "Three-Dimensional Analysis of Stress Concentrations Near Holes in Laminated Composites", VPI-E-72-27, Virginia Polytechnic Institute and State University Report, Blacksburg, Va., 1972.

81. Stanton, E. L., Crain, L. M., and Neu, T. F., "A Parametric Cubic Modeling System for General Solids of Composite Material", *International Journal for Numerical Methods in Engineering*, Vol. 11, 1977, pp. 653–670.

82. Spilker, R. L. and Chou, S. C., "Edge Effects in Symmetric Composite Laminates: Importance of Satisfying the Traction Free Edge Condition", *Journal of Composite Materials*, Vol. 14, 1980, pp. 2–20.

83. Wang, S. S. and Yuan, F. G., "A Hybrid Finite Element Approach to Composite Laminate Elasticity Problems with Singularity", *Journal of Applied Mechanics*, Vol. 50, 1983, pp. 1–10.

84. Griffin, O. H., Jr. and Vidussoni, M. A., "Global/Local Finite Element Analysis of Composite Materials", in: *Computer Aided Design in Composite Material Technology*, C.A. Brebbia, W.P. de Wilde, W.R. Blain, eds., Computational Mechanics Publications, Boston, 1988, pp. 513–523.

85. Ransom, J. B., "Global/Local Finite Element Analysis of Composite Structures", NASA TM 101640, 1989.

86. Thompson, D. M. and Griffin, O. H., Jr., "2-D to 3-D Global/Local Finite Element Analysis of Composite Laminates", Proc. of the 4th Annual American Society for Composites Conference, Blacksburg, VA, October, 1989, pp. 234–243.

87. Whitcomb, J. D., Raju, I. S., and Goree, J. G., "Reliability of the Finite Element Method for Calculating Free Edge Stresses in Composite Materials", *Computers and Structures*, Vol. 15, 1982, pp. 23–37.

88. Wang, S. S. and Choi, I., "Boundary Layer Effects in Composite Materials: Part 1 - Free Edge Stress Singularities", *Journal of Applied Mechanics*, Vol. 49, 1982, pp. 541–548.

89. Wang, S. S. and Choi, I., "Boundary Layer Effects in Composite Laminates: Part 2 - Free Edge Stress Solutions and Basic Characteristics", *Journal of Applied Mechanics*, Vol. 49, 1982, pp. 549–560.

90. Lekhnitskii, S. G., *Theory of Elasticity of an Anisotropic Elastic Body*, Holden-Day, Inc., San Francisco, 1963.

91. Tang, S., "A Boundary Layer Theory - Part I: Laminated Composites in Plane Stress", *Journal of Composite Materials*, Vol. 9, 1975, pp. 33–41.

92. Tang, S. and Levy, A., "A Boundary Layer Theory - Part II: Extension of a Laminated Finite Strip", *Journal of Composite Materials*, Vol. 9, 1975, pp. 42–45.

93. Hsu, P. W. and Herakovich, C. T., "Edge Effects in Angle-Ply Composite Laminates", *Journal of Composite Materials*, Vol. 11, 1977, pp. 422–428.

94. Pagano, N. J., "Stress Fields in Composite Laminates", *International Journal of Solids and Structures*, Vol. 14, 1978, pp. 385–400.

95. Pagano, N. J., "Free Edge Stress Fields in Composite Laminates", *International Journal of Solids and Structures*, Vol. 14, 1978, pp. 401–406.

96. Pagano, N. J. and Soni, S. R., "Global-Local Variational Model", *International Journal of Solids and Structures*, Vol. 19, 1983, pp. 207–228.

97. Johnson, E. R. and Kemp, B. L., "Modeling the Stress Field in Laminated Composite Plates Near Discontinuities", *Composite Structures*, Vol. 3, 1985, pp. 145–166.

98. Kassapoglou, C. and Lagace, P. A., "An Efficient Method for the Calculation of Interlaminar Stresses in Composite Materials", *Journal of Applied Mechanics*, Vol. 53, 1986, pp. 774–750.

99. Salamon, N. J., "An Assessment of the Interlaminar Stress Problem in Laminated Composites", *Journal of Composite Materials*, Vol. 14, 1980, pp. 177–194.

100. Herakovich, C. T., "Free Edge Effects in Laminated Composites", *Handbook of Composites, Vol. 2 - Structures and Design*, C.T. Herakovich and Y.M. Tarnopol'skii, eds., Elsevier Science Publishers, 1988, pp. 187–230.

101. Tong, P. and Pian, T. H. H., "On the Convergence of the Finite Element Method for Problems with Singularity", *International Journal of Solids and Structures*, Vol. 9, 1973, pp. 313–321.

102. Swedlow, J. L., "Singularity Computations", *International Journal for Numerical Methods in Engineering*, Vol. 12, 1978, pp. 1779–1798.

103. Zwiers, R. I., Ting, T. C. T., and Spilker, R. L., "On the Logarithmic Singularity of Free-Edge Stress in Laminated Composites under Uniform Extension", *Journal of Applied Mechanics*, Vol. 49, 1982, pp. 561–569.

104. Liao, C. L. and Reddy, J. N., "An Incremental Total Lagrangian Formulation for General Anisotropic Shell-Type Structures", VPI-E-87-22, Virginia Polytechnic Institute and State University Report, Blacksburg, Va., 1987.

105. Noor, A. K., Starnes, J. H., Jr., and Waters, W. A., Jr., "Numerical and Experimental Simulations of the Postbuckling Response of Laminated Anisotropic Panels", AIAA Paper No. 90-0964-CP, April 1990.

106. Novozhilov, V. V., *Foundations of the Nonlinear Theory of Elasticity*, Graylock Press, Rochester, New York, 1953.

107. Malvern, L. E., *Introduction to the Mechanics of a Continuous Medium*, Prentice-Hall, Inc., Englewood Cliff, NJ, 1965.

108. Reddy, J. N., *Energy and Variational Methods in Applied Mechanics*, John Wiley and Sons, New York, 1984.

109. Frederick, D. and Chang, T. S., *Continuum Mechanics*, Scientific Publishers Inc., Cambridge, MA., 1972.

110. Bathe, K. J., *Finite Element Procedures in Engineering Analysis*, Prentice-Hall, Inc., Englewood Cliffs, New Jersey, 1982.

111. Fung, Y. C., *Foundations of Solid Mechanics*, Prentice-Hall, Englewood Cliffs, New Jersey, 1965.

112. Allen, D. H. and Haisler, W. H., *Introduction to Aerospace Structural Analysis*, John Wiley and Sons, New York, 1985.

113. Simitses, G. J., *An Introduction to the Elastic Stability of Structures*, Prentice-Hall, Englewood Cliffs, New Jersey, 1976.

114. Zienkiewicz, O. C., *The Finite Element Method*, McGraw-Hill, NY, 1977.

115. Reddy, J. N., *An Introduction to the Finite Element Method*, McGraw-Hill, NY, 1984.

116. Noor, A. K., Mathers, M. D., and Anderson, M. S., "Exploiting Symmetries for Efficient Postbuckling Analysis of Composite Plates", *AIAA Journal*, Vol. 15, 1977, pp. 24–32.

117. Thurston, G.A., "Continuation of Newton's Method Through Bifurcation Points", *Journal of Applied Mechanics*, Vol. 36, 1969, pp. 425–430.

118. Thurston, G.A., Brogan, F.A., and Stehlin, P., "Postbucking Analysis Using a General Purpose Code", *AIAA Journal*, Vol. 24, 1986, pp. 1013–1020.

119. Barlow, J., "Optimal Stress Locations in Finite Element Models", *International Journal of Numerical Methods in Engineering*, Vol. 10, 1976, pp. 243–251.

120. Barlow, J., "More on Optimal Points - Reduced Integration, Element Distortions, and Error Estimation", *International Journal of Numerical Methods in Engineering*, Vol. 28, 1989, pp. 1487–1504.

121. Stricklin, J. A. and Haisler, W. E., "Formulations and Solution Procedures for Nonlinear Structural Analysis", *Computers and Structures*, Vol. 7, 1977, pp. 125–136.

122. Wang, T. M., "Nonlinear Bending of Beams With Concentrated Loads", *Journal of the Franklin Institute*, Vol. 285, 1968, pp. 386–390.

123. Holden, J. T., "On the Finite Deflections Of Thin Beams", *International Journal of Solids and Structures*, Vol. 8, 1972, pp. 1051–1055.

124. Timoshenko, S. P. and Gere, J. M., *Theory of Elastic Stability*, McGraw-Hill, New York, 1961.

Appendix A

THE COUPLING BEHAVIOR OF LAMINATED ANISOTROPIC PLATES

This appendix provides a brief review of the coupling behavior of laminated anisotropic plates. As discussed in Chapter 1, laminated composite plates can possess unique coupling characteristics in the deformational response. Two types of coupling effects which can arise in the response of laminated composite plates are laminate coupling and geometric coupling. Laminate coupling, which is also referred to as mechanical, elastic, or thermoelastic coupling, is caused by the directionally dependent material properties of composite materials and/or the heterogeneous construction of laminated plates. For linear thermoelastic materials, laminate coupling is a linear coupling effect which may be present in the membrane response, flexural response, or in a combination of both membrane and flexural response. Geometric coupling refers to the membrane-flexural coupling effect which arises in the finite deflection of elastic plates. Geometric coupling is a nonlinear coupling effect which must be accounted for through the use of a geometrically nonlinear kinematic description.

From the Kirchhoff-Love kinematic assumptions of classical plate theory [23], the strain-displacement equations are given by:

$$\epsilon_{xx} = \epsilon^0_{xx} + z\kappa_x, \qquad \kappa_x = -w_{,xx} \tag{A.1a}$$

$$\epsilon_{yy} = \epsilon^0_{yy} + z\kappa_y, \qquad \kappa_y = -w_{,yy} \tag{A.1b}$$

$$\gamma_{xy} = \gamma^0_{xy} + z\kappa_{xy}, \qquad \kappa_{xy} = -2w_{,xy} \tag{A.1c}$$

ϵ^0_{xx}, ϵ^0_{yy}, and γ^0_{xy}, are the in-plane strains of the laminated plate reference surface (geometric midplane). κ_x, κ_y, and κ_{xy}, are the curvatures of the reference surface. From the von Karman theory [4] for the finite deflection of elastic plates, the

reference surface strains are given by:

$$\epsilon^0_{xx} = u_{,x} + \frac{1}{2} w_{,x} w_{,x} \tag{A.2a}$$

$$\epsilon^0_{yy} = v_{,y} + \frac{1}{2} w_{,y} w_{,y} \tag{A.2b}$$

$$\gamma^0_{xy} = u_{,y} + v_{,x} + w_{,x} w_{,y} \tag{A.2c}$$

The membrane and flexural stress resultants are defined as:

$$(N_x, N_y, N_{xy}) = \int_{-h/2}^{+h/2} (S_{xx}, S_{yy}, S_{xy}) dz \tag{A.3a}$$

$$(M_x, M_y, M_{xy}) = \int_{-h/2}^{+h/2} (S_{xx}, S_{yy}, S_{xy}) z dz \tag{A.3b}$$

Assuming that each lamina is in a state of plane stress, the constitutive equations relating the membrane and flexural stress resultants to the strains and curvatures of the reference surface are given by:

$$\begin{Bmatrix} N_x \\ N_y \\ N_{xy} \\ M_x \\ M_y \\ M_{xy} \end{Bmatrix} = \begin{bmatrix} A_{11} & A_{12} & A_{16} & B_{11} & B_{12} & B_{16} \\ A_{21} & A_{22} & A_{26} & B_{21} & B_{22} & B_{26} \\ A_{61} & A_{62} & A_{66} & B_{61} & B_{62} & B_{66} \\ B_{11} & B_{12} & B_{16} & D_{11} & D_{12} & D_{16} \\ B_{21} & B_{22} & B_{26} & D_{21} & D_{22} & D_{26} \\ B_{61} & B_{62} & B_{66} & D_{61} & D_{62} & D_{66} \end{bmatrix} \begin{Bmatrix} \epsilon^0_{xx} \\ \epsilon^0_{yy} \\ \gamma^0_{xy} \\ \kappa_x \\ \kappa_y \\ \kappa_{xy} \end{Bmatrix} \tag{A.4}$$

where:

$$(A_{ij}, B_{ij}, D_{ij}) = \int_{-h/2}^{+h/2} \bar{Q}_{ij} (1, z, z^2) dz \tag{A.5}$$

The quantities, $\bar{Q}_{ij}$, are the transformed reduced lamina stiffnesses with respect to the global coordinates (x, y, z) of the laminated plate (refer to Appendix B). The constitutive coefficients, A_{ij}, B_{ij}, and D_{ij}, are the membrane, membrane-flexural, and flexural stiffnesses for the laminated plate, respectively. The 3 by 3 submatrices given by the quantities, A_{ij}, B_{ij}, and D_{ij} $(i, j = 1, 2, 6)$, are symmetric as is the entire 6 by 6 constitutive matrix.

The constitutive coefficients, A_{16}, A_{26}, D_{16}, D_{26}, and B_{ij} $(i, j = 1, 2, 6)$, characterize the laminate coupling behavior of a laminated anisotropic plate. The

laminate coupling effects which may be present in a laminated anisotropic plate are summarized in Table A.1. The deformational coupling relationships of laminated anisotropic plates are illustrated in Figure A.1. The constitutive coefficients, A_{16} and A_{26}, characterize the membrane coupling effects between extension and shear. Extension-shear coupling occurs in unbalanced laminates in which there is at least one off-axis layer ($\theta \neq 0°, 90°$) of $+\theta$ orientation which is not balanced by an off-axis layer of equal thickness with $-\theta$ orientation. The constitutive coefficients, B_{ij} $(i,j = 1,2,6)$, characterize the membrane-flexural coupling effects. This coupling occurs in all unsymmetric laminates and is caused by the mismatch in material properties above and below the geometric midplane of the laminate. The constitutive coefficients, B_{11}, B_{22}, and B_{12}, characterize the membrane-flexural coupling effects between extension and bending. The constitutive coefficients, B_{16} and B_{26}, characterize the membrane-flexural coupling effects between extension and twisting and between shear and bending. The constitutive coefficient, B_{66}, characterizes the membrane-flexural coupling effects between shear and twisting. The constitutive coefficients, D_{16} and D_{26}, characterize the flexural coupling effects between bending and twisting. Bending-twisting coupling occurs in non-antisymmetric laminates which possess at least one off-axis layer. An antisymmetric laminate is also an unsymmetric laminate in which there will exist membrane-flexural coupling.

The equations of equilibrium for a laminated composite plate are given by:

$$N_{x,x} + N_{xy,y} = 0 \qquad (A.6a)$$

$$N_{yx,x} + N_{y,y} = 0 \qquad (A.6b)$$

$$N_x w_{,xx} + 2N_{xy} w_{,xy} + N_y w_{,yy} + M_{x,xx} + 2M_{xy,xy} + M_{y,yy} + p_z = 0 \qquad (A.6c)$$

p_z is the transverse pressure acting in the z coordinate direction. Equations (A.4) and (A.6) are nine equations for nine unknowns: N_x, N_y, N_{xy}, M_x, M_y, M_{xy}, u^0, v^0, and w. Substituting equations (A.4) into equations (A.6) results in a system

of three equations of eighth order for the three unknowns: u^0, v^0, and w. The governing equations in terms of displacements are given by:

$$L_{11}u^0 + L_{12}v^0 + L_{13}w = -w_{,x}L_{11}w - w_{,y}L_{12}w \qquad (A.7a)$$

$$L_{21}u^0 + L_{22}v^0 + L_{23}w = -w_{,x}L_{21}w - w_{,y}L_{22}w \qquad (A.7b)$$

$$L_{31}u^0 + L_{32}v^0 + L_{33}w = p_z + F_1 + F_2 \qquad (A.7c)$$

where:

$$F_1 = (u^0_{,x} + \tfrac{1}{2}w^2_{,x})L_1w + (v^0_{,y} + \tfrac{1}{2}w^2_{,y})L_2w + (u^0_{,y} + v^0_{,x} + \tfrac{1}{2}w_{,x}w_{,y})L_3w$$

$$F_2 = -w_{,x}L_{13}w - w_{,y}L_{23}w + (B_{12} - B_{66})(w^2_{,xy} - w_{,xx}w_{,yy})$$

and the linear operators are given by:

$$L_{11} = A_{11}(\ )_{,xx} + 2A_{16}(\ )_{,xy} + A_{66}(\ )_{,yy}$$

$$L_{22} = A_{66}(\ )_{,xx} + 2A_{26}(\ )_{,xy} + A_{22}(\ )_{,yy}$$

$$L_{12} = L_{21} = A_{16}(\ )_{,xx} + (A_{12} + A_{66})(\ )_{,xy} + A_{26}(\ )_{,yy}$$

$$L_{33} = D_{11}(\ )_{,xxxx} + 4D_{16}(\ )_{,xxxy} + 2(D_{12} + 2D_{66})(\ )_{,xxyy} + 4D_{26}(\ )_{,xyyy} + D_{22}(\ )_{,yyyy}$$

$$L_{13} = L_{31} = -B_{11}(\ )_{,xxx} - 3B_{16}(\ )_{,xxy} - (B_{12} + 2B_{66})(\ )_{,xyy} - B_{26}(\ )_{,yyy}$$

$$L_{23} = L_{32} = -B_{16}(\ )_{,xxx} - (B_{12} + 2B_{66})(\ )_{,xxy} - 3B_{26}(\ )_{,xyy} - B_{22}(\ )_{,yyy}$$

$$L_1 = A_{11}(\ )_{,xx} + 2A_{16}(\ )_{,xy} + A_{12}(\ )_{,yy}$$

$$L_2 = A_{12}(\ )_{,xx} + 2A_{26}(\ )_{,xy} + A_{22}(\ )_{,yy}$$

$$L_3 = A_{16}(\ )_{,xx} + 2A_{66}(\ )_{,xy} + A_{26}(\ )_{,yy}$$

The system of equations (A.7) governs the large deflection behavior of unsymmetrically laminated anisotropic plates. The large deflection behavior of unsymmetrically laminated plates exhibits both laminate and geometric membrane-flexural coupling effects. For the small deflection behavior of symmetrically laminated anisotropic plates, neither laminate or geometric coupling exists and the fourth order governing equation is given by:

$$L_{33}w = p_z \qquad (A.8)$$

For the large deflection behavior of symmetrically laminated anisotropic plates, geometric membrane-flexural coupling exists through the geometrically nonlinear kinematic description and the eighth order system of governing equations are given by:

$$L_{11}u^0 + L_{12}v^0 = -w_{,x}L_{11}w - w_{,y}L_{12}w \qquad (A.9a)$$

$$L_{21}u^0 + L_{22}v^0 = -w_{,x}L_{21}w - w_{,y}L_{22}w \qquad (A.9b)$$

$$L_{33}w = p_z + F_1 \qquad (A.9c)$$

Finally, for the small deflection behavior of unsymmetrically laminated anisotropic plates, laminate membrane-flexural coupling exists and the eighth order system of governing equations are given by:

$$L_{11}u^0 + L_{12}v^0 + L_{13}w = 0 \qquad (A.10a)$$

$$L_{21}u^0 + L_{22}v^0 + L_{23}w = 0 \qquad (A.10b)$$

$$L_{31}u^0 + L_{32}v^0 + L_{33}w = p_z \qquad (A.10c)$$

Appendix B
CONSTITUTIVE EQUATIONS

This appendix discusses the transformed constitutive equations for a linear elastic, orthotropic layer or lamina of arbitrary orientation with respect to global coordinates. The transformation accounts for a single rotation about the z-axis from the global coordinate system (x, y, z) of the plate to the principal material coordinate system (X_1, X_2, X_3) of the lamina (Figure 3.1) . The strain-stress equations for a linear elastic orthotropic lamina with respect to the principal material coordinate system are given by:

$$\begin{Bmatrix} \epsilon_{11} \\ \epsilon_{22} \\ \epsilon_{33} \\ \gamma_{23} \\ \gamma_{13} \\ \gamma_{12} \end{Bmatrix} = \begin{bmatrix} s_{11} & s_{12} & s_{13} & 0 & 0 & 0 \\ s_{21} & s_{22} & s_{23} & 0 & 0 & 0 \\ s_{31} & s_{32} & s_{33} & 0 & 0 & 0 \\ 0 & 0 & 0 & s_{44} & 0 & 0 \\ 0 & 0 & 0 & 0 & s_{55} & 0 \\ 0 & 0 & 0 & 0 & 0 & s_{66} \end{bmatrix} \begin{Bmatrix} \sigma_{11} \\ \sigma_{22} \\ \sigma_{33} \\ \tau_{23} \\ \tau_{13} \\ \tau_{12} \end{Bmatrix} \qquad (B.1)$$

The $[s]$ matrix of elastic coefficients given above is symmetric and is referred to as the compliance matrix. The elastic coefficients in terms of elastic engineering coefficients are given by [22]:

$$[s] = \begin{bmatrix} \frac{1}{E_1} & -\frac{\nu_{21}}{E_2} & -\frac{\nu_{31}}{E_3} & 0 & 0 & 0 \\ -\frac{\nu_{12}}{E_1} & \frac{1}{E_2} & -\frac{\nu_{32}}{E_3} & 0 & 0 & 0 \\ -\frac{\nu_{13}}{E_1} & -\frac{\nu_{23}}{E_2} & \frac{1}{E_3} & 0 & 0 & 0 \\ 0 & 0 & 0 & \frac{1}{G_{23}} & 0 & 0 \\ 0 & 0 & 0 & 0 & \frac{1}{G_{13}} & 0 \\ 0 & 0 & 0 & 0 & 0 & \frac{1}{G_{12}} \end{bmatrix} \qquad (B.2)$$

where the elastic engineering constants are defined as follows:

E_1, E_2, E_3 = Young's moduli in the 1, 2, and 3 directions, respectively

G_{23}, G_{13}, G_{12} = shear moduli in the 2-3, 1-3, and 1-2 planes, respectively

ν_{ij} = Poisson's ratios

where:

$\nu_{ij} = -\frac{\epsilon_{jj}}{\epsilon_{ii}}$ for $\sigma_{ii} \neq 0$, all other $\sigma_{ij} = 0$ (no summation implied)

$\frac{\nu_{ij}}{E_{ii}} = \frac{\nu_{ji}}{E_{jj}}$ for $i, j = 1, 2, 3$ (no summation implied)

The stress-strain equations for a linear elastic orthotropic lamina with respect to the principal material coordinate system are given by:

$$\begin{Bmatrix} \sigma_{11} \\ \sigma_{22} \\ \sigma_{33} \\ \tau_{23} \\ \tau_{13} \\ \tau_{12} \end{Bmatrix} = \begin{bmatrix} c_{11} & c_{12} & c_{13} & 0 & 0 & 0 \\ c_{21} & c_{22} & c_{23} & 0 & 0 & 0 \\ c_{31} & c_{32} & c_{33} & 0 & 0 & 0 \\ 0 & 0 & 0 & c_{44} & 0 & 0 \\ 0 & 0 & 0 & 0 & c_{55} & 0 \\ 0 & 0 & 0 & 0 & 0 & c_{66} \end{bmatrix} \begin{Bmatrix} \epsilon_{11} \\ \epsilon_{22} \\ \epsilon_{33} \\ \gamma_{23} \\ \gamma_{13} \\ \gamma_{12} \end{Bmatrix} \qquad (B.3)$$

where the coefficients may be expressed in terms of elastic engineering constants:

$c_{11} = \frac{E_{11}}{\Delta}(1 - \nu_{23}\nu_{32})$

$c_{22} = \frac{E_{22}}{\Delta}(1 - \nu_{13}\nu_{31})$

$c_{33} = \frac{E_{33}}{\Delta}(1 - \nu_{12}\nu_{21})$

$c_{23} = c_{32} = \frac{E_{33}}{\Delta}(\nu_{23} + \nu_{21}\nu_{13}) = \frac{E_{22}}{\Delta}(\nu_{32} + \nu_{12}\nu_{31})$

$c_{13} = c_{31} = \frac{E_{33}}{\Delta}(\nu_{13} + \nu_{12}\nu_{23}) = \frac{E_{11}}{\Delta}(\nu_{31} + \nu_{21}\nu_{32})$

$c_{12} = c_{21} = \frac{E_{22}}{\Delta}(\nu_{12} + \nu_{32}\nu_{13}) = \frac{E_{11}}{\Delta}(\nu_{21} + \nu_{31}\nu_{23})$

$c_{44} = G_{23}$

$c_{55} = G_{13}$

$c_{66} = G_{12}$

$\Delta = 1 - \nu_{23}\nu_{32} - \nu_{13}\nu_{31} - \nu_{12}\nu_{21} - 2\nu_{21}\nu_{32}\nu_{13}$

The $[c]$ matrix of elastic coefficients given above is symmetric and is referred to as the stiffness matrix. The stiffness matrix is the inverse of the compliance matrix, $[c] = [s]^{-1}$.

The equations for transforming a state of stress from global coordinates (x, y, z) to principal material coordinates (X_1, X_2, X_3) are given by:

$$\begin{Bmatrix} \sigma_{11} \\ \sigma_{22} \\ \sigma_{33} \\ \tau_{23} \\ \tau_{13} \\ \tau_{12} \end{Bmatrix} = \begin{bmatrix} m^2 & n^2 & 0 & 0 & 0 & 2mn \\ n^2 & m^2 & 0 & 0 & 0 & -2mn \\ 0 & 0 & 1 & 0 & 0 & 0 \\ 0 & 0 & 0 & m & -n & 0 \\ 0 & 0 & 0 & n & m & 0 \\ -mn & mn & 0 & 0 & 0 & (m^2 - n^2) \end{bmatrix} \begin{Bmatrix} \sigma_{xx} \\ \sigma_{yy} \\ \sigma_{zz} \\ \tau_{yz} \\ \tau_{zx} \\ \tau_{xy} \end{Bmatrix} \qquad (B.4)$$

where:

$m = \cos\theta$

$n = \sin\theta$

The equations for transforming a state of strain from global coordinates (x, y, z) to principal material coordinates (X_1, X_2, X_3) are given by:

$$\begin{Bmatrix} \epsilon_{11} \\ \epsilon_{22} \\ \epsilon_{33} \\ \gamma_{23} \\ \gamma_{13} \\ \gamma_{12} \end{Bmatrix} = \begin{bmatrix} m^2 & n^2 & 0 & 0 & 0 & mn \\ n^2 & m^2 & 0 & 0 & 0 & -mn \\ 0 & 0 & 1 & 0 & 0 & 0 \\ 0 & 0 & 0 & m & -n & 0 \\ 0 & 0 & 0 & n & m & 0 \\ -2mn & 2mn & 0 & 0 & 0 & (m^2 - n^2) \end{bmatrix} \begin{Bmatrix} \epsilon_{xx} \\ \epsilon_{yy} \\ \epsilon_{zz} \\ \gamma_{yz} \\ \gamma_{zx} \\ \gamma_{xy} \end{Bmatrix} \qquad (B.5)$$

where:

$m = \cos\theta$

$n = \sin\theta$

Equations (B.4) and (B.5) can be used with equations (B.3) to derive the transformed stress-strain equations with respect to global coordinates (x, y, z):

$$\begin{Bmatrix} \sigma_{xx} \\ \sigma_{yy} \\ \sigma_{zz} \\ \tau_{yz} \\ \tau_{zx} \\ \tau_{xy} \end{Bmatrix} = \begin{bmatrix} \bar{c}_{11} & \bar{c}_{12} & \bar{c}_{13} & 0 & 0 & \bar{c}_{16} \\ \bar{c}_{12} & \bar{c}_{22} & \bar{c}_{23} & 0 & 0 & \bar{c}_{26} \\ \bar{c}_{13} & \bar{c}_{23} & \bar{c}_{33} & 0 & 0 & \bar{c}_{36} \\ 0 & 0 & 0 & \bar{c}_{44} & \bar{c}_{45} & 0 \\ 0 & 0 & 0 & \bar{c}_{45} & \bar{c}_{55} & 0 \\ \bar{c}_{16} & \bar{c}_{26} & \bar{c}_{36} & 0 & 0 & \bar{c}_{66} \end{bmatrix} \begin{Bmatrix} \epsilon_{xx} \\ \epsilon_{yy} \\ \epsilon_{zz} \\ \gamma_{yz} \\ \gamma_{zx} \\ \gamma_{xy} \end{Bmatrix} \qquad (B.6)$$

where:

$$\bar{c}_{11} = m^4 c_{11} + 2m^2 n^2 (c_{12} + 2c_{66}) + n^4 c_{22} \qquad (B.7a)$$

$$\bar{c}_{22} = n^4 c_{11} + 2m^2 n^2 (c_{12} + 2c_{66}) + m^4 c_{22} \qquad (B.7b)$$

$$\bar{c}_{12} = m^2 n^2 (c_{11} + c_{22} - 4c_{66}) + (m^4 + n^4) c_{12} \qquad (B.7c)$$

$$\bar{c}_{66} = m^2 n^2 (c_{11} + c_{22} - 2c_{12}) + (m^2 + n^2)^2 c_{66} \qquad (B.7d)$$

$$\bar{c}_{16} = mn[m^2 c_{11} - n^2 c_{22} - (m^2 - n^2)(c_{12} + 2c_{66})] \qquad (B.7e)$$

$$\bar{c}_{26} = mn[n^2 c_{11} - m^2 c_{22} + (m^2 - n^2)(c_{12} + 2c_{66})] \qquad (B.7f)$$

$$\bar{c}_{13} = m^2 c_{13} + n^2 c_{23} \tag{B.7g}$$

$$\bar{c}_{23} = n^2 c_{13} + m^2 c_{23} \tag{B.7h}$$

$$\bar{c}_{36} = mn(c_{13} - c_{23}) \tag{B.7i}$$

$$\bar{c}_{44} = m^2 c_{44} + n^2 c_{55} \tag{B.7j}$$

$$\bar{c}_{55} = n^2 c_{44} + m^2 c_{55} \tag{B.7k}$$

$$\bar{c}_{45} = mn(c_{55} - c_{44}) \tag{B.7l}$$

$$\bar{c}_{33} = c_{33} \tag{B.7m}$$

Equations (B.6) represent the stress-strain equations for a linear elastic monoclinic material which is characterized by 13 independent elastic constants.

From classical laminated plate theory, the reduced stress-strain equations for an arbitrarily oriented orthotropic lamina in a state plane stress are given by [22]:

$$\begin{Bmatrix} \sigma_{xx} \\ \sigma_{yy} \\ \tau_{xy} \end{Bmatrix} = \begin{bmatrix} \bar{Q}_{11} & \bar{Q}_{12} & \bar{Q}_{16} \\ \bar{Q}_{12} & \bar{Q}_{22} & \bar{Q}_{26} \\ \bar{Q}_{16} & \bar{Q}_{26} & \bar{Q}_{66} \end{bmatrix} \begin{Bmatrix} \epsilon_{xx} \\ \epsilon_{yy} \\ \gamma_{xy} \end{Bmatrix} \tag{B.8}$$

where:

$$\bar{Q}_{11} = m^4 Q_{11} + 2m^2 n^2 (Q_{12} + 2Q_{66}) + n^4 Q_{22} \tag{B.9a}$$

$$\bar{Q}_{22} = n^4 Q_{11} + 2m^2 n^2 (Q_{12} + 2Q_{66}) + m^4 Q_{22} \tag{B.9b}$$

$$\bar{Q}_{12} = m^2 n^2 (Q_{11} + Q_{22} - 4Q_{66}) + (m^4 + n^4) Q_{12} \tag{B.9c}$$

$$\bar{Q}_{66} = m^2 n^2 (Q_{11} + Q_{22} - 2Q_{12}) + (m^2 + n^2)^2 Q_{66} \tag{B.9d}$$

$$\bar{Q}_{16} = mn[m^2 Q_{11} - n^2 Q_{22} - (m^2 - n^2)(Q_{12} + 2Q_{66})] \tag{B.9e}$$

$$\bar{Q}_{26} = mn[n^2 Q_{11} - m^2 Q_{22} + (m^2 - n^2)(Q_{12} + 2Q_{66})] \tag{B.9f}$$

and:

$$Q_{11} = \frac{E_1}{1 - \nu_{12}\nu_{21}}$$

$$Q_{22} = \frac{E_2}{1 - \nu_{12}\nu_{21}}$$

$$Q_{12} = \frac{E_2 \nu_{12}}{1 - \nu_{12}\nu_{21}} = \frac{E_1 \nu_{21}}{1 - \nu_{12}\nu_{21}}$$

$$Q_{66} = G_{12}$$

For the case of plane stress, Q_{ij} and $\bar{Q}_{ij}$, are the transformed reduced lamina stiffness terms with respect to principal material coordinates (X_1, X_2, X_3) and global coordinates (x, y, z), respectively. Through the use of multiple angle trigonometric identities, the transformed reduced stiffnesses can be written [22]:

$$\bar{Q}_{11} = U_1 + U_2 \cos 2\theta + U_3 \cos 4\theta \qquad (B.10a)$$

$$\bar{Q}_{22} = U_1 - U_2 \cos 2\theta + U_3 \cos 4\theta \qquad (B.10b)$$

$$\bar{Q}_{12} = U_4 - U_3 \cos 4\theta \qquad (B.10c)$$

$$\bar{Q}_{66} = U_5 - U_3 \cos 4\theta \qquad (B.10d)$$

$$\bar{Q}_{16} = \frac{1}{2} U_2 \sin 2\theta + U_3 \sin 4\theta \qquad (B.10e)$$

$$\bar{Q}_{26} = \frac{1}{2} U_2 \sin 2\theta - U_3 \sin 4\theta \qquad (B.10f)$$

where U_1 through U_5 are material invariants which are defined as:

$$U_1 = \tfrac{1}{8}(3Q_{11} + 3Q_{22} + 2Q_{12} + 4Q_{66})$$

$$U_2 = \tfrac{1}{2}(Q_{11} - Q_{22})$$

$$U_3 = \tfrac{1}{8}(3Q_{11} + 3Q_{22} - 2Q_{12} - 4Q_{66})$$

$$U_4 = \tfrac{1}{8}(3Q_{11} + 3Q_{22} + 6Q_{12} - 4Q_{66})$$

$$U_5 = \tfrac{1}{8}(3Q_{11} + 3Q_{22} - 2Q_{12} + 4Q_{66})$$

The in-plane behavior of an orthotropic lamina is characterized by 4 independent elastic constants, namely: E_{11}, E_{22}, ν_{12}, and G_{12}. Therefore, only four of the material invariants given above should be independent [22]:

$$U_5 = \frac{1}{2}(U_1 - U_4) \qquad (B.11)$$

The three-dimensional behavior of a linear elastic orthotropic material is characterized by nine independent elastic constants. A similar set of nine material constants

can be defined as:

$$C_1 = \frac{1}{8}(c_{11} + c_{22}) \qquad (B.12a)$$

$$C_2 = \frac{1}{8}(c_{11} - c_{22}) \qquad (B.12b)$$

$$C_3 = \frac{1}{4}(c_{12} + 2c_{66}) \qquad (B.12c)$$

$$C_4 = \frac{1}{4}(c_{12} - 2c_{66}) \qquad (B.12d)$$

$$C_5 = \frac{1}{2}(c_{13} + c_{23}) \qquad (B.12e)$$

$$C_6 = \frac{1}{2}(c_{13} - c_{23}) \qquad (B.12f)$$

$$C_7 = \frac{1}{2}(c_{44} + c_{55}) \qquad (B.12g)$$

$$C_8 = \frac{1}{2}(c_{44} - c_{55}) \qquad (B.12h)$$

$$C_9 = c_{33} \qquad (B.12i)$$

The first four constants, C_1 through C_4, are associated in-plane behavior of the lamina. Using the material constants defined above with multiple angle trigonometric identities, the transformed stiffness moduli may written:

$$\bar{c}_{11} = (3C_1 + C_3) + 4C_2\cos 2\theta + (C_1 - C_3)\cos 4\theta \qquad (B.13a)$$

$$\bar{c}_{22} = (3C_1 + C_3) - 4C_2\cos 2\theta + (C_1 - C_3)\cos 4\theta \qquad (B.13b)$$

$$\bar{c}_{12} = (C_1 + C_3 + 2C_4) - (C_1 - C_3)\cos 4\theta \qquad (B.13c)$$

$$\bar{c}_{66} = (C_1 - C_4) - (C_1 - C_3)\cos 4\theta \qquad (B.13d)$$

$$\bar{c}_{16} = 2C_2\sin 2\theta + (C_1 - C_3)\sin 4\theta \qquad (B.13e)$$

$$\bar{c}_{26} = 2C_2\sin 2\theta - (C_1 - C_3)\sin 4\theta \qquad (B.13f)$$

$$\bar{c}_{13} = C_5 + C_6\cos 2\theta \qquad (B.13g)$$

$$\bar{c}_{23} = C_5 - C_6\cos 2\theta \qquad (B.13h)$$

$$\bar{c}_{36} = C_6\sin 2\theta \qquad (B.13i)$$

$$\bar{c}_{44} = C_7 + C_8\cos 2\theta \qquad (B.13j)$$

$$\bar{c}_{55} = C_7 - C_8 \cos 2\theta \qquad (B.13k)$$

$$\bar{c}_{45} = -C_8 \sin 2\theta \qquad (B.13l)$$

$$\bar{c}_{33} = C_9 \qquad (B.13m)$$

The reverse of the transformations given above, i.e., the transformation from global coordinates to principal material coordinates, may be obtained by changing the sign of the transformation angle θ. Finally, noting that the engineering shear strain is equal to twice the tensorial shear strain, the transformed stiffness moduli defined above are related to the linear elastic constitutive coefficients used in Chapter 4 as follows:

$$[\bar{c}] = \begin{bmatrix} {}_0C_{1111} & {}_0C_{1122} & {}_0C_{1133} & 0 & 0 & {}_0C_{1166} \\ {}_0C_{2211} & {}_0C_{2222} & {}_0C_{2233} & 0 & 0 & {}_0C_{2266} \\ {}_0C_{3311} & {}_0C_{3322} & {}_0C_{3333} & 0 & 0 & {}_0C_{3366} \\ 0 & 0 & 0 & {}_0C_{4444} & {}_0C_{4455} & 0 \\ 0 & 0 & 0 & {}_0C_{5544} & {}_0C_{5555} & 0 \\ {}_0C_{6611} & {}_0C_{6622} & {}_0C_{6633} & 0 & 0 & {}_0C_{6666} \end{bmatrix} \qquad (B.14)$$

where (Table 5.2):

$e_{yz} = 2e_{23}$, $\epsilon_{yz} = 2\epsilon_{23}$

$e_{xz} = 2e_{13}$, $\epsilon_{xz} = 2\epsilon_{13}$

$e_{xy} = 2e_{12}$, $\epsilon_{xy} = 2\epsilon_{12}$

Appendix C
FINITE ELEMENT EQUATIONS

The derivatives of the interpolation or shape functions with respect to global coordinates are given by:

$$ {}_0\psi^k_{,i} = \sum_{j=1}^{3} J^*_{ij} \frac{\partial \psi^k}{\partial \xi_j} \qquad (C.1) $$

where J^*_{ij} are components of the inverse of the Jacobian given in equation (5.36). The components of the deformation gradient are given by:

$$ {}^t_0x_{i,j} = \sum_{k=1}^{n} {}_0\psi^k_{,j}\, {}^tx^k_i \qquad (C.2) $$

where n is the number of nodes per element. The components of the displacement gradient are given by:

$$ {}^t_0u_{i,j} = \sum_{k=1}^{n} {}_0\psi^k_{,j}\, {}^tu^k_i \qquad (C.3) $$

The linear strain-displacement transformation matrix is given by [110]:

$$ [{}^t_0B_L] = [{}^t_0B_{L0}] + [{}^t_0B_{L1}] \qquad (C.4) $$

The $[{}^t_0B_{L0}]$ matrix is equal to the linear strain-displacement matrix used for geometrically linear analysis. The components of the $[{}^t_0B_{L0}]$ matrix are given by:

$$ [{}^t_0B_{L0}] = \begin{bmatrix} {}_0\psi^1_{,1} & 0 & 0 & {}_0\psi^2_{,1} & \cdots & 0 \\ 0 & {}_0\psi^1_{,2} & 0 & 0 & \cdots & 0 \\ 0 & 0 & {}_0\psi^1_{,3} & 0 & \cdots & {}_0\psi^n_{,3} \\ 0 & {}_0\psi^1_{,3} & {}_0\psi^1_{,2} & 0 & \cdots & {}_0\psi^n_{,2} \\ {}_0\psi^1_{,3} & 0 & {}_0\psi^1_{,1} & {}_0\psi^2_{,3} & \cdots & {}_0\psi^1_{,1} \\ {}_0\psi^1_{,2} & {}_0\psi^1_{,1} & 0 & {}_0\psi^2_{,2} & \cdots & 0 \end{bmatrix} \qquad (C.5) $$

The components of the $[{}^t_0B_{L1}]$ matrix are given by:

$$ [{}^t_0B_{L1}] = \begin{bmatrix} [{}^t_0\tilde{B}^{11}_{L1}] & [{}^t_0\tilde{B}^{12}_{L1}] & \cdots & [{}^t_0\tilde{B}^{1n}_{L1}] \\ [{}^t_0\tilde{B}^{21}_{L1}] & [{}^t_0\tilde{B}^{22}_{L1}] & \cdots & [{}^t_0\tilde{B}^{2n}_{L1}] \end{bmatrix} \qquad (C.6) $$

where the submatrices are defined as:

$$[{}^t_0\tilde{B}^{1k}_{L1}] = \begin{bmatrix} b_{11k1} & b_{21k1} & b_{31k1} \\ b_{12k2} & b_{22k2} & b_{32k2} \\ b_{13k3} & b_{23k3} & b_{33k3} \end{bmatrix} \tag{C.7}$$

$$[{}^t_0\tilde{B}^{2k}_{L1}] = \begin{bmatrix} (b_{12k3} + b_{13k2}) & (b_{22k3} + b_{23k2}) & (b_{32k3} + b_{33k2}) \\ (b_{11k3} + b_{13k1}) & (b_{21k3} + b_{23k1}) & (b_{31k3} + b_{33k1}) \\ (b_{11k2} + b_{12k1}) & (b_{21k2} + b_{31k2}) & (b_{22k1} + b_{33k1}) \end{bmatrix} \tag{C.8}$$

and:

$$b_{ijkl} = {}^t_0u_{i,j0}\psi^k_{,l}$$

The nonlinear strain-displacement transformation matrix is given by [110]:

$$[{}^t_0B_{NL}] = \begin{bmatrix} [{}^t_0\tilde{B}_{NL}] & [\tilde{0}] & [\tilde{0}] \\ [\tilde{0}] & [{}^t_0\tilde{B}_{NL}] & [\tilde{0}] \\ [\tilde{0}] & [\tilde{0}] & [{}^t_0\tilde{B}_{NL}] \end{bmatrix} \tag{C.9}$$

where the submatrices are defined as:

$$[{}^t_0\tilde{B}_{NL}] = \begin{bmatrix} {}_0\psi^1_{,1} & 0 & 0 & {}_0\psi^2_{,1} & \dots & {}_0\psi^n_{,1} \\ {}_0\psi^1_{,2} & 0 & 0 & {}_0\psi^2_{,2} & \dots & {}_0\psi^n_{,2} \\ {}_0\psi^1_{,3} & 0 & 0 & {}_0\psi^2_{,3} & \dots & {}_0\psi^n_{,3} \end{bmatrix} \tag{C.10}$$

$$[\tilde{0}] = \begin{bmatrix} 0 & 0 & 0 & 0 & \dots & 0 \\ 0 & 0 & 0 & 0 & \dots & 0 \\ 0 & 0 & 0 & 0 & \dots & 0 \end{bmatrix} \tag{C.11}$$

The second Piola-Kirchhoff stress matrix is given by [110]:

$$[{}^t_0S] = \begin{bmatrix} [{}^t_0\tilde{S}] & [\tilde{0}] & [\tilde{0}] \\ [\tilde{0}] & [{}^t_0\tilde{S}] & [\tilde{0}] \\ [\tilde{0}] & [\tilde{0}] & [{}^t_0\tilde{S}] \end{bmatrix} \tag{C.12}$$

where the submatrices are defined as:

$$[{}^t_0\tilde{S}] = \begin{bmatrix} {}^t_0S_{11} & {}^t_0S_{12} & {}^t_0S_{13} \\ {}^t_0S_{21} & {}^t_0S_{22} & {}^t_0S_{23} \\ {}^t_0S_{31} & {}^t_0S_{32} & {}^t_0S_{33} \end{bmatrix} \tag{C.13}$$

$$[\tilde{0}] = \begin{bmatrix} 0 & 0 & 0 \\ 0 & 0 & 0 \\ 0 & 0 & 0 \end{bmatrix} \tag{C.14}$$

The transpose of the second Piola-Kirchhoff stress vector is given by:

$$[{}^t_0\hat{S}]^T = [\,{}^t_0S_{11} \quad {}^t_0S_{22} \quad {}^t_0S_{33} \quad {}^t_0S_{23} \quad {}^t_0S_{13} \quad {}^t_0S_{12}\,] \tag{C.15}$$

Appendix D
FINITE ELEMENT MODELS

This appendix provides a summary of the finite element models used in this investigation. The finite element models are divided into three groups: (1) the global and local models for the thin 2.0 square symmetric and unsymmetric laminates, (2) the global models for the thick 4.0 in square symmetric and unsymmetric laminates which were used for comparison with previous results, and (3) the global models for the thin 2.0, 4.0, and 6.0 in. square unsymmetric laminates which were used for preliminary analyses. As discussed in Section 5.2.1, quarter symmetry models were used for the cross-ply laminates and inversion symmetry models [116] were used for the angle-ply and 0/+45 laminates. These symmetries were used to reduce the size of the numerical models.

The loading and boundary conditions used for the finite element models are summarized in Table D.1. The unsymmetric laminates are modeled completely through the thickness. For the geometrically nonlinear analysis of compression-loaded symmetric laminates which buckle out-of-plane, the laminates are modeled completely through the thickness. For the other symmetric laminates, the geometric midplane remains plane during loading and only the upper half of the laminate is modeled, $0 \leq z \leq +h/2$ (Figure 3.2). For thermal loading, inversion symmetry models had an additional constraint, $v(-0.2a, 0, 0) = 0$. This additional constraint was applied to remove the slight rigid body motion observed in the these models. This constraint worked well for the $[+45/-45]_t$ laminate, but a satisfactory constraint could not be determined for the $[0/+45]_t$ laminate. However, any error which may have been present in the model for the $[0/+45]_t$ laminate had no apparent adverse effect upon the predicted interlaminar stress field which contained no stress anomalies or irregularities.

A summary of the global and local finite element models for the 2.0 in. symmetric and unsymmetric laminates is given in Table D.2. A summary of the finite element models for the comparison with previous results and preliminary analyses is given in Table D.3. The finite element models for the comparison with previous results generated the numerical results of section 6.2. Prelimary analyses were conducted to evaluate such factors as finite element mesh refinement, laminate geometry, and geometrically nonlinear response. The preliminary finite element models were used to obtain numerical results for 2.0, 4.0, and 6.0 in. square unsymmetric laminates. The nonlinear solutions from the preliminary analyses provided accurate first approximations to the Newton algorithm for the more refined finite element models listed in Table D.2. The largest model used in this study was the local finite element model for inversion symmetry analysis (Table D.2). This model consisted of 1440 elements which resulted in 43518 equations requiring 313.5 megabytes of memory.

Plots for the finite element meshes or grids are shown in Figures D.1 through D.7. Only the quarter symmetry models are shown in these plots. Inversion symmetry models possesed the same mesh refinement used for the quarter symmetry models and extended from $-a \leq x \leq +a$ (refer to Figure 5.2). The 32-node cubic isoparametric element described in Section 5.1.1 was used for each of these models. For the thin laminates, one element was used through the thickness of each individual layer. For the thicker laminates which were used for comparison with previous results, two elements were used through the thickness of each individual layer. Since interlaminar stress comparisons were made between symmetric and unsymmetric laminates, identical mesh refinement was used all laminates. This was required since certain components of the interlaminar stress field can exhibit singular behavior. A convergence study of the interlaminar stress and displacement fields indicated that in order to achieve more accurate predictions, the maximum element aspect ratio for the three-dimensional elements should be kept to less than

or equal to 10.0. This requirement was satisfied for all models except for the 4.0 and 6.0 in. preliminary models in which a maximum element aspect ratio of 12.5 was used.

Appendix E
GEOMETRICALLY NONLINEAR PLATE ANALYSIS

This appendix discusses the geometrically nonlinear plate analysis which was formulated to predict the linear thermoelastic response of unsymmetrically laminated plates subjected to a uniform change in temperature. The analysis determines the approximate room-temperature shape of a cured unsymmetric laminate. The unsymmetric laminate was idealized as a linear thermoelastic solid which has been cooled from an assumed stress-free state at cure temperature to a residual stress state at room temperature. This analysis was used to provide an initial approximate displacement field for the geometrically nonlinear three-dimensional finite element analysis. The analysis was formulated using classical laminated plate (CLP) theory and the von Karman nonlinear strain-displacement equations (refer to Appendix A). Approximate solutions to the nonlinear boundary value problem were obtained using the Ritz method. The Ritz formulation yielded a system of nonlinear algebraic equations which were solved using Newton's method.

Assuming that the outer surfaces of the plate are traction free, the total potential energy of the laminated plate is given by:

$$\Pi = U_e = \int_{-a}^{+a}\int_{-b}^{+b}\int_{-h/2}^{+h/2}[S_{xx}(\epsilon_{xx} - \alpha_{xx}\Delta T)$$

$$+S_{yy}(\epsilon_{yy} - \alpha_{yy}\Delta T) + S_{xy}(\gamma_{xy} - \alpha_{xy}\Delta T)]dxdydz \qquad (E.1)$$

where:

$$S_{xx} = \bar{Q}_{11}(\epsilon_{xx} - \alpha_{xx}\Delta T) + \bar{Q}_{12}(\epsilon_{yy} - \alpha_{yy}\Delta T) + \bar{Q}_{16}(\gamma_{xy} - \alpha_{xy}\Delta T)$$

$$S_{yy} = \bar{Q}_{12}(\epsilon_{xx} - \alpha_{xx}\Delta T) + \bar{Q}_{22}(\epsilon_{yy} - \alpha_{yy}\Delta T) + \bar{Q}_{26}(\gamma_{xy} - \alpha_{xy}\Delta T)$$

$$S_{xy} = \bar{Q}_{16}(\epsilon_{xx} - \alpha_{xx}\Delta T) + \bar{Q}_{26}(\epsilon_{yy} - \alpha_{yy}\Delta T) + \bar{Q}_{66}(\gamma_{xy} - \alpha_{xy}\Delta T)$$

S_{xx}, S_{yy}, and S_{xy}, are second Piola-Kirchhoff stresses. α_{xx}, α_{yy}, α_{xy}, are coefficients of thermal expansion which vary from layer to layer (i.e., are dependent upon the z coordinate). The in-plane strains, ϵ_{xx}, ϵ_{yy}, and ϵ_{xy}, are defined in

equations (A.1) and (A.2). The transformed reduced lamina stiffness terms, $\bar{Q}_{ij}$, with respect to global coordinates (x, y, z) are also dependent upon the z coordinate and are defined in equations (B.9) and (B.10). The Ritz equations are obtained by taking the first variation of the total potential energy which yields a system of n nonlinear algebraic equations for n unknown displacement parameters, q_i:

$$\frac{\partial \Pi}{\partial q_i} = 0, \qquad i = 1, 2, ..., n \tag{E.2}$$

As discussed in section 4.8, the stability of each equilibrium configuration was determined by evaluating the second variation of the total potential energy of the elastic body:

$$K_{ij} = \frac{\delta^2 \Pi}{\delta q_i \delta q_j}, \qquad i, j = 1, 2, ..., n \tag{E.3}$$

The assumed displacement field for the geometrically nonlinear plate analysis has the following functional form:

$$u = q_1 x + q_2 y + q_3 x^3 + q_4 x^2 y + q_5 x y^2 + q_6 y^3 \tag{E.4a}$$

$$v = q_2 x + q_7 y + q_8 x^3 + q_9 x^2 y + q_{10} x y^2 + q_{11} y^3 \tag{E.4b}$$

$$w = q_{12} x^2 + q_{13} y^2 + q_{14} x y \tag{E.4c}$$

where $q_i, i = 1, 14$, are unknown displacement parameters. The displacement parameter q_2 is used for both the y coefficient in the expression for u and the x coefficient in the expression for v. The same coefficient was required in both expressions in order to obtain an independent set of equations. Kinematically, this forces the linear component of the shearing deformation of the reference surface to be uniform in the x and y directions. Hyer [48-50] proposed a similar geometrically nonlinear plate analysis for his study of the room-temperature shapes of unsymmetric cross-ply laminates. Hyer's Ritz analysis was also based upon CLP theory and the von Karman strain-displacement equations. Using assumptions based upon the kinematics of deformation for unsymmetric cross-ply laminates, Hyer derived

the following functional form in terms of four unknown displacement parameters, $q_i, i = 1,4$:

$$u = q_3 x - \frac{1}{6} q_1 x^3 - \frac{1}{4} q_1 q_2 x y^2 \qquad (E.2a)$$

$$v = q_4 y - \frac{1}{6} q_2 y^3 - \frac{1}{4} q_1 q_2 x^2 y \qquad (E.2b)$$

$$w \frac{1}{2}(q_1 x^2 + q_2 y^2) \qquad (E.5c)$$

A comparison between the theoretical predictions of the present nonlinear analysis and the nonlinear analysis formulated by Hyer is provided in Table E.1 and Figures E.1, E.2, and E.3. Numerical results were generated for square unsymmetrically laminated $[0_4/90_4]_t$ cross-ply laminates subjected to a uniform change in temperature ($\Delta T = -280°F$). Midplane w displacements were predicted for 2.0, 4.0, and 6.0 square laminated plates composed of T300/5208 graphite/epoxy (Table 3.1). The results compare the predictions of: (a) linear CLP theory, (b) the present linear 3D finite element analysis, (c) the nonlinear plate analysis proposed by Hyer [50], (d) the present nonlinear plate analysis, and (e) the present nonlinear 3D finite element analysis.

As discussed in Chapter 6, the out-of-plane (tranverse) w displacements predicted by linear theory are larger than those predicted by nonlinear theory. The linear predictions of the present 3D finite element analysis compare quite well with the predictions of CLP theory. The correlation between the predictions of the three nonlinear analyses is quite good. Each nonlinear analysis predicts that as the L/h ratio increases, the laminate transitions from a saddle to a cylindrical shape. Two stable equilibrium configurations are predicted by all three nonlinear analyses for 4.0 and 6.0 square plates at room temperature. The nonlinear predictions of the present plate analysis compare quite well with the predictions of the present 3D finite element analysis. There is a considerable difference in the nonlinear predictions for the 2.0 in. laminate between the present plate analysis and the plate

analysis proposed by Hyer. This difference may be attributed to the larger number of displacement parameters and more general functional form of the assumed displacement field used in the present plate analysis.

A comparison of experimental and theoretical principal curvatures for several square unsymmetric T300/5208 graphite/epoxy laminates at room temperature is provided in Table E.2. The experimental data was obtained from the previous work of Pagano and Hahn [46], Hyer [47], and Hahn [51]. The theoretical curvatures were determined using the present nonlinear plate analysis. All of the experimentally determined principal curvatures are greater than those predicted by the nonlinear plate analysis. The percent differences between experimental and theoretical maximum curvatures ranged from slightly less than 1 percent to almost 44 percent (Table E.2). The correlation between the experimental [47,51] and theoretical curvatures for the unsymmetric cross-ply laminates with lengths greater than 3.0 in. is fair (differences from 12 to 23 percent). The correlation for laminates with lengths less than 3.0 in. is not very good (differences from 27 to 44 percent). The correlation between the experimental [46] and theoretical curvatures for the unsymmetric angle-ply laminates is quite good (differences from 1 to 13 percent). Finally, the correlation between experiment [47] and theory for the $[0_4/+\theta_4]_t$ laminates is not very good (differences of approximately 30 percent). In addition, the correlation between the nonlinear predictions of the present plate analysis and the 3D finite element analysis is also not very good. This poor correlation for the $[0_4/+\theta_4]_t$ laminates may be an indication that the functional form of the displacement field is not very complete and additional displacement parameters may be required.

Appendix F

RESULTS USING REDUCED 3D NONLINEAR STRAIN

The geometrically nonlinear finite element analysis results presented in Chapter 6 were generated using the Green-Lagrange nonlinear strain tensor (using the tensorial notation of Chapter 4):

$$ {}_0^t E_{ij} = \frac{1}{2}({}_0^t u_{i,j} + {}_0^t u_{j,i} + {}_0^t u_{k,i} {}_0^t u_{k,j}) \qquad (F.1) $$

In the present study, numerical results were also generated using a reduced form of three-dimensional nonlinear strain defined as:

$$ {}_0^t E_{11}^R = {}_0^t u_{1,1} + \frac{1}{2} {}_0^t u_{3,1} {}_0^t u_{3,1} \qquad (F.2a) $$

$$ {}_0^t E_{22}^R = {}_0^t u_{2,2} + \frac{1}{2} {}_0^t u_{3,2} {}_0^t u_{3,2} \qquad (F.2b) $$

$$ {}_0^t E_{33}^R = {}_0^t u_{3,3} \qquad (F.2c) $$

$$ {}_0^t E_{23}^R = \frac{1}{2}({}_0^t u_{2,3} + {}_0^t u_{3,2}) \qquad (F.2d) $$

$$ {}_0^t E_{13}^R = \frac{1}{2}({}_0^t u_{1,3} + {}_0^t u_{3,1}) \qquad (F.2e) $$

$$ {}_0^t E_{12}^R = \frac{1}{2}({}_0^t u_{1,2} + {}_0^t u_{2,1} + {}_0^t u_{3,1} {}_0^t u_{3,2}) \qquad (F.2f) $$

where:

$$ {}^t u_i = {}^t u_i({}^0 x_1, {}^0 x_2, {}^0 x_3) $$

This reduced form of three-dimensional nonlinear strain retains the same nonlinear strain-displacement terms that are retained in von Karman plate theory [4], although in the present analysis no restrictions are placed upon the functional dependence of the out-of-plane (transverse) ${}^t u_3$ displacement. Numerical results were generated using this reduced form of 3D nonlinear strain in order to compare with the results generated using Green-Lagrange nonlinear strain. These comparisons were made in order to determine if this reduced form of 3D strain could accurately

predict for the geometrically nonlinear three-dimensional response of thin laminated plates.

For the purposes of comparison, three geometrically nonlinear finite element analyses were conducted using the reduced 3D nonlinear strain given in equations (F.2). Analyses were conducted for a 2.0 in. square unsymmetric $[0_4/90_4]_t$ laminate subjected to extensional, compressive, and thermal loading. A comparison of out-of-plane displacement and interlaminar stress predictions are given in Tables F.1 and F.2, respectively. The out-of-plane displacements predicted using the reduced form of 3D nonlinear strain compared quite well with the predictions of Green-Lagrange strain (less than one-half percent difference). The interlaminar stresses predicted using the reduced form of 3D nonlinear strain compared fairly well with the predictions of Green-Lagange strain. The maximum differences between the two interlaminar stress predictions were less than ten percent. In general, a nonlinear analysis using the reduced 3D nonlinear strain required less computations than a nonlinear analysis using Green-Lagrange strain. In summary, for the example cases considered, the predictions of the reduced form of 3D nonlinear strain compared fairly well with the predictions of Green-Lagrange nonlinear strain.

Table 3.1 Lamina material properties for T300/5208 graphite/epoxy.

Material Property	Value
E_1, psi	$26.25(10)^6$
E_2, psi	$1.49(10)^6$
E_3, psi	$1.49(10)^6$
G_{23}, psi	$0.502(10)^6$
G_{13}, psi	$1.04(10)^6$
G_{12}, psi	$1.04(10)^6$
ν_{23}	0.49
ν_{13}	0.28
ν_{12}	0.28
α_1, in. / (in.–°F)	$-0.059(10)^{-6}$
α_2, in. / (in.–°F)	$+14.222(10)^{-6}$
α_3, in. / (in.–°F)	$+14.222(10)^{-6}$
ply thickness, in.	0.005

Table 3.2 Square laminated plate geometry for comparisons between symmetric and unsymmetric laminates.

Laminate*	L, in.	h, in.	L/h
$[0_4/90_4]_t$	2.0	0.04	50
$[90_4/0_4]_s$	2.0	0.08	25
$[0_4/90_4]_s$	2.0	0.08	25
$[+45_4/-45_4]_t$	2.0	0.04	50
$[-45_4/+45_4]_s$	2.0	0.08	25
$[+45_4/-45_4]_s$	2.0	0.08	25
$[0_4/+45_4]_t$	2.0	0.04	50
$[+45_4/0_4]_s$	2.0	0.08	25
$[0_4/+45_4]_s$	2.0	0.08	25

* T300/5208 graphite/epoxy composite material system (Table 3.1).

Table 3.3 Loading and boundary conditions.

Loading-type	Loading and Boundary Conditions
Extensional	$u(\pm a, y, z)/a = \pm 0.01$
(clamped loaded edges*,	$v(\pm a, 0, 0) = 0$
free unloaded edges)	$w(\pm a, y, 0) = 0$
Compressive	$u(\pm a, y, z)/a = \mp 0.01$
(clamped loaded edges*,	$v(\pm a, 0, 0) = 0$
free unloaded edges)	$w(\pm a, y, 0) = 0$
Thermal	$\Delta T = -280°F$
(all surfaces free)	$u(0, 0, 0) = 0$
	$v(0, 0, 0) = 0$
	$w(0, 0, 0) = 0$

* Loosely clamped condition; plates are free to undergo Poisson deformation.

Table 3.4 Material property mismatch between adjacent layers.

Lamina Material Properties and Thermal Strain					
	Mechanical		Thermal*		
Layer	ν_{xy}	$\eta_{xy,x}$	$\alpha_x \Delta T$	$\alpha_y \Delta T$	$\alpha_{xy} \Delta T$
0	+0.280	0	$+0.016(10)^{-3}$	$-3.982(10)^{-3}$	0
90	+0.016	0	$-3.982(10)^{-3}$	$+0.016(10)^{-3}$	0
+45	+0.167	−0.768	$-1.983(10)^{-3}$	$-1.983(10)^{-3}$	$+3.999(10)^{-3}$
−45	+0.167	+0.768	$-1.983(10)^{-3}$	$-1.983(10)^{-3}$	$-3.999(10)^{-3}$

Difference or Mismatch Between Adjacent Layers					
	Mechanical		Thermal*		
Layers	ν_{xy}	$\eta_{xy,x}$	$\alpha_x \Delta T$	$\alpha_y \Delta T$	$\alpha_{xy} \Delta T$
0/90	+0.246	0	$+3.998(10)^{-3}$	$-3.998(10)^{-3}$	0
+45/−45	0	−1.536	0	0	$+7.998(10)^{-3}$
0/+45	+0.113	+0.768	$-1.999(10)^{-3}$	$-1.999(10)^{-3}$	$-3.999(10)^{-3}$

* $\Delta T = -280°F$.

Table 3.5 Unsymmetrically laminated plate stiffnesses.

Laminate	A_{11}	A_{22}	A_{12}	A_{66}	A_{16}	A_{26}
	Membrane stiffnesses A_{ij}, 10^3 pounds/in.					
$[0_4/90_4]_t$	+557.3	+557.3	+16.8	+41.6	0	0
$[+45_4/-45_4]_t$	+328.6	+328.6	+245.4	+270.3	0	0
$[0_4/+45_4]_t$	+691.7	+194.2	+131.1	+155.9	+124.4	+124.4
	Membrane-flexural stiffnesses B_{ij}, pounds					
Laminate	B_{11}	B_{22}	B_{12}	B_{66}	B_{16}	B_{26}
$[0_4/90_4]_t$	−4974	+4974	0	0	0	0
$[+45_4/-45_4]_t$	0	0	0	0	−2487	−2487
$[0_4/+45_4]_t$	+3630	+1344	+1143	+1143	+1244	+1244
	Flexural stiffnesses D_{ij}, pounds-in.					
Laminate	D_{11}	D_{22}	D_{12}	D_{66}	D_{16}	D_{26}
$[0_4/90_4]_t$	+74.3	+74.3	+2.2	+5.5	0	0
$[+45_4/-45_4]_t$	+43.8	+43.8	+32.7	+36.0	0	0
$[0_4/+45_4]_t$	+92.2	+25.9	+17.5	+20.8	+16.6	+16.6
	Reduced flexural stiffnesses D^*_{ij}, pounds-in.					
Laminate	D^*_{11}	D^*_{22}	D^*_{12}	D^*_{66}	D^*_{16}	D^*_{26}
$[0_4/90_4]_t$	+29.9	+29.9	+0.9	+5.5	0	0
$[+45_4/-45_4]_t$	+20.9	+20.9	+9.8	+14.5	0	0
$[0_4/+45_4]_t$	+44.5	+14.7	+7.3	+11.2	+8.7	+6.2

Table 3.6 Symmetrically laminated plate stiffnesses.

	Membrane stiffnesses A_{ij}, 10^3 pounds/in.					
Laminate	A_{11}	A_{22}	A_{12}	A_{66}	A_{16}	A_{26}
$[90_4/0_4]_s$	+1114.6	+1114.6	+33.5	+33.5	0	0
$[0_4/90_4]_s$	+1114.6	+1114.6	+33.5	+33.5	0	0
$[-45_4/+45_4]_s$	+657.2	+657.2	+490.8	+540.5	0	0
$[+45_4/-45_4]_s$	+657.2	+657.2	+490.8	+540.5	0	0
$[+45_4/0_4]_s$	+1383.3	+388.5	+262.2	+311.9	+248.7	+248.7
$[0_4/+45_4]_s$	+1383.3	+388.5	+262.2	+311.9	+248.7	+248.7

	Flexural stiffnesses D_{ij}, pounds-in.					
Laminate	D_{11}	D_{22}	D_{12}	D_{66}	D_{16}	D_{26}
$[90_4/0_4]_s$	+196.5	+992.4	+17.9	+44.4	0	0
$[0_4/90_4]_s$	+992.4	+196.5	+17.9	+44.4	0	0
$[-45_4/+45_4]_s$	+350.5	+350.5	+261.8	+288.3	−199.0	−199.0
$[+45_4/-45_4]_s$	+350.5	+350.5	+261.8	+288.3	+199.0	+199.0
$[+45_4/0_4]_s$	+447.3	+314.7	+231.3	+257.8	+232.1	+232.1
$[0_4/+45_4]_s$	+1028.2	+99.7	+48.4	+74.9	+33.2	+33.2

Table 3.7 Square unsymmetrically laminated plate geometry for preliminary analyses.

Laminate*	L, in.	h, in.	L/h
$[0_4/90_4]_t$	2.0	0.04	50
$[0_4/90_4]_t$	4.0	0.04	100
$[0_4/90_4]_t$	6.0	0.04	150
$[+45_4/-45_4]_t$	2.0	0.04	50
$[+45_4/-45_4]_t$	4.0	0.04	100
$[+45_4/-45_4]_t$	6.0	0.04	150
$[0_4/+45_4]_t$	2.0	0.04	50
$[0_4/+45_4]_t$	4.0	0.04	100
$[0_4/+45_4]_t$	6.0	0.04	150

* T300/5208 graphite/epoxy composite material system (Table 3.1).

Table 3.8 Lamina material properties for a typical graphite/epoxy composite material system.

Material Property	Value
E_1, psi	$20.0(10)^6$
E_2, psi	$2.1(10)^6$
E_3, psi	$2.1(10)^6$
G_{23}, psi	$0.85(10)^6$
G_{13}, psi	$0.85(10)^6$
G_{12}, psi	$0.85(10)^6$
ν_{23}	0.21
ν_{13}	0.21
ν_{12}	0.21
ply thickness, in.	0.005

Table 3.9 Square laminated plate geometry for comparisons with previous results.

Laminate*	L, in.	h, in.	L/h
$[0_{50}/90_{50}]_t$	4.0	0.5	8
$[90_{50}/0_{50}]_s$	4.0	1.0	4
$[0_{50}/90_{50}]_s$	4.0	1.0	4
$[+45_{50}/-45_{50}]_t$	4.0	0.5	8
$[-45_{50}/+45_{50}]_s$	4.0	1.0	4
$[+45_{50}/-45_{50}]_s$	4.0	1.0	4

* Typical graphite/epoxy composite material system (Table 3.8).

Table 5.1 Order of element interpolations.

Nodes per Element	Order of Interpolation		
	ξ_1	ξ_2	ξ_3
16	quadratic	quadratic	linear
20	quadratic	quadratic	quadratic
24	cubic	cubic	linear
32	cubic	cubic	cubic

Table 5.2 Comparison of tensorial and conventional notations.

Quantity	Tensorial	Conventional
Coordinates	x_1, x_2, x_3	x, y, z
Displacements	u_1, u_2, u_3	u, v, w
Linear normal strain	e_{11}, e_{22}, e_{33}	e_{xx}, e_{yy}, e_{zz}
Linear shear strain	$2e_{23}, 2e_{13}, 2e_{12}$	e_{yz}, e_{xz}, e_{xy}
Green-Lagrange normal strain	E_{11}, E_{22}, E_{33}	E_{xx}, E_{yy}, E_{zz}
Green-Lagrange shear strain	$2E_{23}, 2E_{13}, 2E_{12}$	E_{yz}, E_{xz}, E_{xy}
Cauchy normal stress	$\sigma_{11}, \sigma_{22}, \sigma_{33}$	$\sigma_{xx}, \sigma_{yy}, \sigma_{zz}$
Cauchy shear stress	$\sigma_{23}, \sigma_{13}, \sigma_{12}$	$\tau_{yz}, \tau_{xz}, \tau_{xy}$
2nd Piola-Kirchoff normal stress	S_{11}, S_{22}, S_{33}	S_{xx}, S_{yy}, S_{zz}
2nd Piola-Kirchoff shear stress	S_{23}, S_{13}, S_{12}	S_{yz}, S_{xz}, S_{xy}

Table 6.1 Effects of geometric nonlinearity upon the predicted out-of-plane w displacements for the unsymmetric laminates.

Effects of Geometric Nonlinearity (w displacements from nonlinear theory as compared to linear theory)		
Loading	w	Comments on Nonlinear Solution
Extensional	Smaller	Unique nonlinear solution
Compressive	Larger	Changes in mode shape predicted
Thermal	Smaller	Multiple stable shapes may exist

Table 6.2 Effects of laminate membrane-flexural coupling and geometric nonlinearity upon the predicted interlaminar stresses due to material property mismatch ($u/a = +0.01$).

Effects of Laminate Membrane-Flexural Coupling

(Stresses in unsymmetric laminates as compared to symmetric laminates.)

Property Mismatch Causing Stresses	Effect of Couping Upon S_{zz}	S_{yz}	S_{xz}
ν_{xy}	See below*	Smaller	0
$\eta_{xy,x}$	Larger	Vanishes	Smaller

Effects of Geometric Nonlinearity

(Stresses from nonlinear theory as compared to linear theory.**)

Property Mismatch Causing Stresses	Effect of Nonlinearity Upon S_{zz}	S_{yz}	S_{xz}
ν_{xy}	Smaller	Larger	0
$\eta_{xy,x}$	Smaller	0	Larger

* Depending upon symmetric laminate stacking sequence, smaller or much larger.

** Comparison of stresses in unsymmetric laminates only.

Table 6.3 Effects of laminate membrane-flexural coupling and geometric nonlinearity upon the predicted interlaminar stresses due to material property mismatch ($u/a = -0.0005$, before a change in mode shape occurs).

Effects of Laminate Membrane-Flexural Coupling

(Stresses in unsymmetric laminates as compared to symmetric laminates.)

Property Mismatch Causing Stresses	Effect of Coupling Upon S_{xz}	S_{yz}	S_{zz}
ν_{xy}	See below*	Smaller	0
$\eta_{xy,x}$	Larger	Vanishes	Smaller

Effects of Geometric Nonlinearity

(Stresses from nonlinear theory as compared to linear theory.**)

Property Mismatch Causing Stresses	Effect of Nonlinearity Upon S_{xz}	S_{yz}	S_{zz}
ν_{xy}	Negligible	Negligible	0
$\eta_{xy,x}$	Negligible	0	Negligible

* Depending upon symmetric laminate stacking sequence, smaller or much larger.

** Comparison of stresses in unsymmetric laminates only.

Table 6.4 Effects of laminate membrane-flexural coupling and geometric nonlinearity upon the predicted interlaminar stresses due to material property mismatch ($\Delta T = -280\,^{\circ}F$).

Effects of Laminate Membrane-Flexural Coupling

(Stresses in unsymmetric laminates as compared to symmetric laminates.)

Property Mismatch Causing Stresses	Stress Location	Effect of Coupling Upon S_{zz}	S_{yz}	S_{xz}
α_x	$y = 0$	See below*	0	Smaller
α_y	$x = 0$	See below*	Smaller	0
α_{xy}	$y = 0$	Larger	Smaller	Vanishes
α_{xy}	$x = 0$	Larger	Vanishes	Smaller

Effects of Geometric Nonlinearity

(Stresses from nonlinear theory as compared to linear theory.**)

Property Mismatch Causing Stresses	Stress Location	Effect of Nonlinearity Upon S_{zz}	S_{yz}	S_{xz}
α_x	$y = 0$	Larger	0	Larger
α_y	$x = 0$	Larger	Larger	0
α_{xy}	$y = 0$	Smaller	Smaller	0
α_{xy}	$x = 0$	Smaller	0	Smaller

* Depending upon symmetric laminate stacking sequence, smaller or much larger.

** Comparison of stresses in unsymmetric laminates only.

Table 6.5 Midplane w/h displacement extrema for the thick 4.0 in. square unsymmetric laminates ($u/a = +0.01$).

		Linear		Nonlinear	
Laminate*	L/h	$(w/h)_{min}$	$(w/h)_{max}$	$(w/h)_{min}$	$(w/h)_{max}$
$[0_{50}/90_{50}]_t$	8	−0.0070	+0.0029	−0.0062	+0.0024
$[+45_{50}/-45_{50}]_t$	8	−0.0063	+0.0063	−0.0061	+0.0061

* Typical graphite/epoxy composite material system (Table 3.8).

Table 6.6 Interlaminar stresses* along $x = 0$ at the 0/90 interface for the thick 4.0 in. square $0_{50}/90_{50}$ laminates ($u/a = +0.01$).

Linear Results (Cauchy stress, psi)

Laminate**	$(\sigma_{zz})_{min}$	$(\sigma_{zz})_{max}$	$(\tau_{yz})_{min}$	$(\tau_{yz})_{max}$	$(\tau_{zz})_{min}$	$(\tau_{zz})_{max}$
$[0_{50}/90_{50}]_t$	−236	+2618	0	+1407	−3	+8
$[90_{50}/0_{50}]_s$	−781	+715	0	+1793	0	0
$[0_{50}/90_{50}]_s$	−314	+3114	−1667	0	0	0

Nonlinear Results (second Piola-Kirchhoff stress, psi)

Laminate**	$(S_{zz})_{min}$	$(S_{zz})_{max}$	$(S_{yz})_{min}$	$(S_{yz})_{max}$	$(S_{zz})_{min}$	$(S_{zz})_{max}$
$[0_{50}/90_{50}]_t$	−255	+2583	0	+1413	−2	+6
$[90_{50}/0_{50}]_s$	−782	+732	0	+1802	0	0
$[0_{50}/90_{50}]_s$	−315	+3137	−1673	0	0	0

* Gauss point stress extrema from global finite element analysis.

** Typical graphite/epoxy composite material system (Table 3.8).

Table 6.7 Interlaminar stresses* along $x = 0$ at the +45/–45 interface for the thick 4.0 in. square $+45_{50}/-45_{50}$ laminates ($u/a = +0.01$).

Linear Results (Cauchy stress, psi)

Laminate**	$(\sigma_{zz})_{min}$	$(\sigma_{zz})_{max}$	$(\tau_{yz})_{min}$	$(\tau_{yz})_{max}$	$(\tau_{zz})_{min}$	$(\tau_{zz})_{max}$
$[+45_{50}/-45_{50}]_t$	–5700	+529	0	+3	0	+14476
$[-45_{50}/+45_{50}]_s$	–4610	+447	–146	+46	–8	+15443
$[+45_{50}/-45_{50}]_s$	–4610	+447	–146	+46	–15443	+8

Nonlinear Results (second Piola-Kirchhoff stress, psi)

Laminate**	$(S_{zz})_{min}$	$(S_{zz})_{max}$	$(S_{yz})_{min}$	$(S_{yz})_{max}$	$(S_{zz})_{min}$	$(S_{zz})_{max}$
$[+45_{50}/-45_{50}]_t$	–5620	+533	0	+3	0	+14627
$[-45_{50}/+45_{50}]_s$	–4567	+444	–150	+47	–8	+15537
$[+45_{50}/-45_{50}]_s$	–4567	+444	–150	+47	–15537	+8

* Gauss point stress extrema from global finite element analysis.

** Typical graphite/epoxy composite material system (Table 3.8).

Table 6.8 Midplane w/h displacement extrema for the 2.0, 4.0, and 6.0 in. square unsymmetric laminates ($u/a = +0.01$).

		Linear		Nonlinear	
Laminate	L/h	$(w/h)_{min}$	$(w/h)_{max}$	$(w/h)_{min}$	$(w/h)_{max}$
$[0_4/90_4]_t$	50	−0.205	+0.080	−0.060	+0.012
	100	−0.807	+0.316	−0.128	+0.027
	150	−1.810	+0.709	−0.196	+0.042
$[+45_4/-45_4]_t$	50	−0.015	+0.015	−0.012	+0.012
	100	−0.015	+0.015	−0.013	+0.013
	150	−0.015	+0.015	−0.013	+0.013
$[0_4/+45_4]_t$	50	−0.022	+0.037	−0.006	+0.020
	100	−0.063	+0.165	−0.016	+0.045
	150	−0.123	+0.385	−0.017	+0.069

Table 6.9 Interlaminar stresses* along $x = 0$ at the 0/90 interface for the 2.0 in. square $0_4/90_4$ laminates ($u/a = +0.01$).

Linear Results (Cauchy stress, psi)						
Laminate	$(\sigma_{zz})_{min}$	$(\sigma_{zz})_{max}$	$(\tau_{yz})_{min}$	$(\tau_{yz})_{max}$	$(\tau_{zz})_{min}$	$(\tau_{zz})_{max}$
$[0_4/90_4]_t$	−307	+3230	0	+1194	0	+4
$[90_4/0_4]_s$	−892	+998	−2	+1688	0	0
$[0_4/90_4]_s$	−338	+3523	−1478	0	0	0

Nonlinear Results (second Piola-Kirchhoff stress, psi)						
Laminate	$(S_{zz})_{min}$	$(S_{zz})_{max}$	$(S_{yz})_{min}$	$(S_{yz})_{max}$	$(S_{zz})_{min}$	$(S_{zz})_{max}$
$[0_4/90_4]_t$	−312	+3223	0	+1209	0	+1
$[90_4/0_4]_s$	−894	+1015	−2	+1696	0	0
$[0_4/90_4]_s$	−338	+3543	−1483	0	0	0

* Gauss point stress extrema from local finite element analysis.

Table 6.10 Interlaminar stresses* along $x = 0$ at the +45/–45 interface for the 2.0 in. square $+45_4/-45_4$ laminates ($u/a = +0.01$).

Linear Results (Cauchy stress, psi)

Laminate	$(\sigma_{zz})_{min}$	$(\sigma_{zz})_{max}$	$(\tau_{yz})_{min}$	$(\tau_{yz})_{max}$	$(\tau_{zz})_{min}$	$(\tau_{zz})_{max}$
$[+45_4/-45_4]_t$	–3098	+319	0	0	0	+15593
$[-45_4/+45_4]_s$	–2465	+377	–283	+90	0	+15632
$[+45_4/-45_4]_s$	–2465	+377	–283	+90	–15632	0

Nonlinear Results (second Piola-Kirchhoff stress, psi)

Laminate	$(S_{zz})_{min}$	$(S_{zz})_{max}$	$(S_{yz})_{min}$	$(S_{yz})_{max}$	$(S_{zz})_{min}$	$(S_{zz})_{max}$
$[+45_4/-45_4]_t$	–2991	+316	0	0	0	+15682
$[-45_4/+45_4]_s$	–2321	+375	–293	+94	0	+15719
$[+45_4/-45_4]_s$	–2321	+375	–293	+94	–15719	0

* Gauss point stress extrema from local finite element analysis.

Table 6.11 Interlaminar stresses* along $x = 0$ at the 0/+45 interface for the 2.0 in. square $0_4/+45_4$ laminates ($u/a = +0.01$).

Linear Results (Cauchy stress, psi)						
Laminate	$(\sigma_{zz})_{min}$	$(\sigma_{zz})_{max}$	$(\tau_{yz})_{min}$	$(\tau_{yz})_{max}$	$(\tau_{zz})_{min}$	$(\tau_{zz})_{max}$
$[0_4/+45_4]_t$	−1020	+110	−255	0	−7510	0
$[+45_4/0_4]_s$	−571	+211	−408	0	−7556	+1
$[0_4/+45_4]_s$	−1017	+55	0	+299	0	+7605

Nonlinear Results (second Piola-Kirchhoff stress, psi)						
Laminate	$(S_{zz})_{min}$	$(S_{zz})_{max}$	$(S_{yz})_{min}$	$(S_{yz})_{max}$	$(S_{zz})_{min}$	$(S_{zz})_{max}$
$[0_4/+45_4]_t$	−1047	+118	−269	0	−7558	0
$[+45_4/0_4]_s$	−544	+224	−431	0	−7654	0
$[0_4/+45_4]_s$	−1030	+56	0	+316	0	+7709

* Gauss point stress extrema from local finite element analysis.

Table 6.12 Midplane w/h displacement extrema for the 2.0, 4.0, and 6.0 in. square symmetric and unsymmetric laminates ($u/a = -0.01$).

		Linear		Nonlinear	
Laminate	L/h	$(w/h)_{min}$	$(w/h)_{max}$	$(w/h)_{min}$	$(w/h)_{max}$
$[0_4/90_4]_t$	50	–0.080	+0.205	0.000	+3.106
	100	–0.316	+0.807	0.000	+6.307
	150	–0.709	+1.810	0.000	+9.946
$[90_4/0_4]_s$	25	–0.000	+0.000	–1.455	+0.008
$[0_4/90_4]_s$	25	–0.000	+0.000	–0.861	+0.014
$[+45_4/-45_4]_t$	50*	–0.015	+0.015	–3.099	+0.006
	100*	–0.015	+0.015	–6.391	+0.000
	150*	–0.015	+0.015	–9.601	+0.000
$[0_4/+45_4]_t$	50	–0.037	+0.022	–0.006	+3.183
	100	–0.165	+0.063	–0.000	+6.440
	150	–0.385	+0.123	–0.000	+9.653

* This is one of the two stable nonlinear solutions.

Table 6.13 Critical compressive edge displacements at which a change in mode shape occurs for the 2.0 in. square symmetric and unsymmetric laminates.

Laminate	L/h	Predicted Critical Values N_x^{*a}	N_x^{*b}	N_x^{*c}	u/a^c
$[0_4/90_4]_t$	50	–753	–295	–291	–0.00054
$[90_4/0_4]_s$	25	–1939	–1939	–1857	–0.00167
$[0_4/90_4]_s$	25	–9795	–9795	–7912	–0.00714
$[+45_4/-45_4]_t$	50	–432	–207	–193	–0.00134
$[0_4/+45_4]_t$	50	–910	–439	–422	–0.00080

* Average critical membrane stress resultant N_x, pounds/in.

[a] Wide-column theory for an orthotropic beam.

[b] Wide-column theory with reduced flexural stiffness approximation.

[c] Nonlinear three-dimensional finite element analysis.

Table 6.14 Interlaminar stresses* at the 0/90 interface for the 2.0 in. square $0_4/90_4$ laminates ($u/a = -0.01$).

Linear Results** (Cauchy stress, psi)							
Laminate	(z/h)	$(\sigma_{zz})_{min}$	$(\sigma_{zz})_{max}$	$(\tau_{yz})_{min}$	$(\tau_{yz})_{max}$	$(\tau_{zz})_{min}$	$(\tau_{zz})_{max}$
$[0_4/90_4]_t$	+0.00	−2805	+317	−1123	0	−9	+1
$[90_4/0_4]_s$	+0.25	−627	+975	−1686	+5	0	0
$[0_4/90_4]_s$	+0.25	−3101	+343	−1498	0	0	0

Nonlinear Results (second Piola-Kirchhoff stress, psi)							
Laminate	(z/h)	$(S_{zz})_{min}$	$(S_{zz})_{max}$	$(S_{yz})_{min}$	$(S_{yz})_{max}$	$(S_{zz})_{min}$	$(S_{zz})_{max}$
$[0_4/90_4]_t$	+0.00	−1603	+737	−396	+297	−1584	+1514
$[90_4/0_4]_s$	−0.25	−1289	+370	−536	+1387	0	+2575
$[90_4/0_4]_s$	+0.25	−1294	+376	−1392	+533	0	+2575
$[0_4/90_4]_s$	−0.25	−7504	+270	−2236	+45	0	+14188
$[0_4/90_4]_s$	+0.25	−7511	+270	−44	+2241	0	+14188

* Gauss point stress extrema from global finite element analysis.

** Linear stress extrema are given along $x = 0$ only.

Table 6.15 Interlaminar stresses* at the +45/−45 interface for a 2.0 in. square unsymmetric $[+45_4/-45_4]_t$ laminate ($u/a = -0.01$).

Linear Results** (Cauchy stress, psi)

Laminate	$(\sigma_{zz})_{min}$	$(\sigma_{zz})_{max}$	$(\tau_{yz})_{min}$	$(\tau_{yz})_{max}$	$(\tau_{zz})_{min}$	$(\tau_{zz})_{max}$
$[+45_4/-45_4]_t$	−398	+2578	0	0	−15197	0

Nonlinear Results (second Piola-Kirchhoff stress, psi)

Laminate	$(S_{zz})_{min}$	$(S_{zz})_{max}$	$(S_{yz})_{min}$	$(S_{yz})_{max}$	$(S_{zz})_{min}$	$(S_{zz})_{max}$
$[+45_4/-45_4]_t$	−18774	+19152	−6954	+2468	−36705	+29241

* Gauss point stress extrema from global finite element analysis.

** Linear stress extrema are given along $x = 0$ only.

Table 6.16 Interlaminar stresses* at the 0/+45 interface for a 2.0 in. square unsymmetric $[0_4/+45_4]_t$ laminate ($u/a = -0.01$).

Linear Results** (Cauchy stress, psi)						
Laminate	$(\sigma_{zz})_{min}$	$(\sigma_{zz})_{max}$	$(\tau_{yz})_{min}$	$(\tau_{yz})_{max}$	$(\tau_{zz})_{min}$	$(\tau_{zz})_{max}$
$[0_4/+45_4]_t$	−115	+850	0	+249	0	+7196

Nonlinear Results (second Piola-Kirchhoff stress, psi)						
Laminate	$(S_{zz})_{min}$	$(S_{zz})_{max}$	$(S_{yz})_{min}$	$(S_{yz})_{max}$	$(S_{zz})_{min}$	$(S_{zz})_{max}$
$[0_4/+45_4]_t$	−15712	+2165	−8160	+16574	−13887	+36648

* Gauss point stress extrema from global finite element analysis.

** Linear stress extrema are given along $x = 0$ only.

Table 6.17 Midplane w/h displacement extrema for the 2.0, 4.0, and 6.0 in. square unsymmetric laminates ($\Delta T = -280\,°F$).

		Linear		Nonlinear	
Laminate	L/h	$(w/h)_{min}$	$(w/h)_{max}$	$(w/h)_{min}$	$(w/h)_{max}$
$[0_4/90_4]_t$	50	−0.946	+0.946	−0.742	+0.742
	100*	−3.781	+3.781	−0.577	+3.195
	150*	−8.505	+8.505	−0.166	+8.081
$[+45_4/-45_4]_t$	50	−1.910	+1.910	−1.642	+1.642
	100*	−7.597	+7.597	−2.620	+6.981
	150*	−17.063	+17.063	−2.466	+17.151
$[0_4/+45_4]_t$	50	−1.203	+1.191	−1.065	+1.012
	100	−4.787	+4.762	−3.354	+2.009
	150*	−10.752	+10.714	−9.166	+0.699

* This is one of the two stable nonlinear solutions.

Table 6.18 Interlaminar stresses* along $x = 0$ and $y = 0$ at the 0/90 interface for the 2.0 in. square $0_4/90_4$ laminates ($\Delta T = -280°F$).

Linear Results (Cauchy stress, psi)

Laminate	location	$(\sigma_{zz})_{min}$	$(\sigma_{zz})_{max}$	$(\tau_{yz})_{min}$	$(\tau_{yz})_{max}$	$(\tau_{zx})_{min}$	$(\tau_{zx})_{max}$
$[0_4/90_4]_t$	$x = 0$	−456	+4877	-1	+1728	0	0
$[0_4/90_4]_t$	$y = 0$	−456	+4877	0	0	−1728	+1
$[90_4/0_4]_s$	$x = 0$	−1306	+1461	−3	+2471	0	0
$[90_4/0_4]_s$	$y = 0$	−494	+5156	0	0	−2163	0
$[0_4/90_4]_s$	$x = 0$	−494	+5156	−2163	0	0	0
$[0_4/90_4]_s$	$y = 0$	−1306	+1461	0	0	−3	+2471

Nonlinear Results (second Piola-Kirchhoff stress, psi)

Laminate	location	$(S_{zz})_{min}$	$(S_{zz})_{max}$	$(S_{yz})_{min}$	$(S_{yz})_{max}$	$(S_{zx})_{min}$	$(S_{zx})_{max}$
$[0_4/90_4]_t$	$x = 0$	−466	+4975	0	+1790	−1	+1
$[0_4/90_4]_t$	$y = 0$	−466	+4975	−1	+1	−1790	0
$[90_4/0_4]_s$	$x = 0$	−1301	+1489	−3	+2470	0	0
$[90_4/0_4]_s$	$y = 0$	−492	+5165	0	0	−2160	0
$[0_4/90_4]_s$	$x = 0$	−492	+5165	−2160	0	0	0
$[0_4/90_4]_s$	$y = 0$	−1301	+1489	0	0	−3	+2470

* Gauss point stress extrema from local finite element analysis.

Table 6.19 Interlaminar stresses* along $x = 0$ and $y = 0$ at the +45/−45 interface for the 2.0 in. square $+45_4/-45_4$ laminates ($\Delta T = -280°F$).

Linear Results (Cauchy stress, psi)

Laminate	location	$(\sigma_{zz})_{min}$	$(\sigma_{zz})_{max}$	$(\tau_{yz})_{min}$	$(\tau_{yz})_{max}$	$(\tau_{zx})_{min}$	$(\tau_{zx})_{max}$
$[+45_4/-45_4]_t$	$x = 0$	−531	+4814	0	0	−3984	+2
$[+45_4/-45_4]_t$	$y = 0$	−531	+4814	−3984	0	0	0
$[-45_4/+45_4]_s$	$x = 0$	−133	+868	−32	+99	−5500	0
$[-45_4/+45_4]_s$	$y = 0$	−133	+868	−5500	0	−32	+99
$[+45_4/-45_4]_s$	$x = 0$	−133	+868	−31	+99	0	+5500
$[+45_4/-45_4]_s$	$y = 0$	−133	+868	0	+5500	−32	+99

Nonlinear Results (second Piola-Kirchhoff stress, psi)

Laminate	location	$(S_{zz})_{min}$	$(S_{zz})_{max}$	$(S_{yz})_{min}$	$(S_{yz})_{max}$	$(S_{zx})_{min}$	$(S_{zx})_{max}$
$[+45_4/-45_4]_t$	$x = 0$	−440	+3997	0	+1	−2807	0
$[+45_4/-45_4]_t$	$y = 0$	−440	+3997	−2807	0	−1	0
$[-45_4/+45_4]_s$	$x = 0$	−133	+887	−31	+98	−5499	0
$[-45_4/+45_4]_s$	$y = 0$	−133	+887	−5499	0	−31	+98
$[+45_4/-45_4]_s$	$x = 0$	−133	+887	−31	+98	0	+5499
$[+45_4/-45_4]_s$	$y = 0$	−133	+887	0	+5499	−31	+98

* Gauss point stress extrema from local finite element analysis.

Table 6.20 Interlaminar stresses* along $x = 0$ and $y = 0$ at the 0/+45 interface for the 2.0 in. square $0_4/+45_4$ laminates ($\Delta T = -280°F$).

Linear Results (Cauchy stress, psi)

Laminate	location	$(\sigma_{zz})_{min}$	$(\sigma_{zz})_{max}$	$(\tau_{yz})_{min}$	$(\tau_{yz})_{max}$	$(\tau_{zx})_{min}$	$(\tau_{zx})_{max}$
$[0_4/+45_4]_t$	$x = 0$	−222	+1940	0	+836	0	+1785
$[0_4/+45_4]_t$	$y = 0$	−325	+3213	−9	+2035	−568	+1
$[+45_4/0_4]_s$	$x = 0$	−616	+183	−2	+1158	0	+2622
$[+45_4/0_4]_s$	$y = 0$	−144	+1402	−7	+3310	−903	0
$[0_4/+45_4]_s$	$x = 0$	−228	+1912	−1032	0	−2789	0
$[0_4/+45_4]_s$	$y = 0$	−449	+146	−3231	+4	0	+1005

Nonlinear Results (second Piola-Kirchhoff stress, psi)

Laminate	location	$(S_{zz})_{min}$	$(S_{zz})_{max}$	$(S_{yz})_{min}$	$(S_{yz})_{max}$	$(S_{zx})_{min}$	$(S_{zx})_{max}$
$[0_4/+45_4]_t$	$x = 0$	−212	+1853	0	+820	0	+1654
$[0_4/+45_4]_t$	$y = 0$	−305	+3086	0	+1651	−819	0
$[+45_4/0_4]_s$	$x = 0$	−615	+183	−2	+1158	0	+2623
$[+45_4/0_4]_s$	$y = 0$	−144	+1414	−7	+3308	−903	0
$[0_4/+45_4]_s$	$x = 0$	−227	+1916	−1031	0	−2788	0
$[0_4/+45_4]_s$	$y = 0$	−499	+160	−3232	+4	0	+1005

* Gauss point stress extrema from local finite element analysis.

Table A.1 The coupling behavior of laminated anisotropic plates.

Deformation	Stiffness Term	Laminate Coupling
Membrane	A_{16}, A_{26}	Extension-Shear
Membrane-Flexural	B_{11}, B_{22}, B_{12}	Extension-Bending
	B_{16}, B_{26}	Extension-Twisting, Shear-Bending
	B_{66}	Shear-Twisting
Flexural	D_{16}, D_{26}	Bending-Twisting

Table D.1 Loading and boundary conditions for finite element models.

Loading-type	Quarter Symmetry	Inversion Symmetry
Extensional	$u(0,y,z) = 0$	$u(0,0,z) = 0$
(clamped loaded edges*,	$v(x,0,z) = 0$	$v(0,0,z) = 0$
free unloaded edges)	$w(+a,y,0) = 0^u$	$w(\pm a,y,0) = 0^u$
$u(\pm a,y,z)/a = \pm 0.01$	$w(x,y,0) = 0^s$	$w(x,y,0) = 0^s$
Compressive	$u(0,y,z) = 0$	$u(0,0,z) = 0$
(clamped loaded edges*,	$v(x,0,z) = 0$	$v(0,0,z) = 0$
free unloaded edges)	$w(+a,y,0) = 0^c$	$w(\pm a,y,0) = 0^c$
$u(\pm a,y,z)/a = \mp 0.01$		
Thermal	$u(0,y,z) = 0$	$u(0,0,z) = 0$
(all surfaces free)	$v(x,0,z) = 0$	$v(0,0,z) = 0$
$\Delta T = -280°F$	$w(0,0,0) = 0^u$	$w(0,0,0) = 0^u$
	$w(x,y,0) = 0^s$	$w(x,y,0) = 0^s$
		$v(-0.2a,0,0) = 0$

* Loosely clamped condition; plates are free to undergo Poisson deformation.

[u] Boundary condition for unsymmetric laminates.

[s] Boundary condition for symmetric laminates.

[c] For linear analysis of compression-loaded symmetric laminates, $w(x,y,0) = 0$.

Table D.2 Summary of global and local finite element models.

Summary of Global Models

Elements (x,y,z)	Model Symmetry*	Nodes	Equations	Mean SBW**	Memory (Mbytes)
450 (15,15,2)	QS	4672	13611	861	94.2
900 (15,15,4)	QS	8128	23668	1416	269.8
900 (30,15,2)	IS	9142	26825	1308	281.8

Summary of Local Models

Elements (x,y,z)	Model Symmetry*	Nodes	Equations	Mean SBW**	Memory (Mbytes)
750 (25,15,2)	QS	7652	22754	896	162.1
1440 (48,15,2)	IS	14506	43518	896	313.5

* QS = quarter symmetry, IS = inversion symmetry

** SBW = semi-bandwith

Table D.3 Summary of finite element models for comparisons with previous results and preliminary analyses.

Models for Comparisons with Previous Results

Elements (x,y,z)	Model Symmetry*	Nodes	Equations	Mean SBW**	Memory (Mbytes)
432 (9,12,4)	QS	4060	11634	1111	103.9
864 (18,12,4)	IS	7831	22773	1596	291.7

Models for Preliminary Analyses

Elements (x,y,z)	Model Symmetry*	Nodes	Equations	Mean SBW**	Memory (Mbytes)
128 (8,8,2)	QS	1431	4070	493	16.3
288 (12,12,2)	QS	3055	8838	688	49.0
512 (16,16,2)	QS	5287	15430	918	113.4
256 (16,8,2)	IS	2751	7923	706	45.0
576 (24,12,2)	IS	5947	17357	1050	145.9
1024 (32,16,2)	IS	10359	30437	1394	339.7

* QS = quarter symmetry, IS = inversion symmetry

** SBW = semi-bandwith

Table E.1 Comparison of midplane w/h displacement extrema predictions for 2.0, 4.0, and 6.0 in. square unsymmetric $[0_4/90_4]_t$ laminates* ($\Delta T = -280°F$).

L, in.	Analysis	$(w/h)_{min}$	$(w/h)_{max}$
2.0 ($L/h = 50$)	Linear CLP theory	–0.945	+0.945
	Linear 3D FEM	–0.946	+0.946
	Hyer [50]	–0.619	+0.619
	Nonlinear plate theory	–0.723	+0.723
	Nonlinear 3D FEM	–0.742	+0.742
4.0 ($L/h = 100$)	Linear CLP theory	–3.779	+3.779
	Linear 3D FEM	–3.781	+3.781
	Hyer [50]**	–0.226	+3.440
	Nonlinear plate theory**	–0.591	+3.074
	Nonlinear 3D FEM**	–0.577	+3.195
6.0 ($L/h = 150$)	Linear CLP theory	–8.503	+8.503
	Linear 3D FEM	–8.505	+8.505
	Hyer [50]**	–0.095	+8.152
	Nonlinear plate theory**	–0.227	+8.092
	Nonlinear 3D FEM**	–0.166	+8.081

* T300/5208 graphite/epoxy material system (Table 3.1).

** One of two possible stable equilibrium configurations.

Table E.2 Comparison of experimental and theoretical curvatures for several square unsymmetric laminates ($\Delta T = -280\,^{\circ}F$).

		Experimental			Theoretical**		
Laminate*	L, in.	κ_1, in.$^{-1}$	κ_2, in.$^{-1}$	ϕ, deg.	κ_1, in.$^{-1}$	κ_2, in.$^{-1}$	ϕ, deg.
$[0_2/90_2]_t$[a]	4.00	–0.1758	–0.0059	2°	–0.1454	+0.0013	0°
$[0_2/90_2]_t$[a]	6.00	–0.1902	+0.0000	0°	–0.1464	+0.0002	0°
$[0_4/90_4]_t$[b]	1.33	–0.1239	+0.1210	0°	–0.0696	+0.0696	0°
$[0_4/90_4]_t$[b]	2.66	–0.0641	+0.0458	0°	–0.0467	+0.0467	0°
$[0_4/90_4]_t$[b]	5.32	–0.0833	+0.0000	0°	–0.0700	+0.0033	0°
$[0_4/90_4]_t$[b]	10.63	–0.0833	+0.0000	0°	–0.0731	+0.0002	0°
$[+15_4/-15_4]_t$[c]	3.00	–0.0430	+0.0430	+45°	–0.0373	+0.0373	+45°
$[+30_4/-30_4]_t$[c]	3.00	–0.0498	+0.0498	+45°	–0.0453	+0.0453	+45°
$[+45_4/-45_4]_t$[c]	3.00	–0.0477	+0.0477	+45°	–0.0473	+0.0473	+45°
$[0_4/+30_4]_t$[a]	4.00	–0.0400	+0.0292	−27°	–0.0284	+0.0284	−30°
$[0_4/+60_4]_t$[a]	4.00	–0.0617	+0.0220	−13°	–0.0427	+0.0230	−17°

* T300/5208 graphite/epoxy material system (Table 3.1).

** Geometrically nonlinear plate analysis.

[a] Hyer [47]

[b] Hahn [51]

[c] Pagano and Hahn [46]

Table F.1 Comparison of midplane w/h displacement extrema predictions between Green-Lagrange and reduced 3D nonlinear strain for a 2.0 in. square unsymmetric $[0_4/90_4]_t$ laminate.

Loading	Strain	$(w/h)_{min}$	$(w/h)_{max}$
Extension	Green-Lagrange	–0.060253	+0.012169
$(u/a = +0.01)$	Reduced 3D	–0.060404	+0.012223
Compression	Green-Lagrange	0.000000	+3.105609
$(u/a = -0.01)$	Reduced 3D	0.000000	+3.116095
Thermal	Green-Lagrange	–0.741869	+0.741869
$(\Delta T = -280°F)$	Reduced 3D	–0.740636	+0.740636

Table F.2 Comparison of interlaminar stress* predictions between Green-Lagrange and reduced 3D nonlinear strain for a 2.0 in. square unsymmetric $[0_4/90_4]_t$ laminate.

Extensional Loading ($u/a = +0.01$)

(Second Piola-Kirchhoff stresses**, psi)

Strain	$(S_{zz})_{min}$	$(S_{zz})_{max}$	$(S_{yz})_{min}$	$(S_{yz})_{max}$	$(S_{xz})_{min}$	$(S_{xz})_{max}$
GL	−323	+2792	0	+1135	0	+2
R3D	−330	+2758	0	+1130	0	+2

Compressive Loading ($u/a = -0.01$)

(Second Piola-Kirchhoff stresses, psi)

Strain	$(S_{zz})_{min}$	$(S_{zz})_{max}$	$(S_{yz})_{min}$	$(S_{yz})_{max}$	$(S_{xz})_{min}$	$(S_{xz})_{max}$
GL	−1603	+737	−396	+297	−1584	+1514
R3D	−1590	+763	−389	+309	−1596	+1622

Thermal Loading ($\Delta T = -280°F$)

(Second Piola-Kirchhoff stresses**, psi)

Strain	$(S_{zz})_{min}$	$(S_{zz})_{max}$	$(S_{yz})_{min}$	$(S_{yz})_{max}$	$(S_{xz})_{min}$	$(S_{xz})_{max}$
GL	−481	+4324	0	+1683	−1	+1
R3D	−535	+4204	0	+1680	−1	+1

* Gauss point stress extrema from global finite element analysis.

** Stress extrema along $x = 0$.

GL = Green-Lagrange nonlinear strain tensor, equations (4.27).

R3D = reduced form of 3D nonlinear strain, equations (F.1).

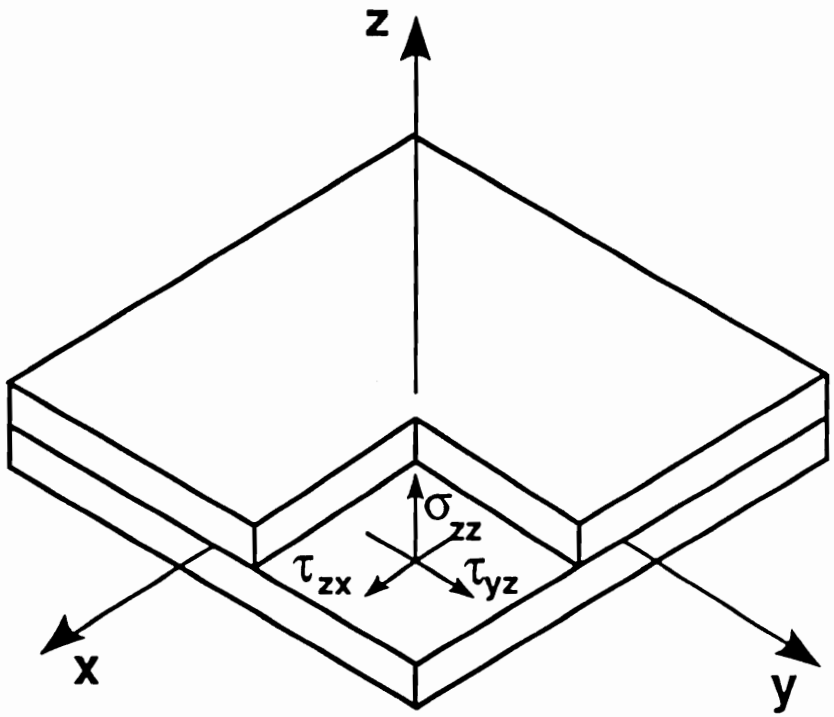

Figure 1.1 The interlaminar components of stress.

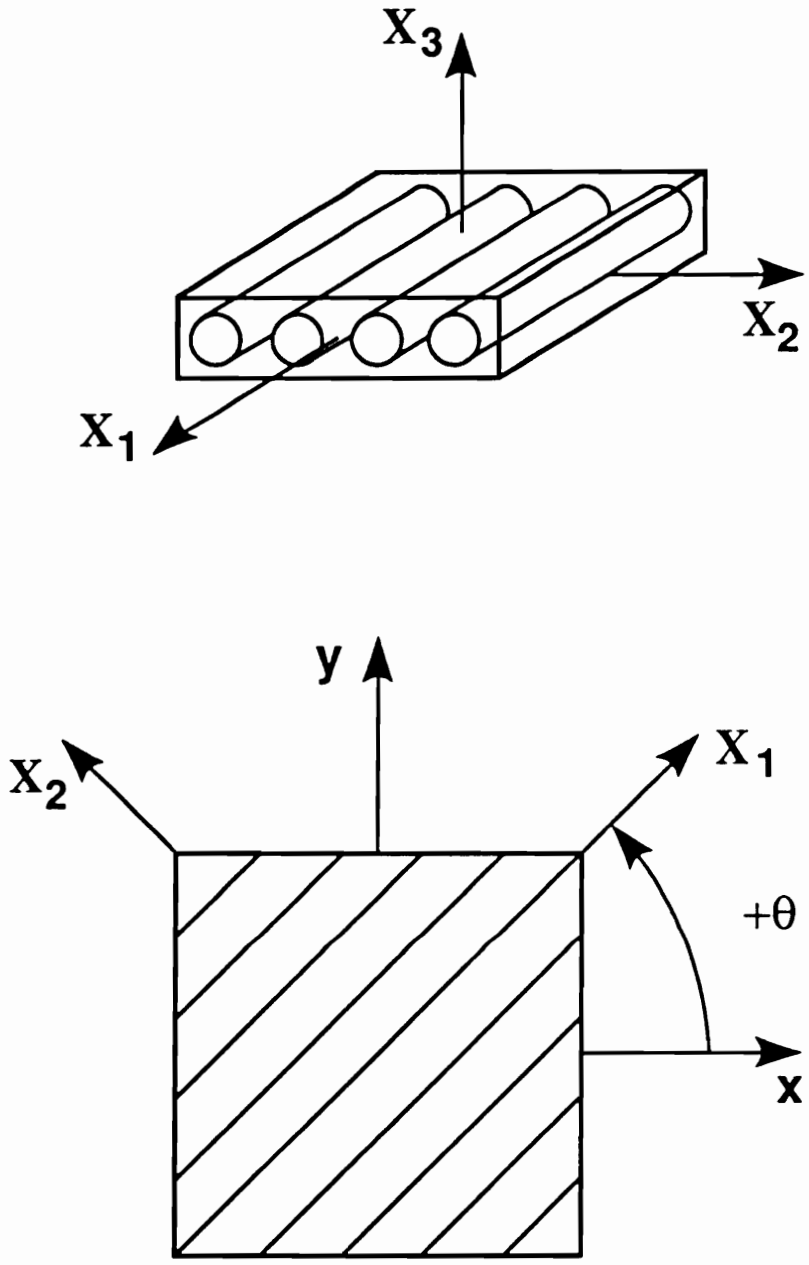

Figure 3.1 Lamina principal material coordinate system and angle of orientation.

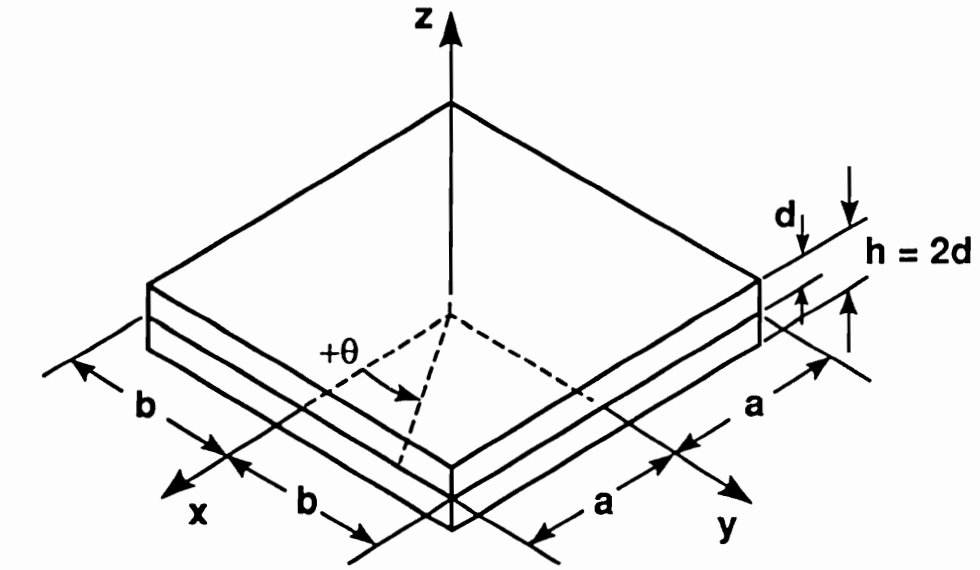

(a) Unsymmetric laminate

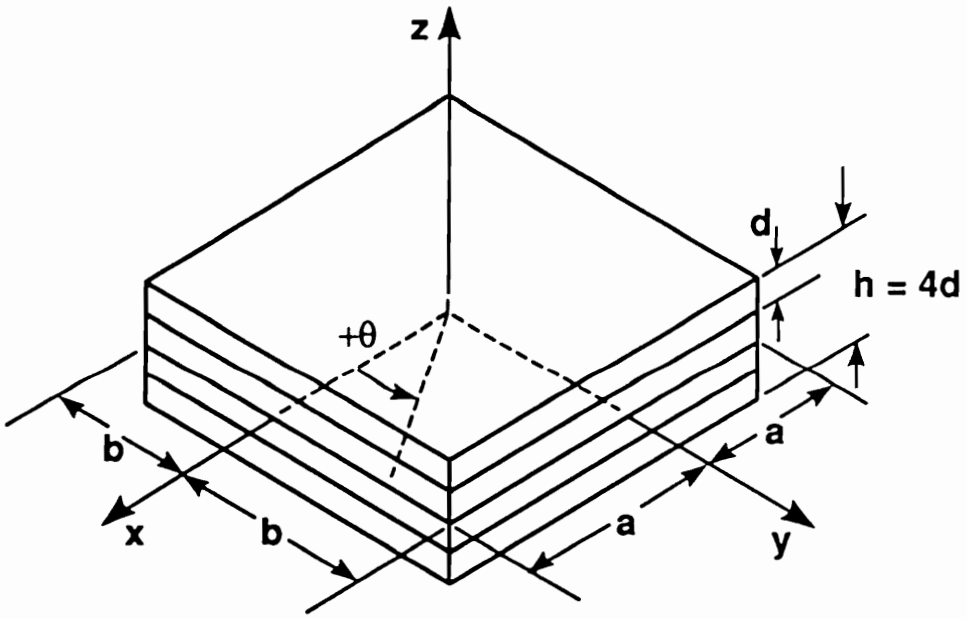

(b) Symmetric laminate

Figure 3.2 Unsymmetric and symmetric laminated plate geometry.

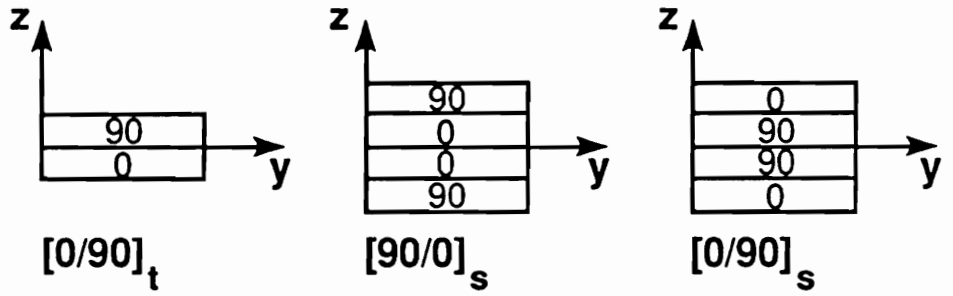

(a) 0/90 laminates

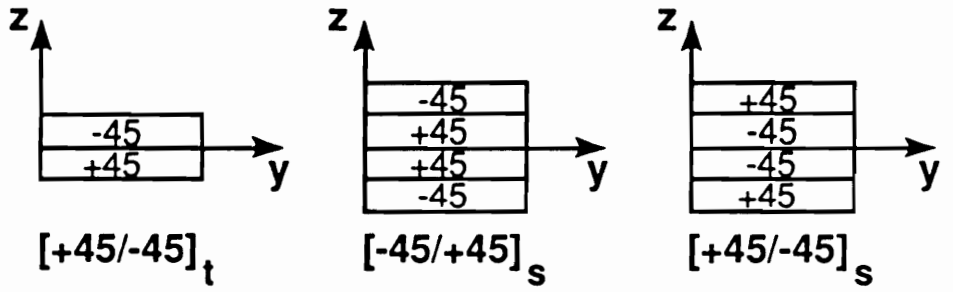

(b) +45/-45 laminates

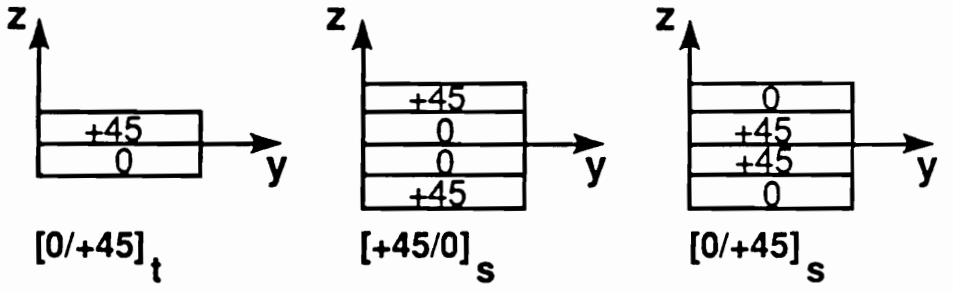

(c) 0/+45 laminates

Figure 3.3 Laminate stacking sequences.

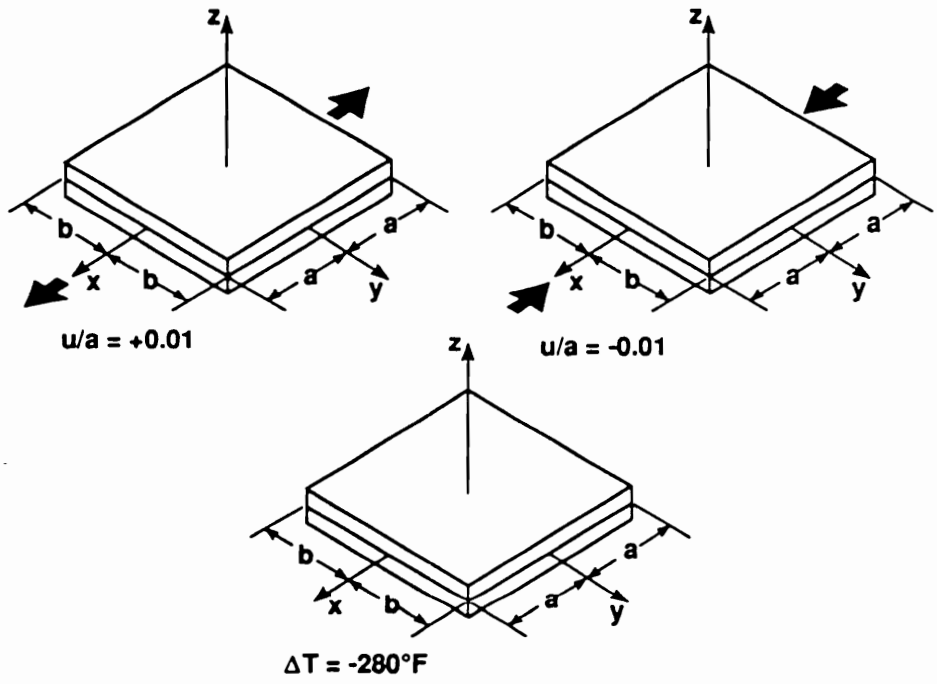

Figure 3.4 External loading conditions.

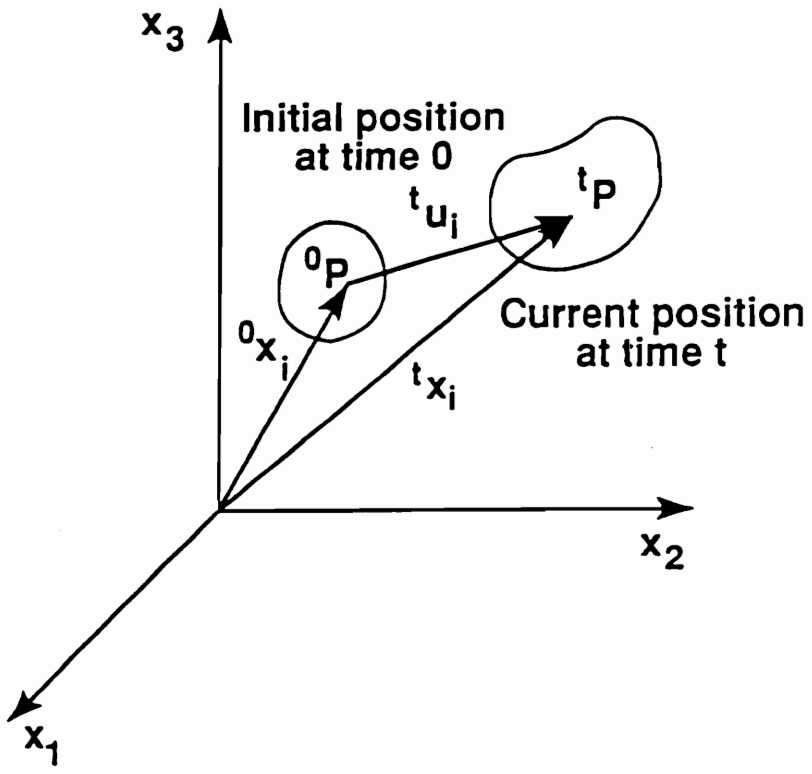

Figure 4.1 Motion of a material particle.

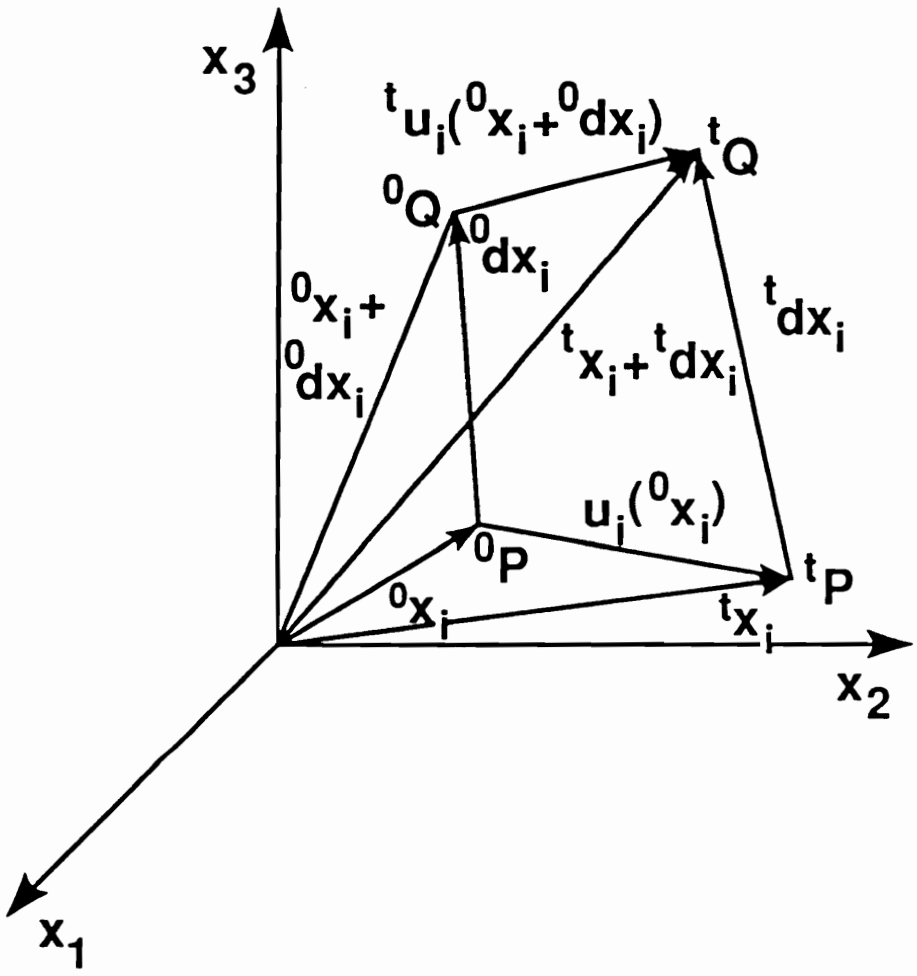

Figure 4.2 Relative displacement between two neighboring points.

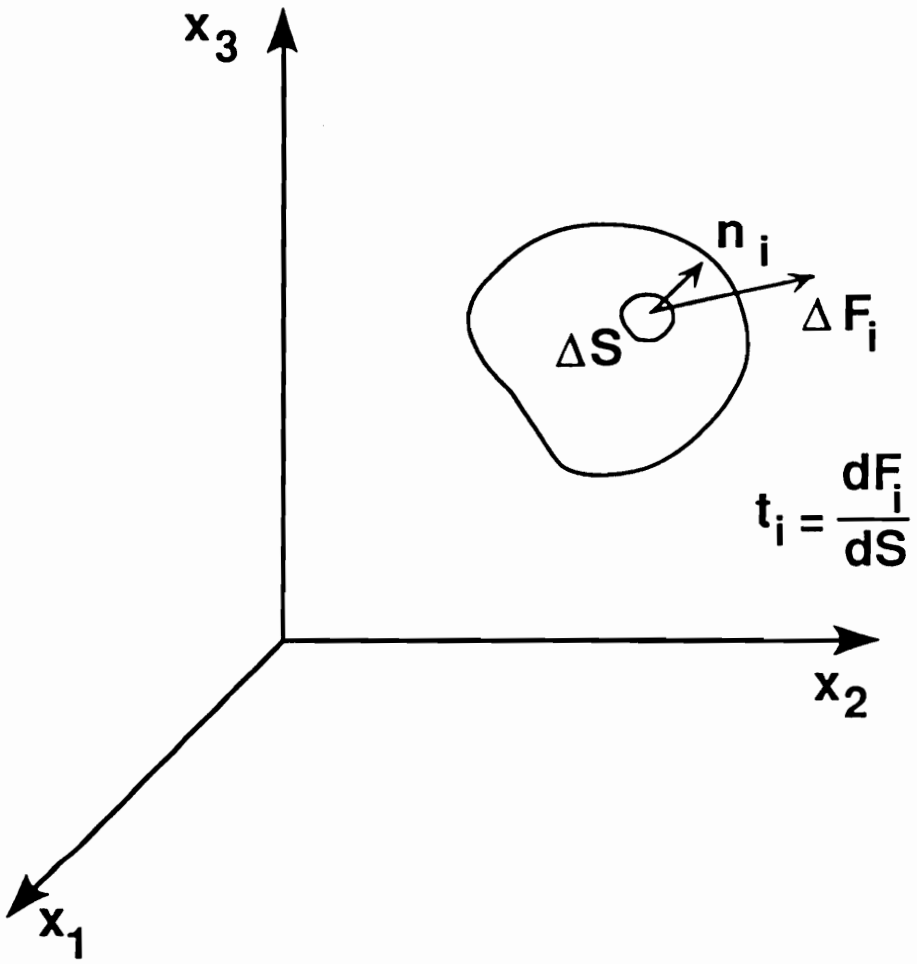

Figure 4.3 Traction vector acting upon the surface of the body.

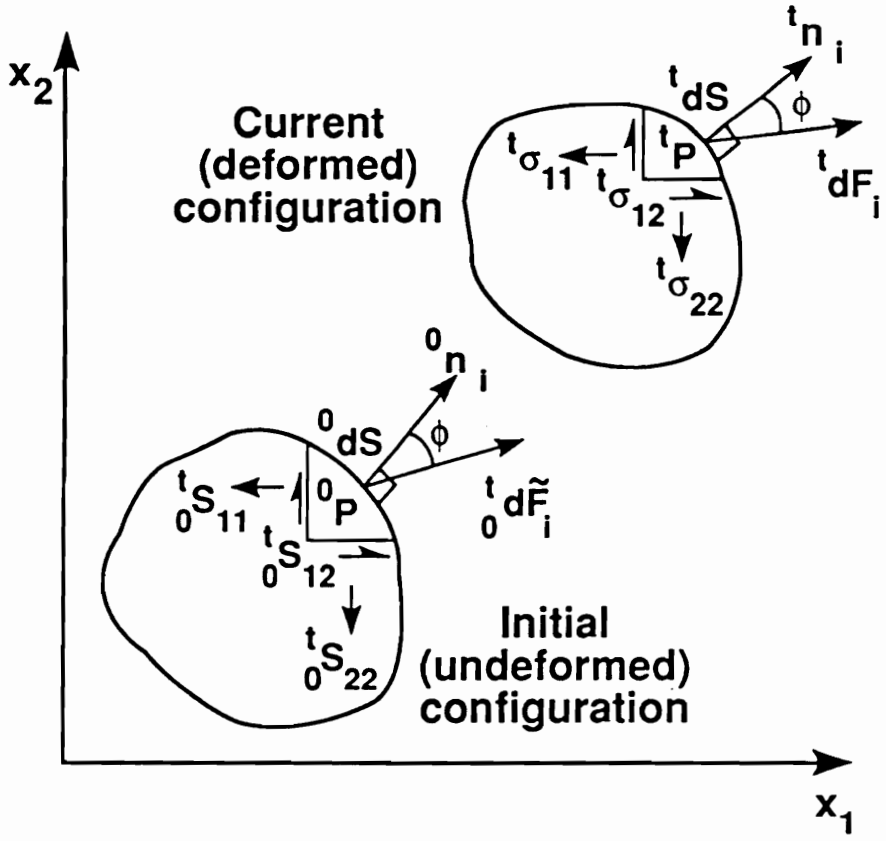

Figure 4.4 Two-dimensional components of second Piola-Kirchhoff stress ${}^t_0S_{ij}$ and Cauchy stress ${}^t\sigma_{ij}$.

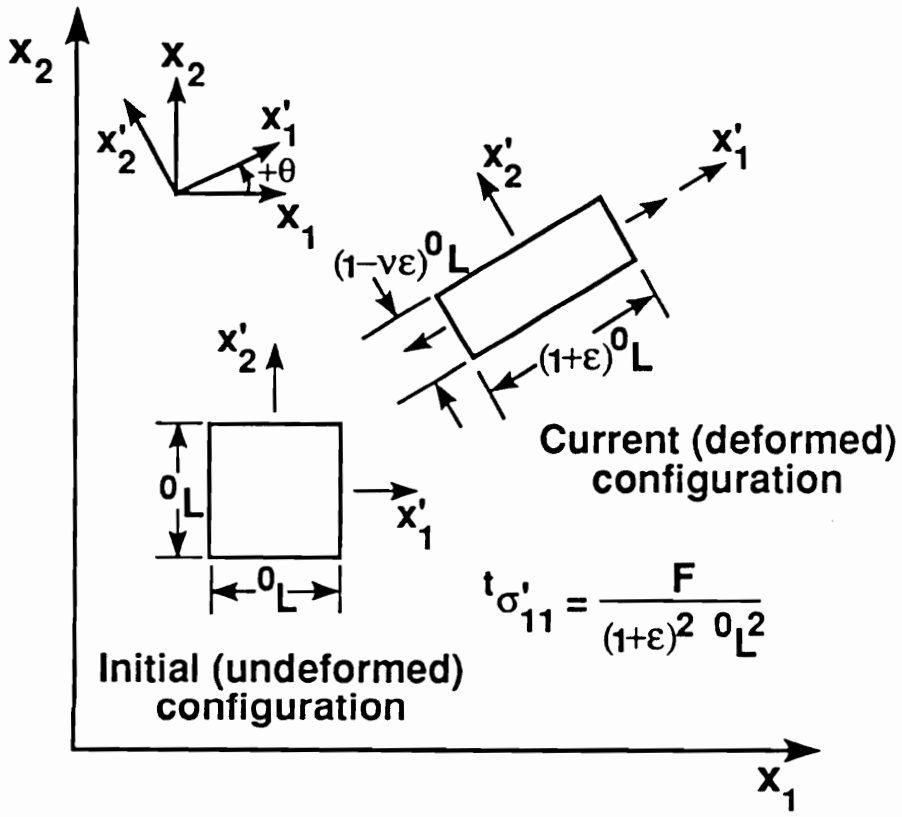

Figure 4.5 Finite deformation of an elastic body.

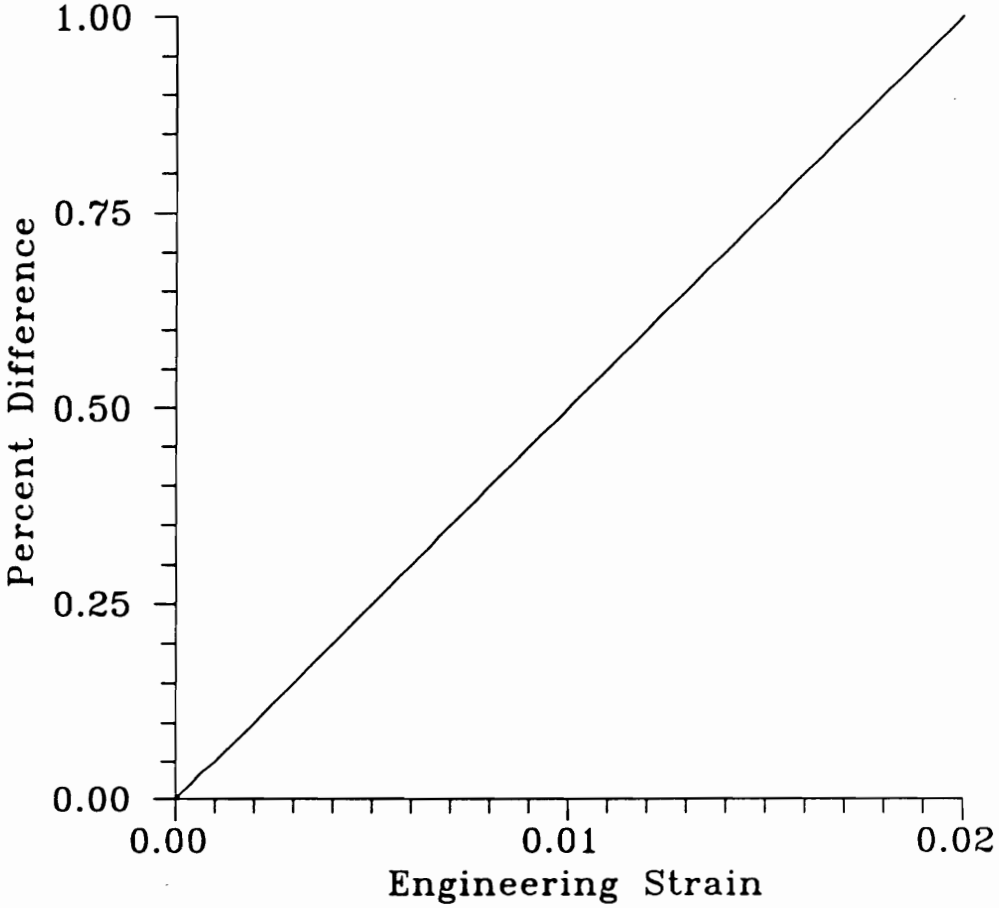

Figure 4.6 Percent difference between ${}^{t}_{0}E_{11}$ and ${}^{t}\epsilon'_{11}$ $(= \epsilon)$ versus engineering strain ϵ for the elastic body shown in Figure 4.5.

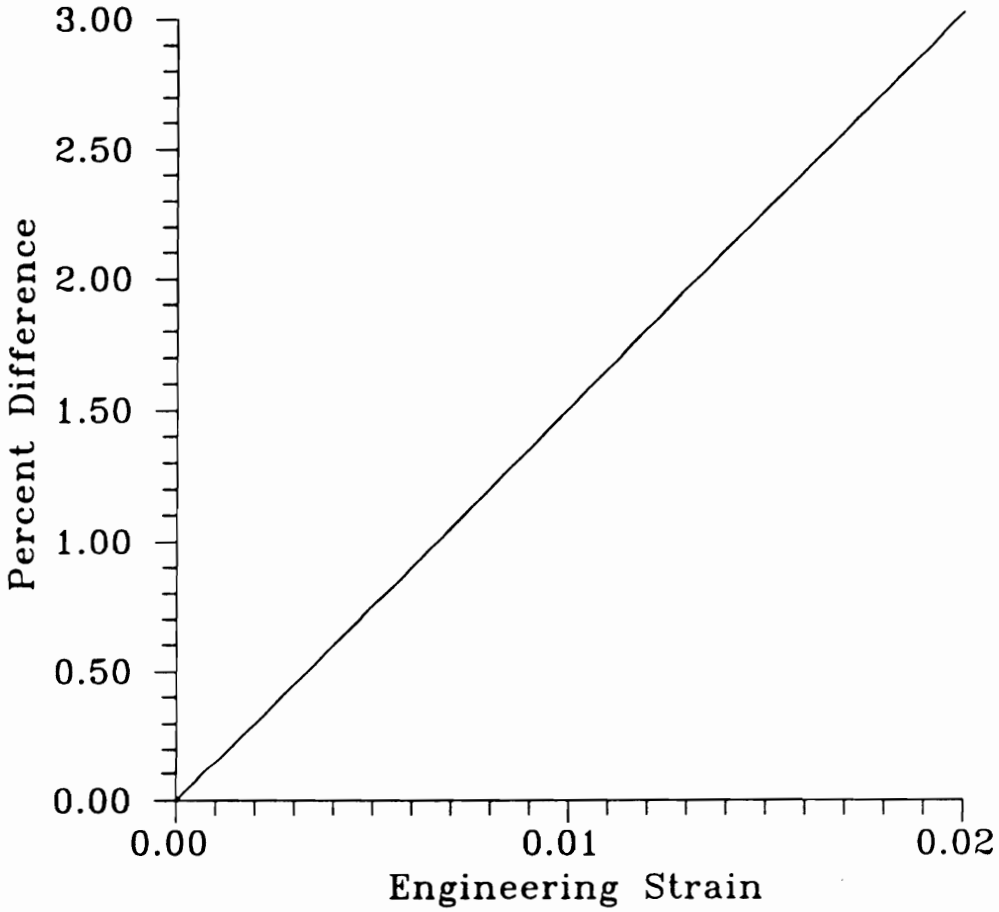

Figure 4.7 Percent difference between ${}^{t}_{0}S_{11}$ and ${}^{t}\sigma'_{11}$ versus engineering strain ϵ for the elastic body shown in Figure 4.5 ($\nu = 0.25$).

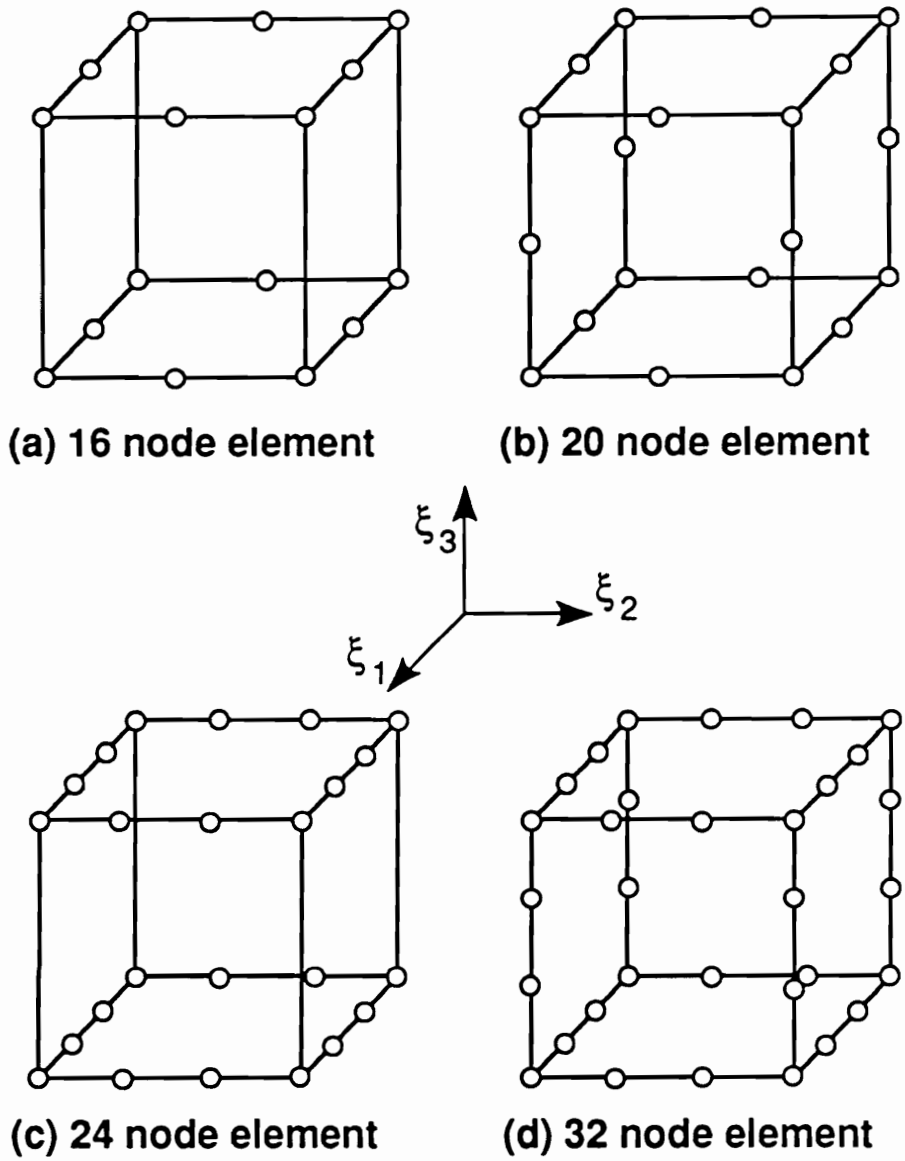

Figure 5.1 Element geometry.

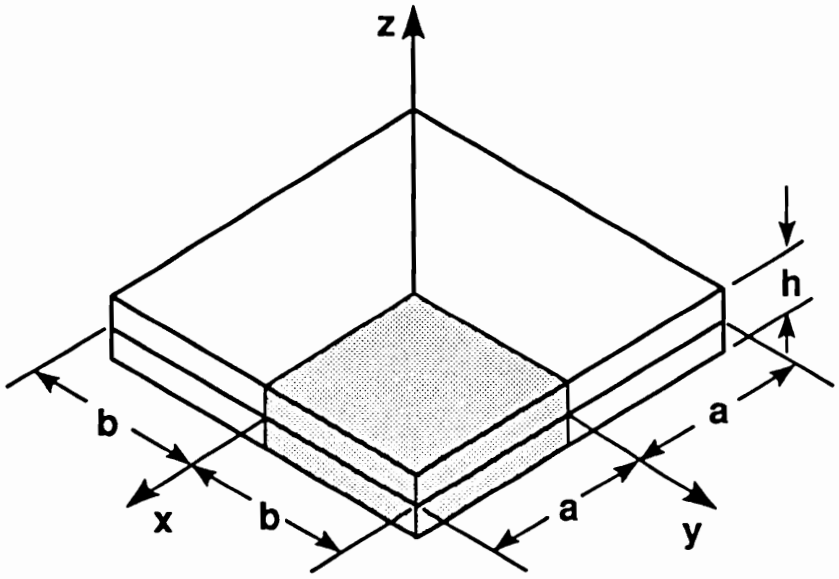

(a) Quarter symmetry

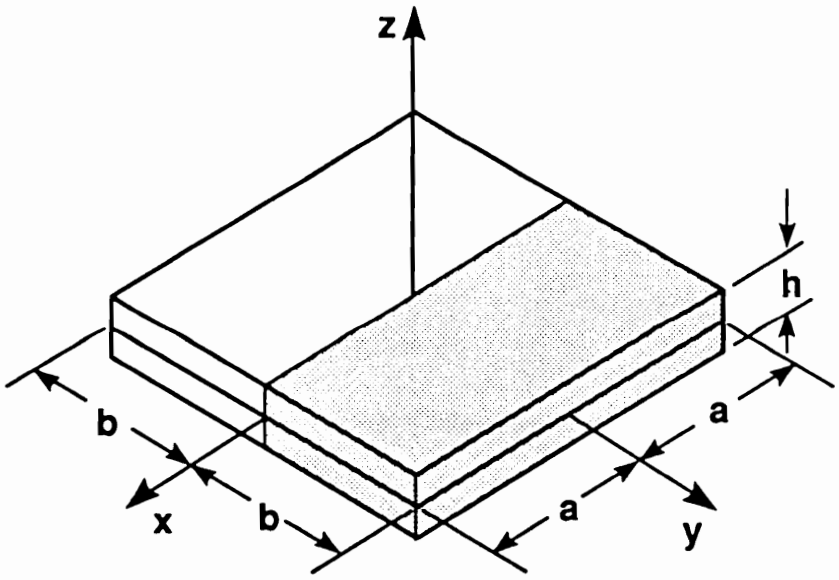

(b) Inversion symmetry

Figure 5.2 Quarter and inversion symmetry finite element models.

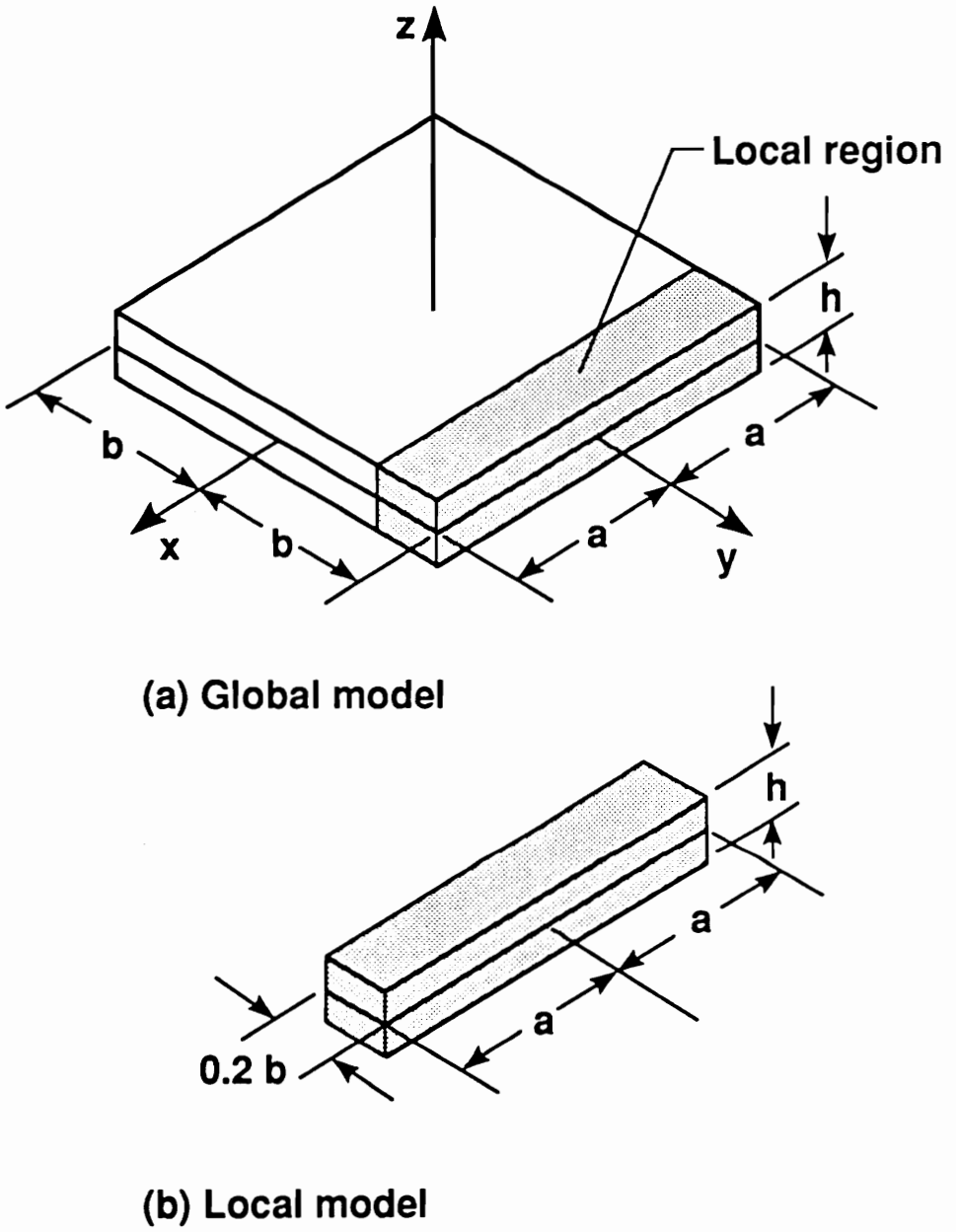

Figure 5.3 Geometry of global/local finite element analysis.

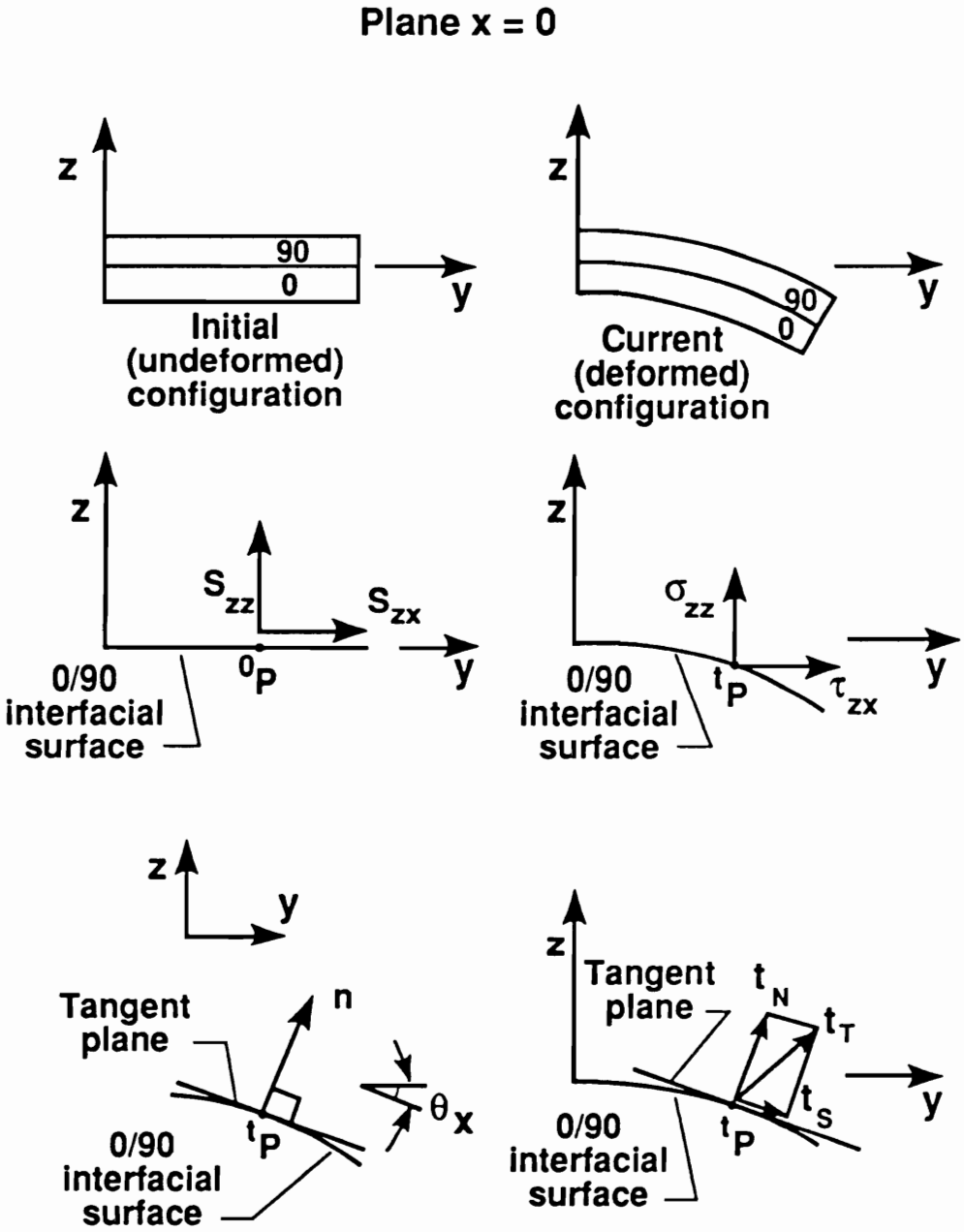

Figure 5.4 Comparison of interlaminar stresses for nonlinear analysis.

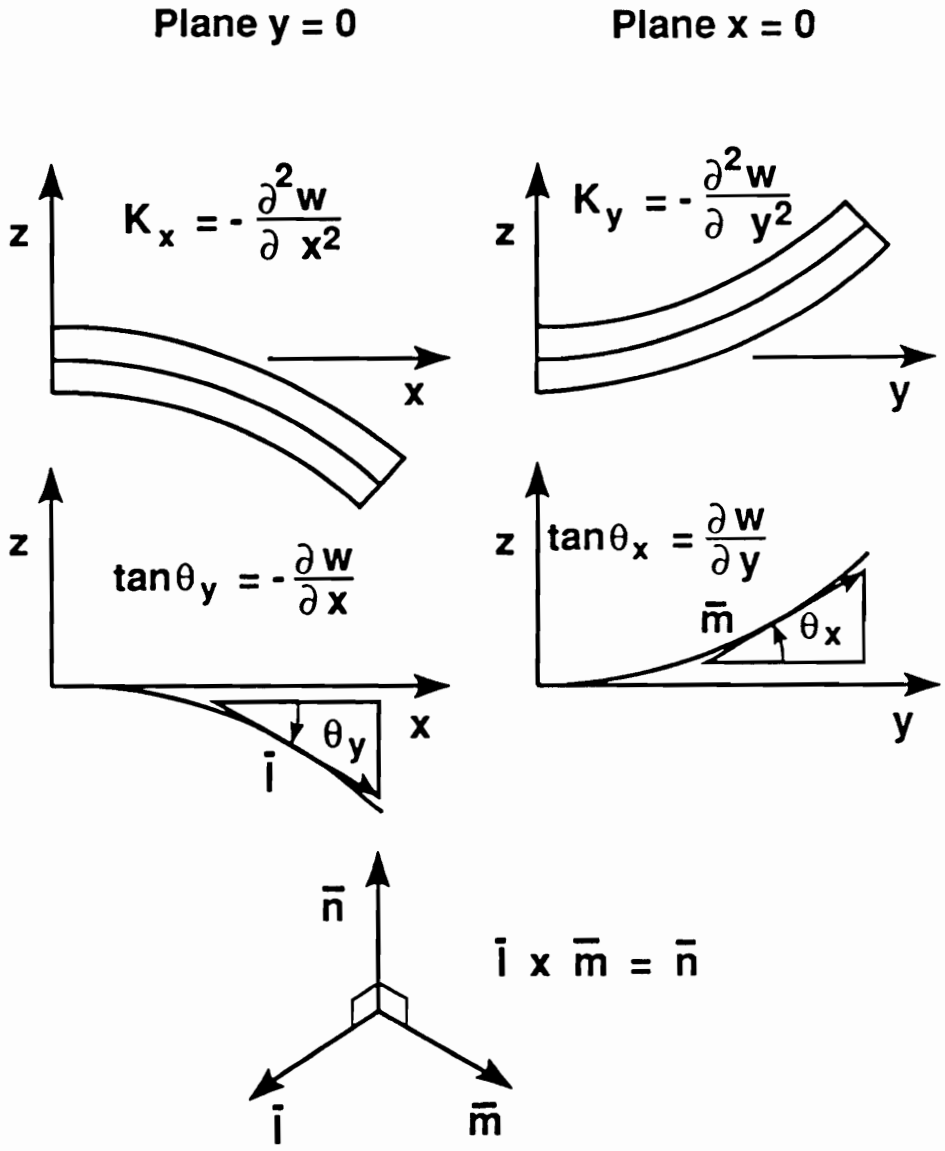

Figure 5.5 Computation of a vector normal to the interfacial surface.

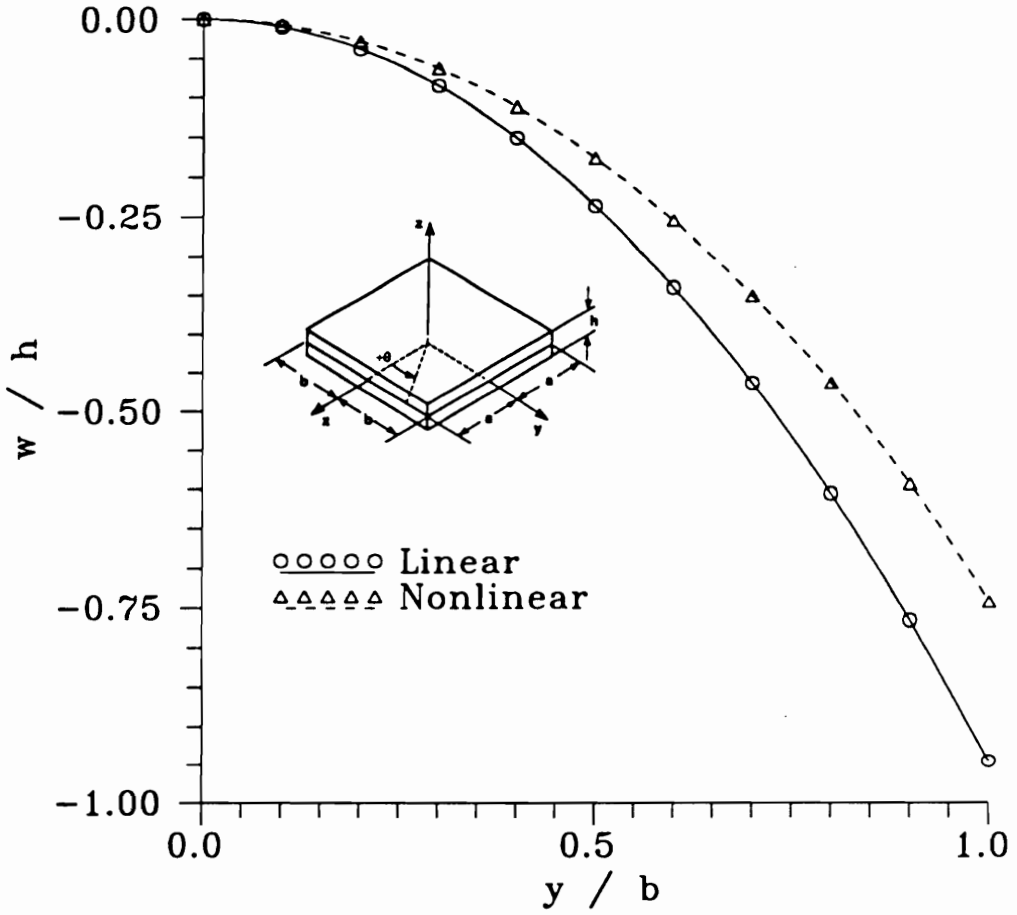

Figure 5.6 Midplane w/h displacement along $x = 0$ for a 2.0 in. square unsymmetric $[0_4/90_4]_t$ laminate ($\Delta T = -280°F$).

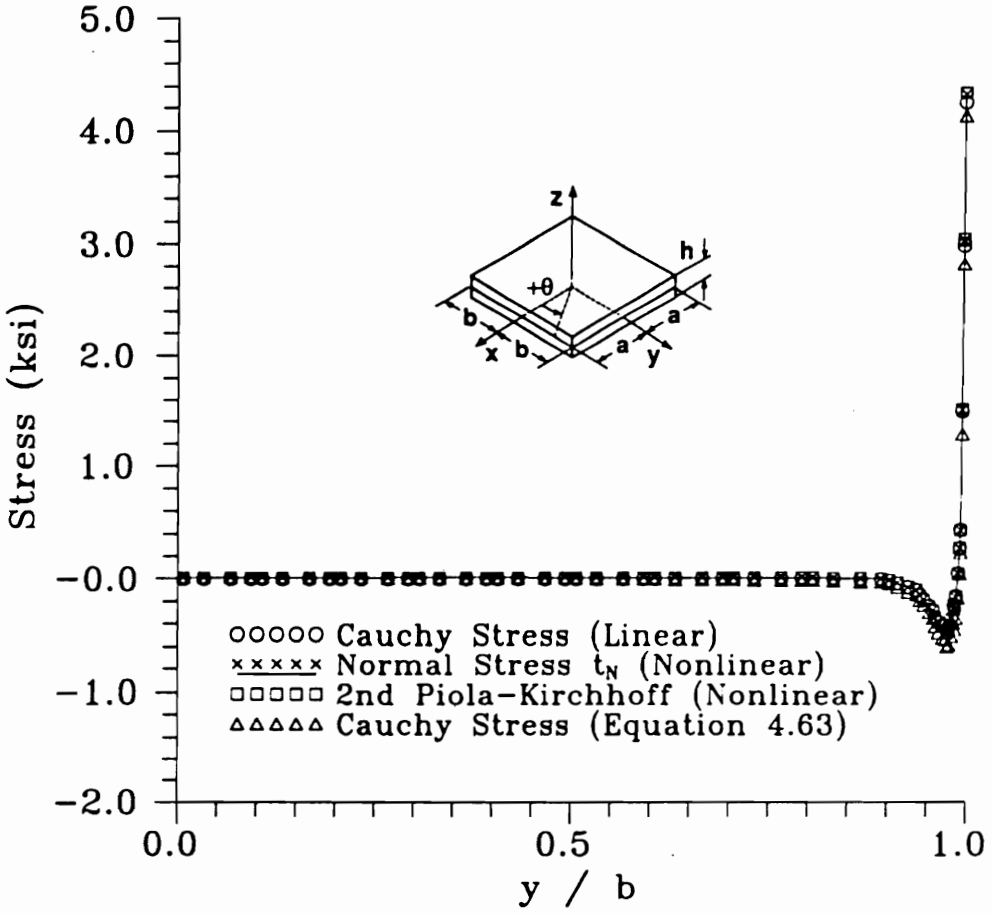

Figure 5.7 Comparison of interlaminar normal stress predictions along $x = 0$ for a 2.0 in. square unsymmetric $[0_4/90_4]_t$ laminate ($\Delta T = -280°F$).

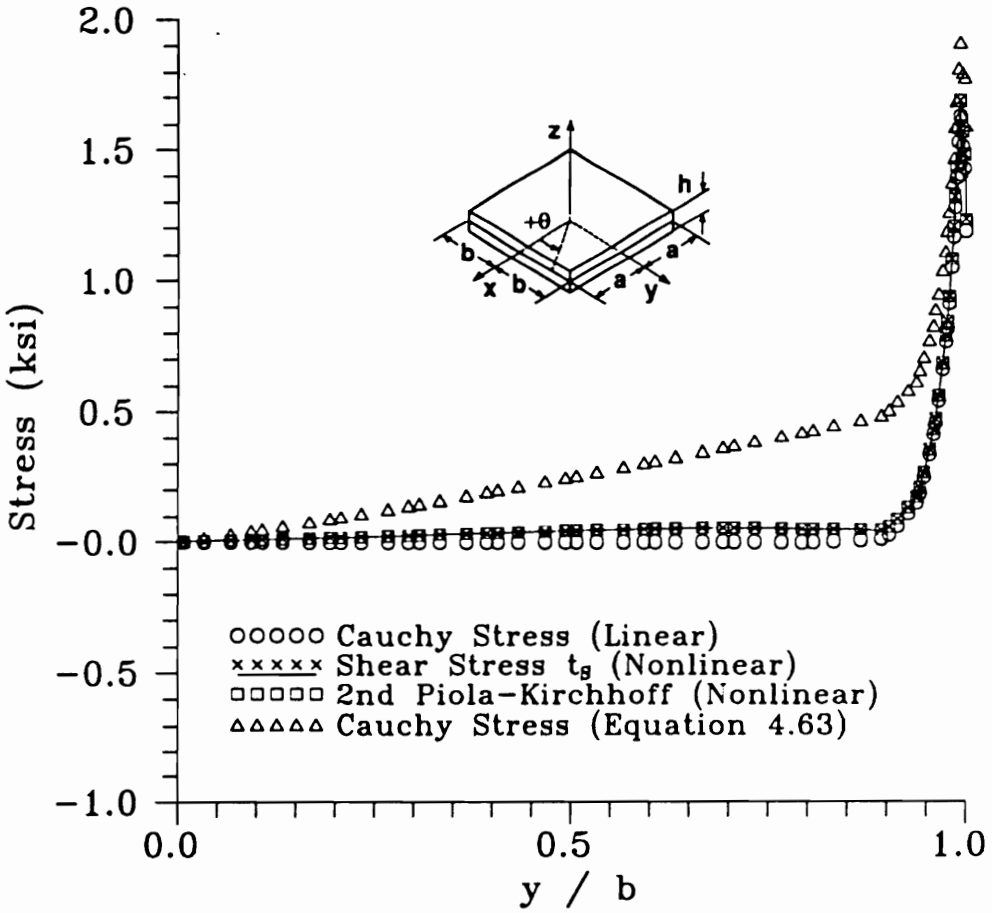

Figure 5.8 Comparison of interlaminar shear stress predictions along $x = 0$ for a 2.0 in. square unsymmetric $[0_4/90_4]_t$ laminate ($\Delta T = -280°F$).

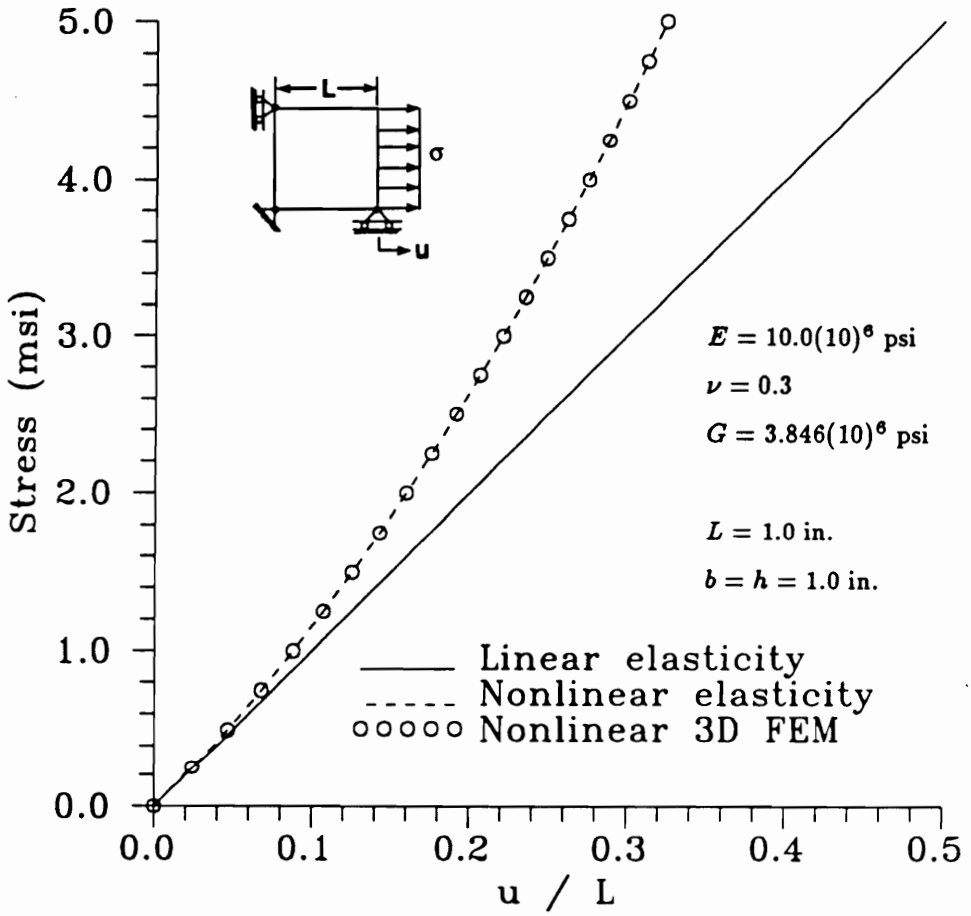

Figure 5.9 Comparison of u/L displacement predictions for the uniaxial extension of an isotropic bar.

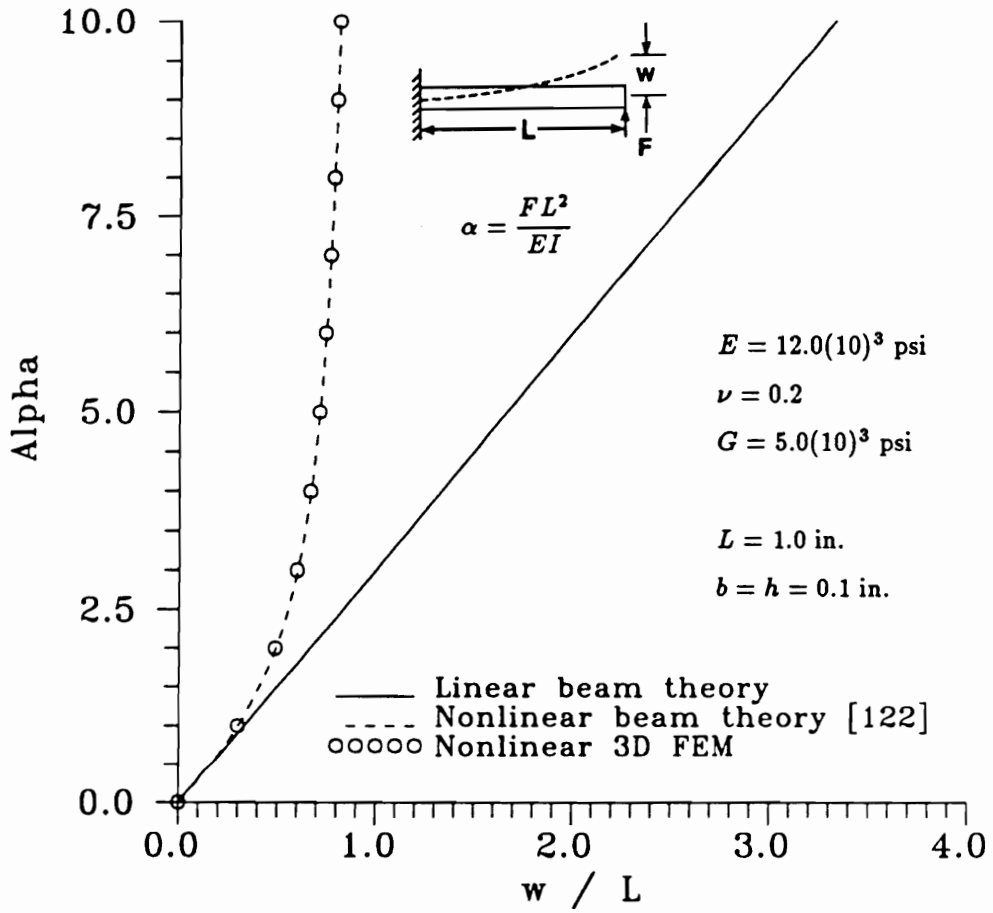

Figure 5.10 Comparison of transverse end w/h displacement predictions for a cantilever beam subjected to a transverse end load.

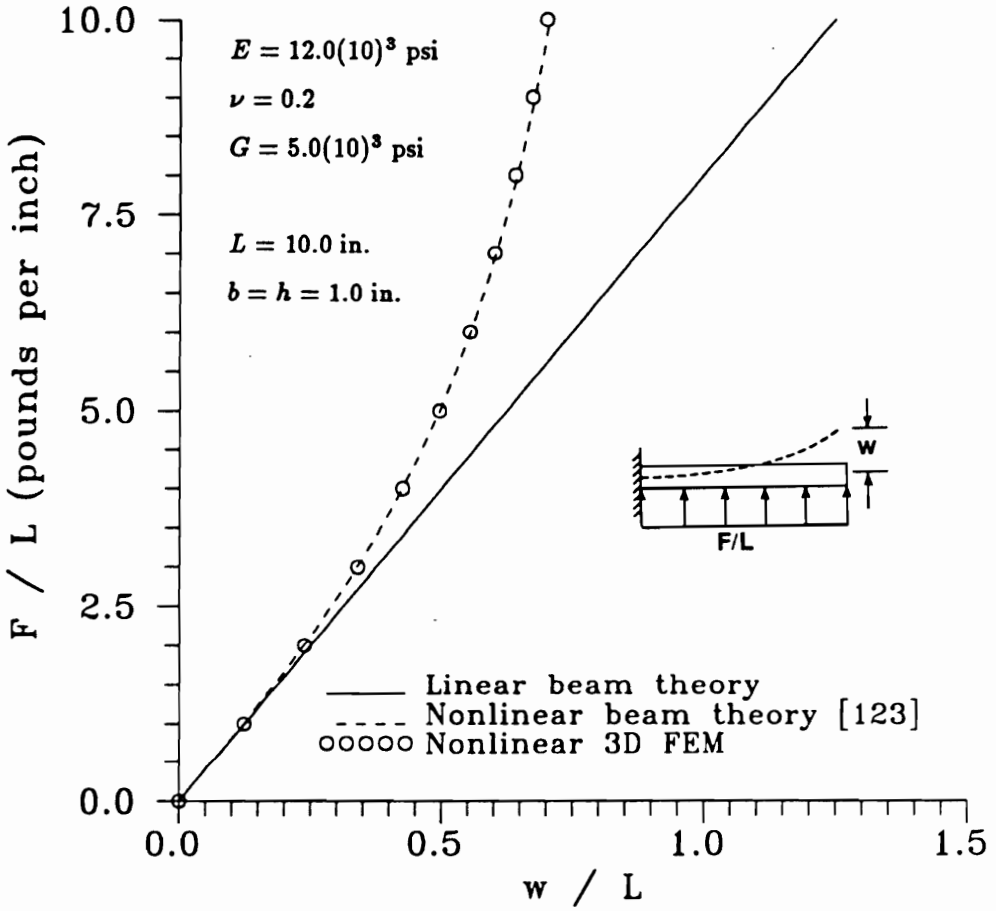

Figure 5.11 Comparison of transverse end w/h displacement predictions for a cantilever beam subjected to uniformly distributed loading.

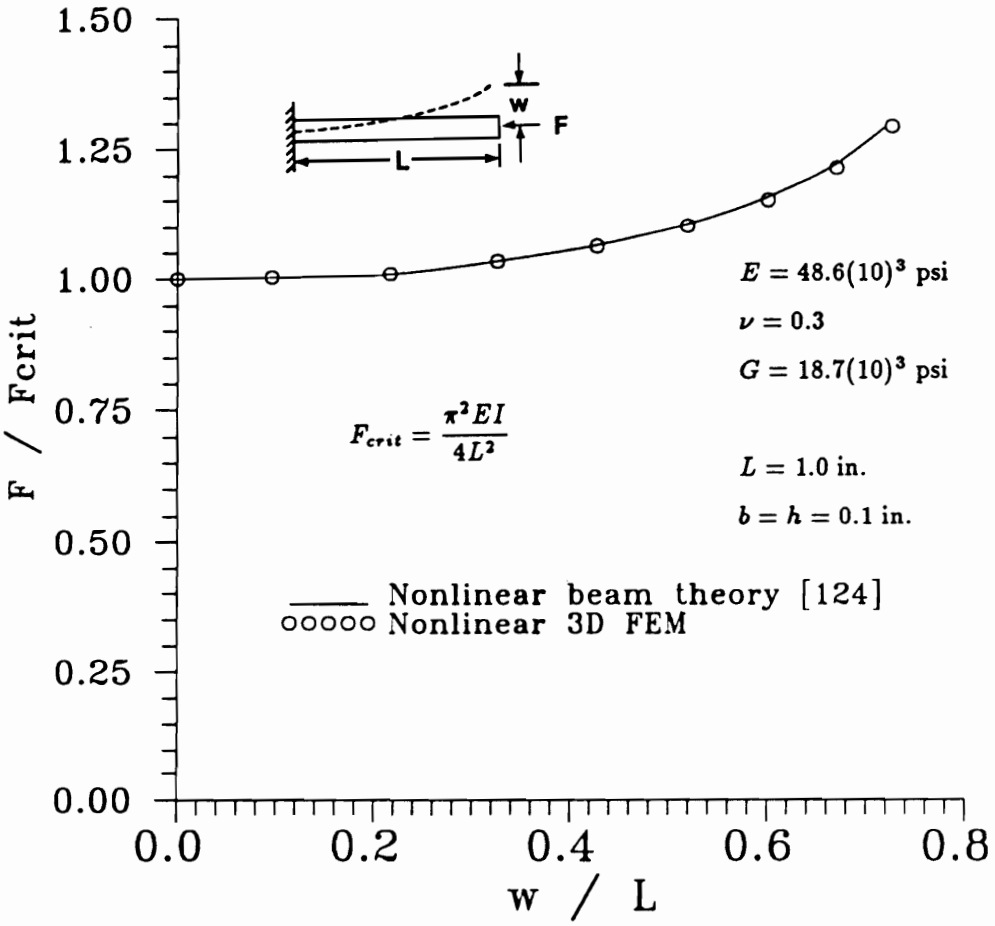

Figure 5.12 Comparison of transverse end w/h displacement predictions for the elastica (cantilever beam subjected to a compressive axial end load).

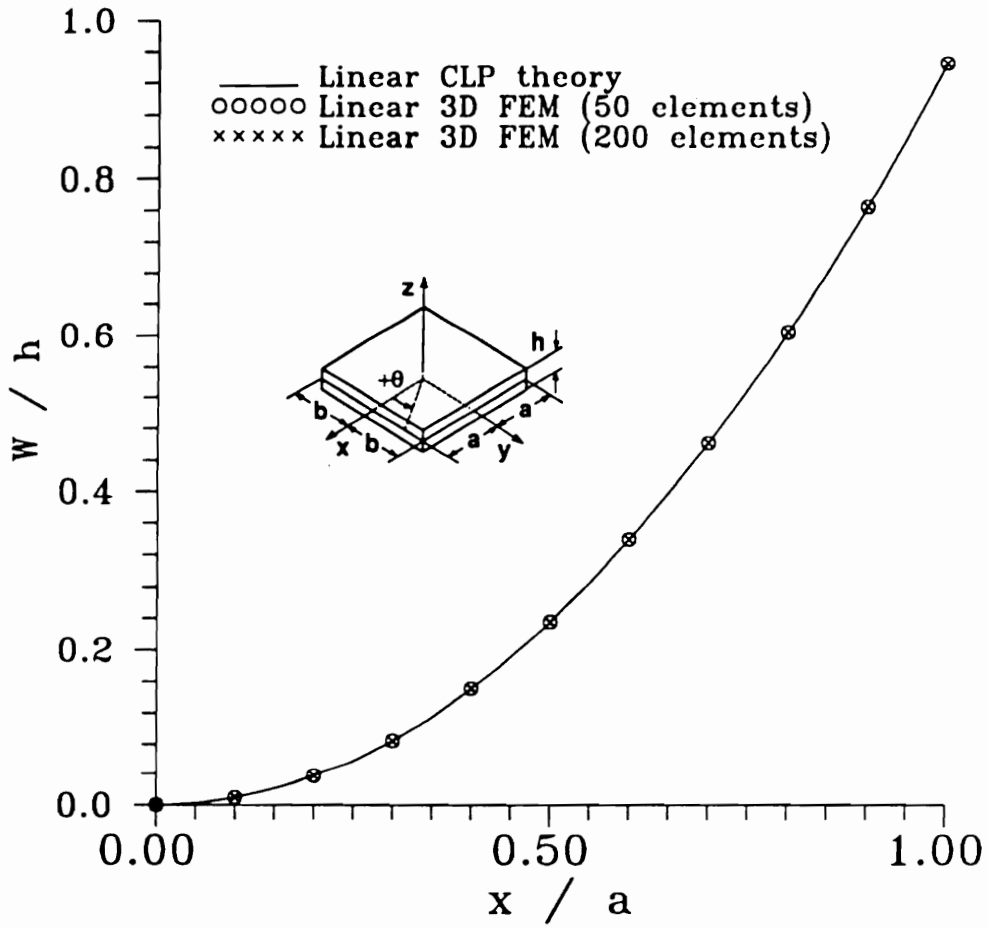

Figure 5.13 Comparison of linear midplane w/h displacement predictions along $y = 0$ for a 2.0 in. square unsymmetric $[0_4/90_4]_t$ laminate ($\Delta T = -280°F$).

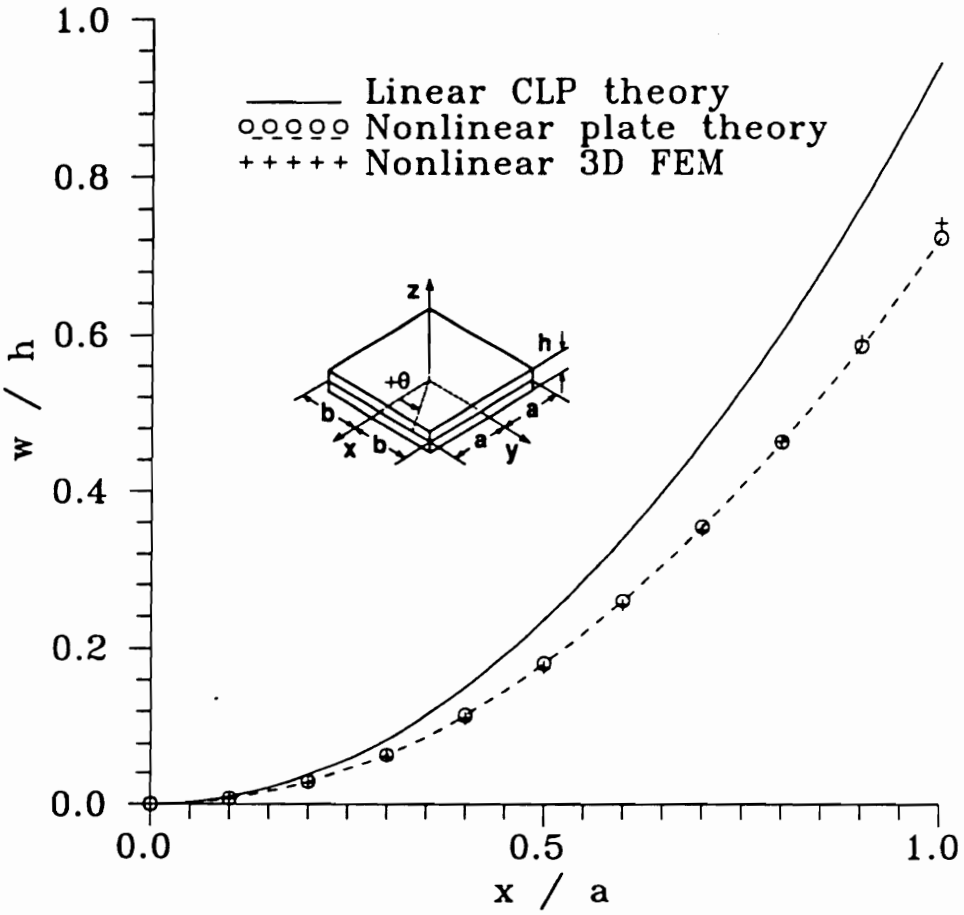

Figure 5.14 Comparison of nonlinear midplane w/h displacement predictions along $y = 0$ for a 2.0 in. square unsymmetric $[0_4/90_4]_t$ laminate ($\Delta T = -280°F$).

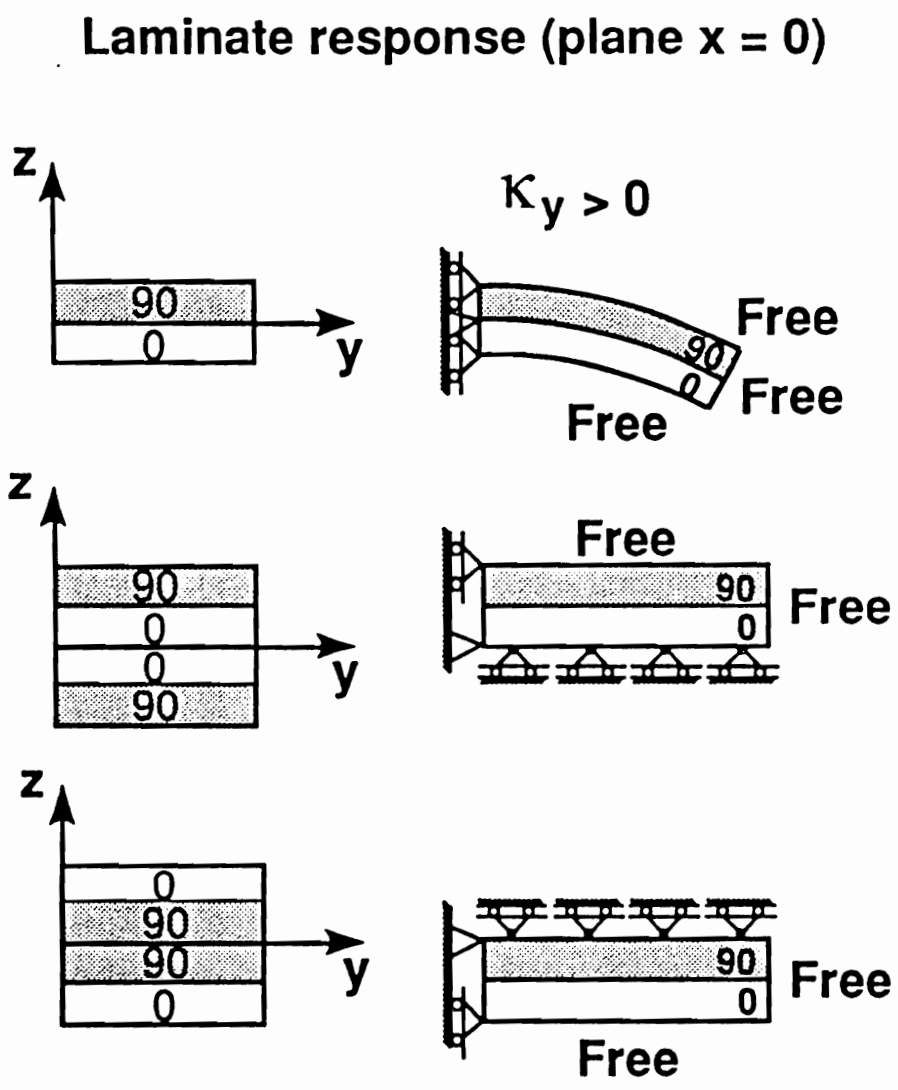

Figure 6.1 Displacement response within the plane $x = 0$ of the cross-ply laminates subjected to extensional loading.

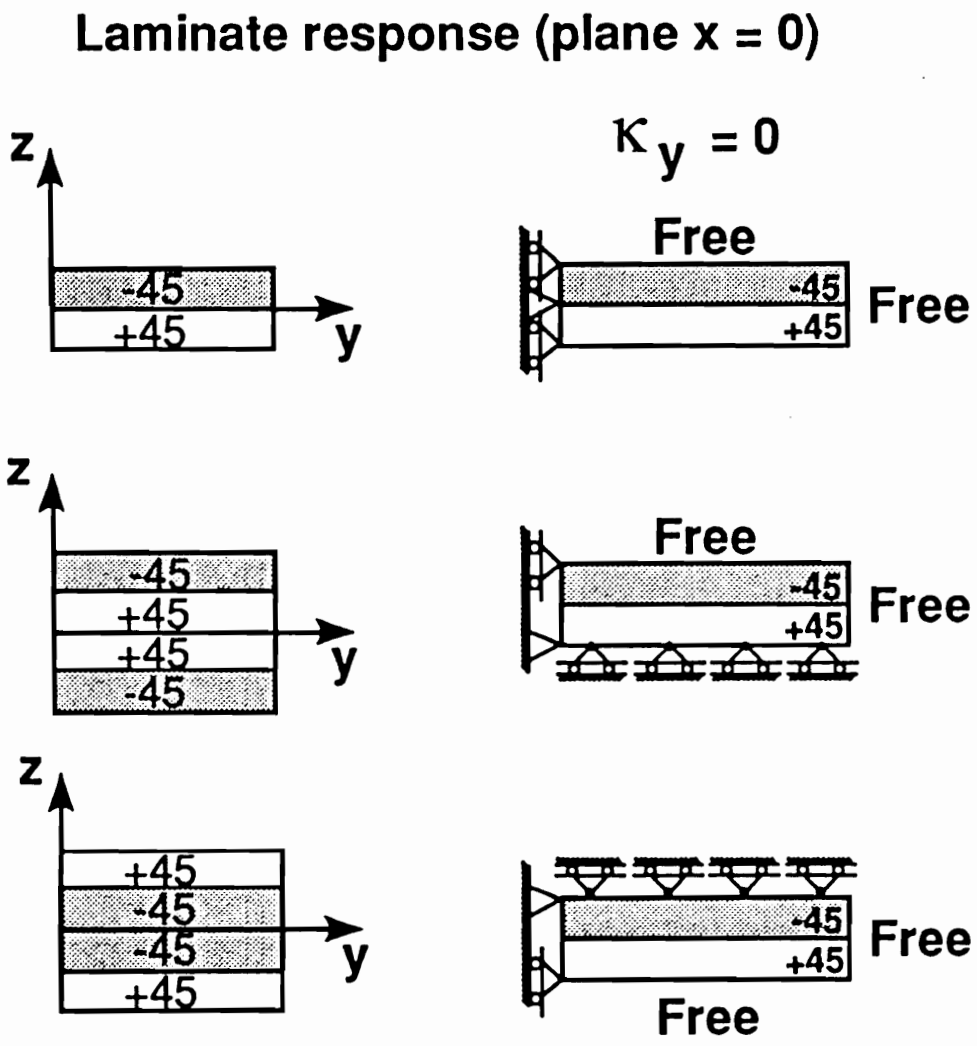

Figure 6.2 Displacement response within the plane $x = 0$ of the angle-ply laminates subjected to extensional loading.

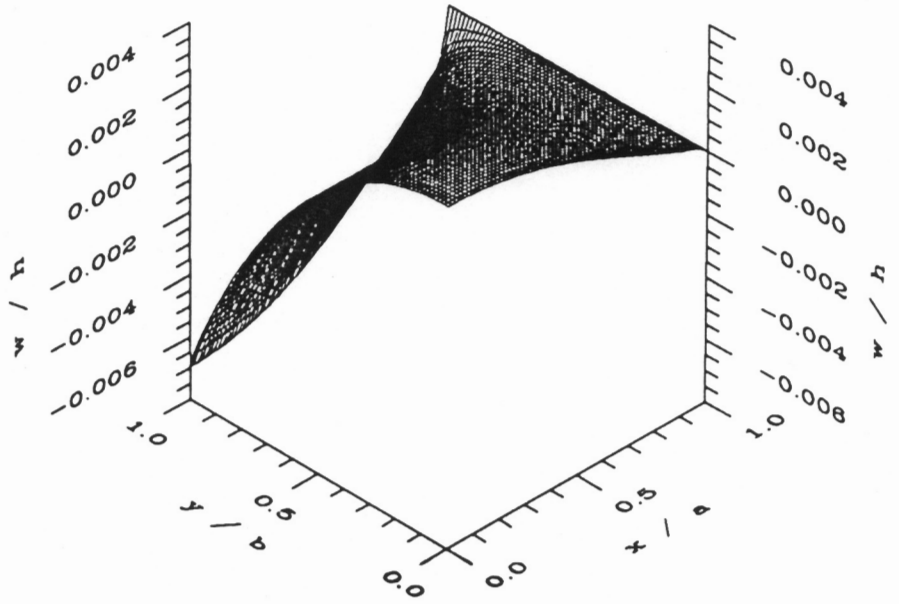

(a) Linear theory

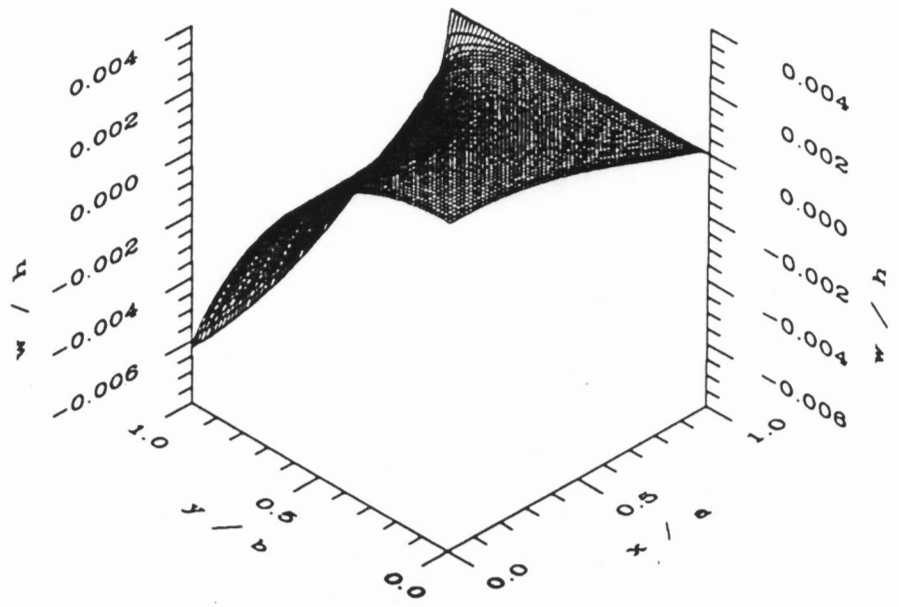

(b) Nonlinear theory

Figure 6.3 Midplane w/h displacement for a 4.0 in. square unsymmetric $[0_{50}/90_{50}]_t$ laminate (u/a = +0.01).

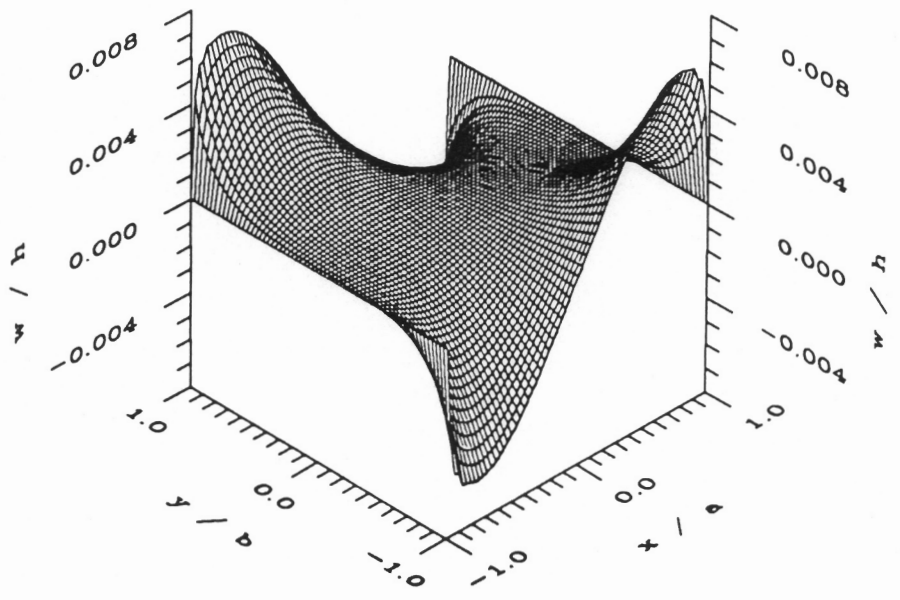

(a) Linear theory

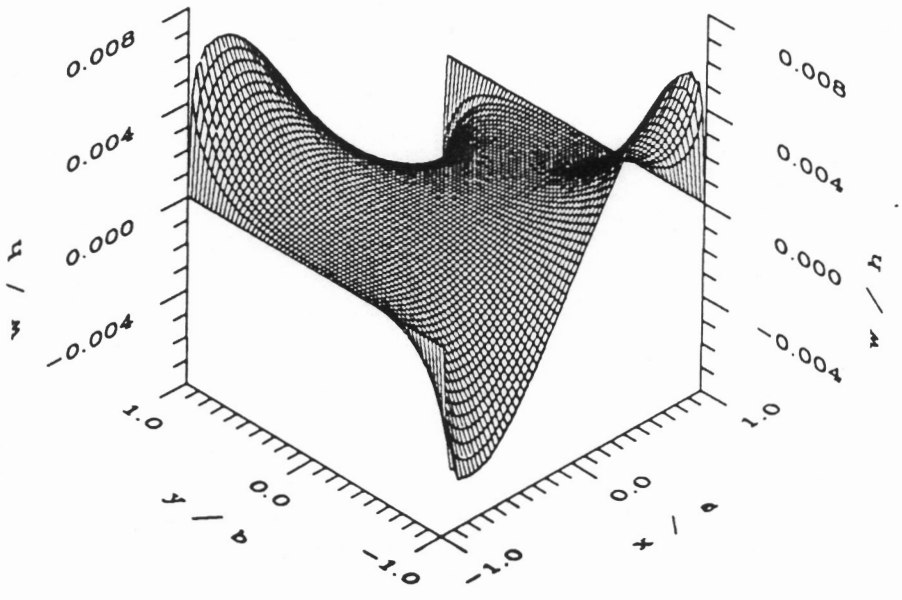

(b) Nonlinear theory

Figure 6.4 Midplane w/h displacement for a 4.0 in. square unsymmetric $[+45_{50}/-45_{50}]_t$ laminate (u/a = +0.01).

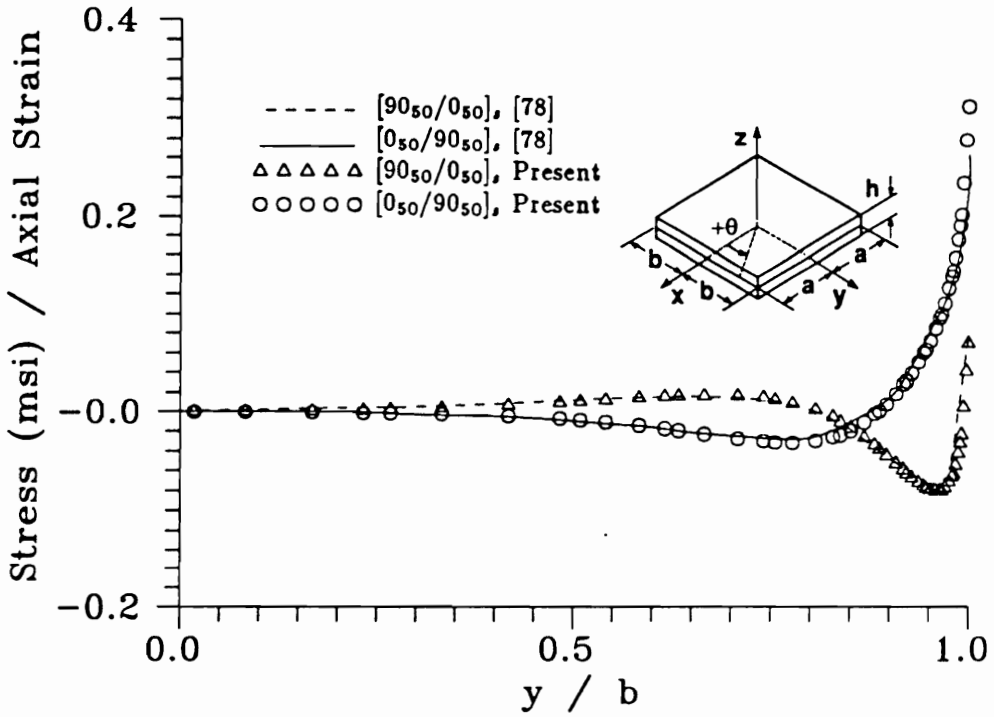

Figure 6.5 Comparison with previous results [78] for σ_{zz} stress at the 0/90 interface for the 4.0 in. square symmetric $0_{50}/90_{50}$ laminates $(u/a = +0.01)$.

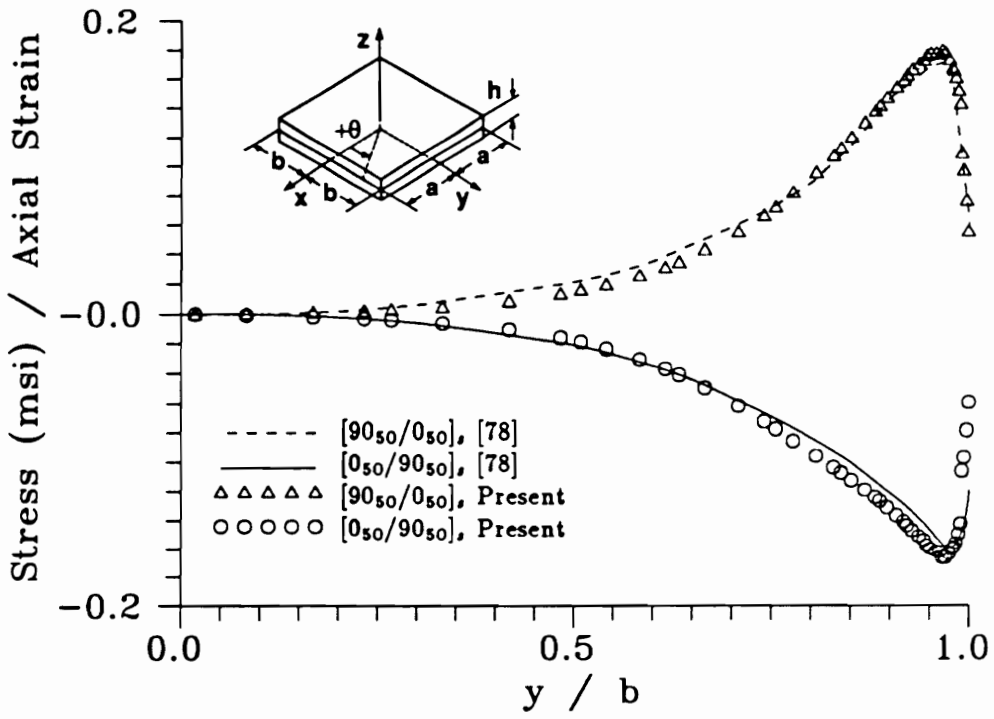

Figure 6.6 Comparison with previous results [78] for τ_{yz} stress at the 0/90 interface for the 4.0 in. square symmetric $0_{50}/90_{50}$ laminates ($u/a = +0.01$).

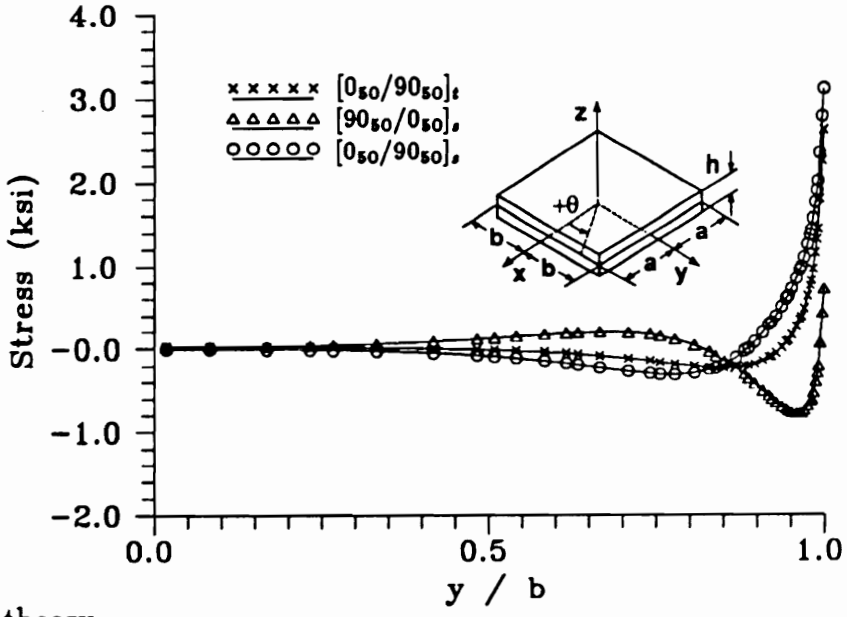

(a) Linear theory

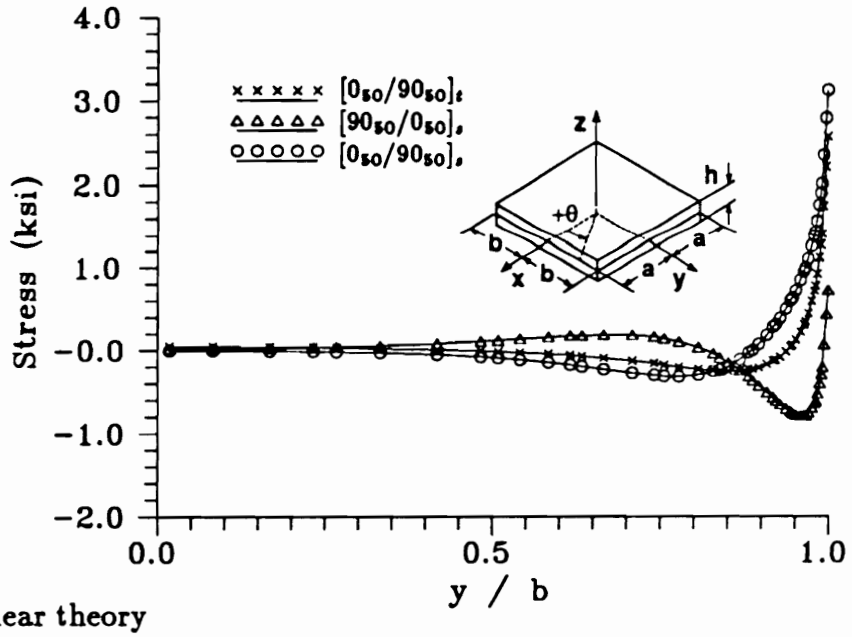

(b) Nonlinear theory

Figure 6.7 σ_{zz} and S_{zz} stress along $x = 0$ at the 0/90 interface for the 4.0 in. square $0_{50}/90_{50}$ laminates ($u/a = +0.01$).

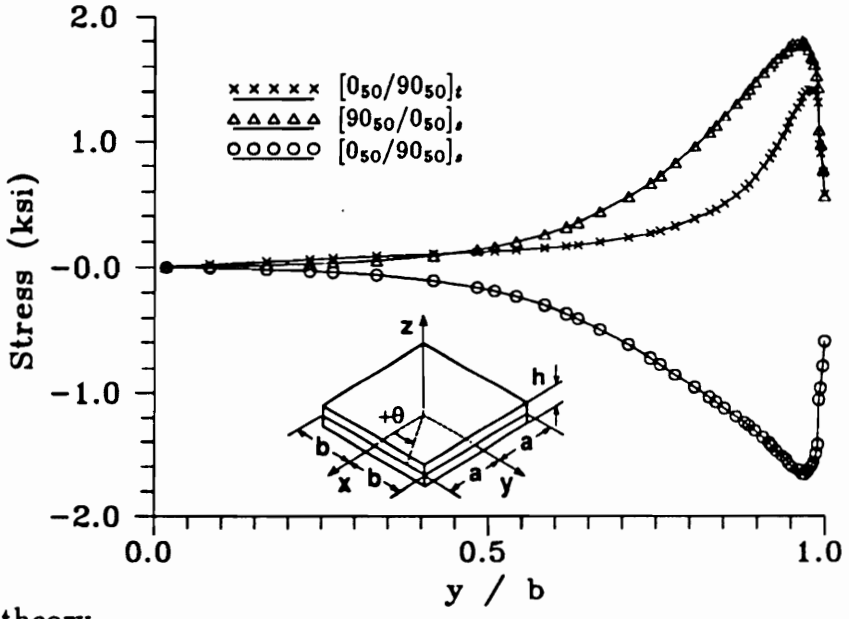

(a) Linear theory

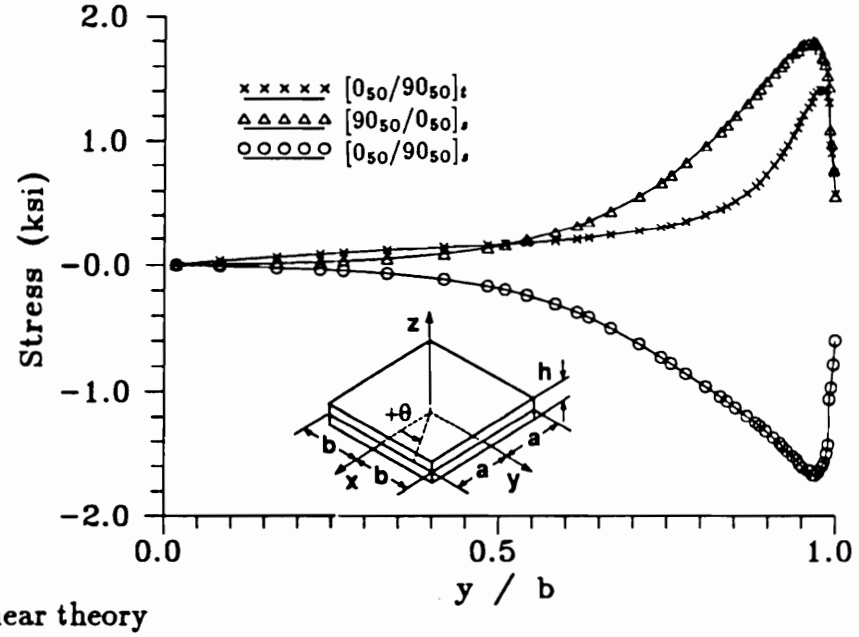

(b) Nonlinear theory

Figure 6.8 τ_{yz} and S_{yz} stress along $x = 0$ at the 0/90 interface for the 4.0 in. square $0_{50}/90_{50}$ laminates ($u/a = +0.01$).

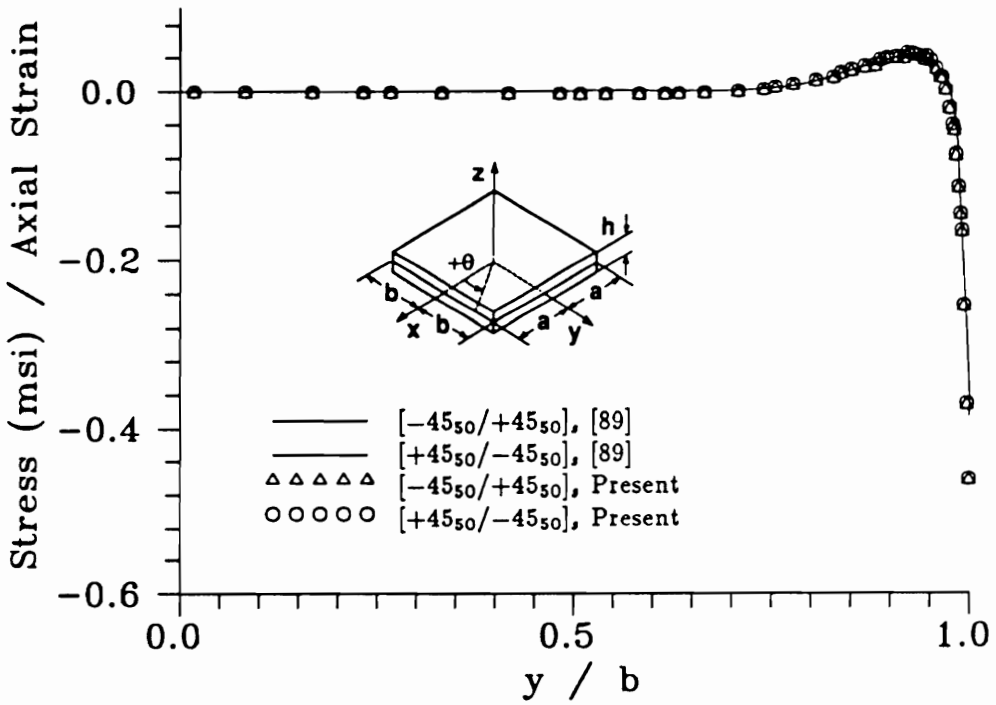

Figure 6.9 Comparison with previous results [89] for σ_{zz} stress at the +45/−45 interface for the 4.0 in. symmetric $+45_{50}/-45_{50}$ laminates ($u/a = +0.01$).

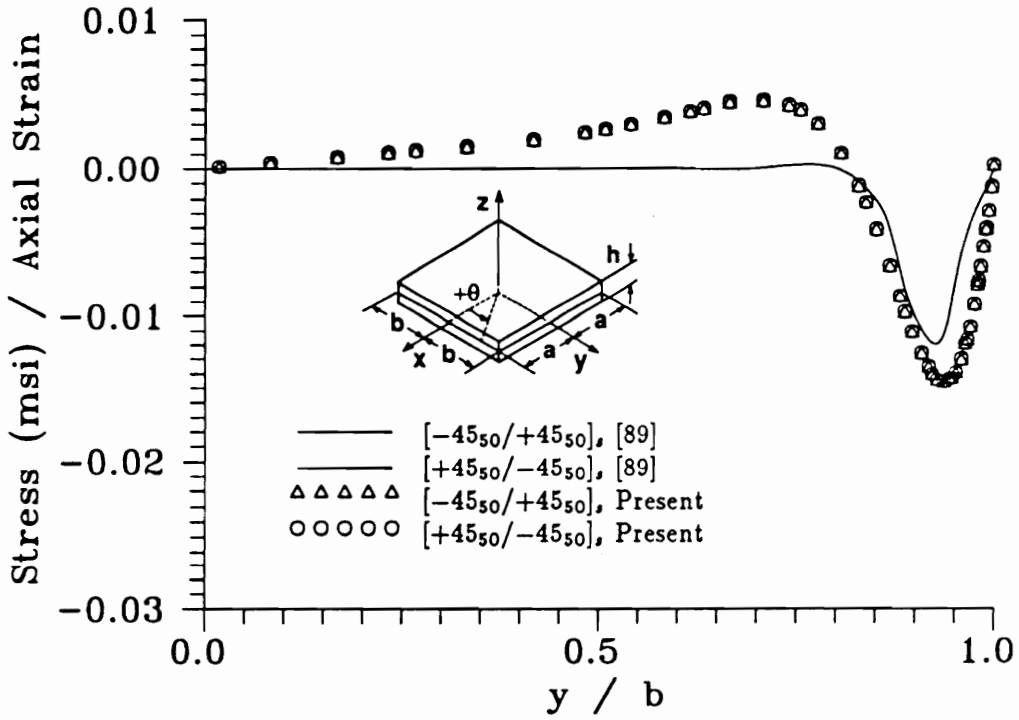

Figure 6.10 Comparison with previous results [89] for τ_{yz} stress at the +45/–45 interface for the 4.0 in. symmetric $+45_{50}/-45_{50}$ laminates ($u/a = +0.01$).

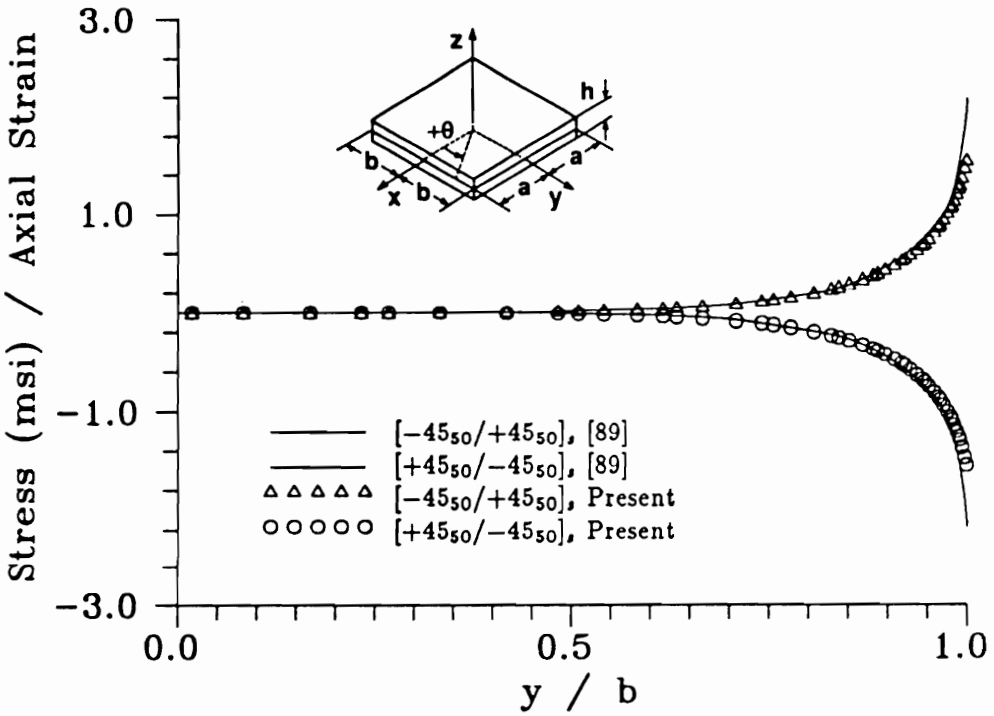

Figure 6.11 Comparison with previous results [89] for τ_{zz} stress at the +45/−45 interface for the 4.0 in. symmetric $+45_{50}/-45_{50}$ laminates ($u/a = +0.01$).

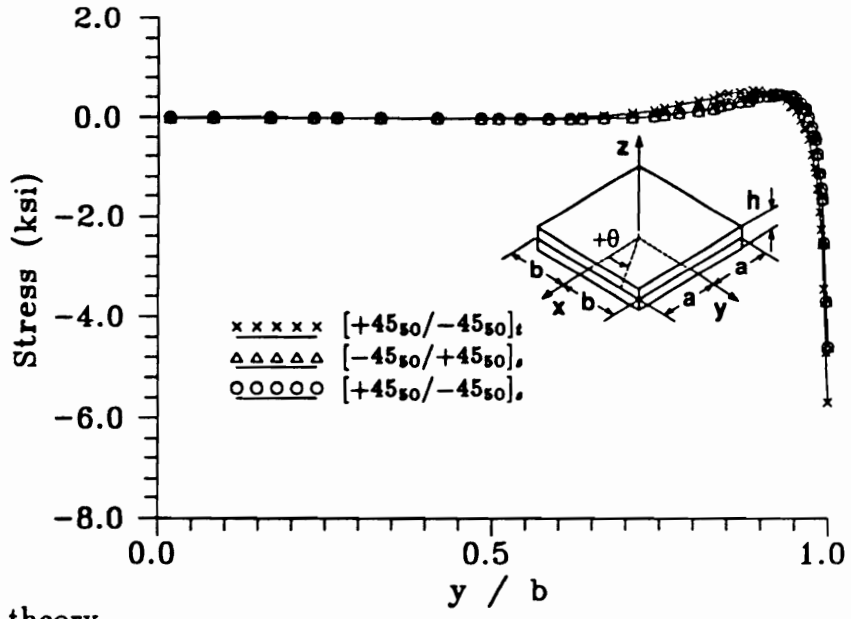

(a) Linear theory

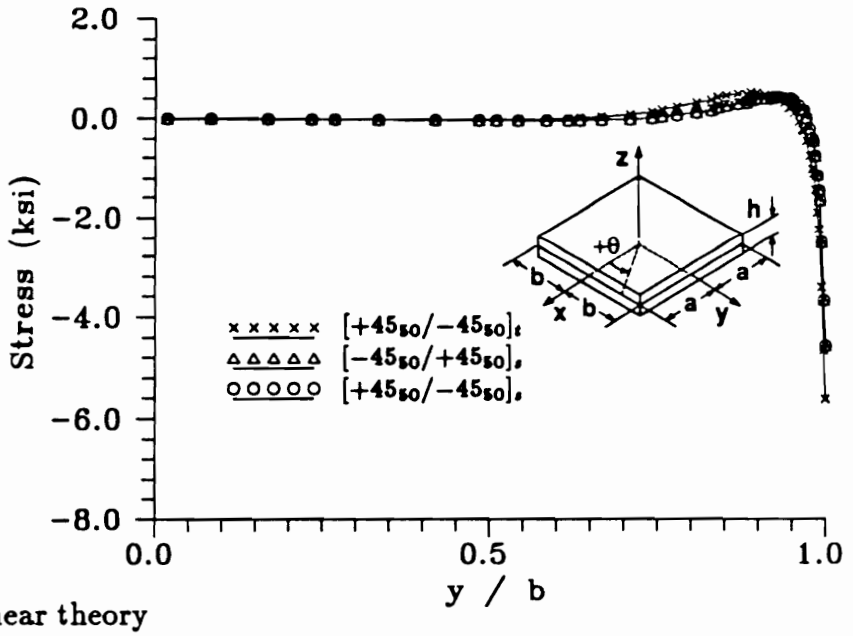

(b) Nonlinear theory

Figure 6.12 σ_{zz} and S_{zz} stress along $x = 0$ at the +45/−45 interface for the 4.0 in. square $+45_{50}/-45_{50}$ laminates ($u/a = +0.01$).

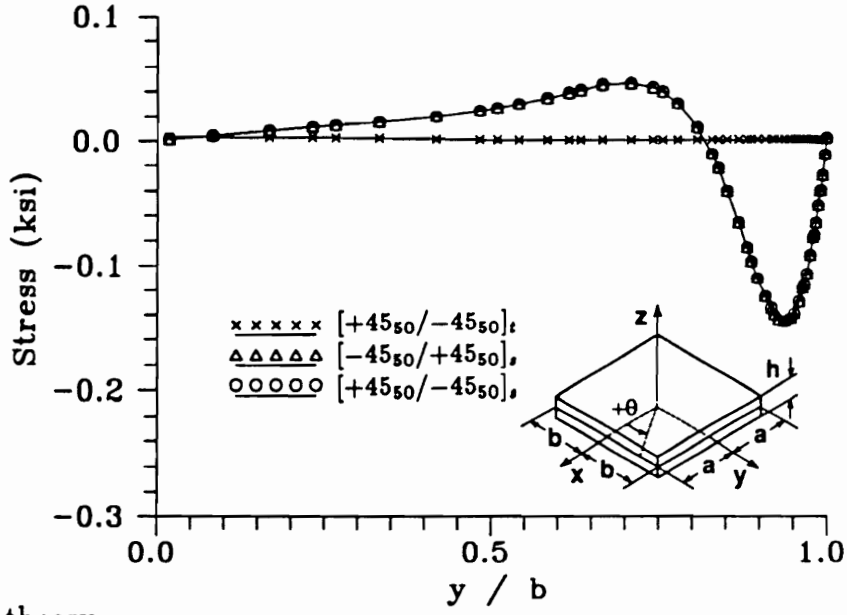

(a) Linear theory

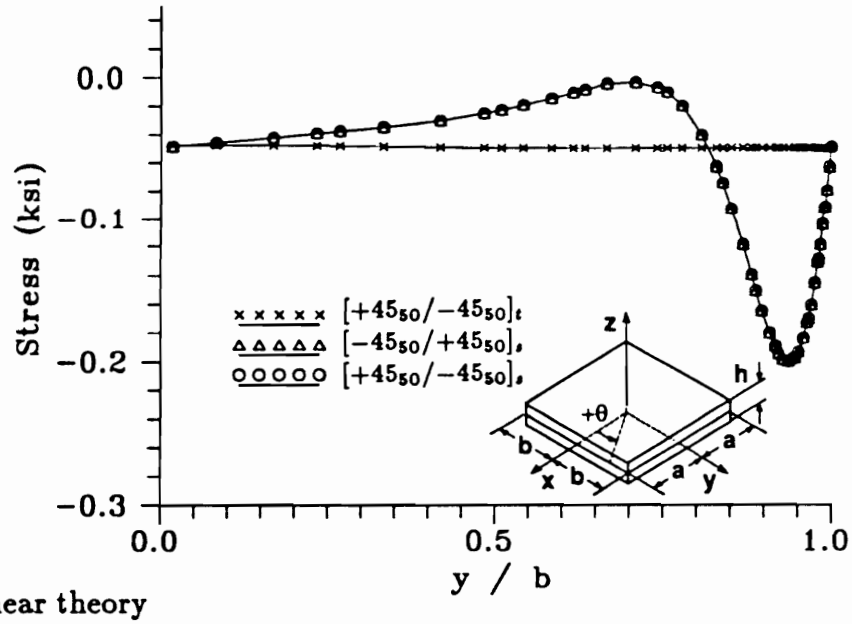

(b) Nonlinear theory

Figure 6.13 τ_{yz} and S_{yz} stress along $x = 0$ at the +45/–45 interface for the 4.0 in. square $+45_{50}/-45_{50}$ laminates ($u/a = +0.01$).

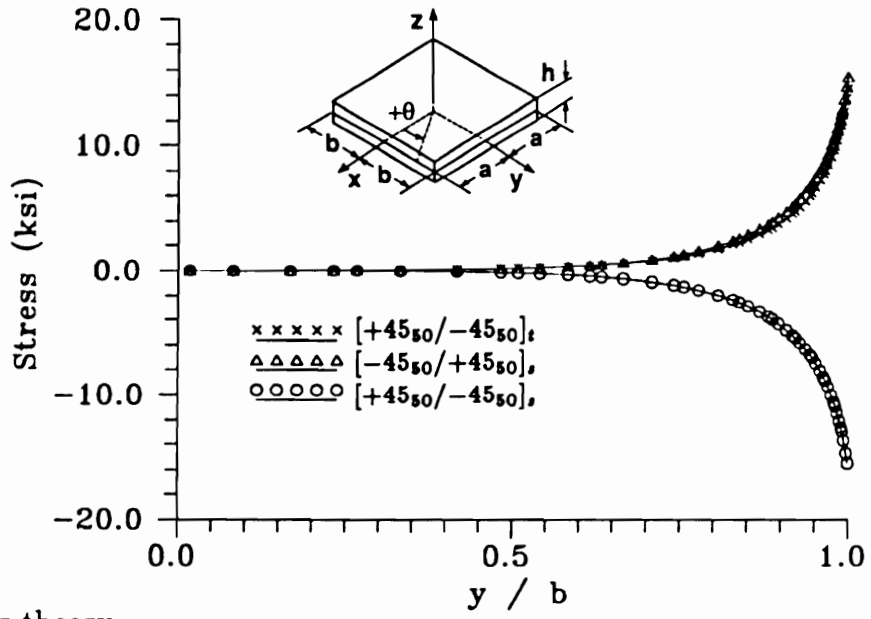

(a) Linear theory

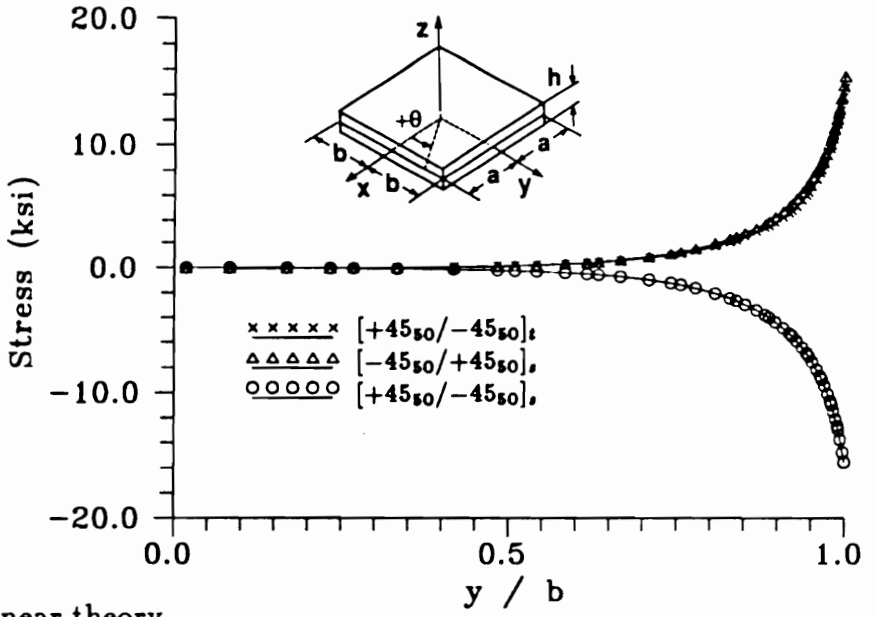

(b) Nonlinear theory

Figure 6.14 τ_{xz} and S_{xz} stress along $x = 0$ at the +45/−45 interface for the 4.0 in. square $+45_{50}/-45_{50}$ laminates ($u/a = +0.01$).

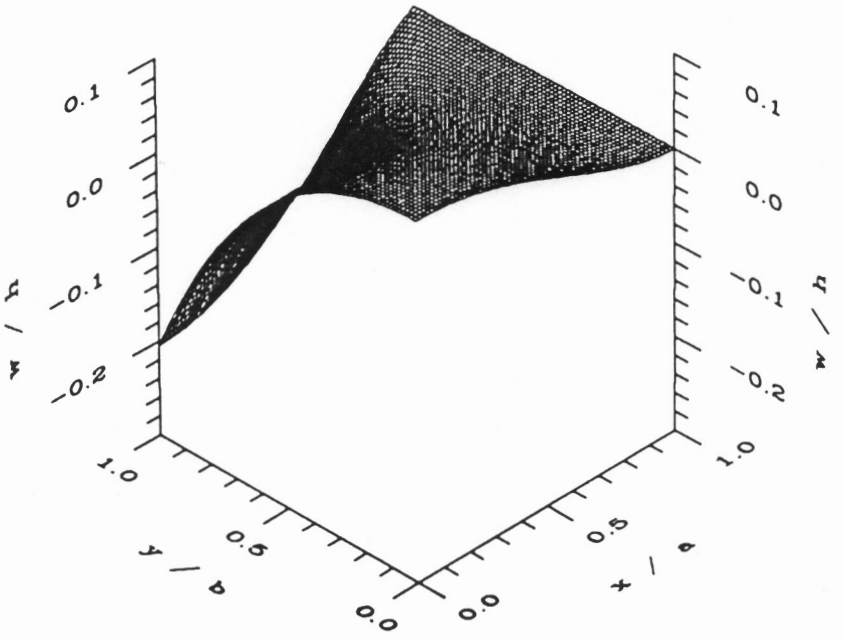

(a) Linear theory

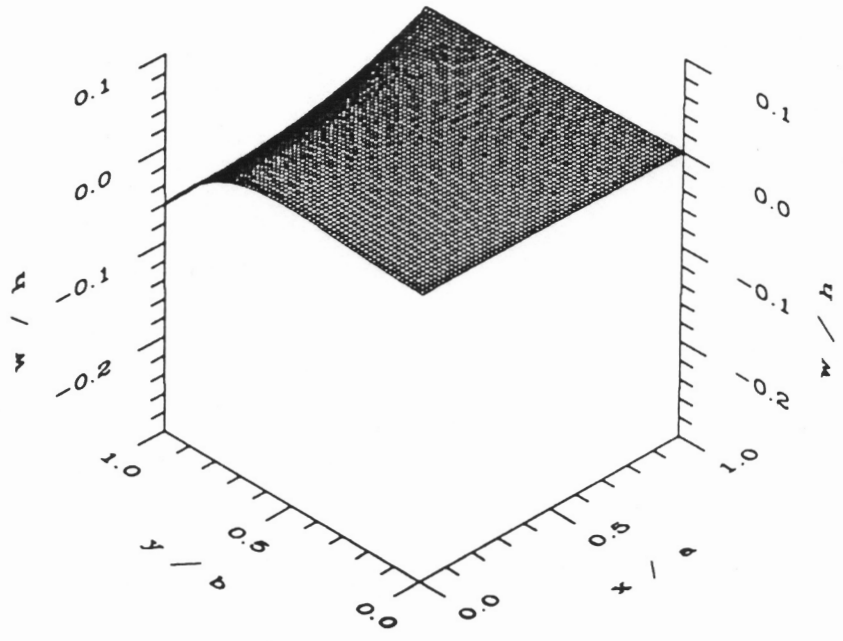

(b) Nonlinear theory

Figure 6.15 Midplane w/h displacement for a 2.0 in. square unsymmetric $[0_4/90_4]_t$ laminate ($u/a = +0.01$).

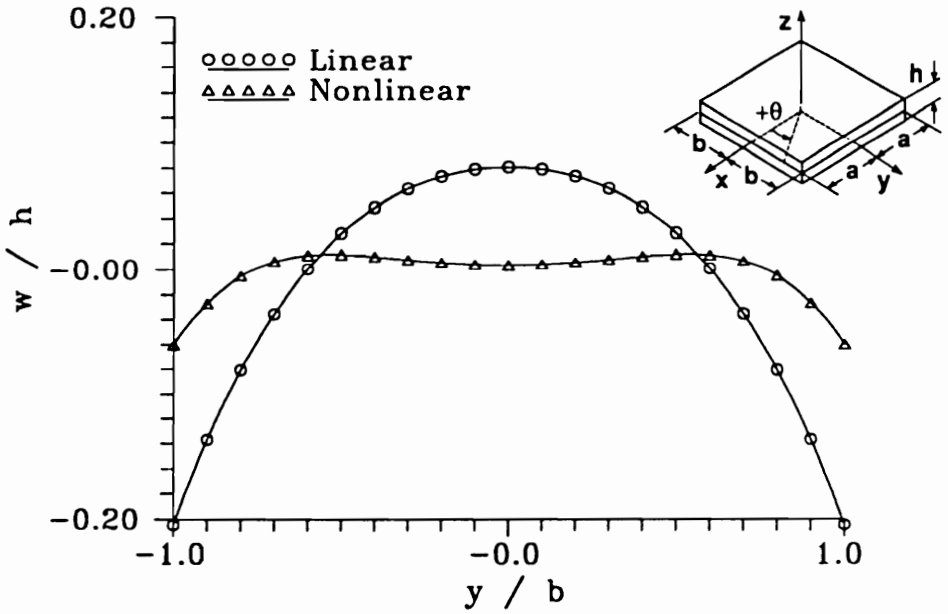

(a) $x = 0$

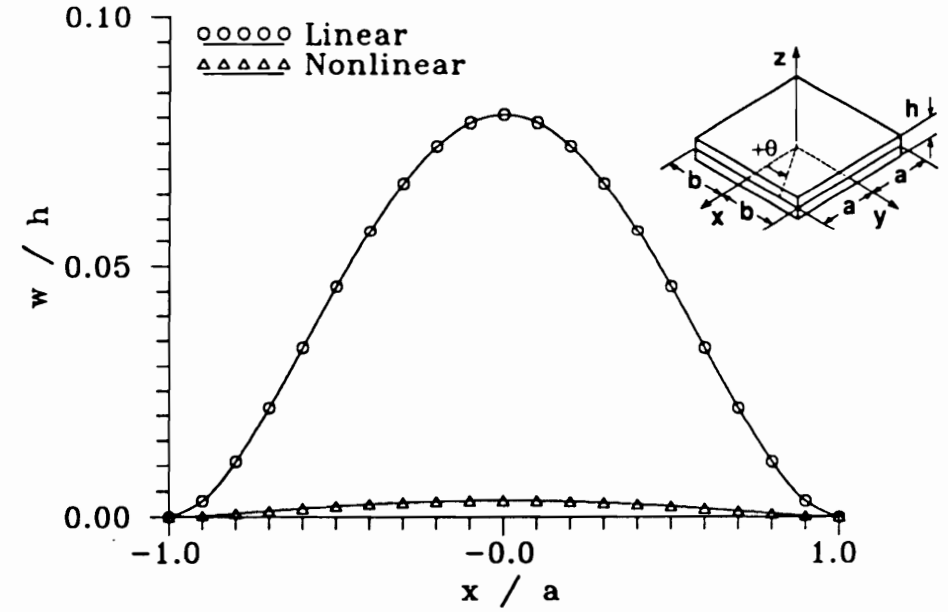

(b) $y = 0$

Figure 6.16 Midplane w/h displacement along $x = 0$ and $y = 0$ for a 2.0 in. square unsymmetric $[0_4/90_4]_t$ laminate ($u/a = +0.01$).

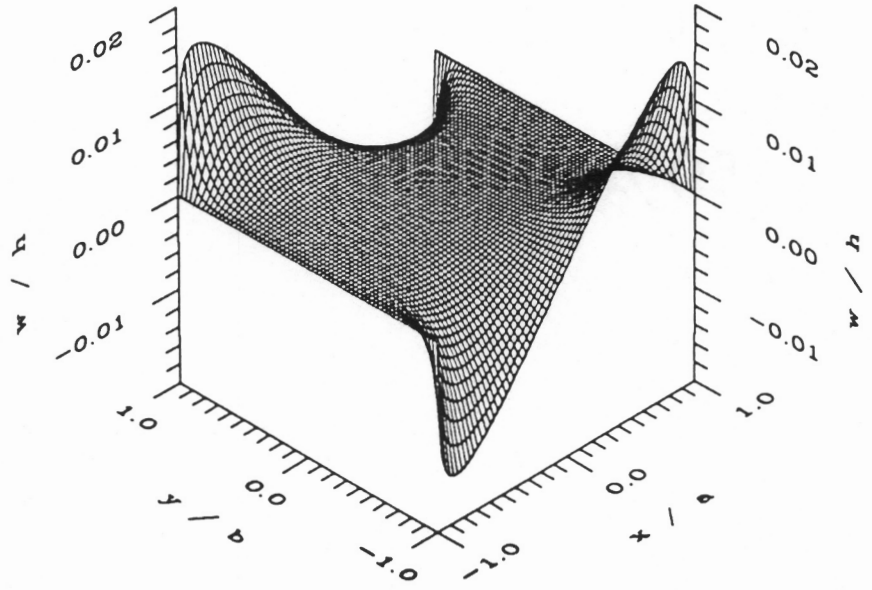

(a) Linear theory

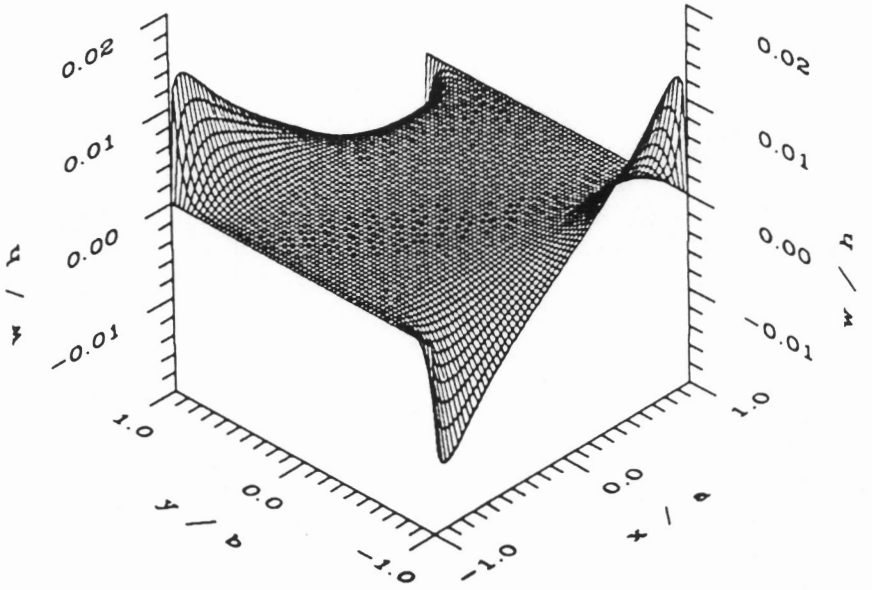

(b) Nonlinear theory

Figure 6.17 Midplane w/h displacement for a 2.0 in. square unsymmetric $[+45_4/-45_4]_t$ laminate ($u/a = +0.01$).

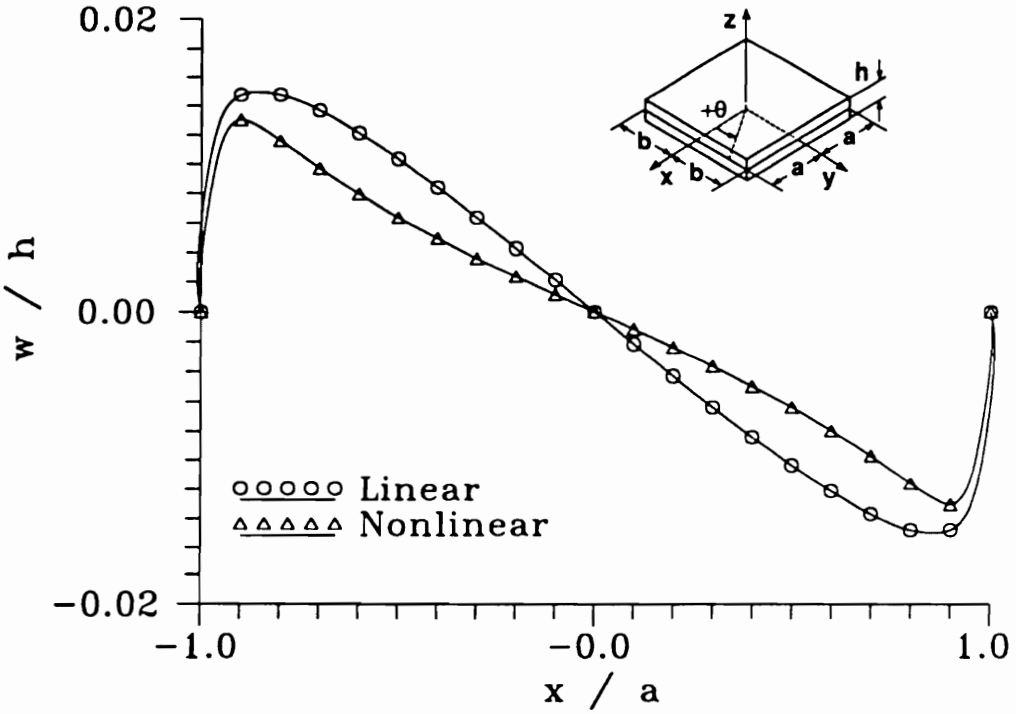

Figure 6.18 Midplane w/h displacement along $y/b = 1$ for a 2.0 in. square unsymmetric $[+45_4/-45_4]_t$ laminate ($u/a = +0.01$).

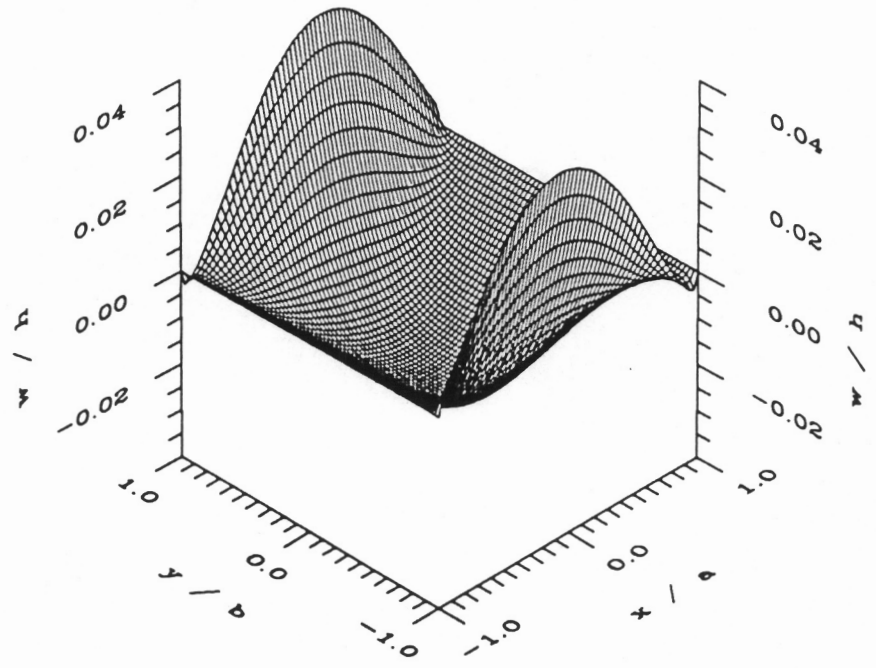

(a) Linear theory

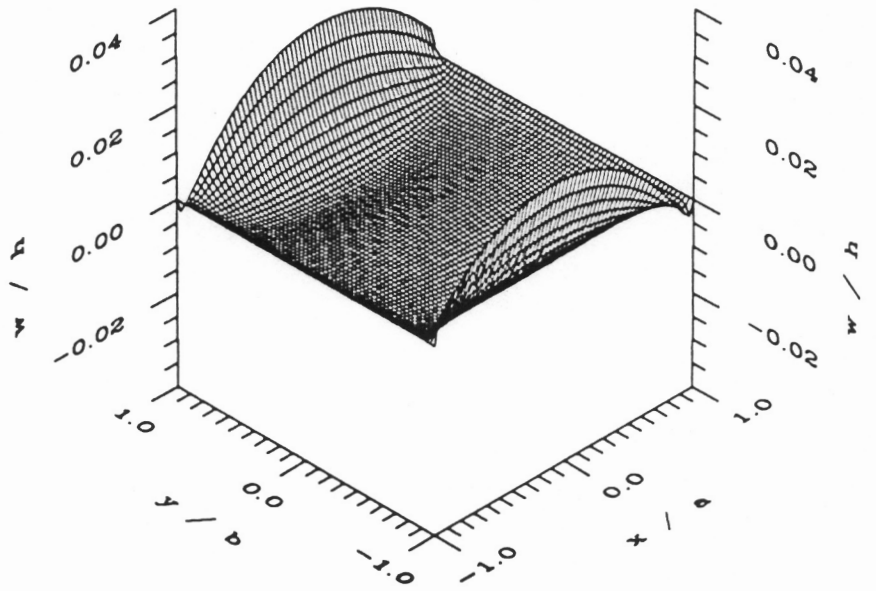

(b) Nonlinear theory

Figure 6.19 Midplane w/h displacement for a 2.0 in. square unsymmetric $[0_4/+45_4]_t$ laminate ($u/a = +0.01$).

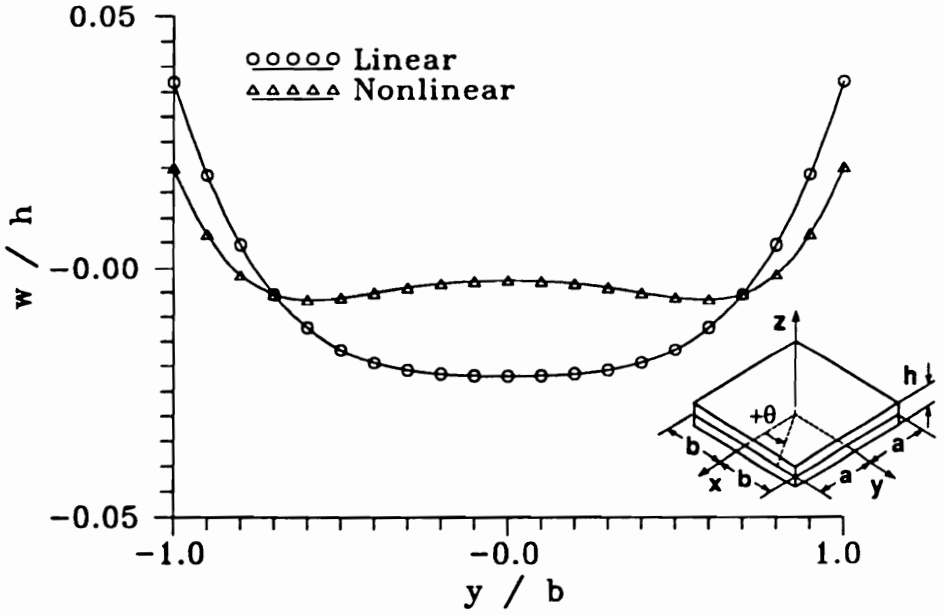

(a) $x = 0$

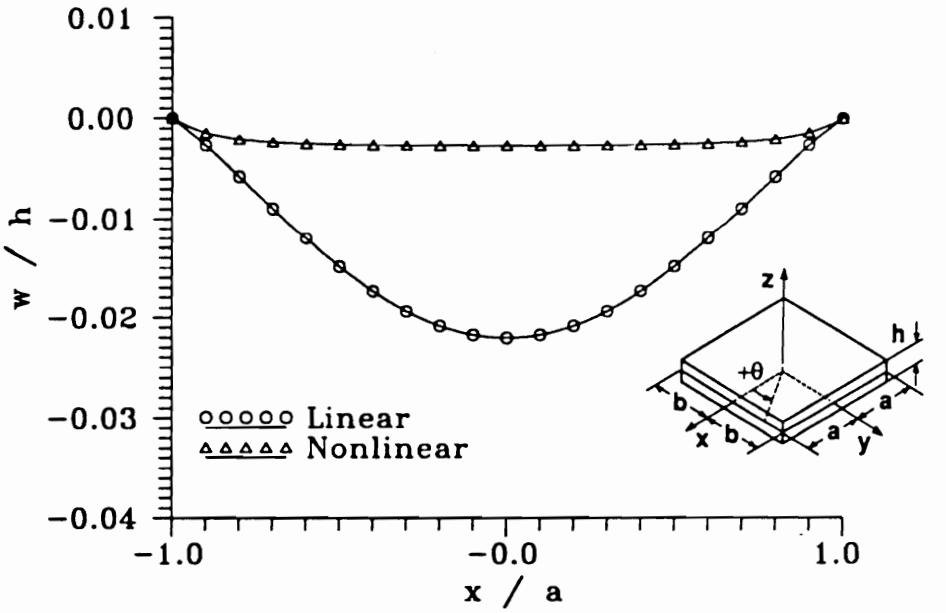

(b) $y = 0$

Figure 6.20 Midplane w/h displacement along $x = 0$ and $y = 0$ for a 2.0 in. square unsymmetric $[0_4/+45_4]_t$ laminate $(u/a = +0.01)$.

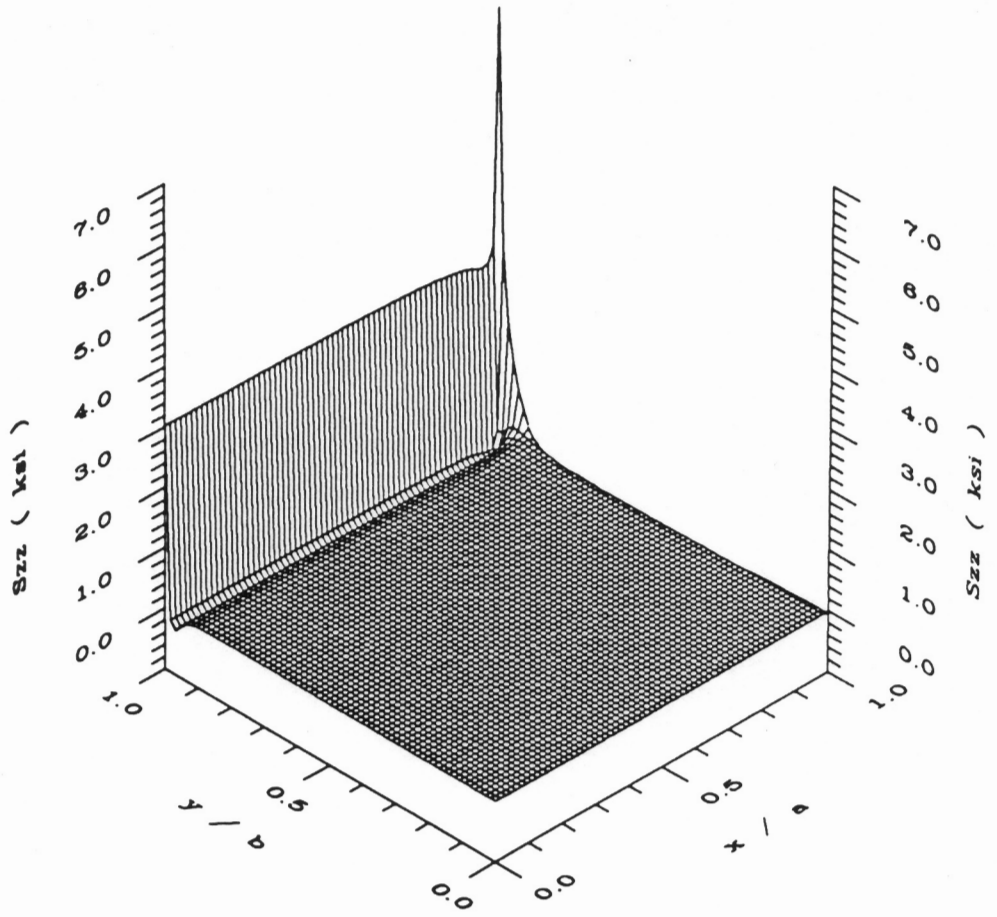

Figure 6.21 S_{zz} stress at the 0/90 interface for a 2.0 in. square unsymmetric $[0_4/90_4]_t$ laminate $(u/a = +0.01)$.

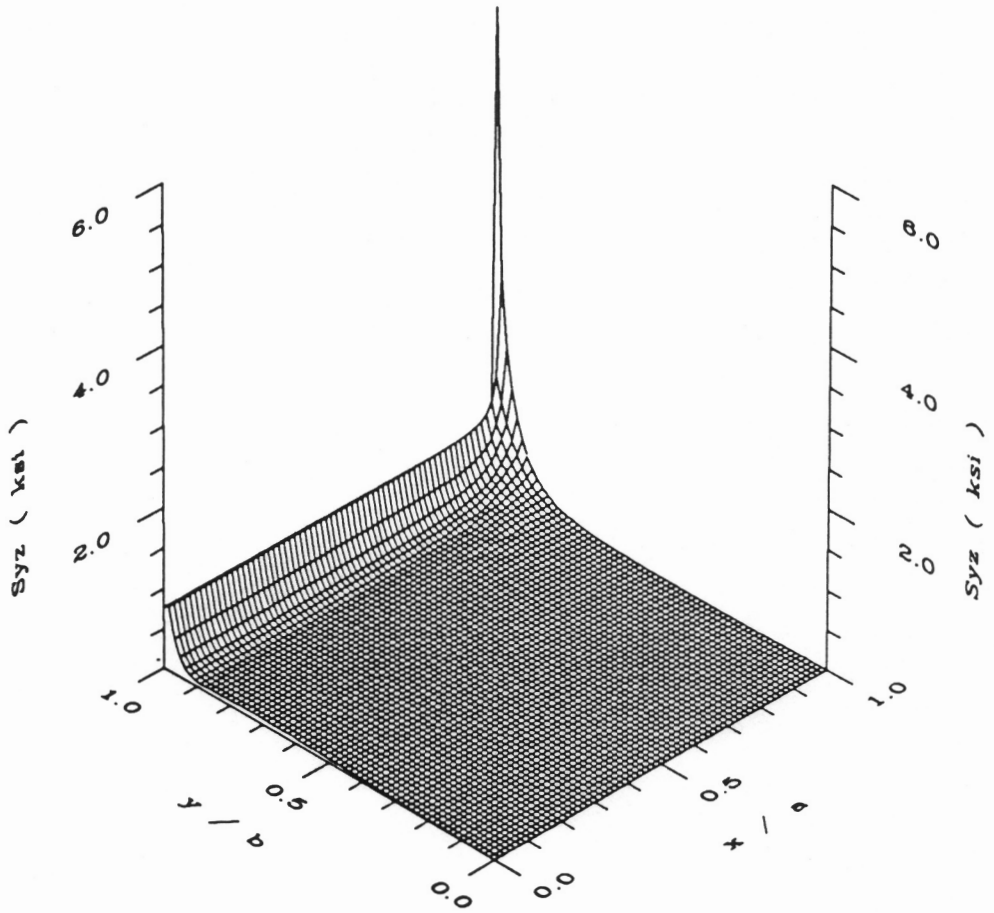

Figure 6.22 S_{yz} stress at the 0/90 interface for a 2.0 in. square unsymmetric $[0_4/90_4]_t$ laminate $(u/a = +0.01)$.

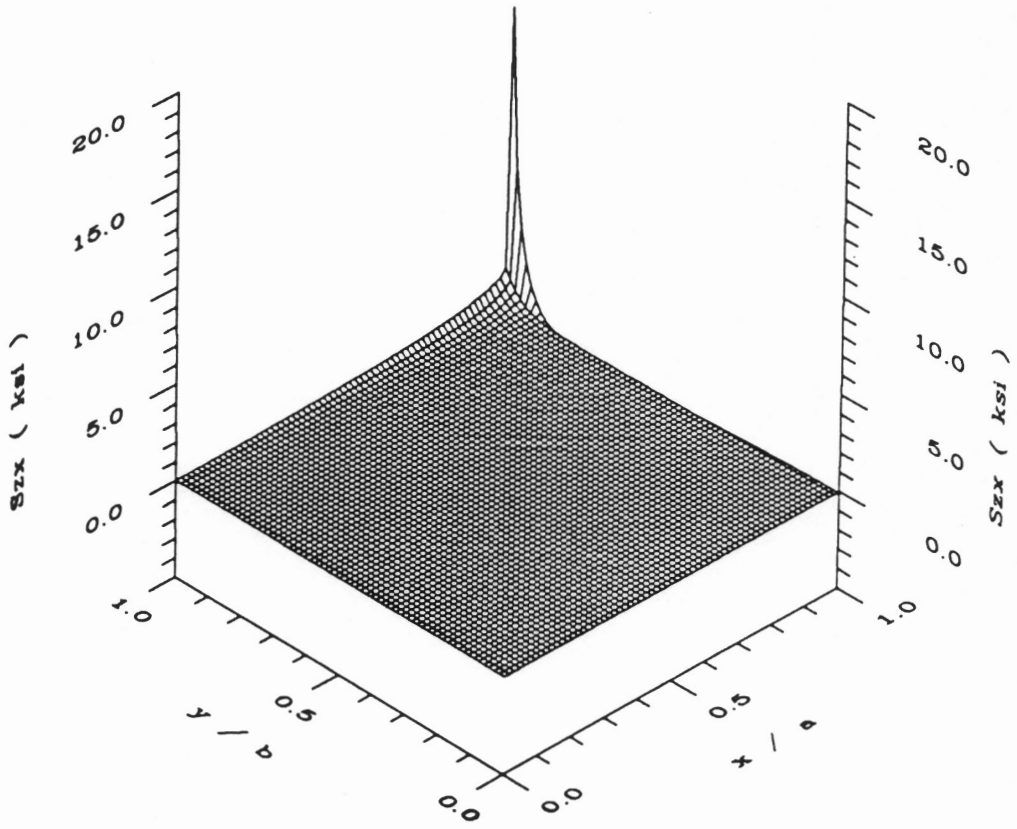

Figure 6.23 S_{zz} stress at the 0/90 interface for a 2.0 in. square unsymmetric $[0_4/90_4]_t$ laminate ($u/a = +0.01$).

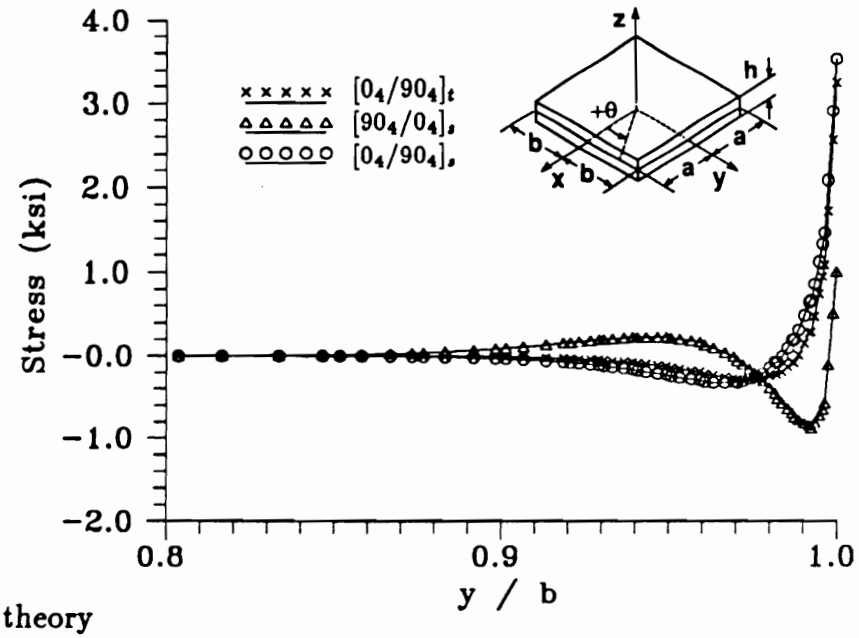

(a) Linear theory

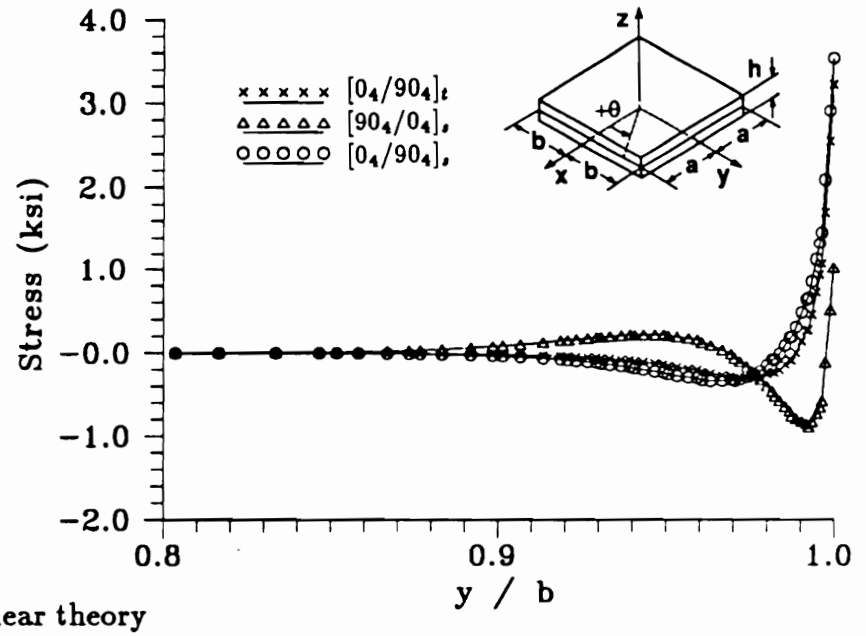

(b) Nonlinear theory

Figure 6.24 σ_{zz} and S_{zz} stress along $x = 0$ at the 0/90 interface for the 2.0 in. square $0_4/90_4$ laminates ($u/a = +0.01$, local analysis).

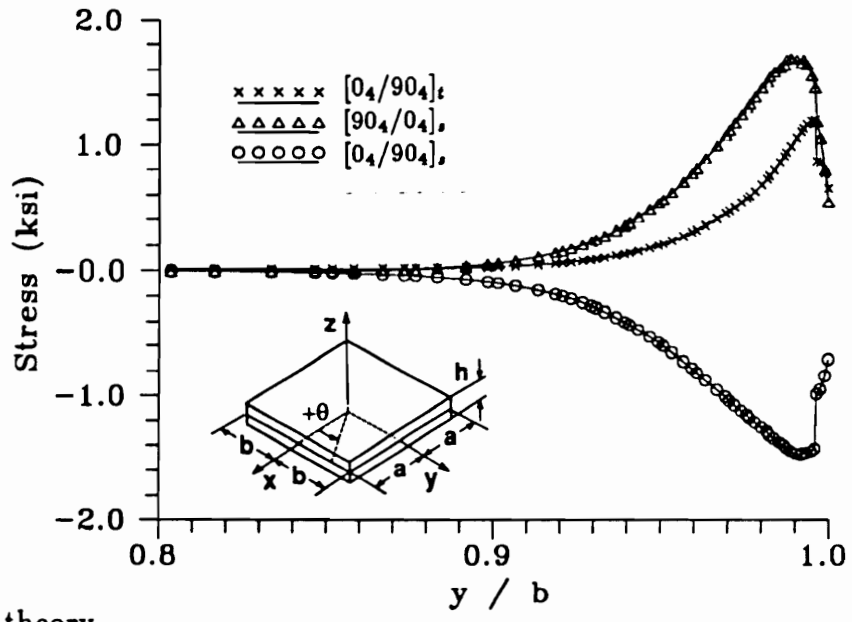

(a) Linear theory

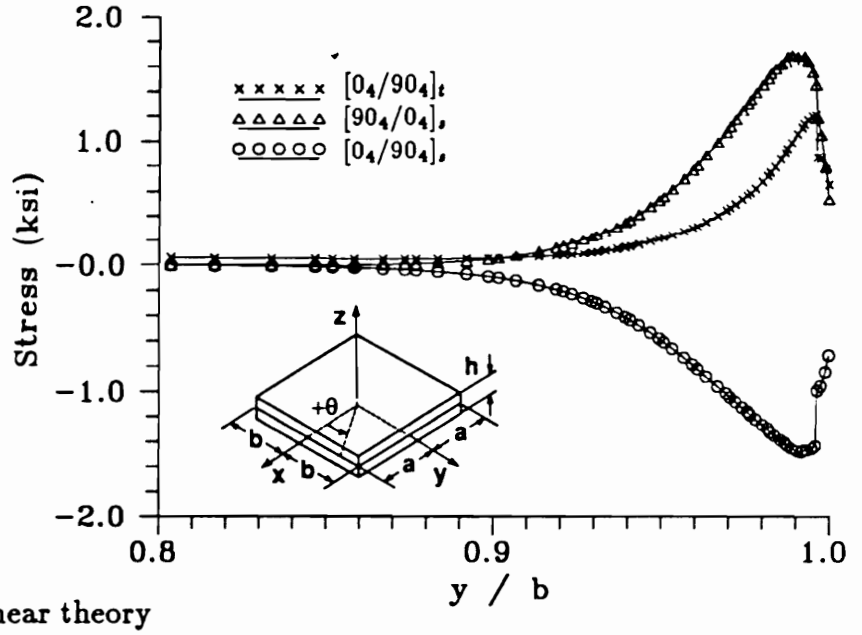

(b) Nonlinear theory

Figure 6.25 τ_{yz} and S_{yz} stress along $x = 0$ at the 0/90 interface for the 2.0 in. square $0_4/90_4$ laminates ($u/a = +0.01$, local analysis).

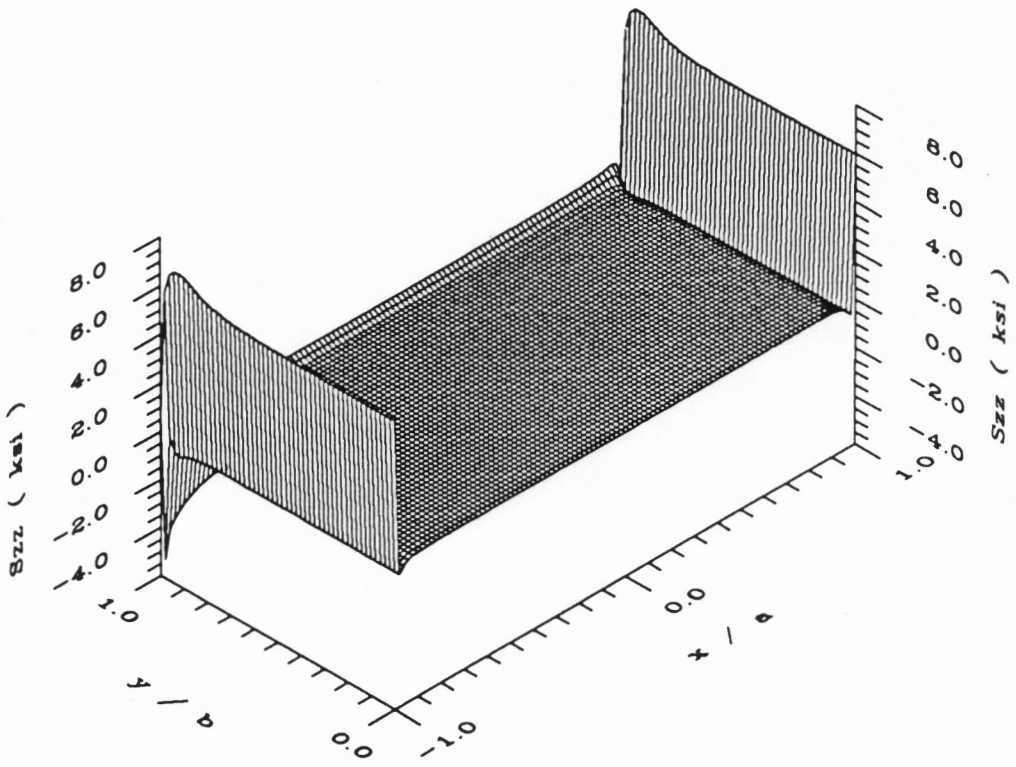

Figure 6.26 S_{zz} stress at the +45/–45 interface for a 2.0 in. square unsymmetric $[+45_4/-45_4]_t$ laminate $(u/a = +0.01)$.

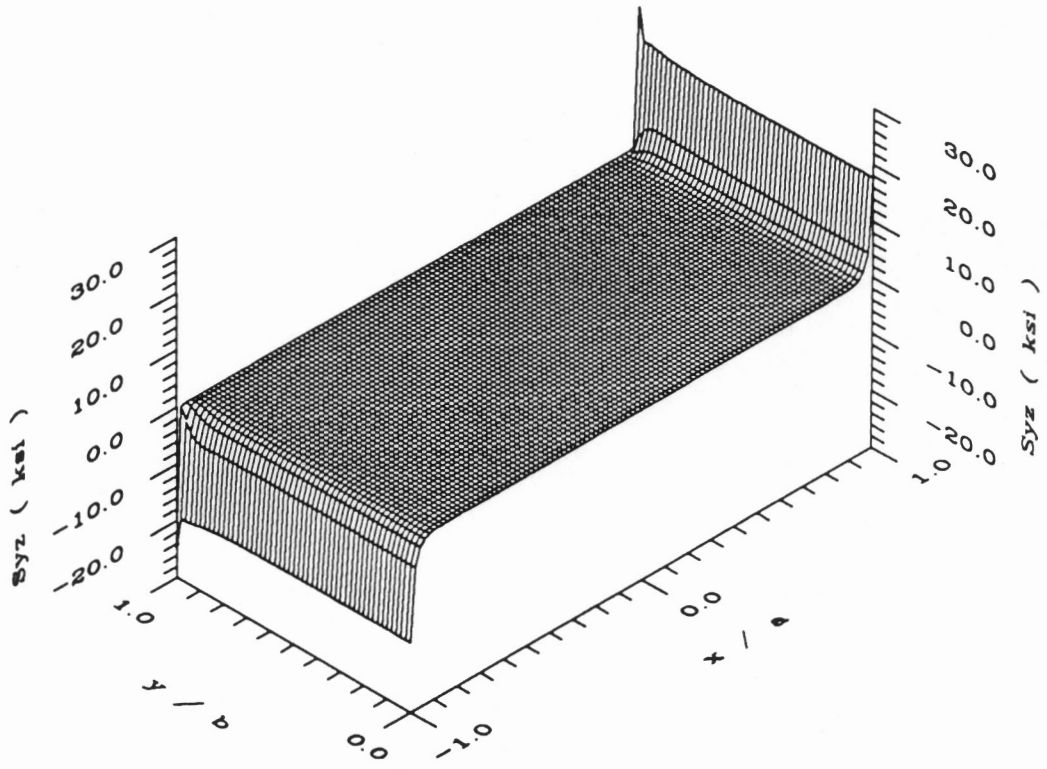

Figure 6.27 S_{yz} stress at the +45/–45 interface for a 2.0 in. square unsymmetric $[+45_4/-45_4]_t$ laminate ($u/a = +0.01$).

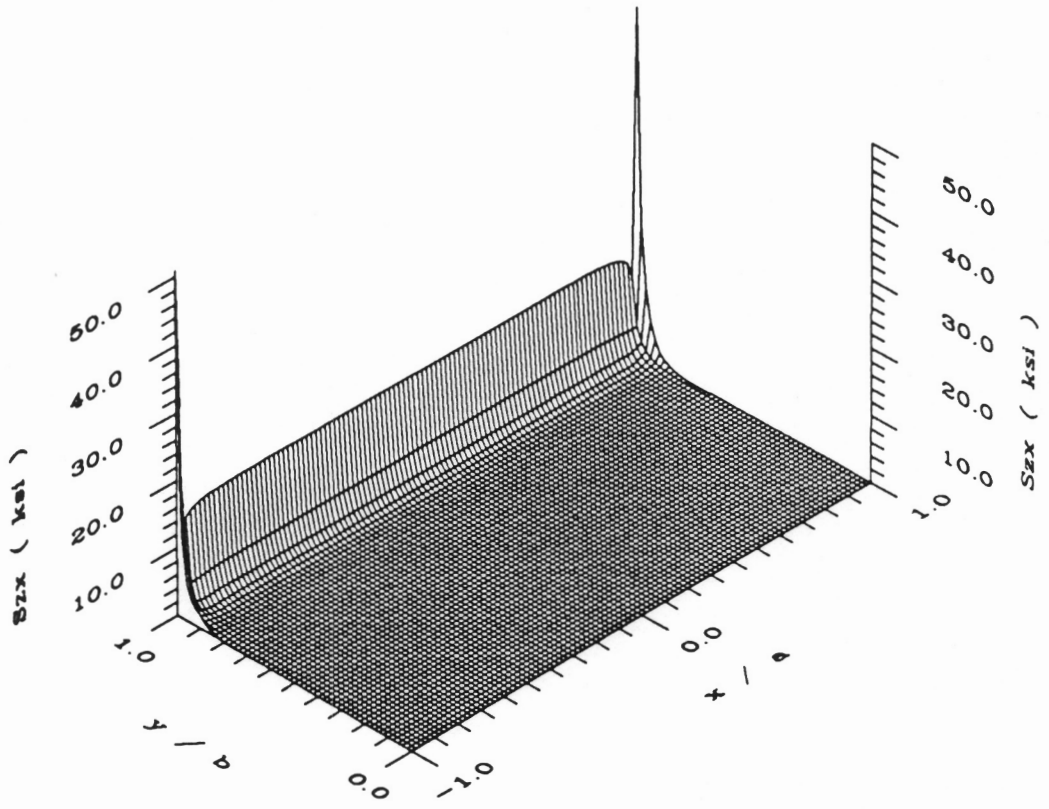

Figure 6.28 S_{zz} stress at the +45/–45 interface for a 2.0 in. square unsymmetric $[+45_4/-45_4]_t$ laminate ($u/a = +0.01$).

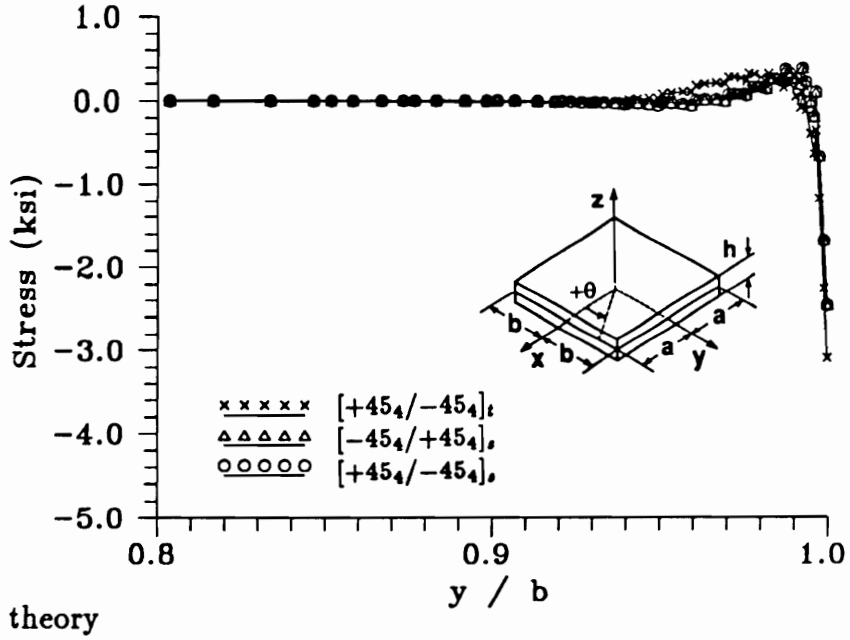

(a) Linear theory

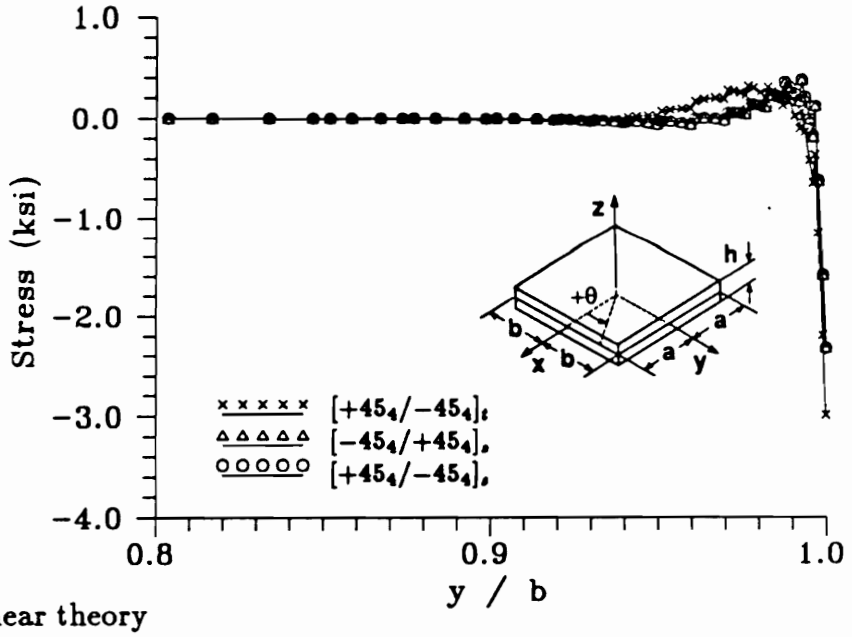

(b) Nonlinear theory

Figure 6.29 σ_{zz} and S_{zz} stress along $x = 0$ at the +45/−45 interface for the 2.0 in. square $+45_4/-45_4$ laminates ($u/a = +0.01$, local analysis).

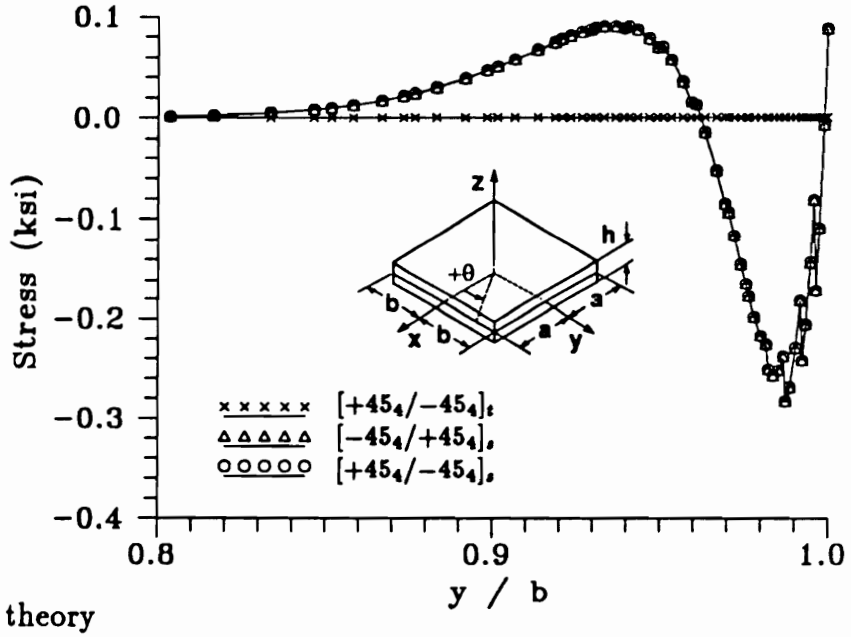

(a) Linear theory

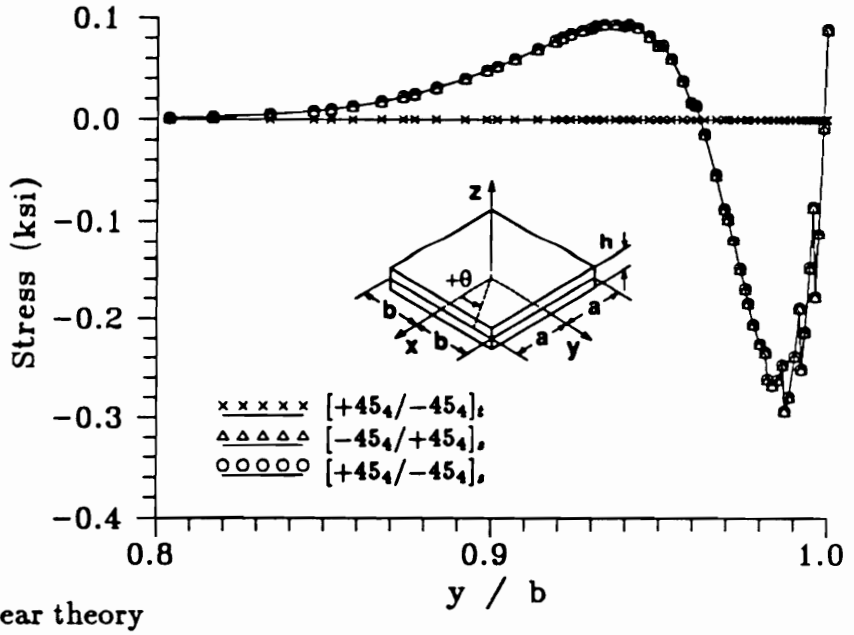

(b) Nonlinear theory

Figure 6.30 τ_{yz} and S_{yz} stress along $x = 0$ at the +45/−45 interface for the 2.0 in. square $+45_4/-45_4$ laminates ($u/a = +0.01$, local analysis).

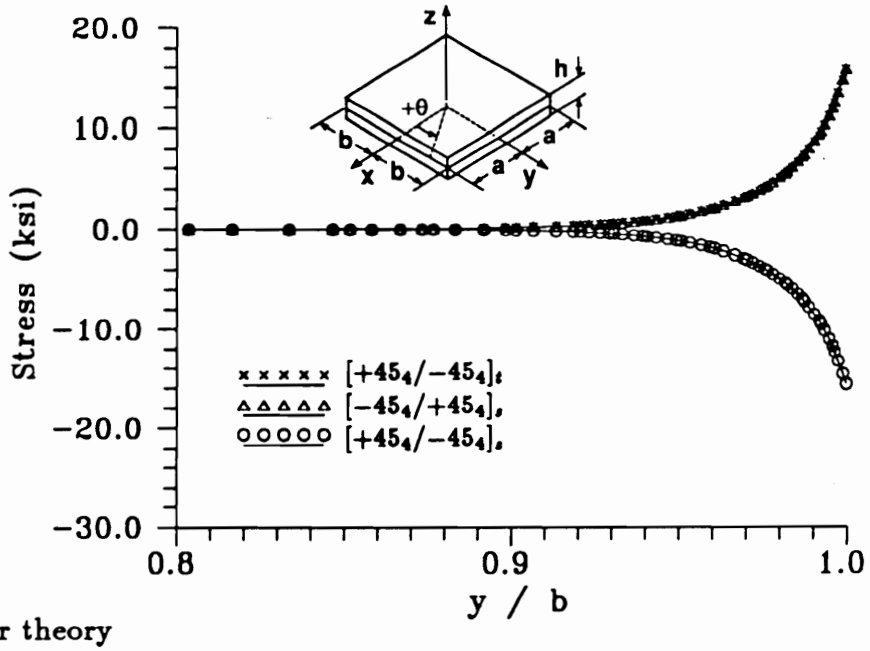

(a) Linear theory

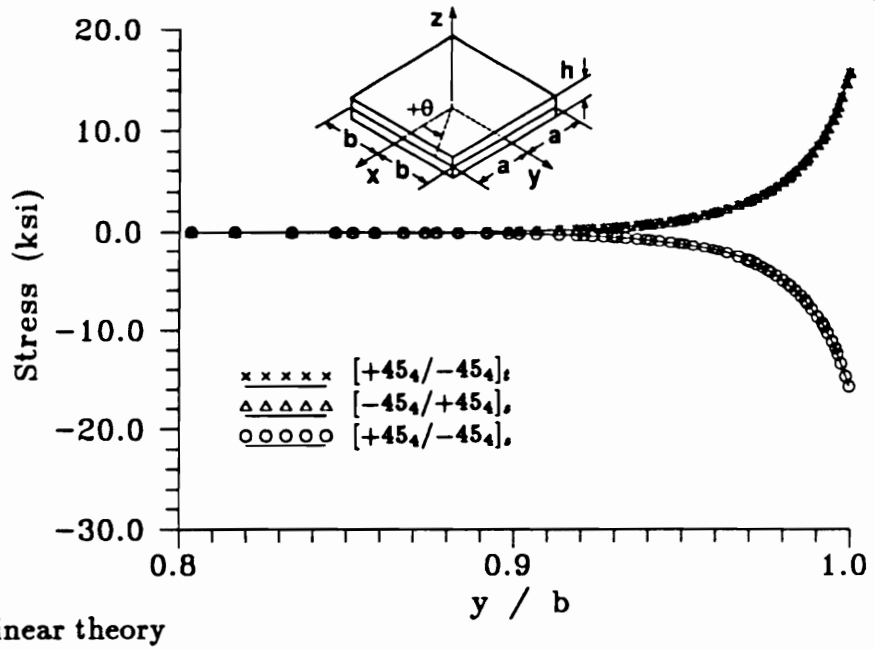

(b) Nonlinear theory

Figure 6.31 τ_{zz} and S_{zz} stress along $x = 0$ at the +45/−45 interface for the 2.0 in. square $-45_4/+45_4$ laminates ($u/a = +0.01$, local analysis).

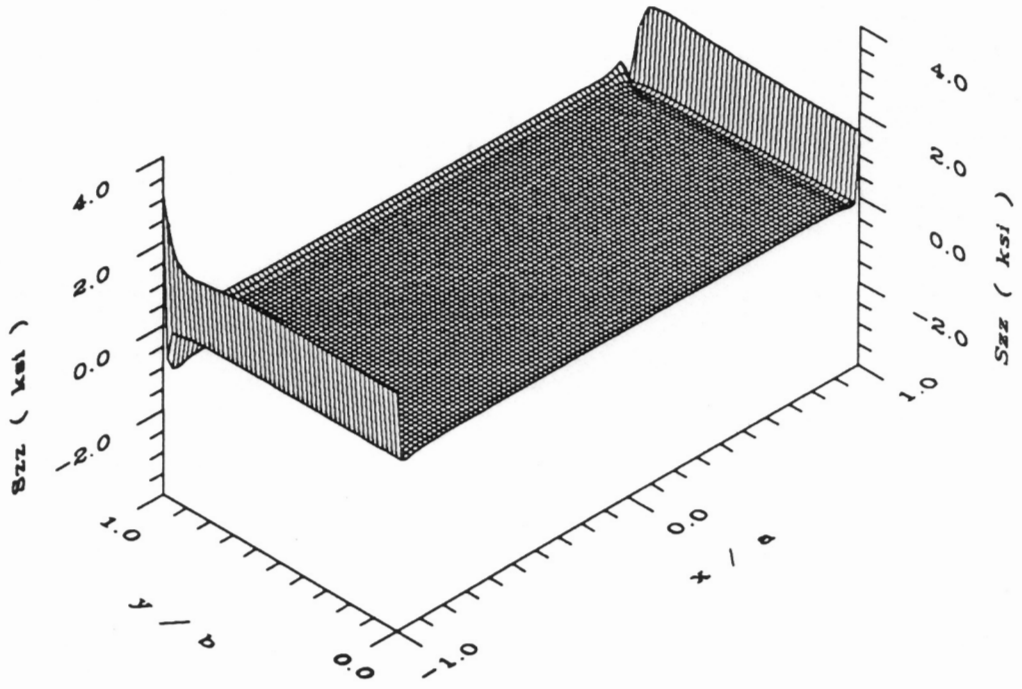

Figure 6.32 S_{zz} stress at the $0/+45$ interface for a 2.0 in. square unsymmetric $[0_4/+45_4]_t$ laminate $(u/a = +0.01)$.

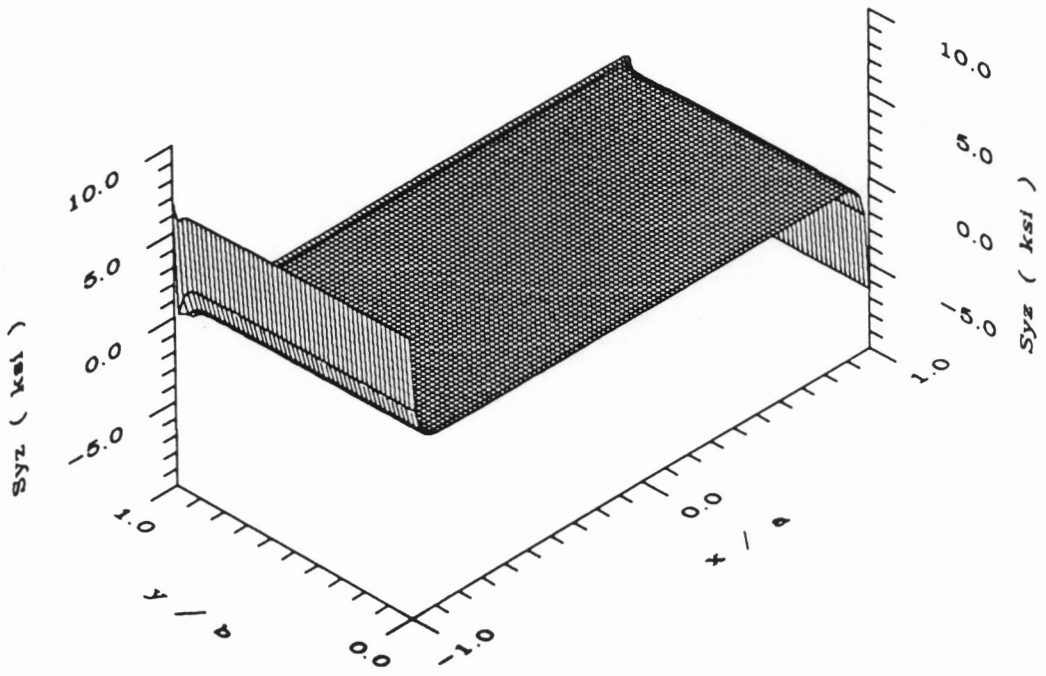

Figure 6.33 S_{yz} stress at the $0/+45$ interface for a 2.0 in. square unsymmetric $[0_4/+45_4]_t$ laminate $(u/a = +0.01)$.

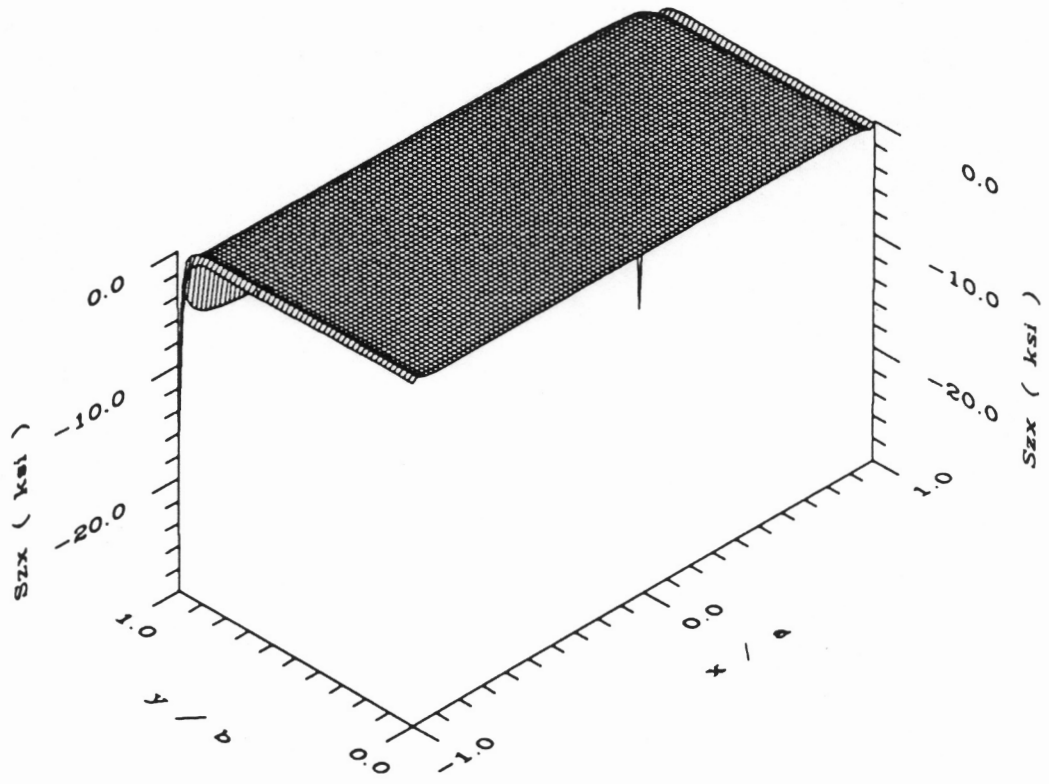

Figure 6.34 S_{zx} stress at the 0/+45 interface for a 2.0 in. square unsymmetric $[0_4/+45_4]_t$ laminate ($u/a = +0.01$).

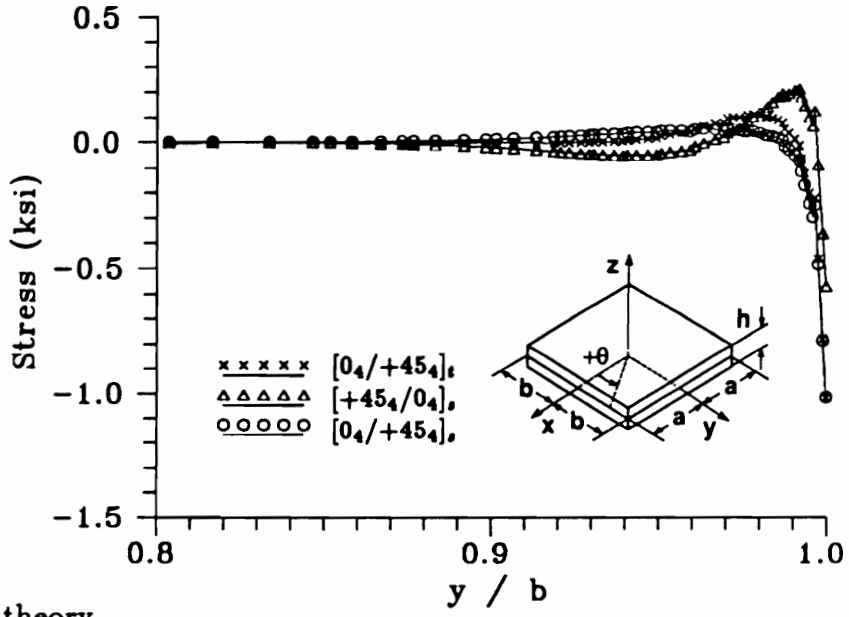

(a) Linear theory

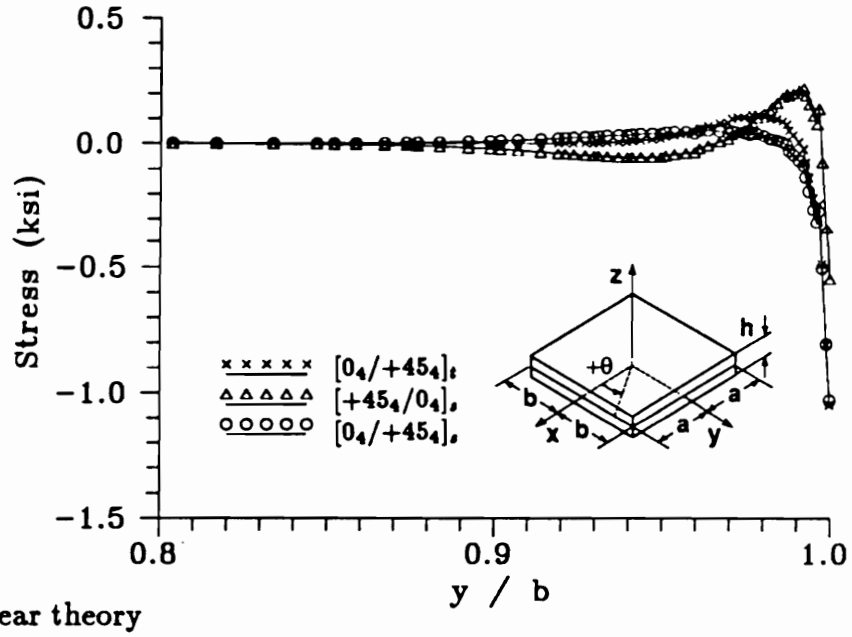

(b) Nonlinear theory

Figure 6.35 σ_{zz} and S_{zz} stress along $x = 0$ at the $0/+45$ interface for the 2.0 in. square $0_4/+45_4$ laminates ($u/a = +0.01$, local analysis).

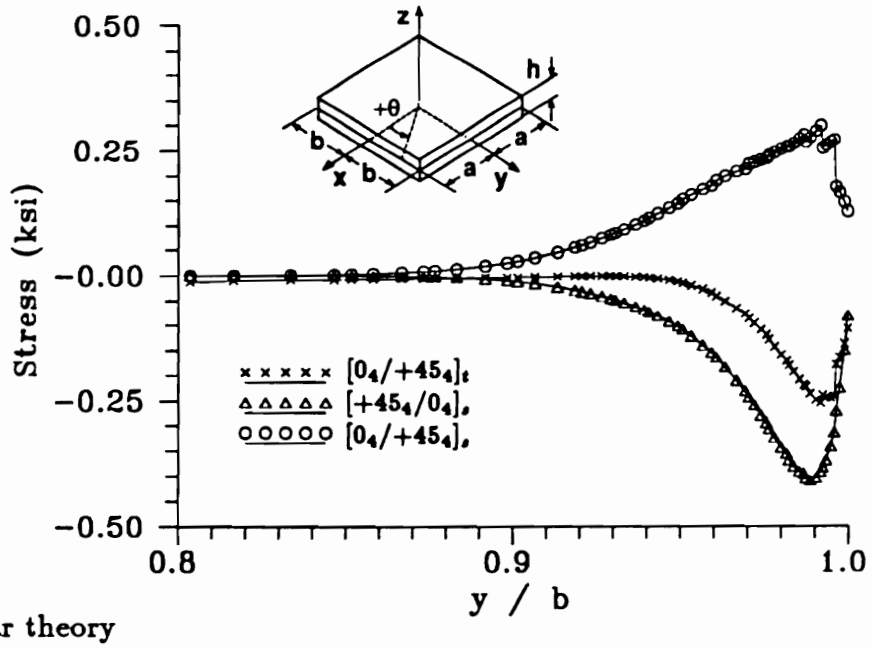

(a) Linear theory

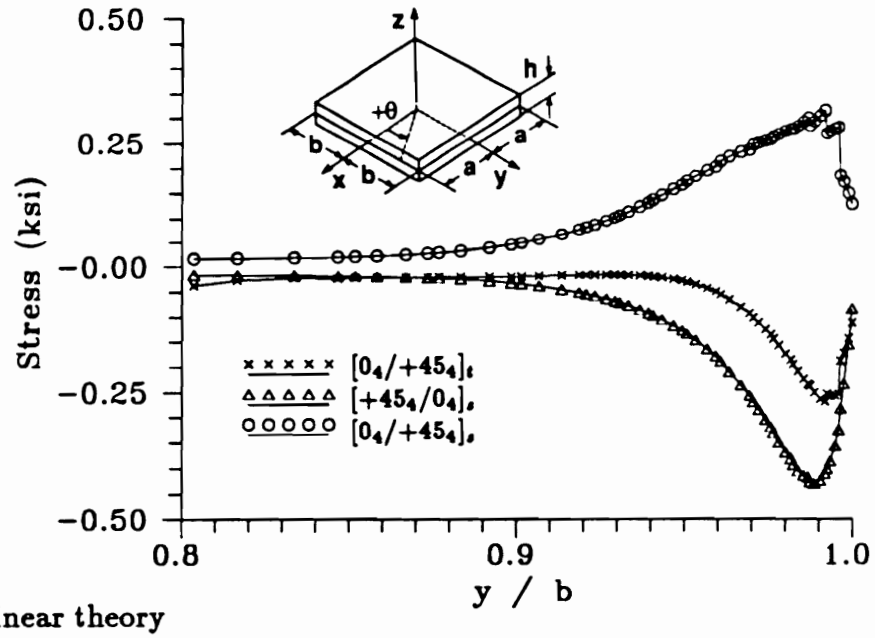

(b) Nonlinear theory

Figure 6.36 τ_{yz} and S_{yz} stress along $x = 0$ at the $0/+45$ interface for the 2.0 in. square $0_4/+45_4$ laminates ($u/a = +0.01$, local analysis).

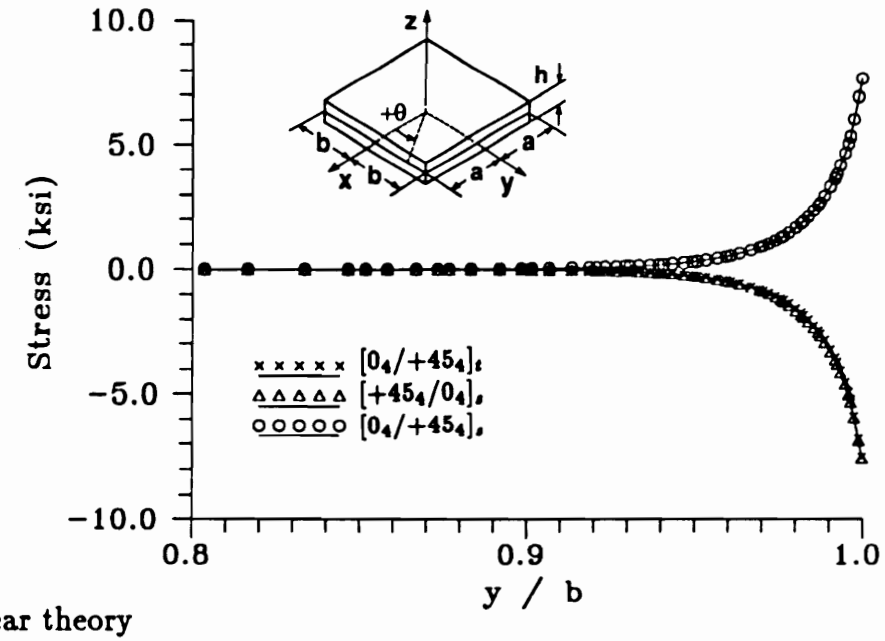

(a) Linear theory

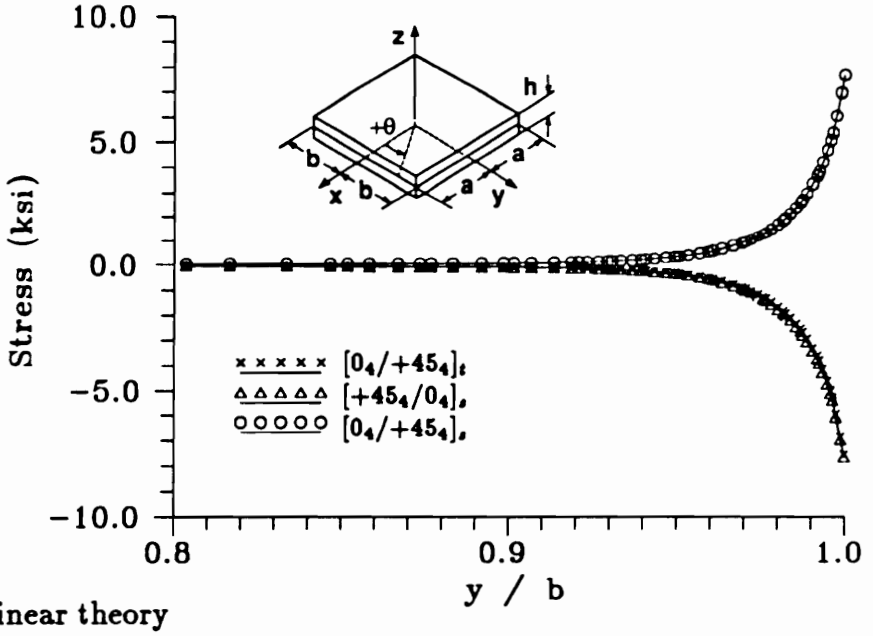

(b) Nonlinear theory

Figure 6.37 τ_{xz} and S_{xz} stress along $x = 0$ at the 0/+45 interface for the 2.0 in. square $0_4/+45_4$ laminates ($u/a = +0.01$, local analysis).

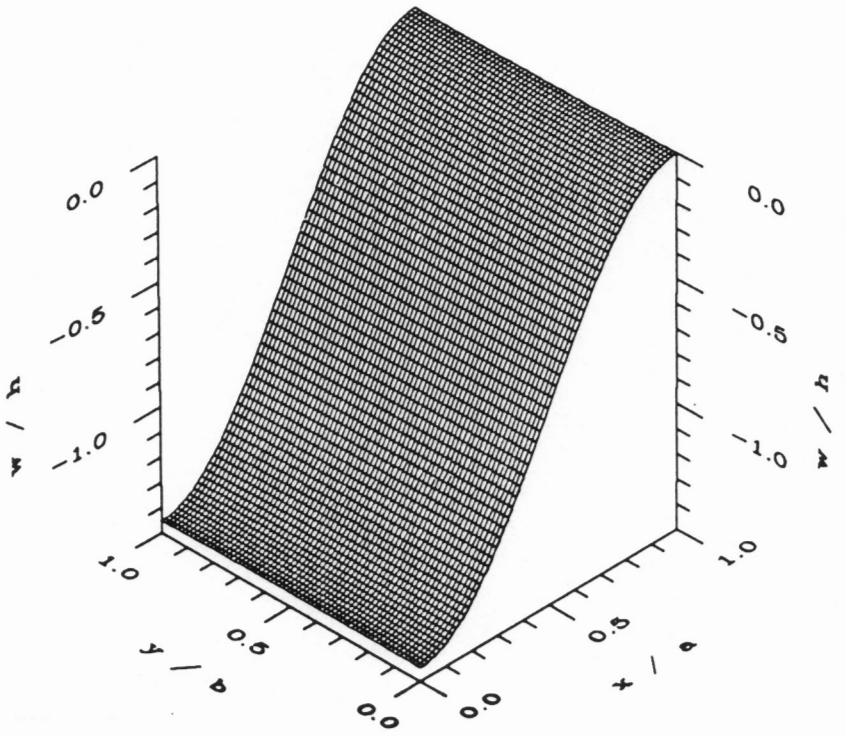

(a) $[90_4/0_4]_s$ laminate

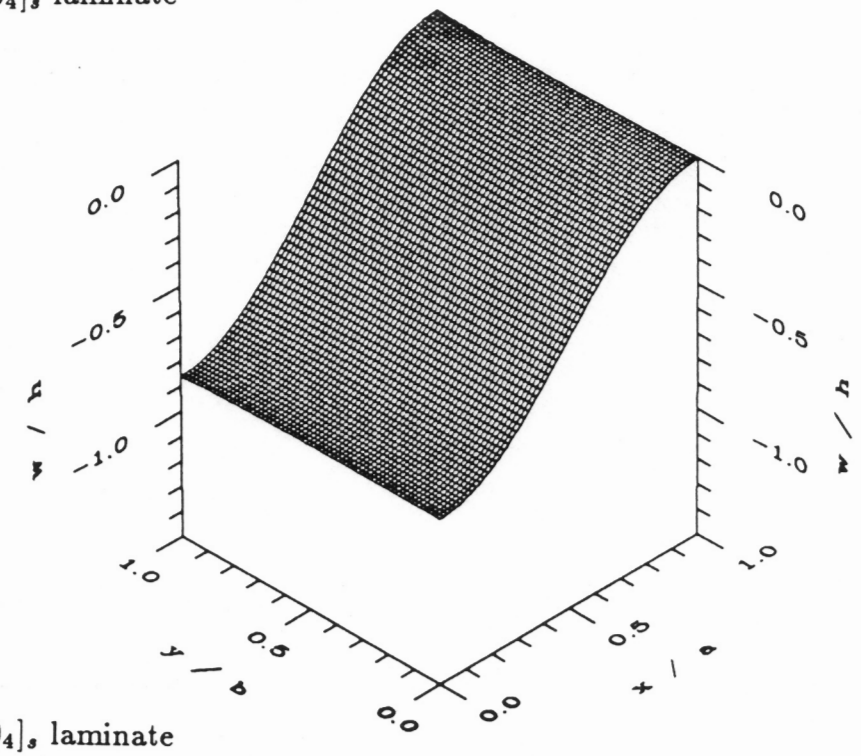

(b) $[0_4/90_4]_s$ laminate

Figure 6.38 Midplane w/h displacement for the 2.0 in. square symmetric $[90_4/0_4]_s$ and $[0_4/90_4]_s$ laminates ($u/a = -0.01$).

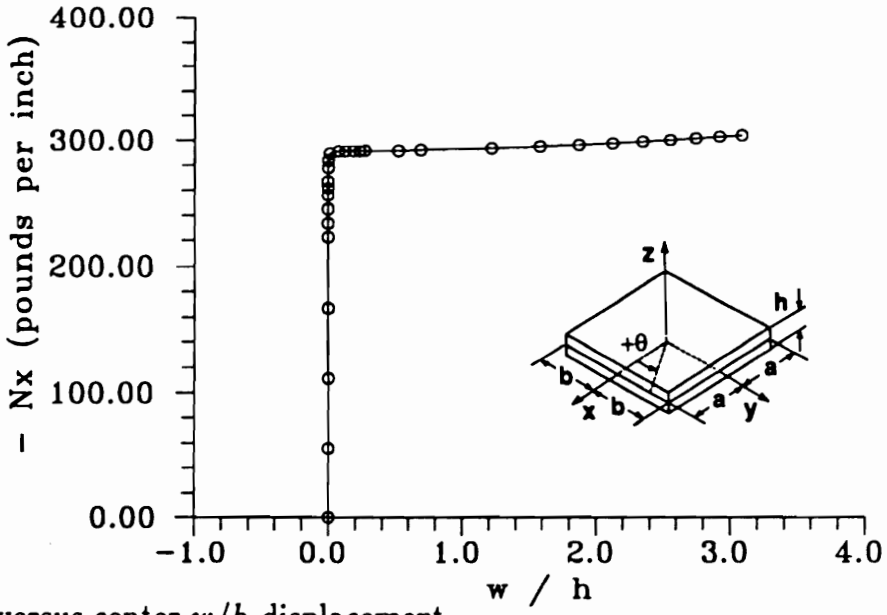

(a) N_x versus center w/h displacement

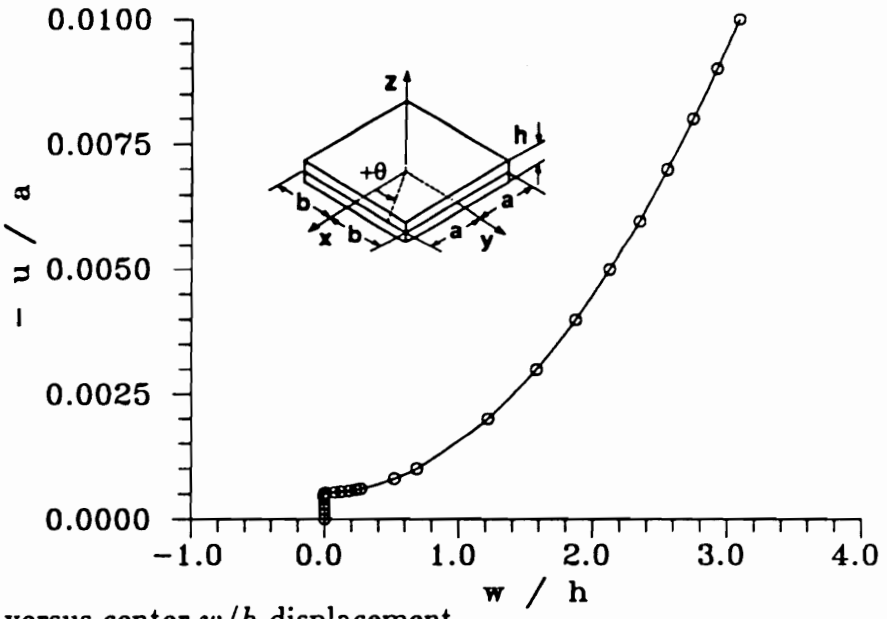

(b) u/a versus center w/h displacement

Figure 6.39 Load-displacement plots for a 2.0 in. square unsymmetric $[0_4/90_4]_t$ laminate ($u/a = -0.01$).

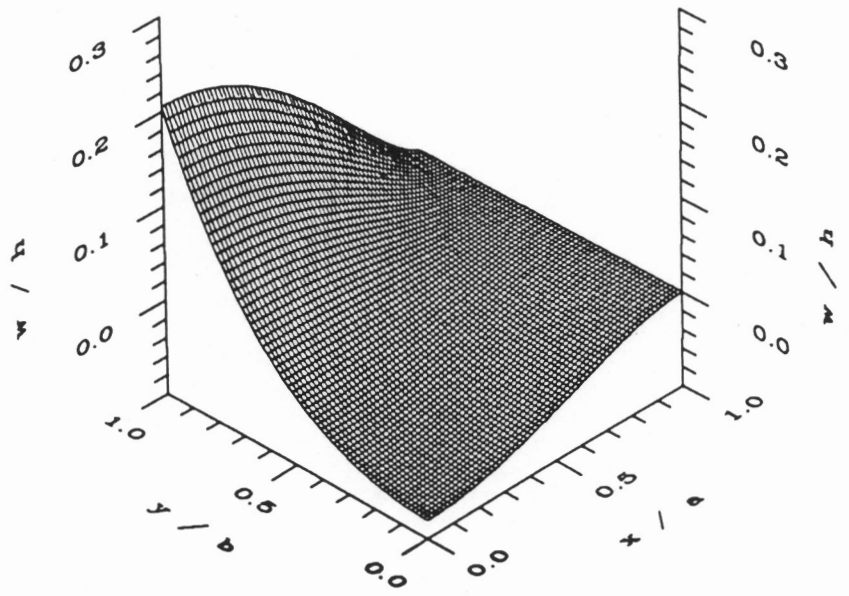

(a) Linear theory

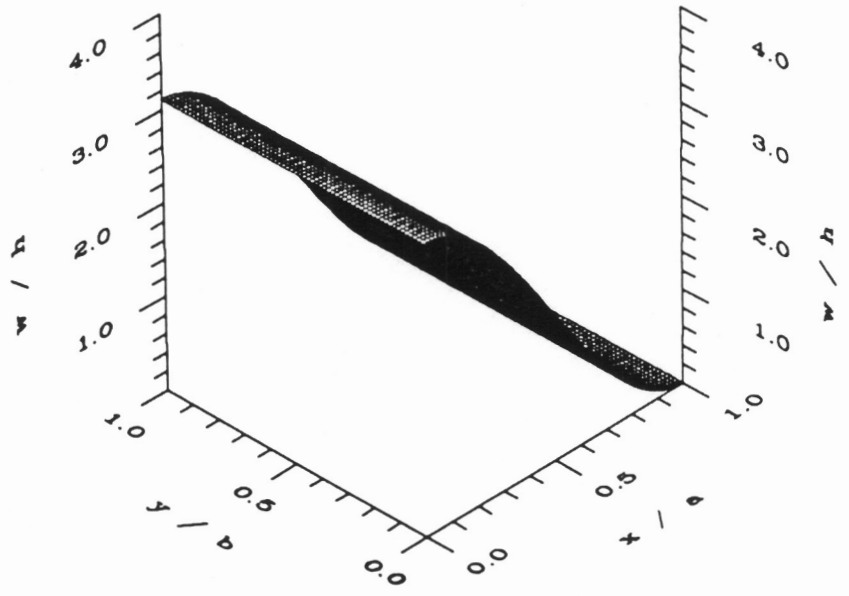

(b) Nonlinear theory

Figure 6.40 Midplane w/h displacement for a 2.0 in. square unsymmetric $[0_4/90_4]_t$ laminate ($u/a = -0.01$).

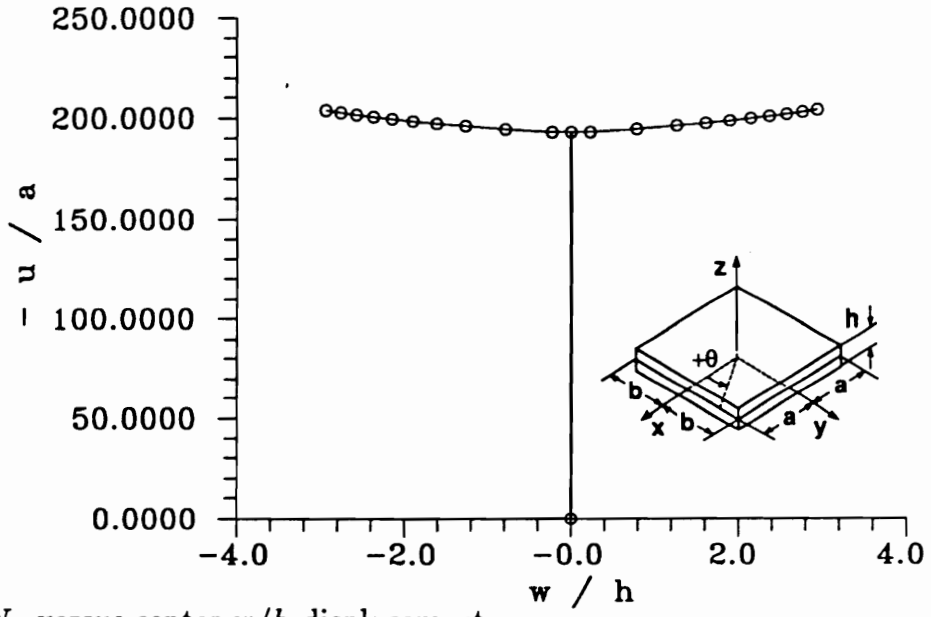

(a) N_x versus center w/h displacement

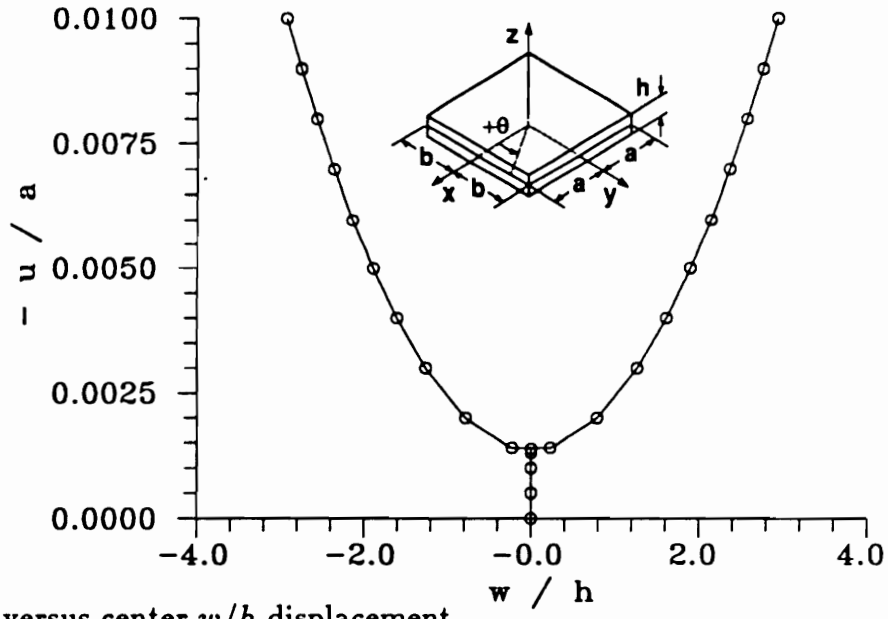

(b) u/a versus center w/h displacement

Figure 6.41 Load-displacement plots for a 2.0 in. square unsymmetric $[+45_4/-45_4]_t$ laminate ($u/a = -0.01$).

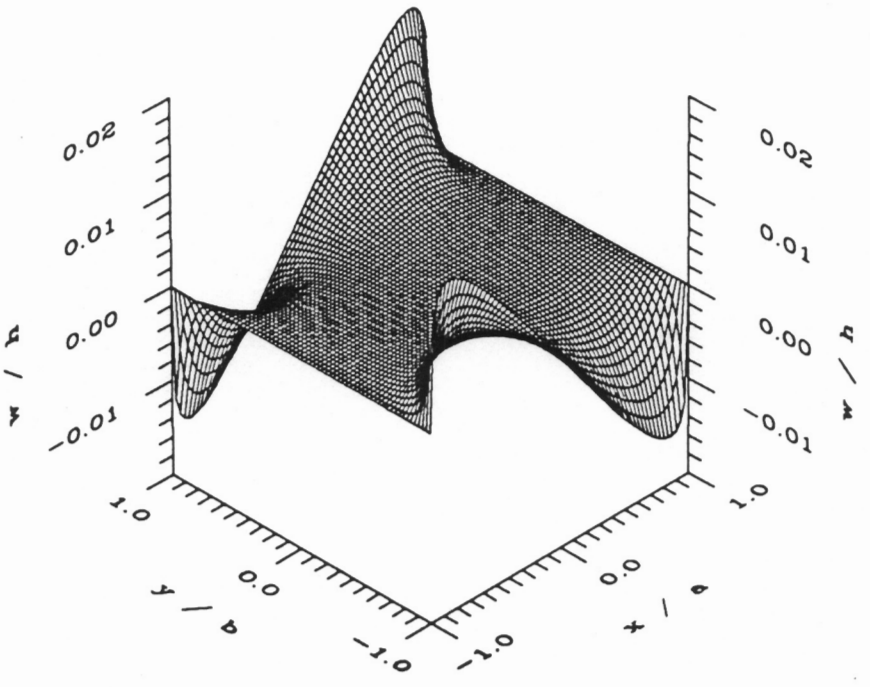

(a) Linear theory

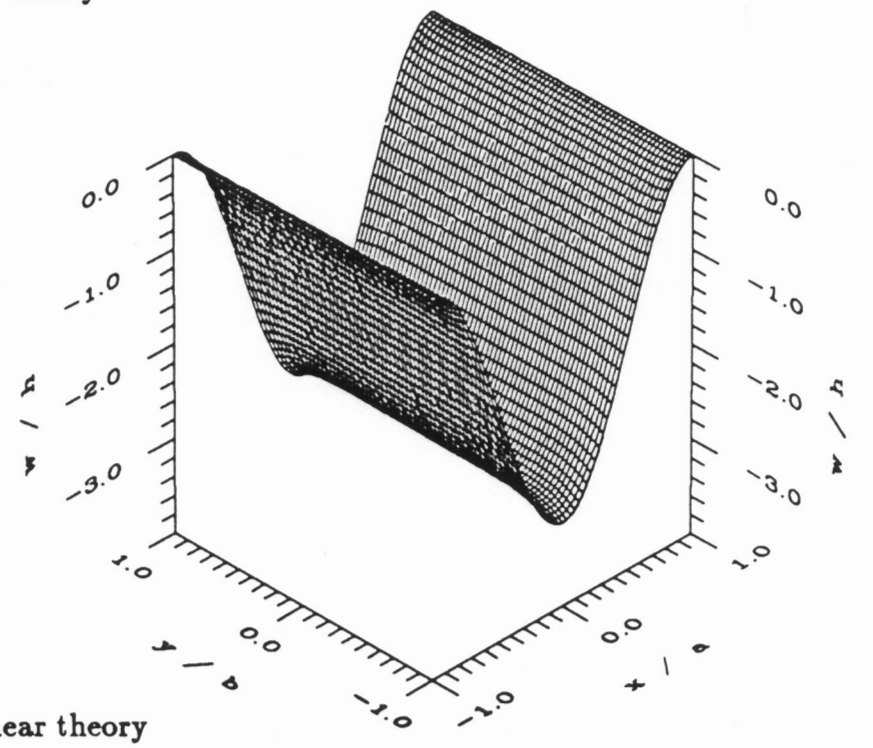

(b) Nonlinear theory

Figure 6.42 Midplane w/h displacement for a 2.0 in. square unsymmetric $[+45_4/-45_4]_t$ laminate ($u/a = -0.01$).

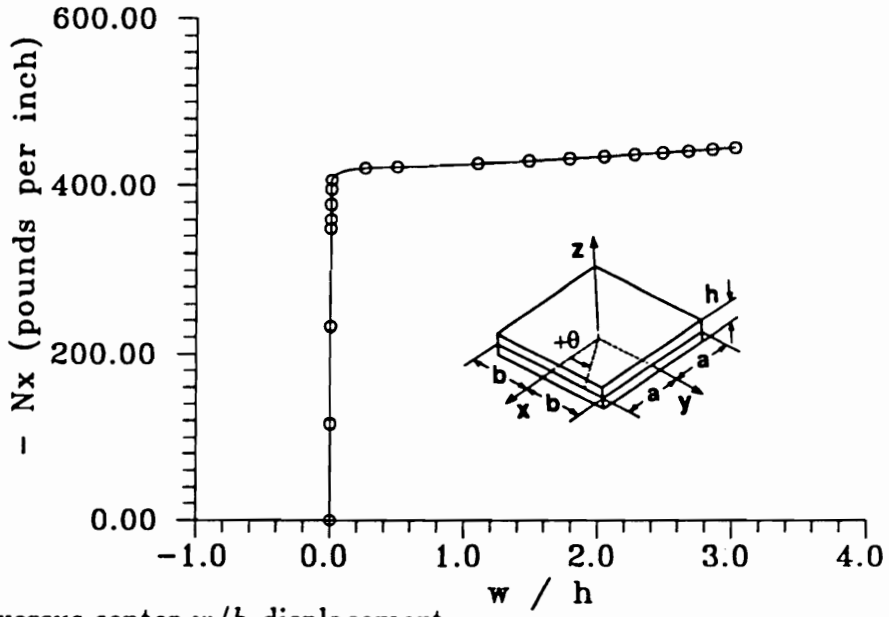

(a) N_x versus center w/h displacement

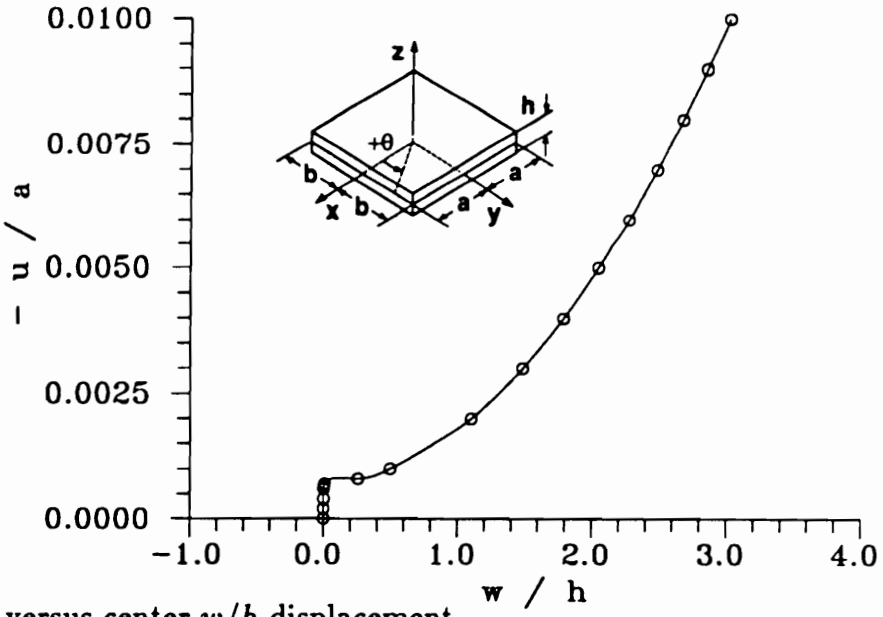

(b) u/a versus center w/h displacement

Figure 6.43 Load-displacement plots for a 2.0 in. square unsymmetric $[0_4/+45_4]_t$ laminate ($u/a = -0.01$).

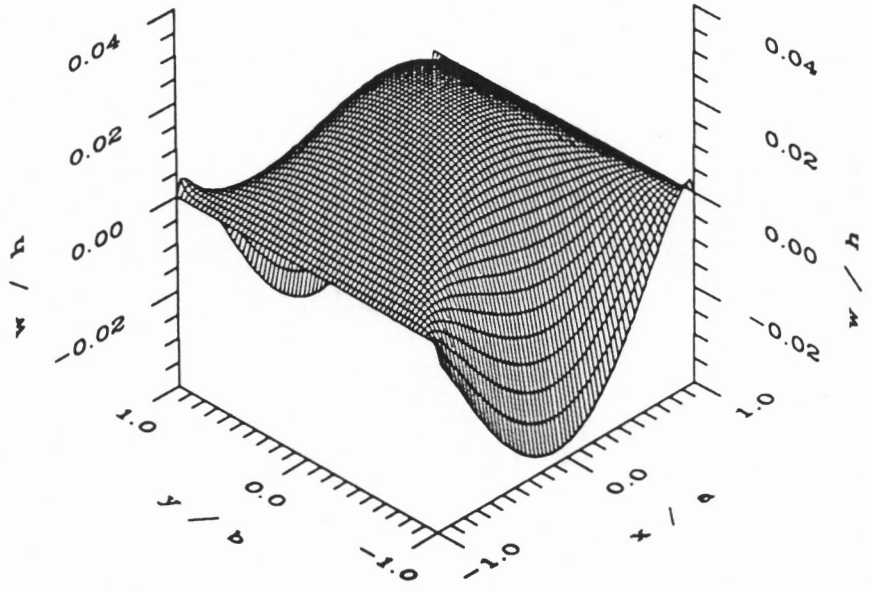

(a) Linear theory

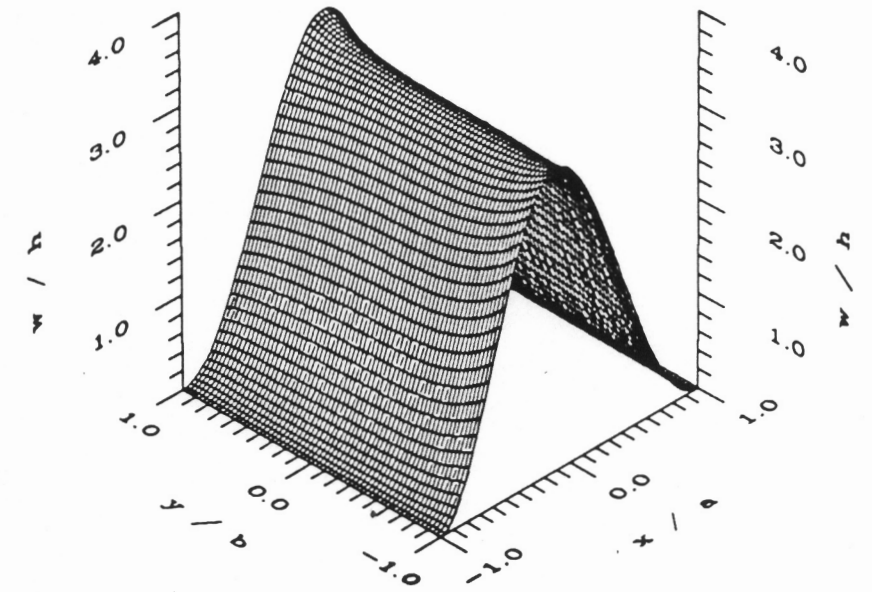

(b) Nonlinear theory

Figure 6.44 Midplane w/h displacement for a 2.0 in. square unsymmetric $[0_4/+45_4]_t$ laminate ($u/a = -0.01$).

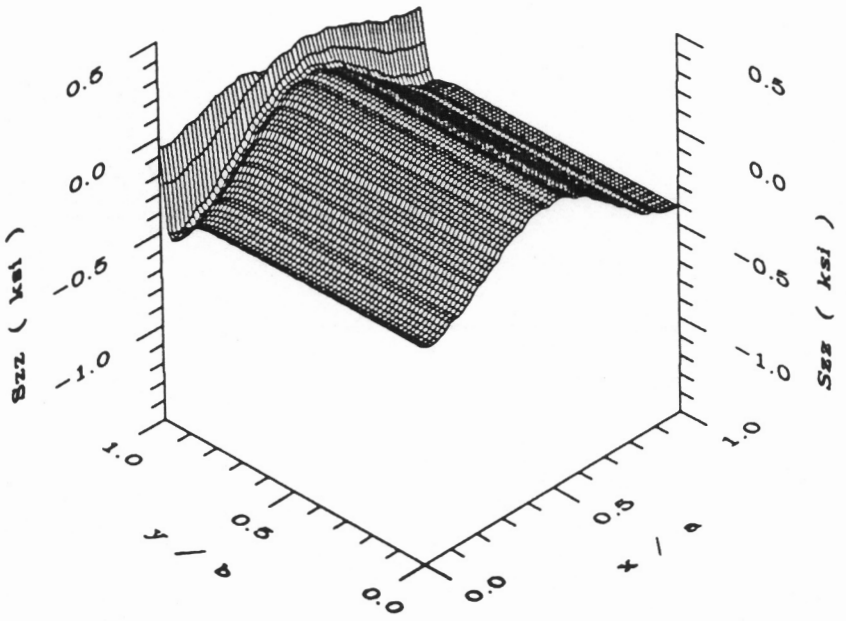

(a) $z/h = +0.25$

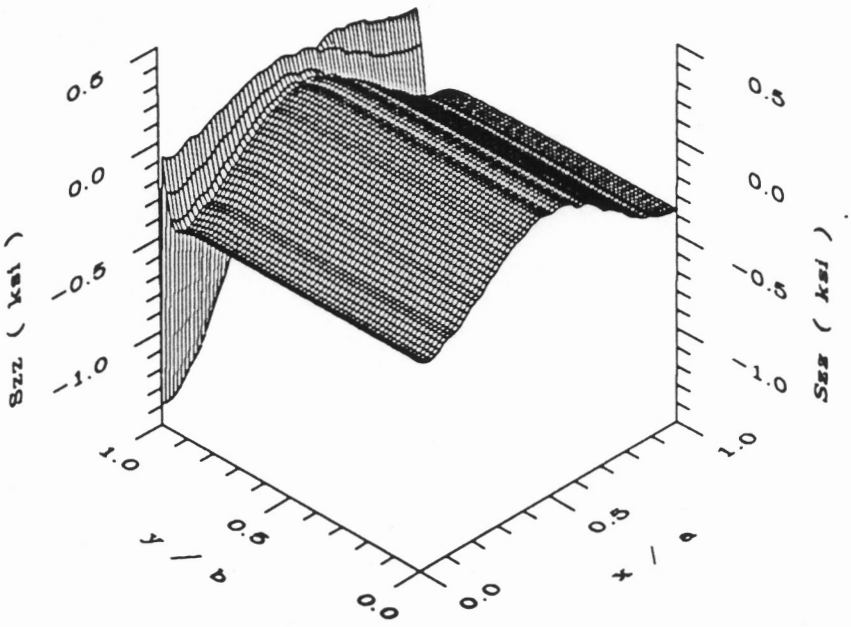

(b) $z/h = -0.25$

Figure 6.45 S_{zz} stress at the 0/90 interfaces for a 2.0 in. square symmetric $[90_4/0_4]_s$ laminate ($u/a = -0.01$).

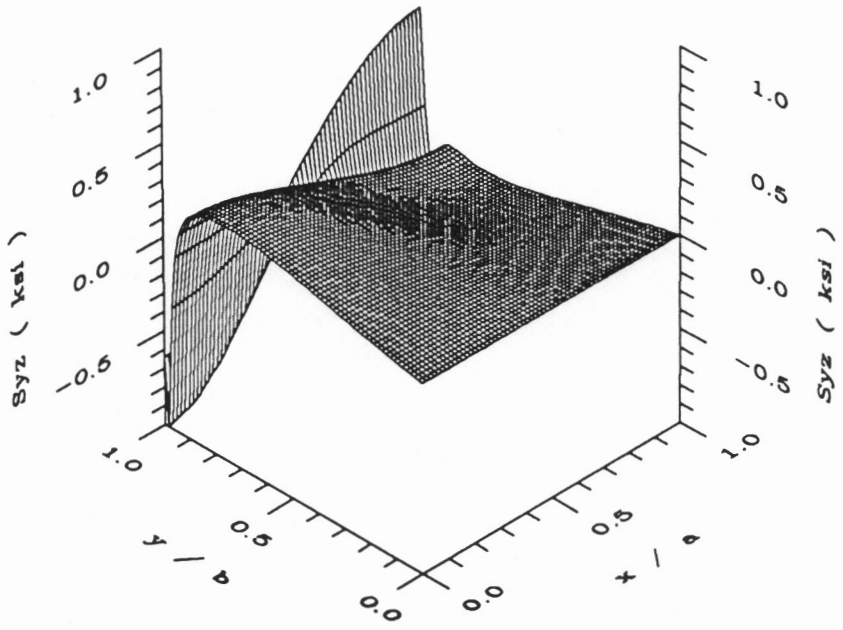

(a) $z/h = +0.25$

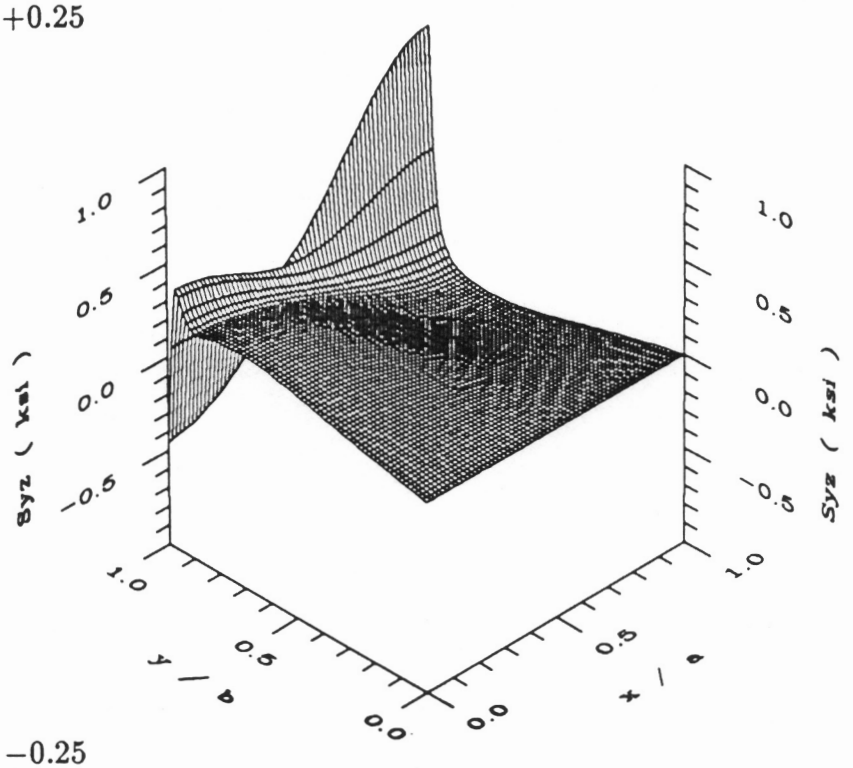

(b) $z/h = -0.25$

Figure 6.46 S_{yz} stress at the 0/90 interfaces for a 2.0 in. square symmetric $[90_4/0_4]_s$ laminate $(u/a = -0.01)$.

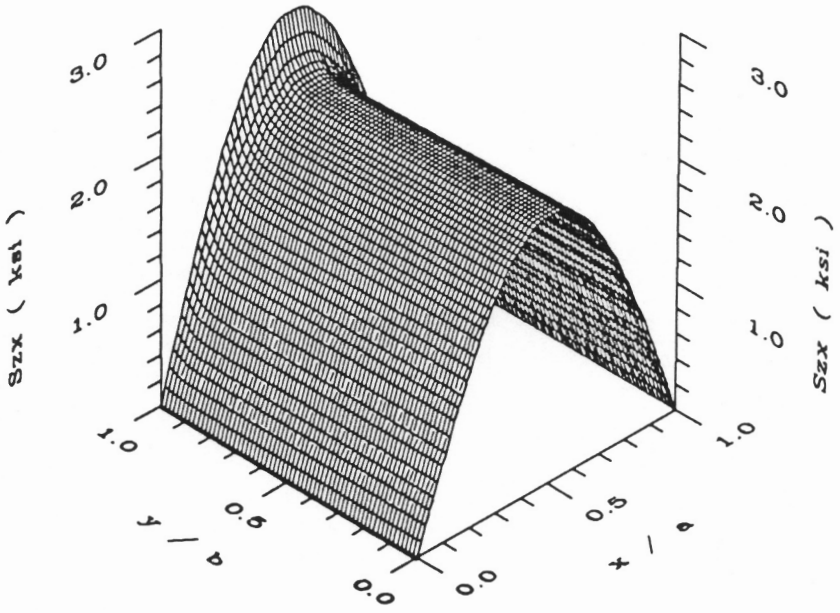

(a) $z/h = +0.25$

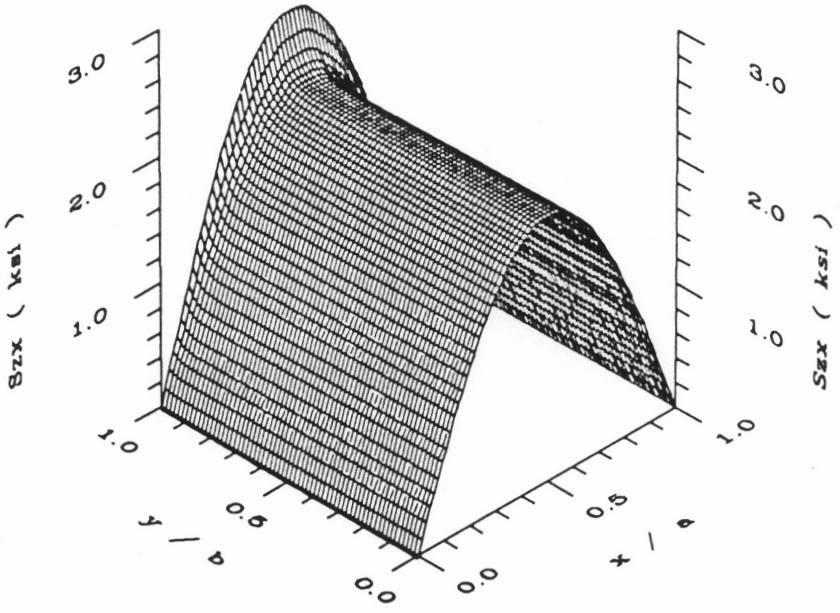

(b) $z/h = -0.25$

Figure 6.47 S_{zz} stress at the 0/90 interfaces for a 2.0 in. square symmetric $[90_4/0_4]_s$ laminate $(u/a = -0.01)$.

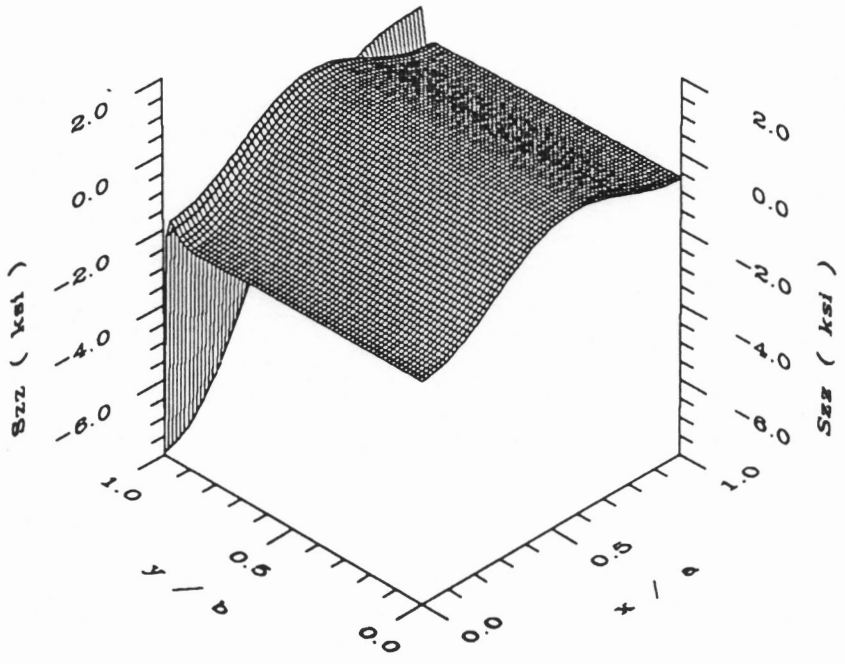

(a) $z/h = +0.25$

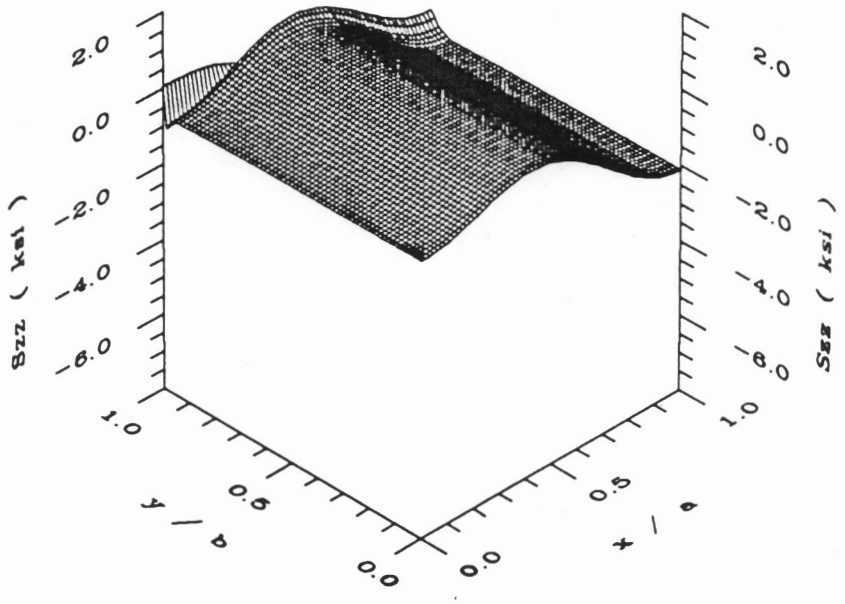

(b) $z/h = -0.25$

Figure 6.48 S_{zz} stress at the 0/90 interfaces for a 2.0 in. square symmetric $[0_4/90_4]_s$ laminate $(u/a = -0.01)$.

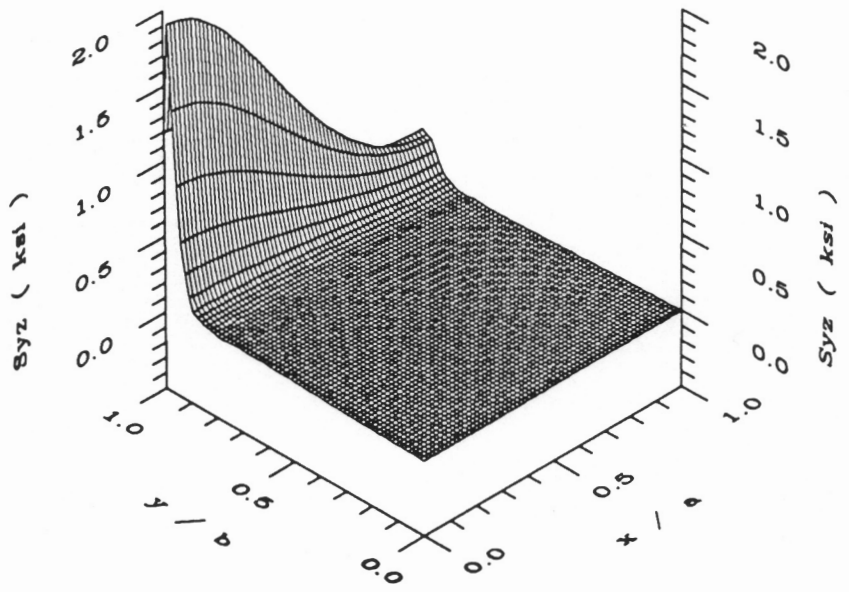

(a) $z/h = +0.25$

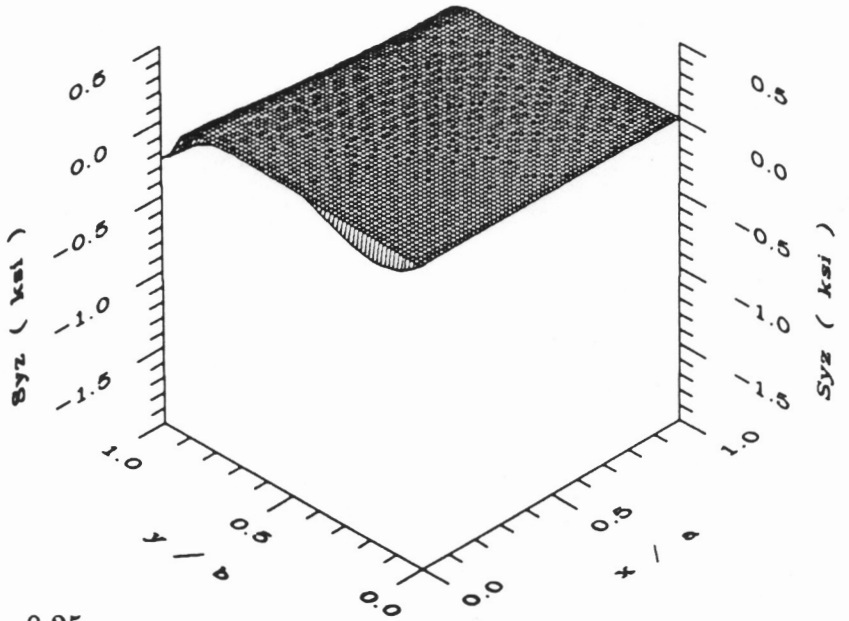

(b) $z/h = -0.25$

Figure 6.49 S_{yz} stress at the 0/90 interfaces for a 2.0 in. square symmetric $[0_4/90_4]_s$ laminate $(u/a = -0.01)$.

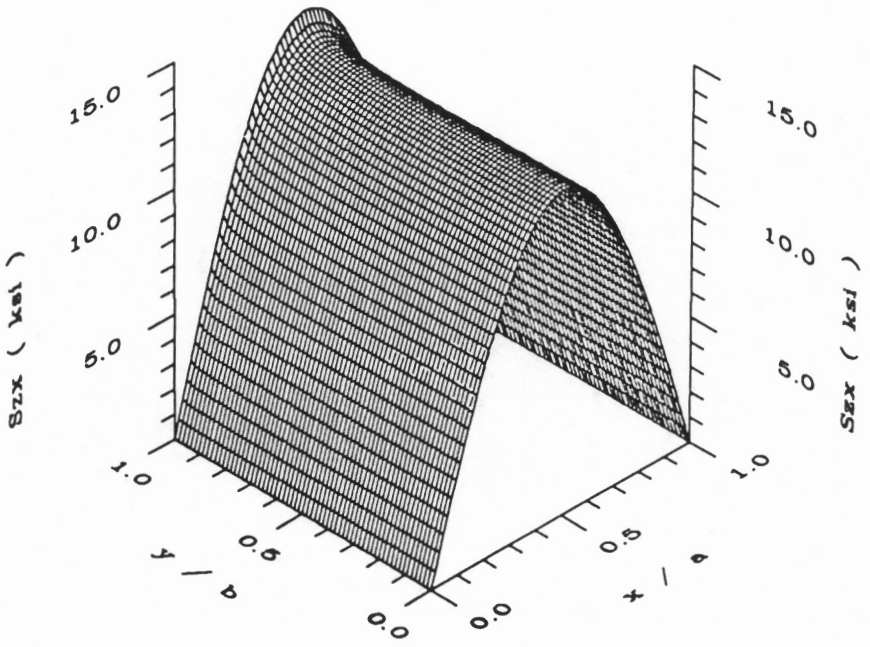

(a) $z/h = +0.25$

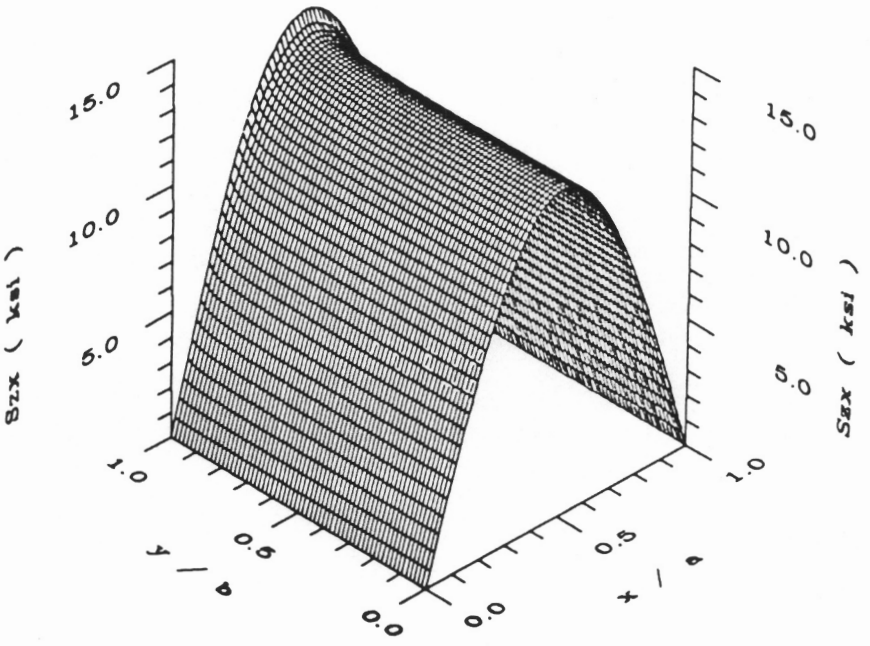

(b) $z/h = -0.25$

Figure 6.50 S_{zz} stress at the 0/90 interfaces for a 2.0 in. square symmetric $[0_4/90_4]_s$ laminate $(u/a = -0.01)$.

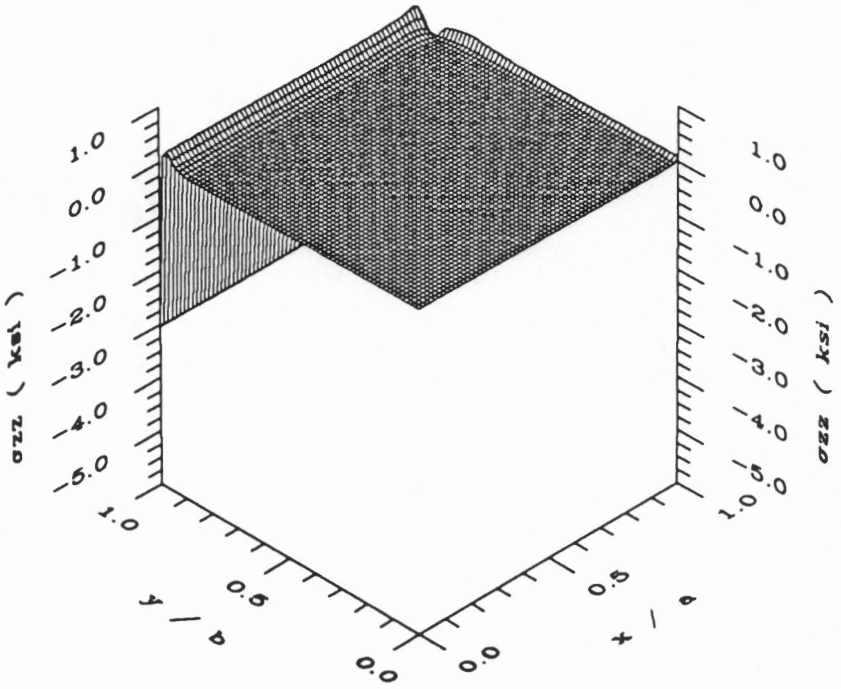

(a) Linear theory

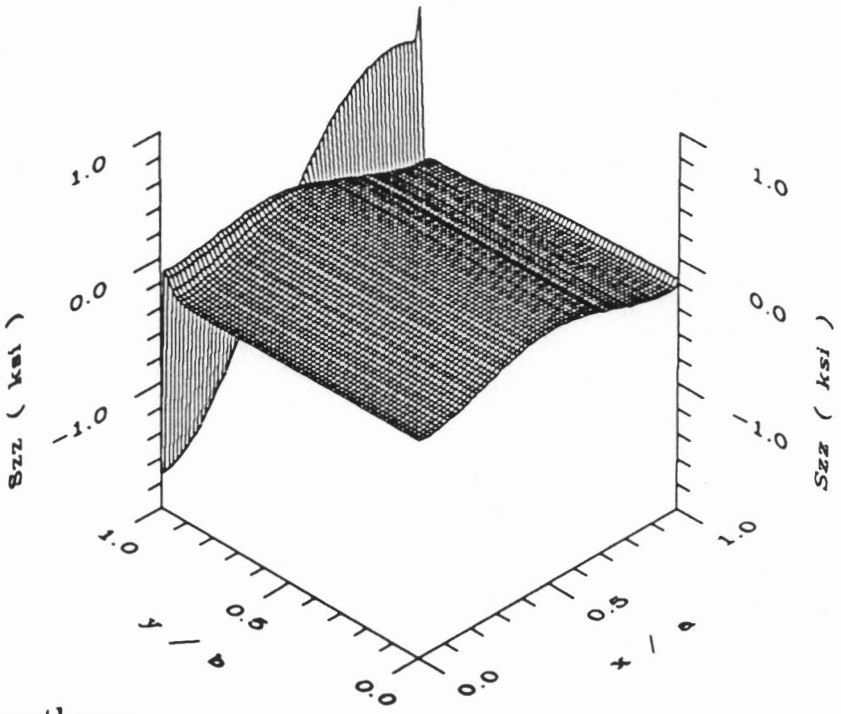

(b) Nonlinear theory

Figure 6.51 σ_{zz} and S_{zz} stress at the 0/90 interface for a 2.0 in. square unsymmetric $[0_4/90_4]_t$ laminate ($u/a = -0.01$).

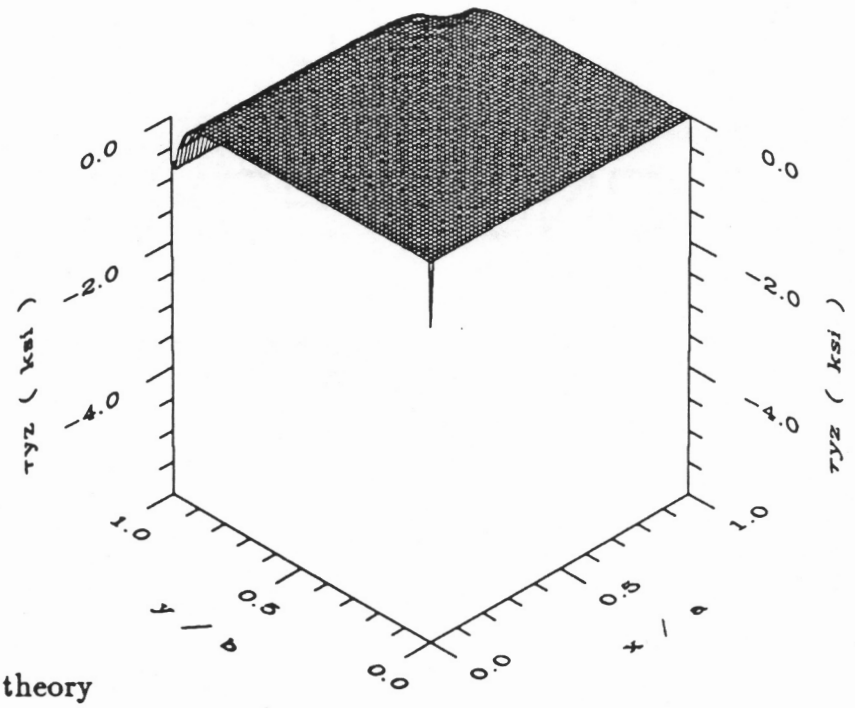

(a) Linear theory

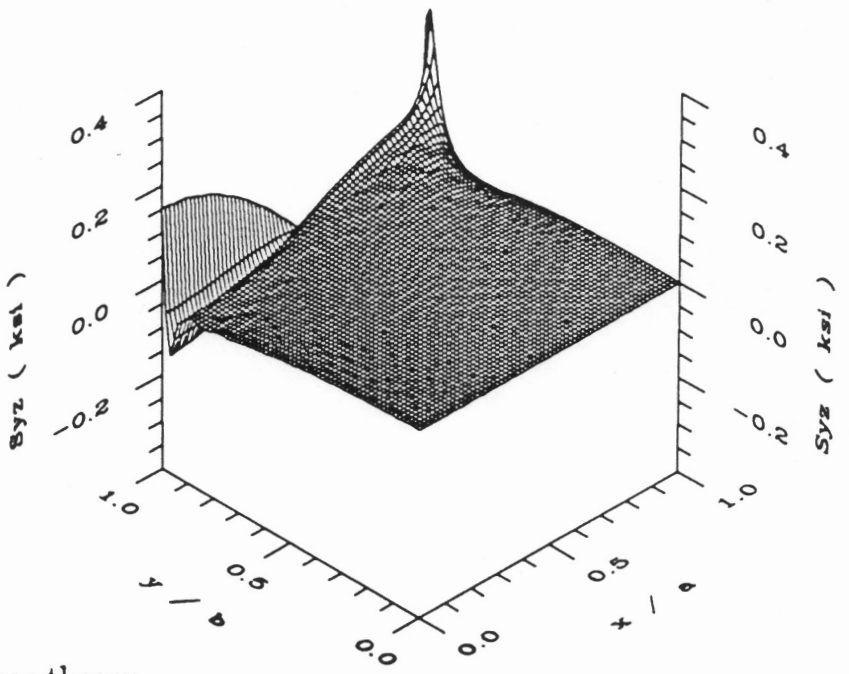

(b) Nonlinear theory

Figure 6.52 τ_{yz} and S_{yz} stress at the 0/90 interface for a 2.0 in. square unsymmetric $[0_4/90_4]_t$ laminate ($u/a = -0.01$).

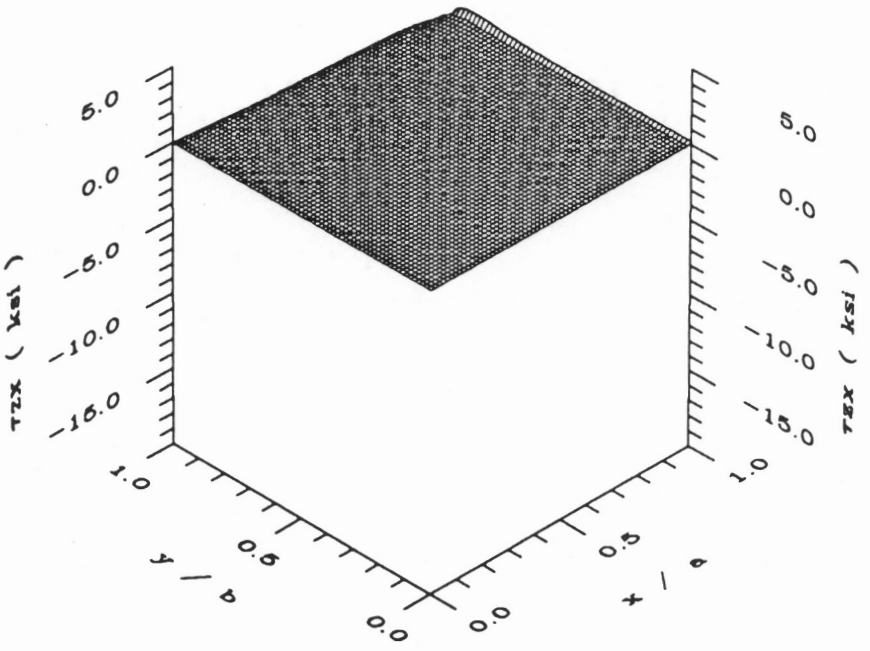

(a) Linear theory

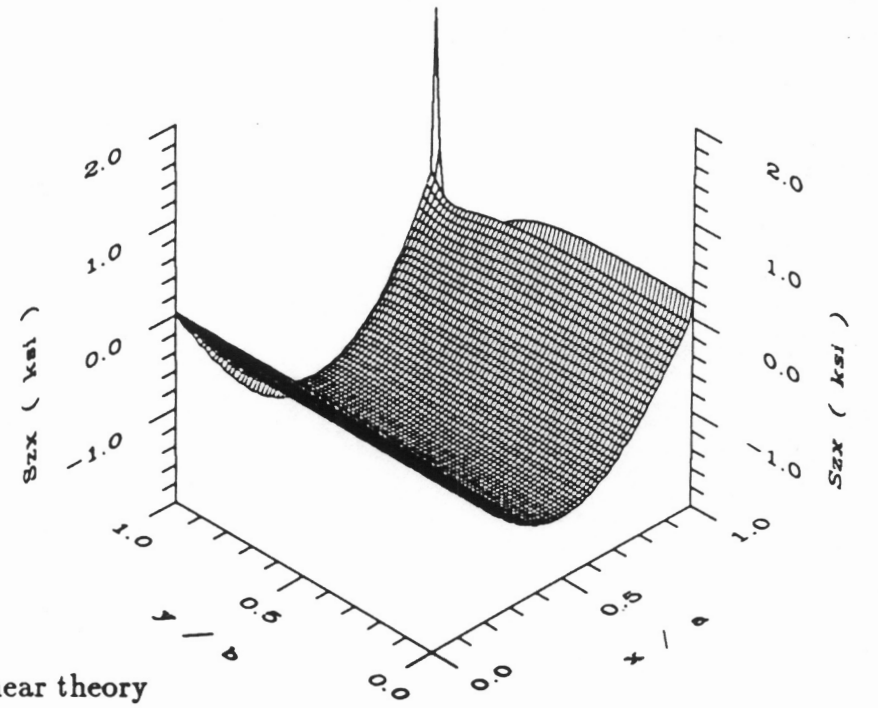

(b) Nonlinear theory

Figure 6.53 τ_{zx} and S_{zx} stress at the 0/90 interface for a 2.0 in. square unsymmetric $[0_4/90_4]_t$ laminate ($u/a = -0.01$).

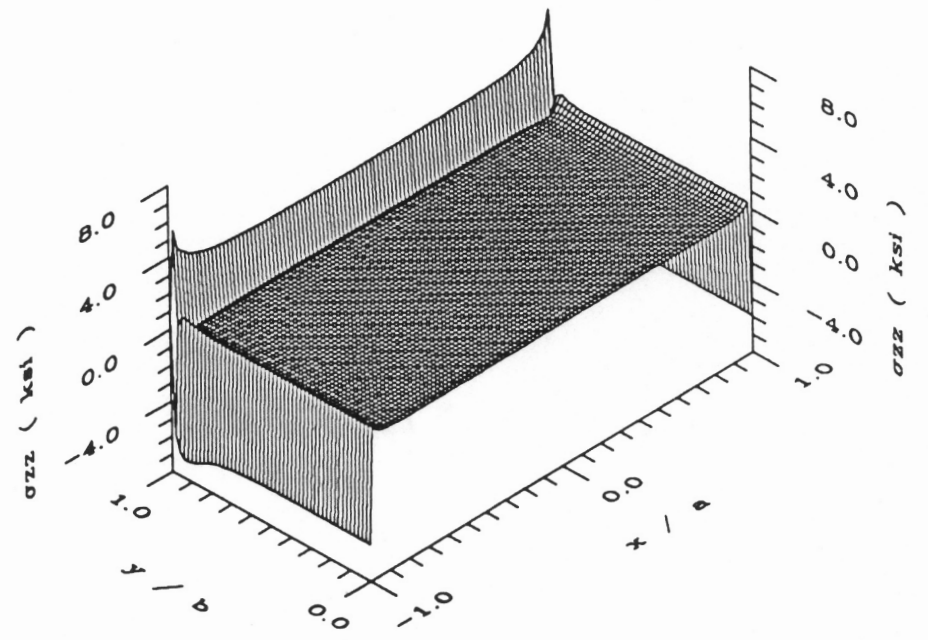

(a) Linear theory

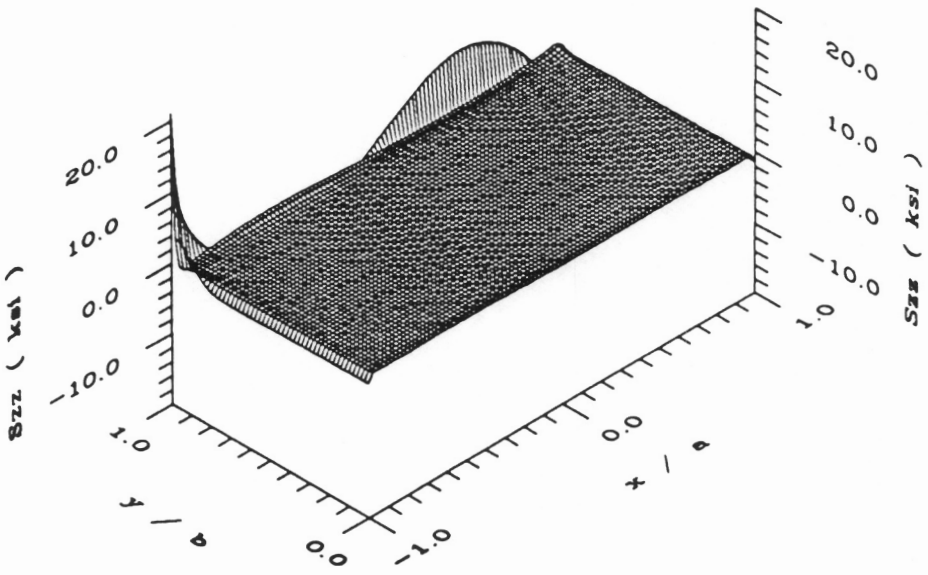

(b) Nonlinear theory

Figure 6.54 σ_{zz} and S_{zz} stress at the +45/–45 interface for a 2.0 in. square unsymmetric $[+45_4/-45_4]_t$ laminate ($u/a = -0.01$).

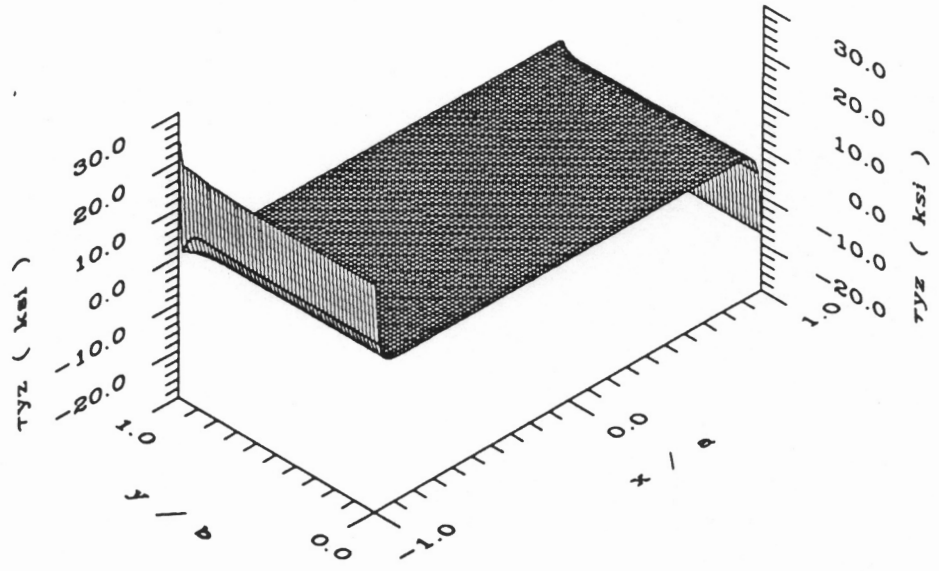

(a) Linear theory

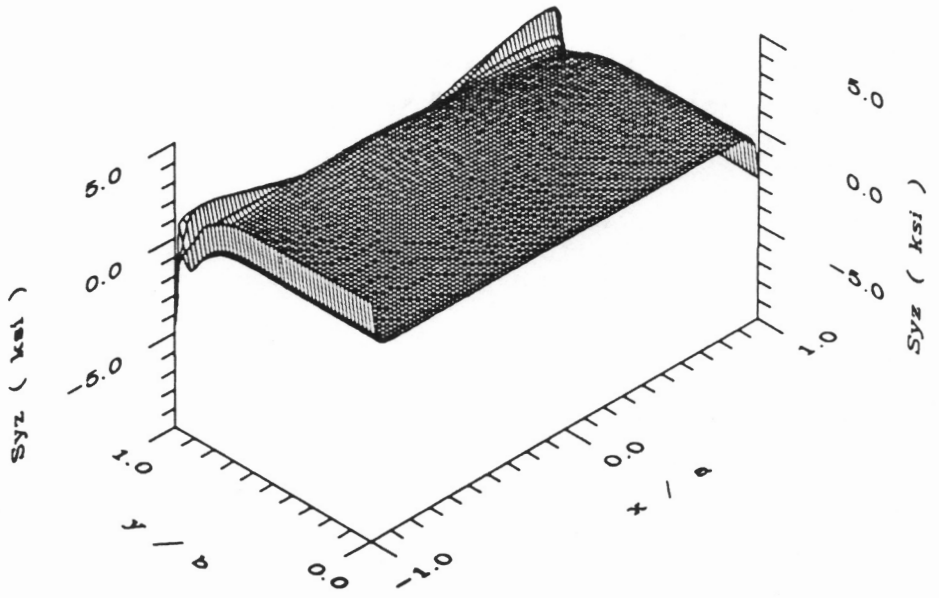

(b) Nonlinear theory

Figure 6.55 τ_{yz} and S_{yz} stress at the +45/–45 interface for a 2.0 in. square unsymmetric $[+45_4/-45_4]_t$ laminate ($u/a = -0.01$).

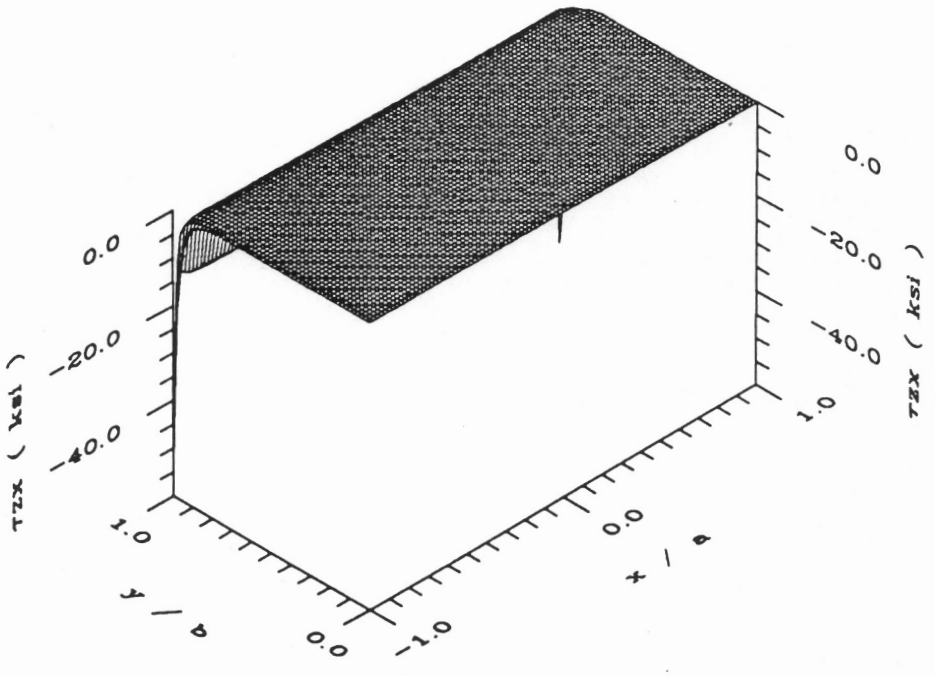

(a) Linear theory

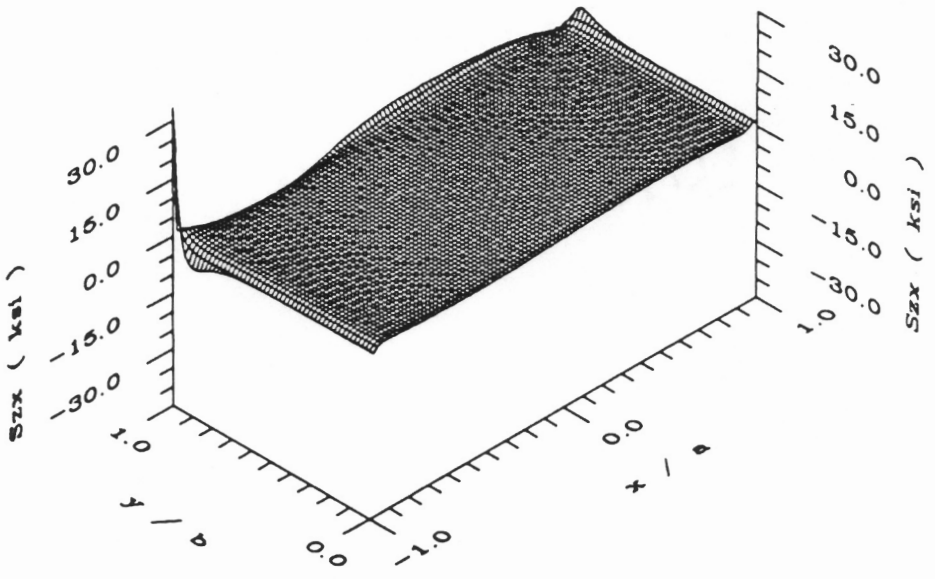

(b) Nonlinear theory

Figure 6.56 τ_{zx} and S_{zx} stress at the +45/–45 interface for a 2.0 in. square unsymmetric $[+45_4/-45_4]_t$ laminate $(u/a = -0.01)$.

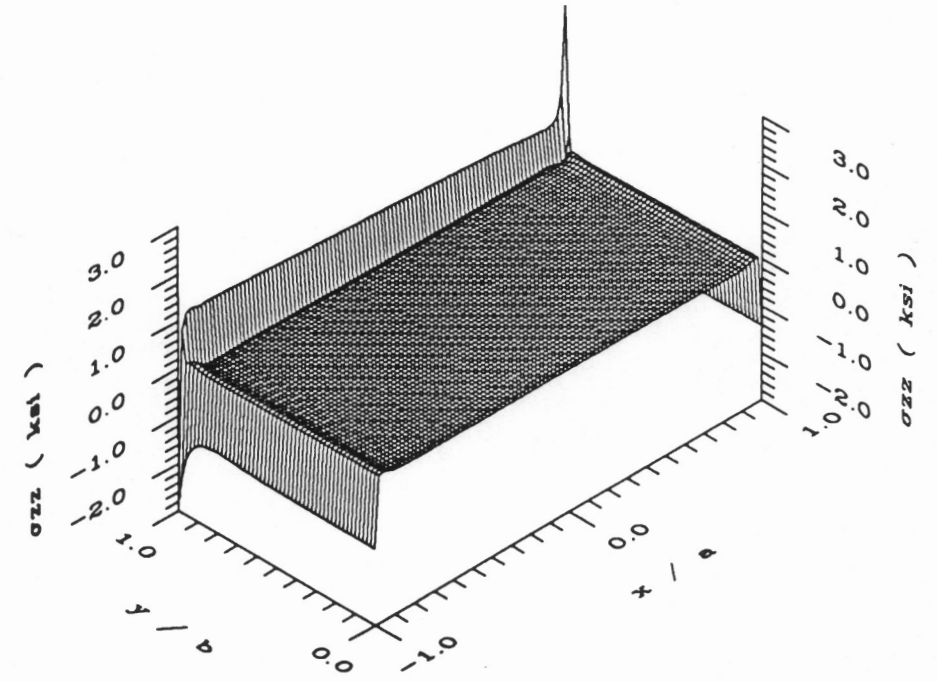

(a) Linear theory

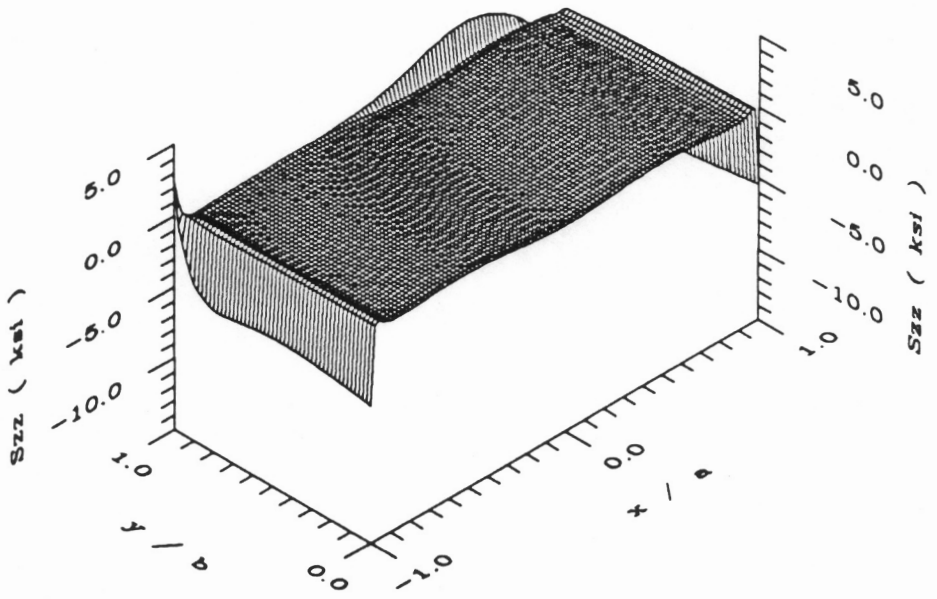

(b) Nonlinear theory

Figure 6.57 σ_{zz} and S_{zz} stress at the $0/+45$ interface for a 2.0 in. square unsymmetric $[0_4/+45_4]_t$ laminate ($u/a = -0.01$).

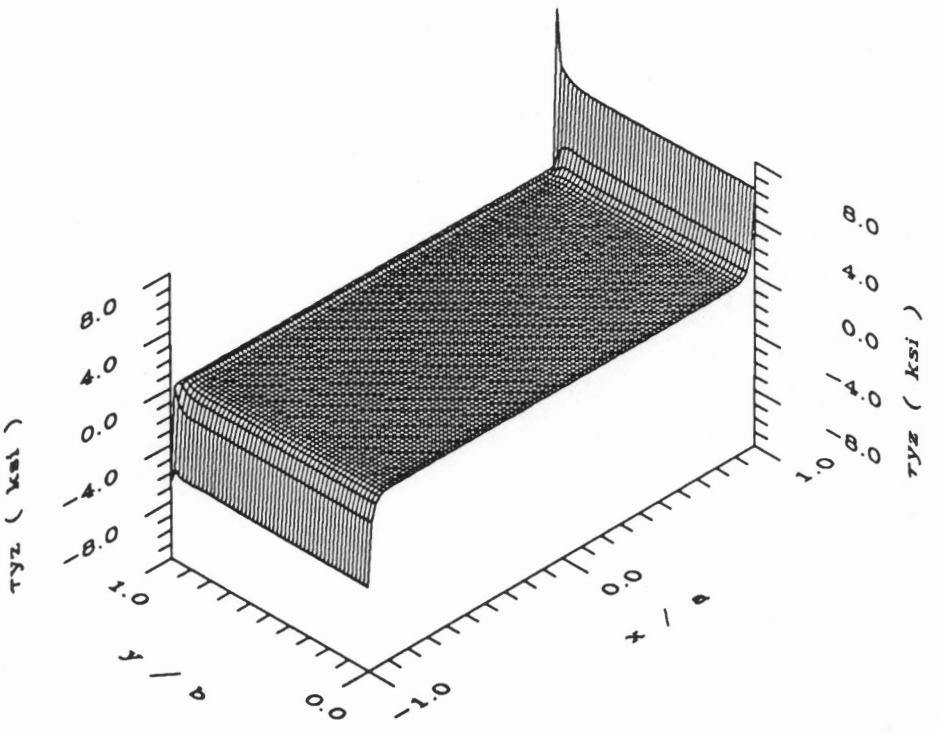

(a) Linear theory

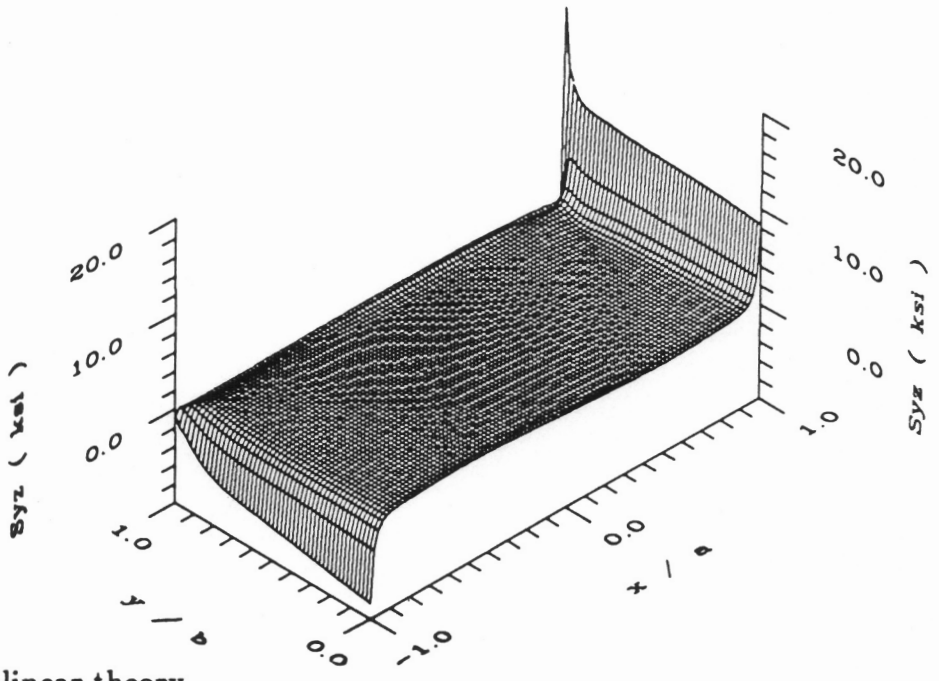

(b) Nonlinear theory

Figure 6.58 τ_{yz} and S_{yz} stress at the $0/+45$ interface for a 2.0 in. square unsymmetric $[0_4/+45_4]_t$ laminate $(u/a = -0.01)$.

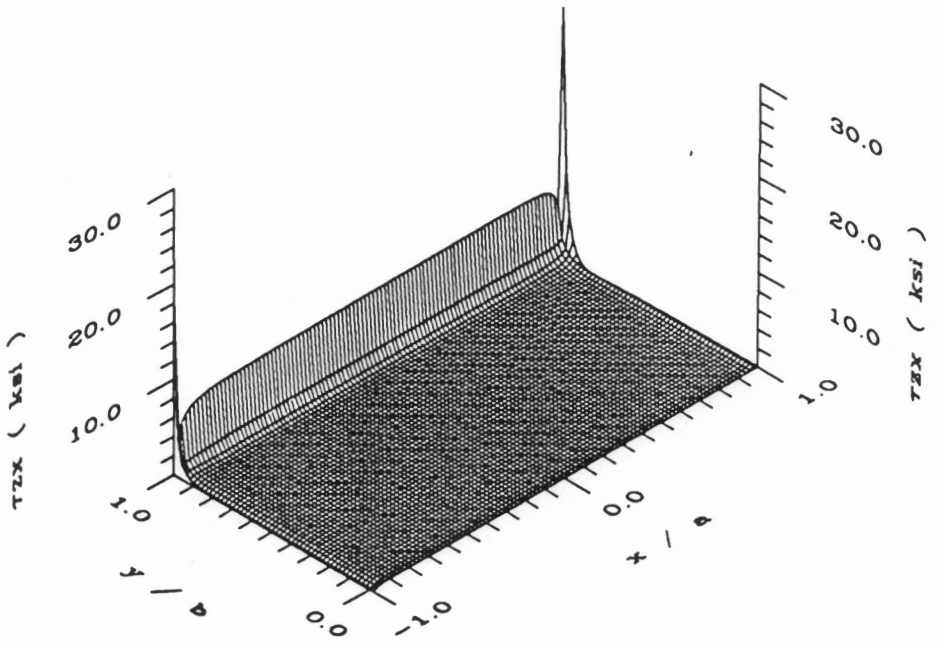

(a) Linear theory

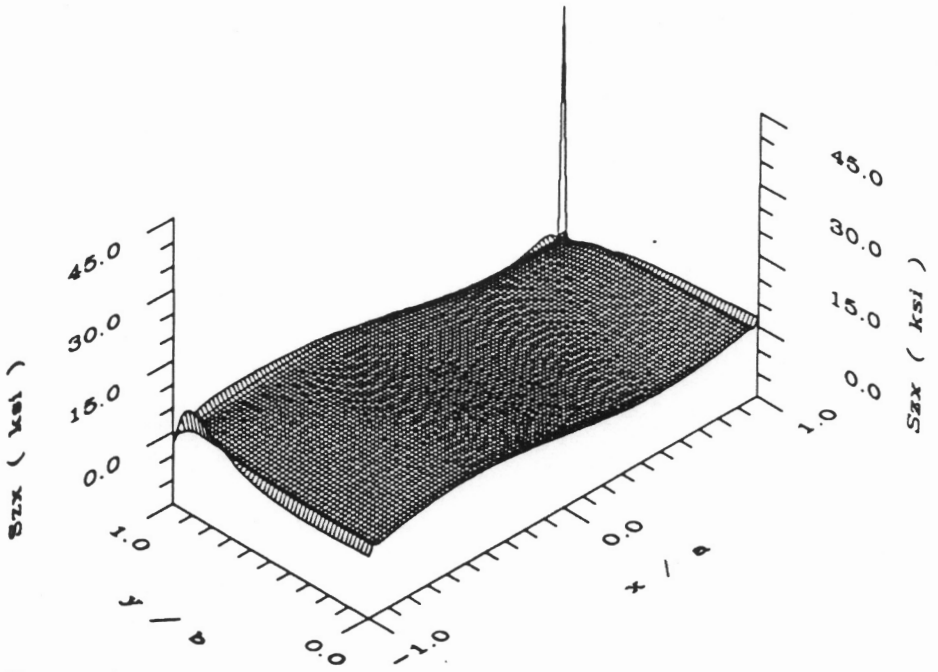

(b) Nonlinear theory

Figure 6.59 τ_{zx} and S_{zx} stress at the 0/+45 interface for a 2.0 in. square unsymmetric $[0_4/+45_4]_t$ laminate ($u/a = -0.01$).

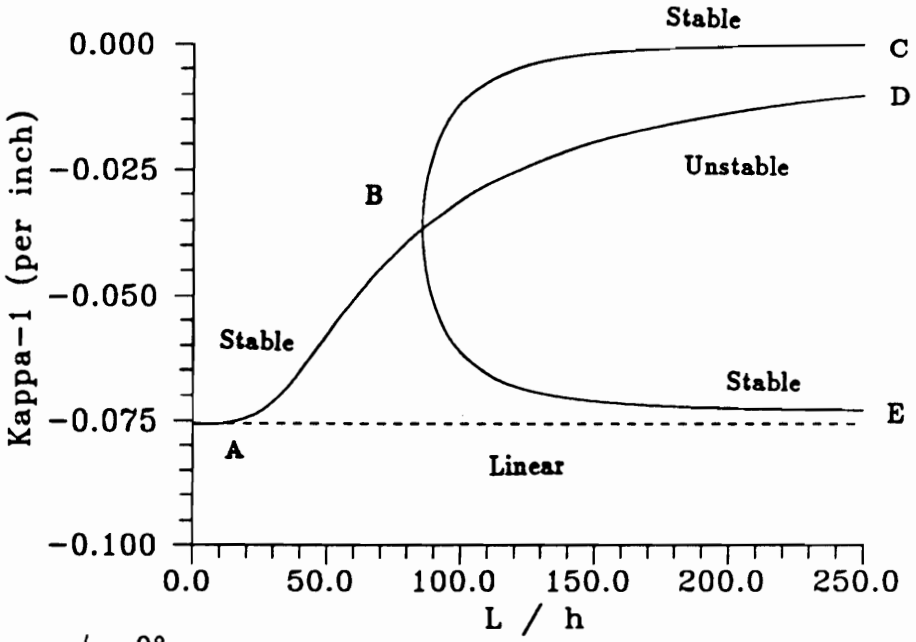

(a) $\kappa_1 = \kappa_x$, $\phi = 0°$

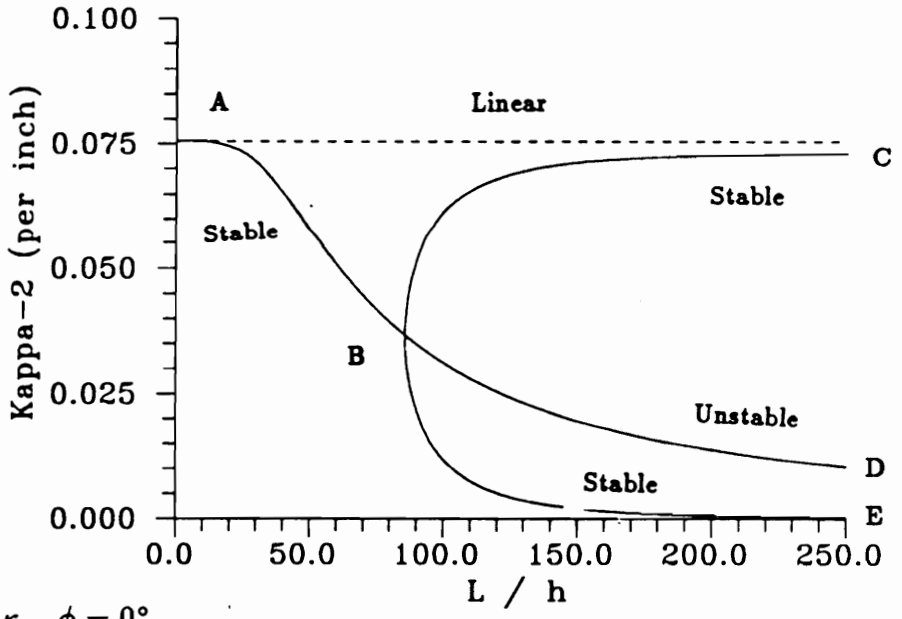

(b) $\kappa_2 = \kappa_y$, $\phi = 0°$

Figure 6.60 Principal curvature versus L/h for square unsymmetric $[0_4/90_4]_t$ laminates ($\Delta T = -280°F$).

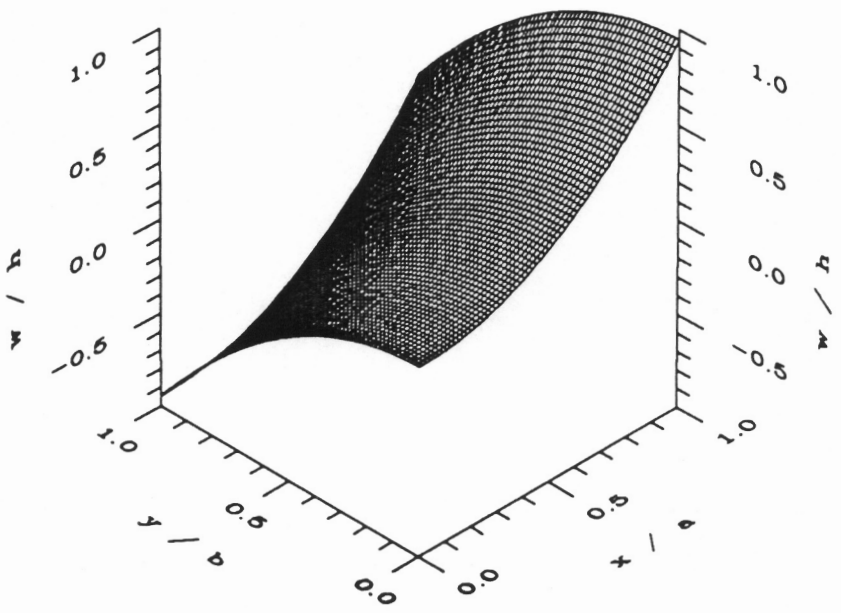

(a) Linear theory

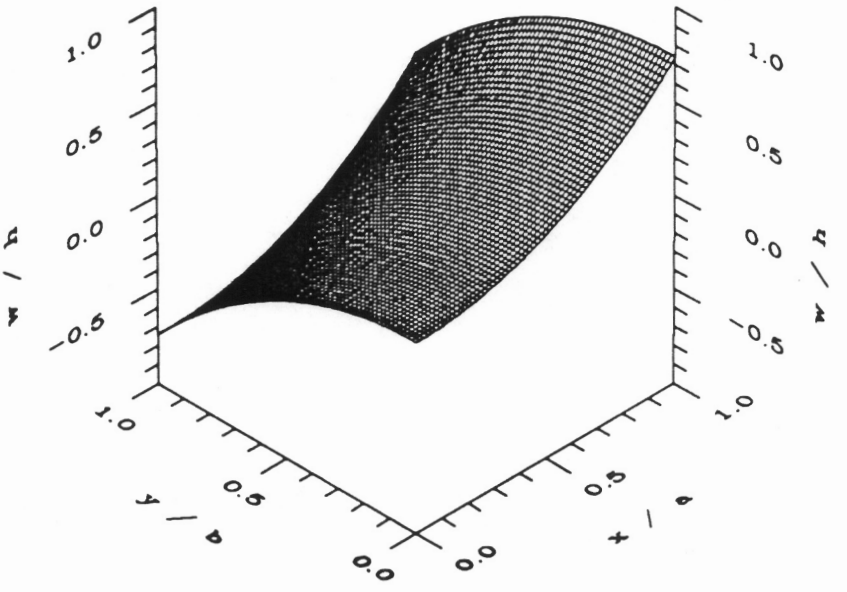

(b) Nonlinear theory

Figure 6.61 Midplane w/h displacement for a 2.0 in. square unsymmetric $[0_4/90_4]_t$ laminate ($\Delta T = -280°F$).

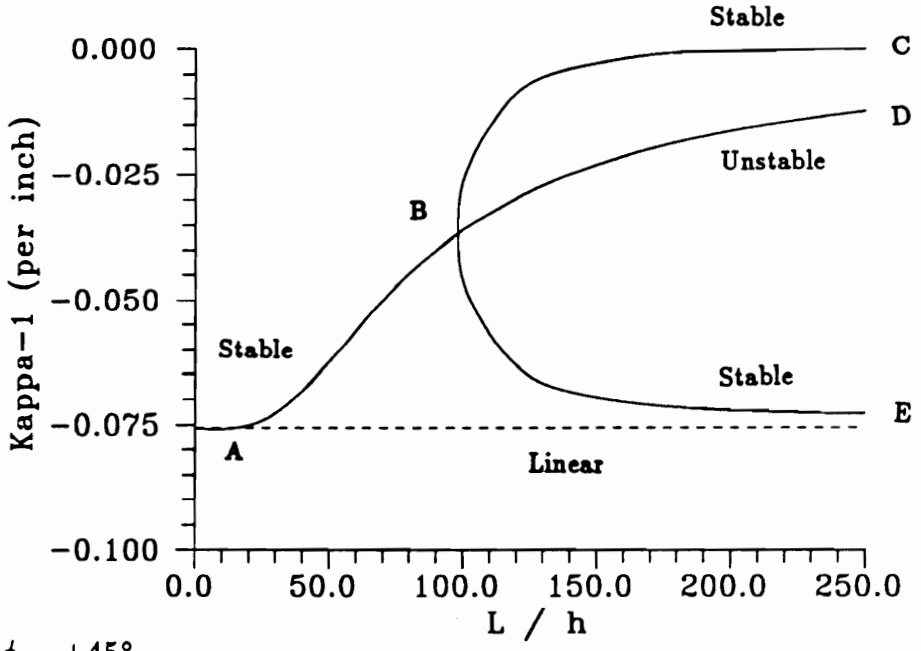

(a) κ_1, $\phi = +45°$

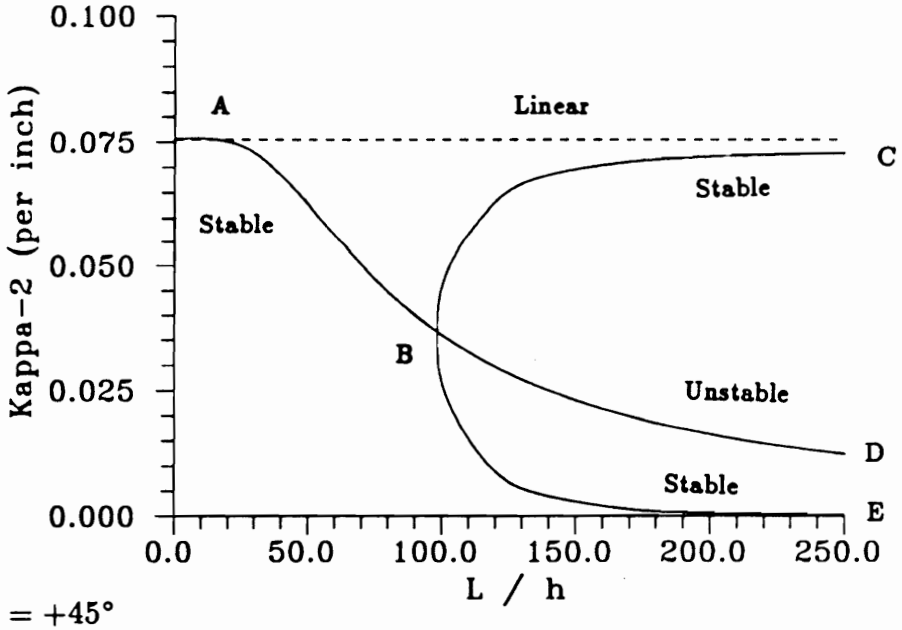

(b) κ_2, $\phi = +45°$

Figure 6.62 Principal curvature versus L/h for square unsymmetric $[+45_4/-45_4]_t$ laminates ($\Delta T = -280°F$).

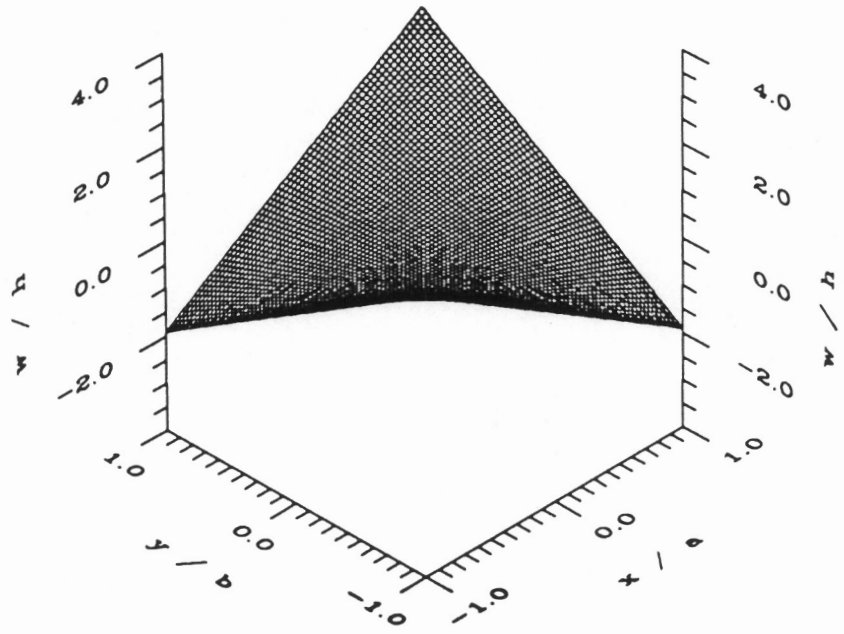

(a) Linear theory

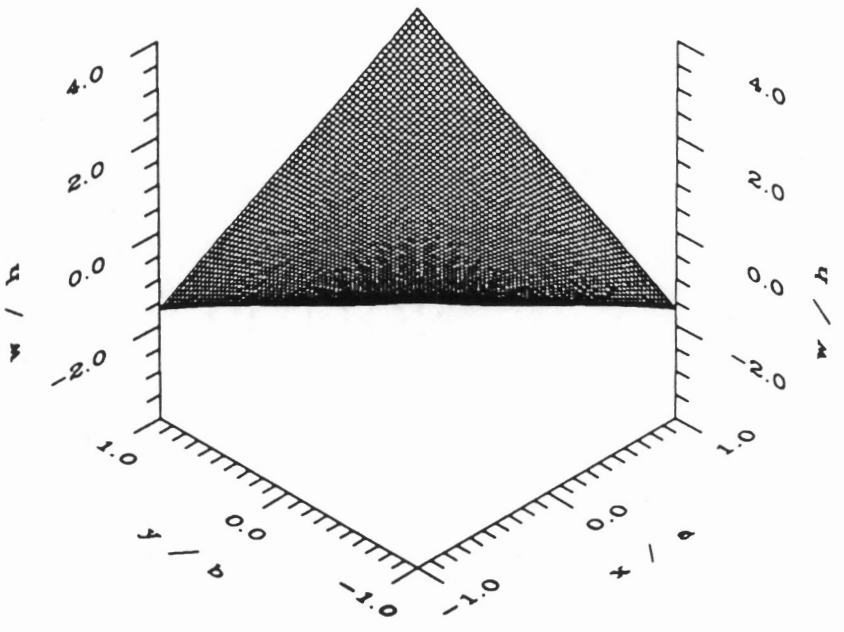

(b) Nonlinear theory

Figure 6.63 Midplane w/h displacement for a 2.0 in. square unsymmetric $[+45_4/-45_4]_t$ laminate ($\Delta T = -280°F$).

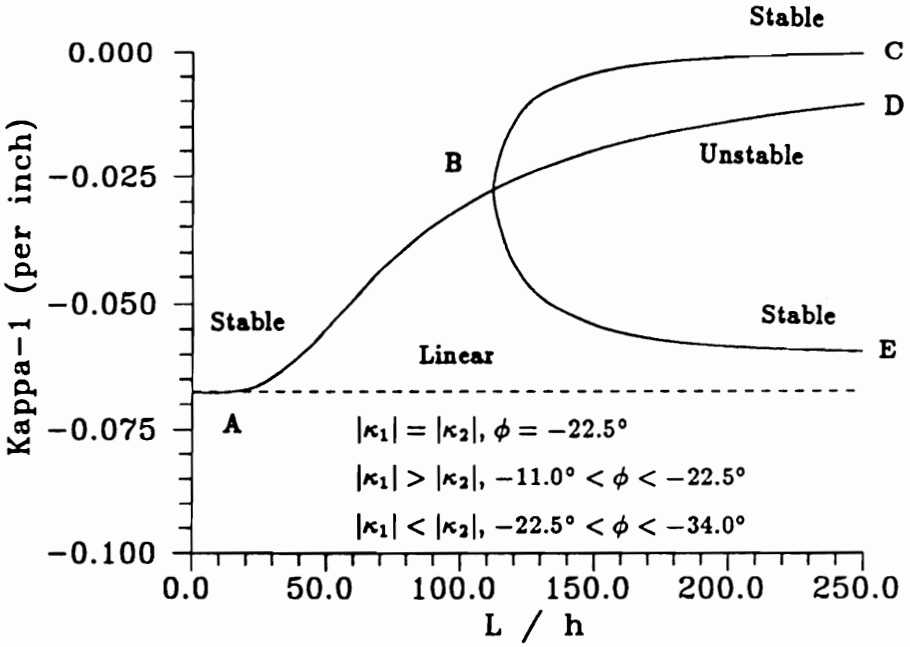

(a) κ_1

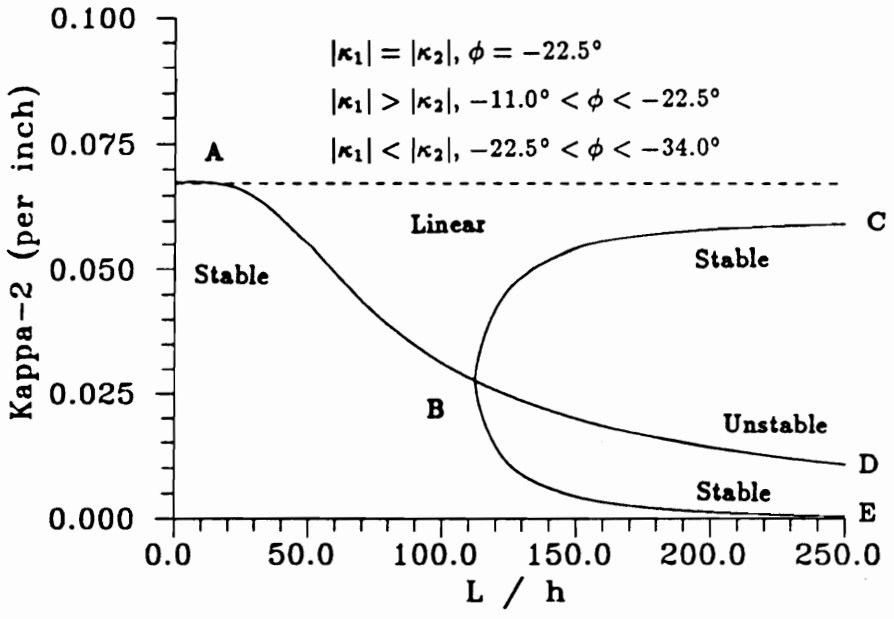

(b) κ_2

Figure 6.64 Principal curvature versus L/h for square unsymmetric $[0_4/+45_4]_t$ laminates ($\Delta T = -280°F$).

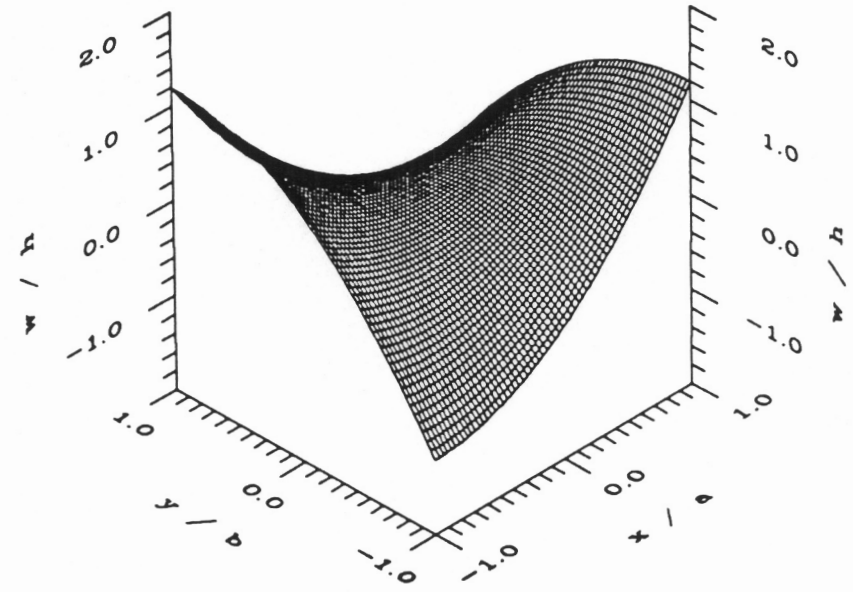

(a) Linear theory

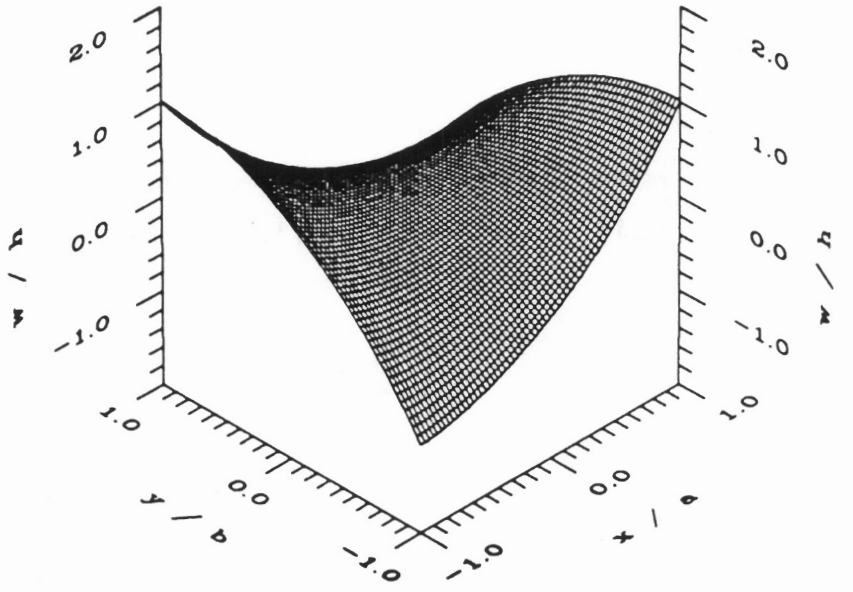

(b) Nonlinear theory

Figure 6.65 Midplane w/h displacement for a 2.0 in. square unsymmetric $[0_4/+45_4]_t$ laminate ($\Delta T = -280°F$).

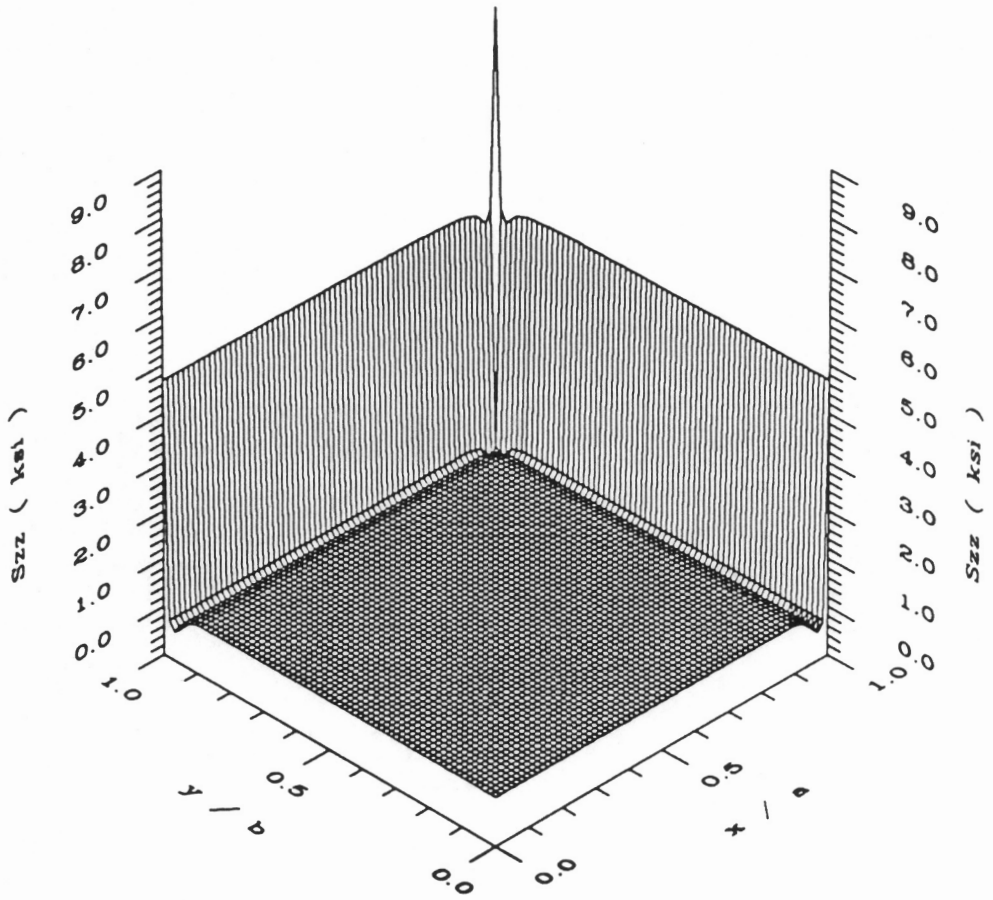

Figure 6.66 S_{zz} stress at the 0/90 interface for a 2.0 in. square unsymmetric $[0_4/90_4]_t$ laminate ($\Delta T = -280°F$).

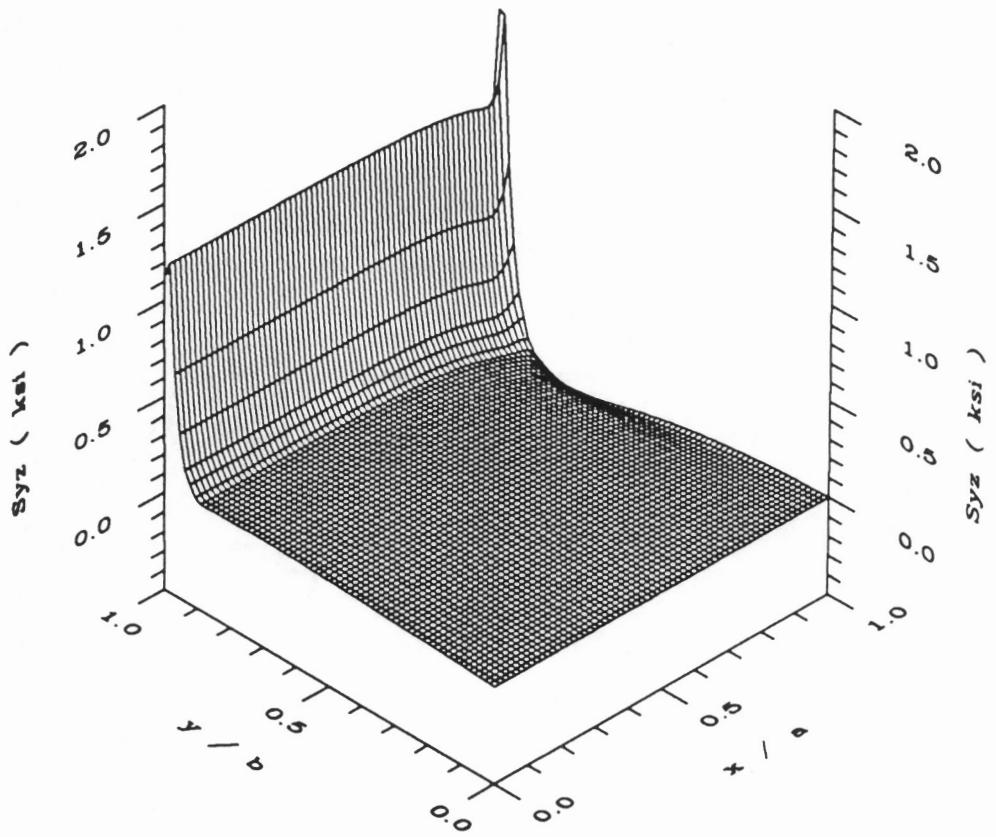

Figure 6.67 S_{yz} stress at the 0/90 interface for a 2.0 in. square unsymmetric $[0_4/90_4]_t$ laminate ($\Delta T = -280°F$).

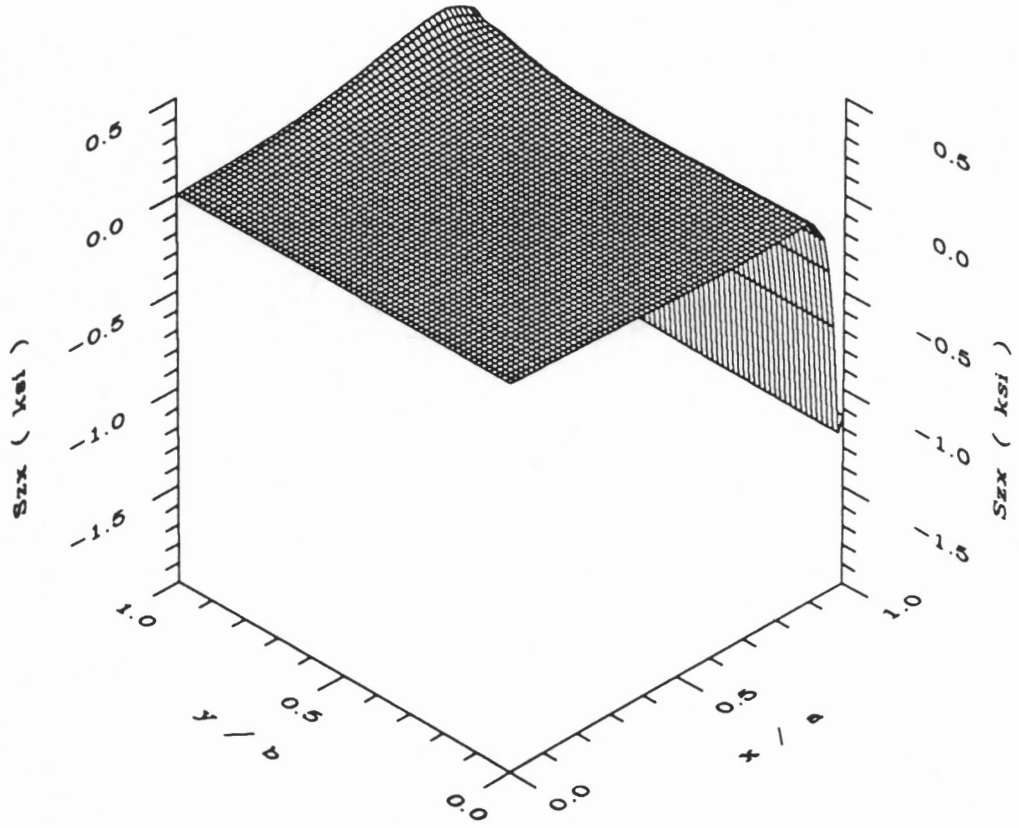

Figure 6.68 S_{zx} stress at the 0/90 interface for a 2.0 in. square unsymmetric $[0_4/90_4]_t$ laminate ($\Delta T = -280°F$).

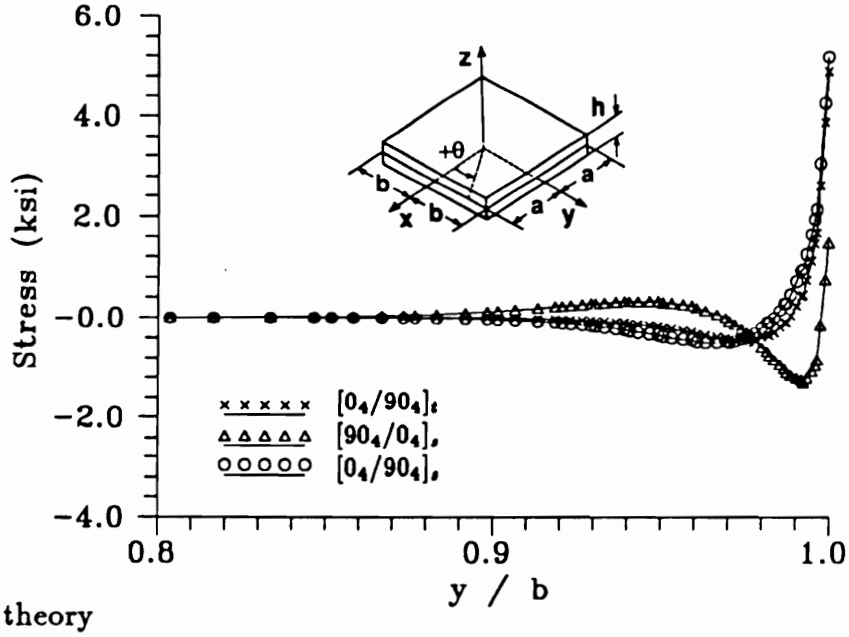

(a) Linear theory

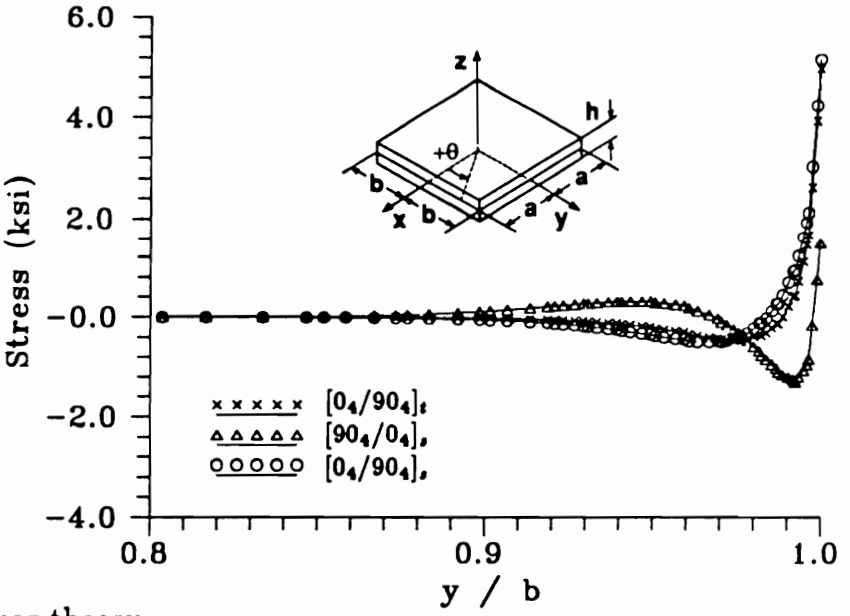

(b) Nonlinear theory

Figure 6.69 σ_{zz} and S_{zz} stress along $x = 0$ at the 0/90 interface for the 2.0 in. square $0_4/90_4$ laminates ($\Delta T = -280°F$, local analysis).

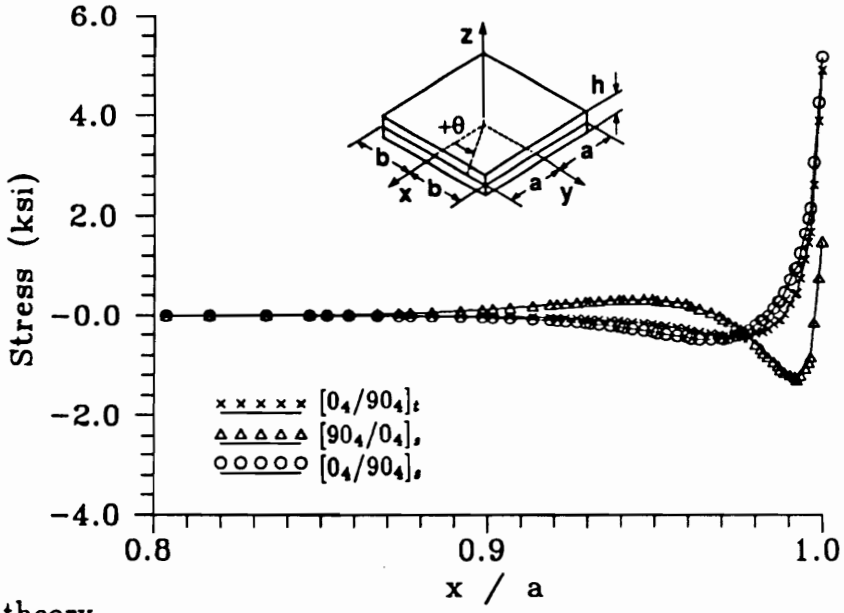

(a) Linear theory

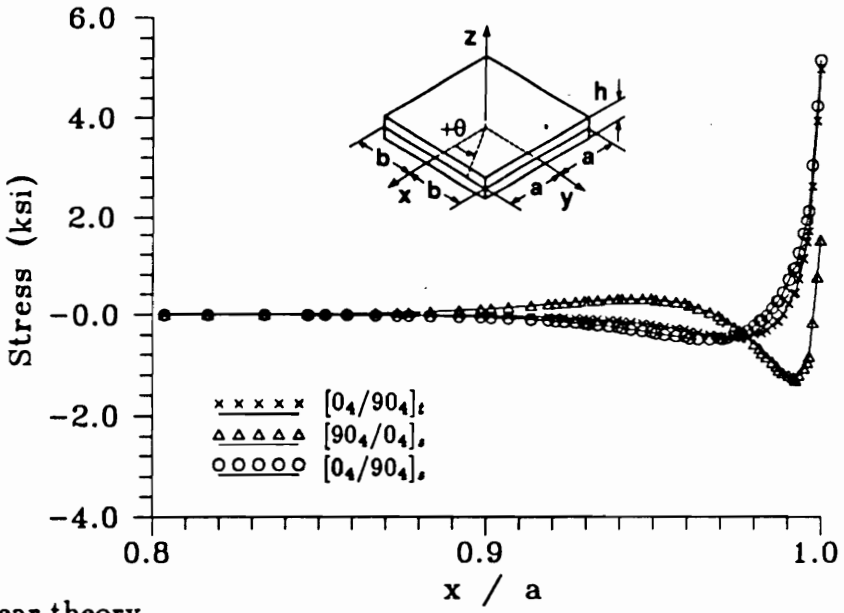

(b) Nonlinear theory

Figure 6.70 σ_{zz} and S_{zz} stress along $y = 0$ at the 0/90 interface for the 2.0 in. square $0_4/90_4$ laminates ($\Delta T = -280°F$, local analysis).

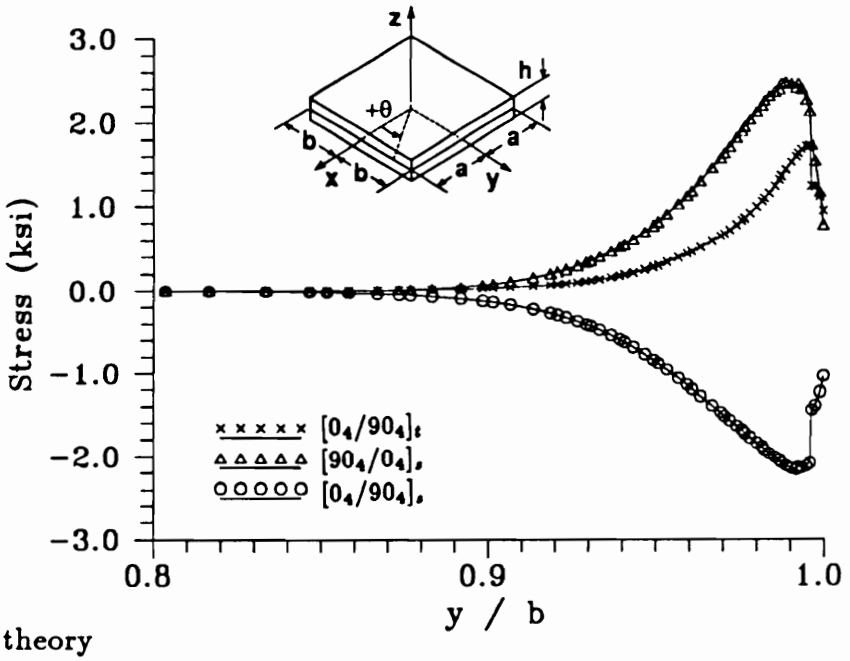

(a) Linear theory

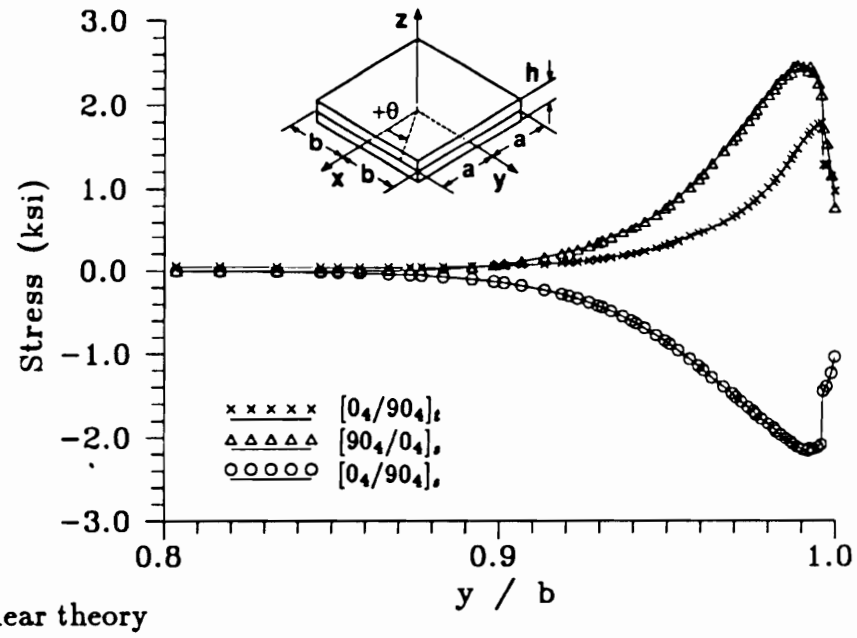

(b) Nonlinear theory

Figure 6.71 τ_{yz} and S_{yz} stress along $x = 0$ at the 0/90 interface for the 2.0 in. square $0_4/90_4$ laminates ($\Delta T = -280°F$, local analysis).

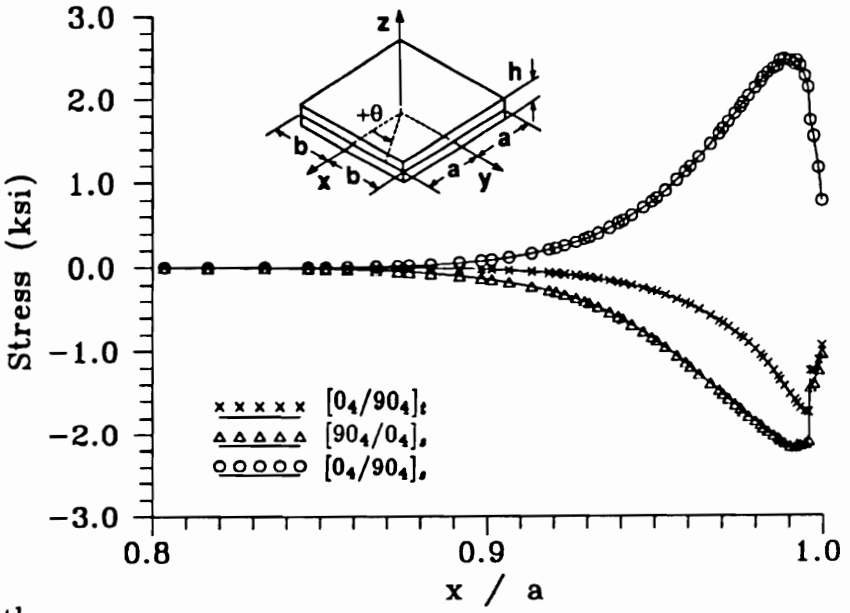

(a) Linear theory

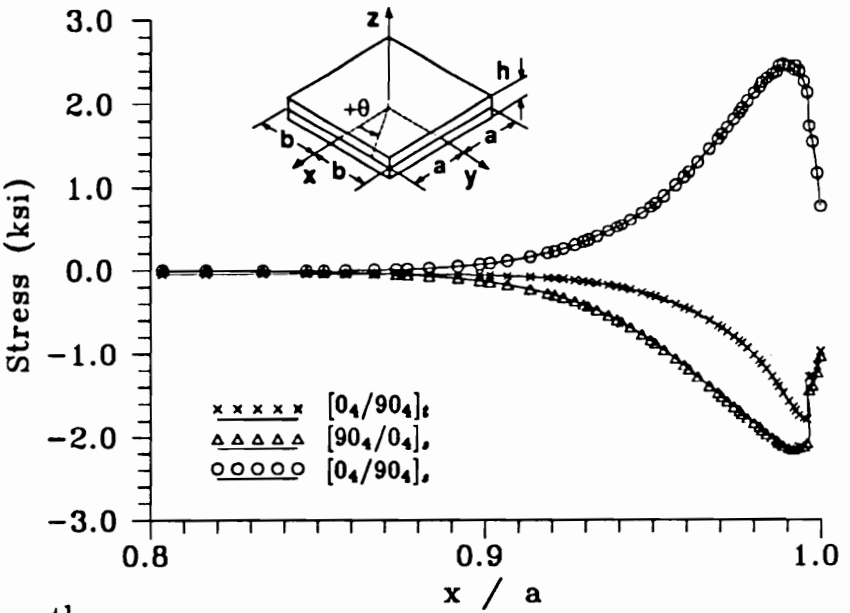

(b) Nonlinear theory

Figure 6.72 τ_{zz} and S_{zz} stress along $y = 0$ at the 0/90 interface for the 2.0 in. square $0_4/90_4$ laminates ($\Delta T = -280°F$, local analysis).

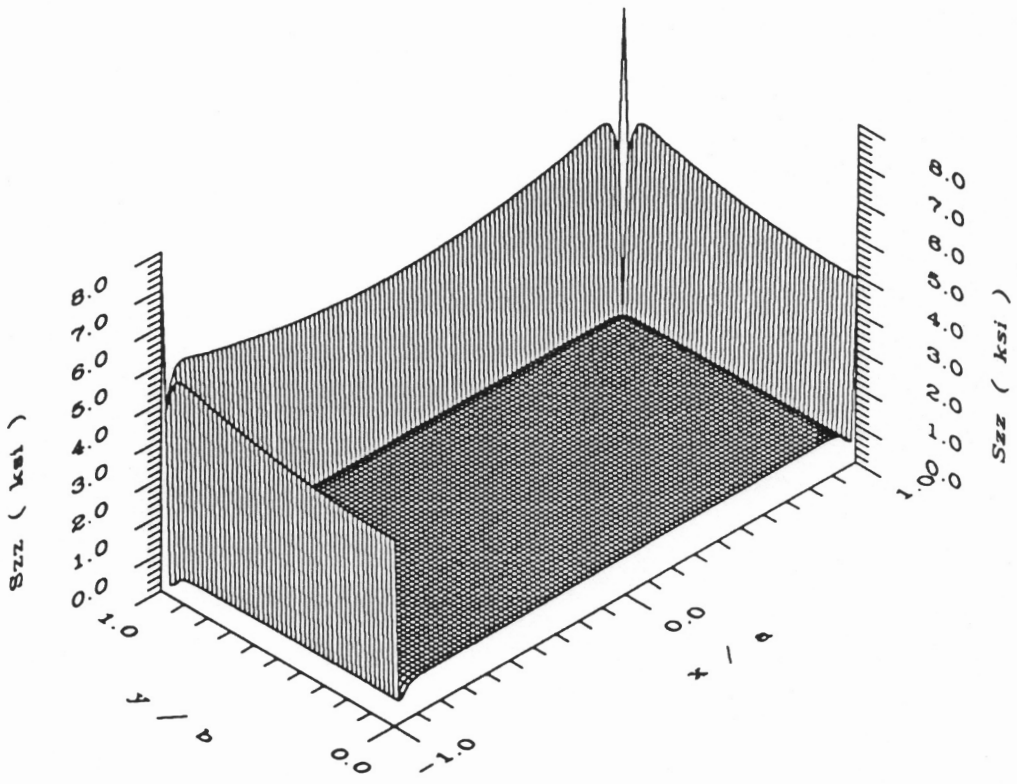

Figure 6.73 S_{zz} stress at the +45/–45 interface for a 2.0 in. square unsymmetric $[+45_4/-45_4]_t$ laminate ($\Delta T = -280°F$).

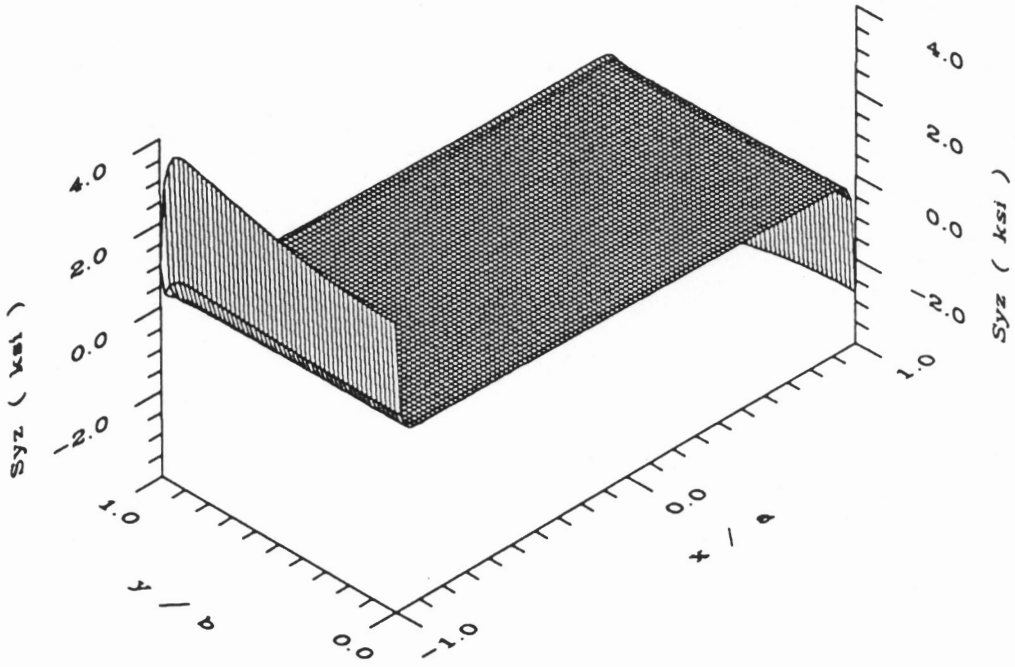

Figure 6.74 S_{yz} stress at the +45/–45 interface for a 2.0 in. square unsymmetric $[+45_4/-45_4]_t$ laminate ($\Delta T = -280°F$).

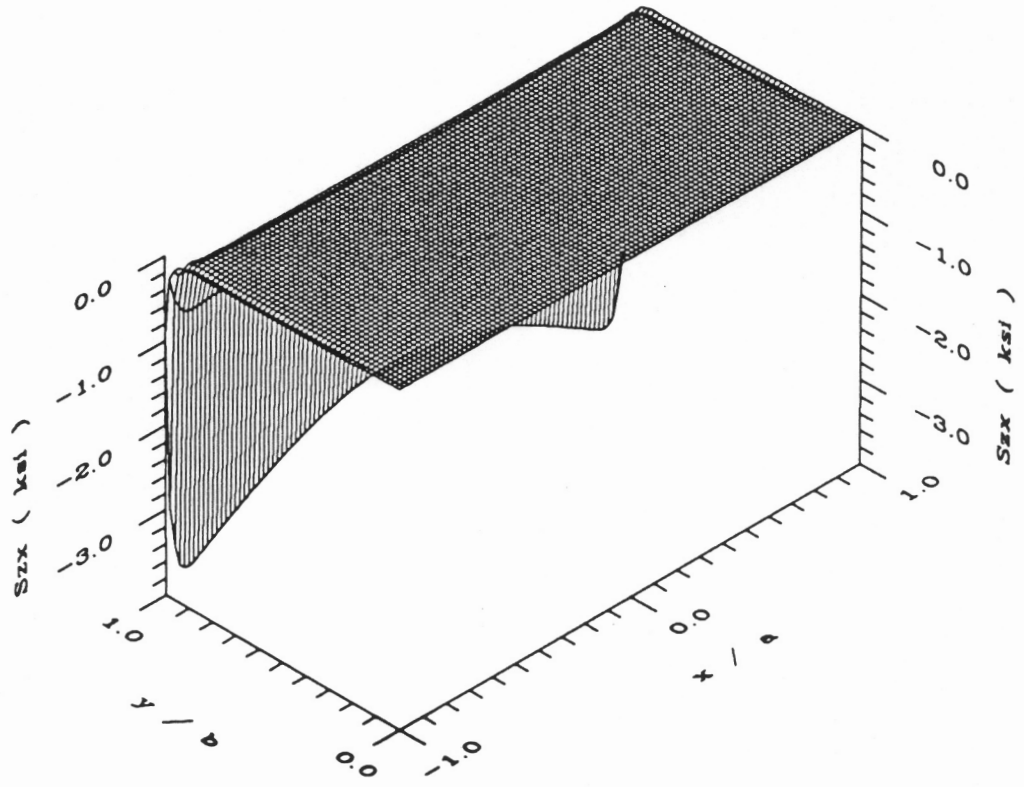

Figure 6.75 S_{zx} stress at the +45/–45 interface for a 2.0 in. square unsymmetric $[+45_4/-45_4]_t$ laminate ($\Delta T = -280°F$).

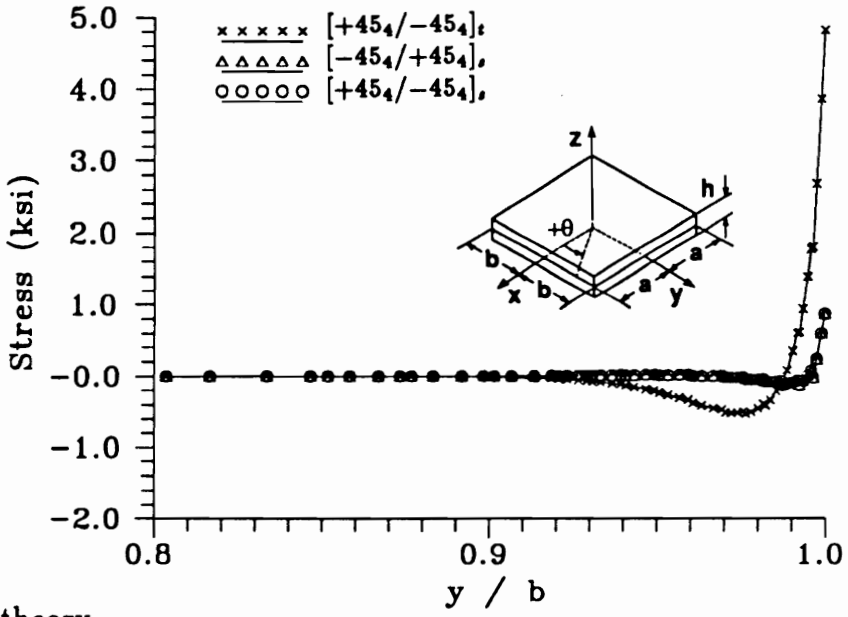

(a) Linear theory

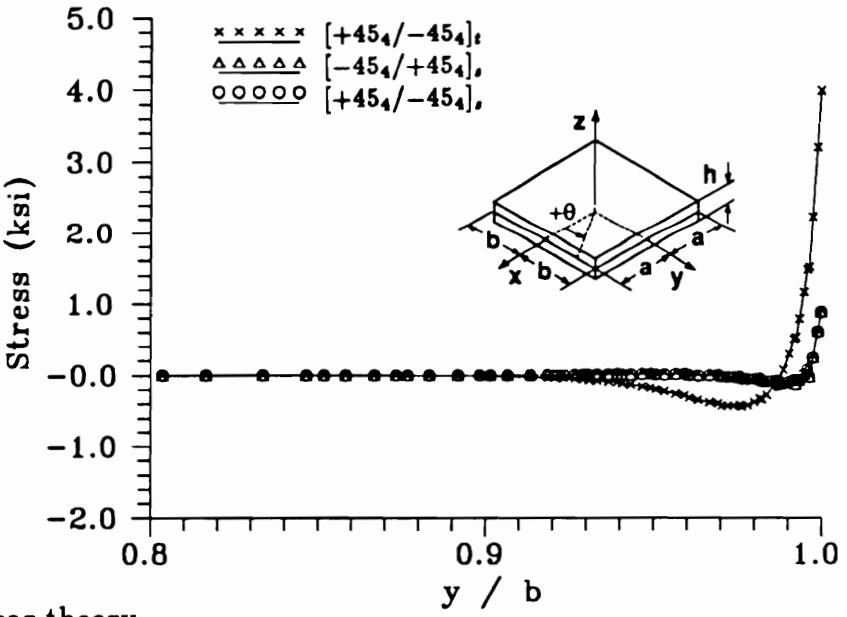

(b) Nonlinear theory

Figure 6.76 σ_{zz} and S_{zz} stress along $x = 0$ at the +45/−45 interface for the 2.0 in. square $+45_4/-45_4$ laminates ($\Delta T = -280°F$, local analysis).

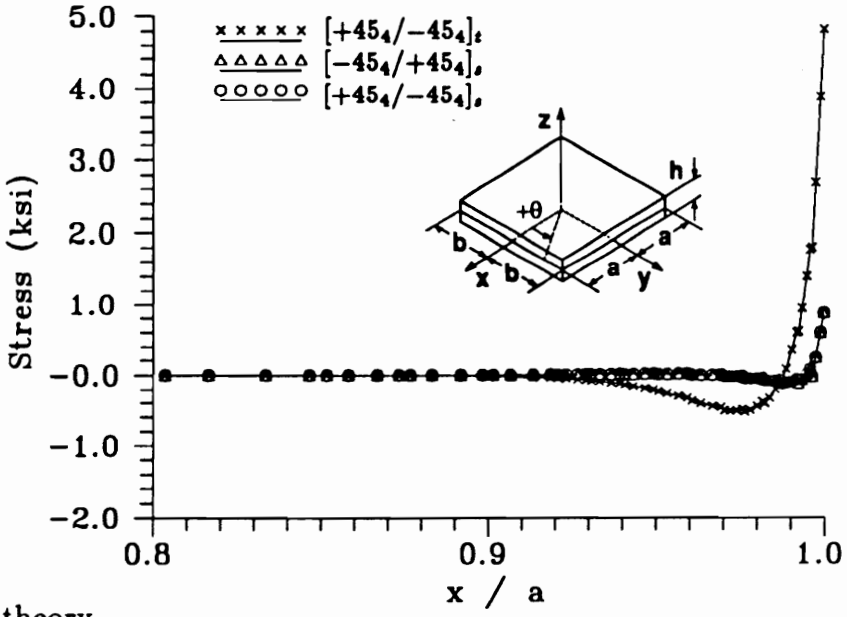

(a) Linear theory

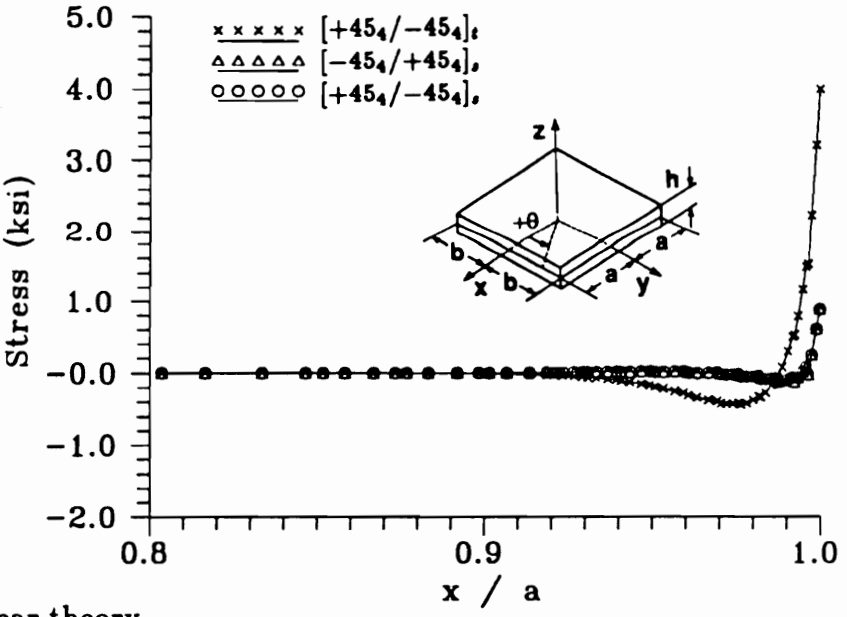

(b) Nonlinear theory

Figure 6.77 σ_{zz} and S_{zz} stress along $y = 0$ at the +45/−45 interface for the 2.0 in. square $+45_4/-45_4$ laminates ($\Delta T = -280°F$, local analysis).

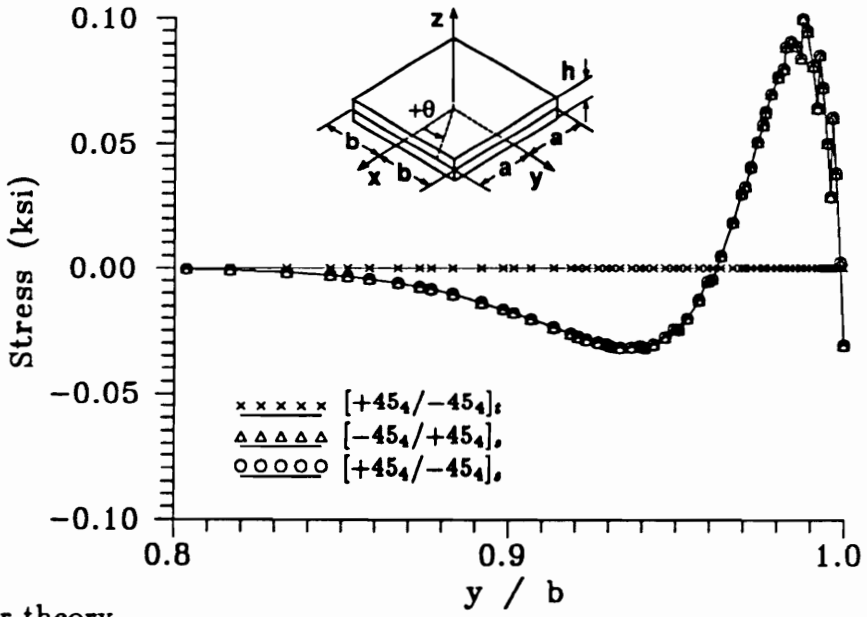

(a) Linear theory

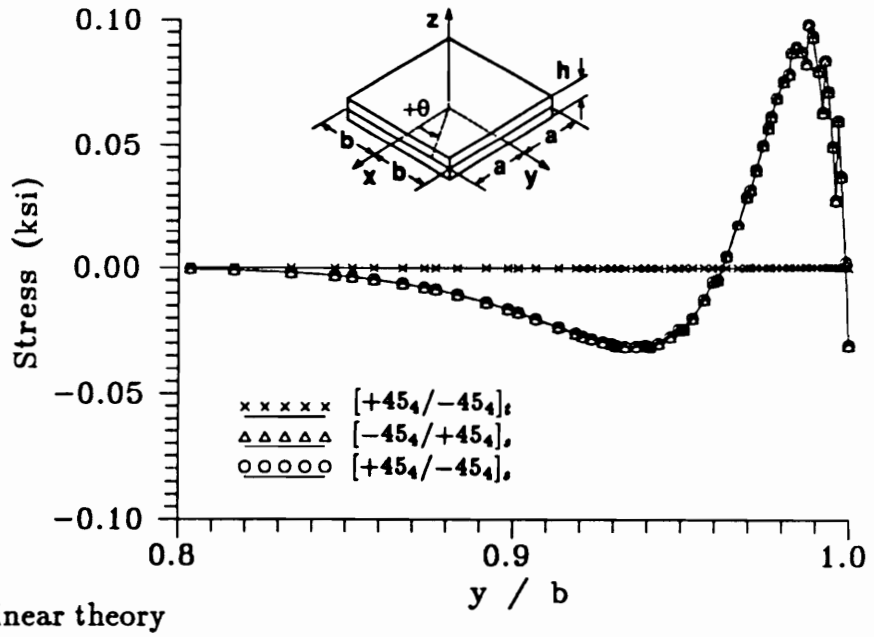

(b) Nonlinear theory

Figure 6.78 τ_{yz} and S_{yz} stress along $x = 0$ at the +45/−45 interface for the 2.0 in. square $+45_4/-45_4$ laminates ($\Delta T = -280°F$, local analysis).

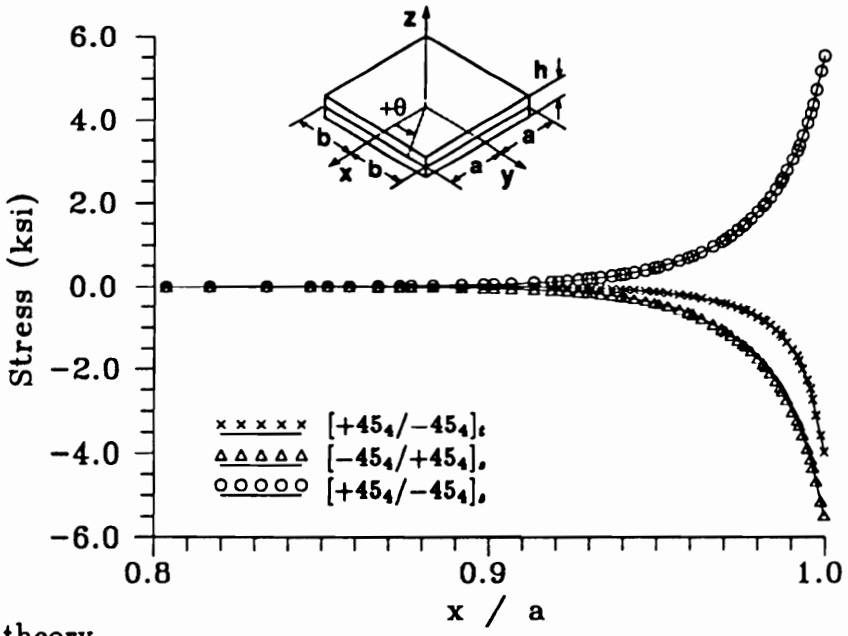

(a) Linear theory

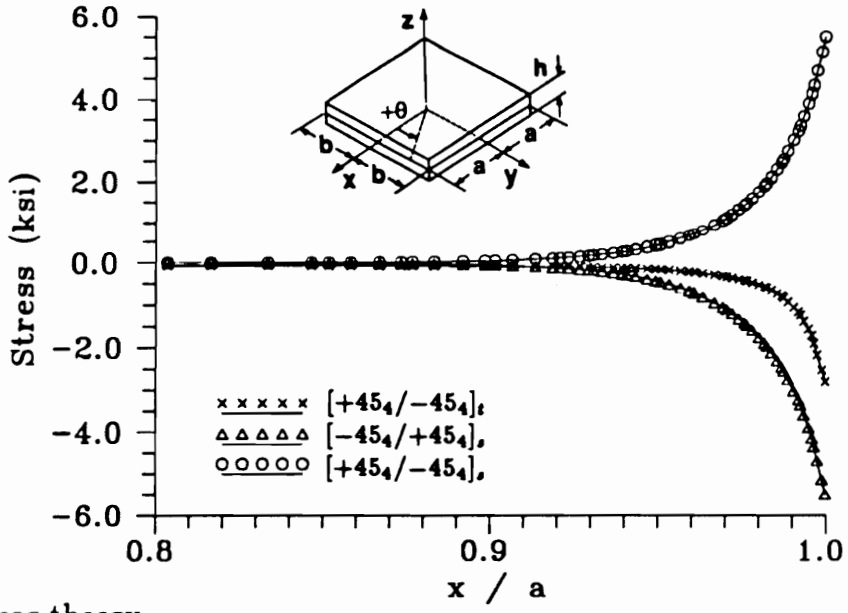

(b) Nonlinear theory

Figure 6.79 τ_{yz} and S_{yz} stress along $y = 0$ at the +45/−45 interface for the 2.0 in. square $+45_4/-45_4$ laminates ($\Delta T = -280°F$, local analysis).

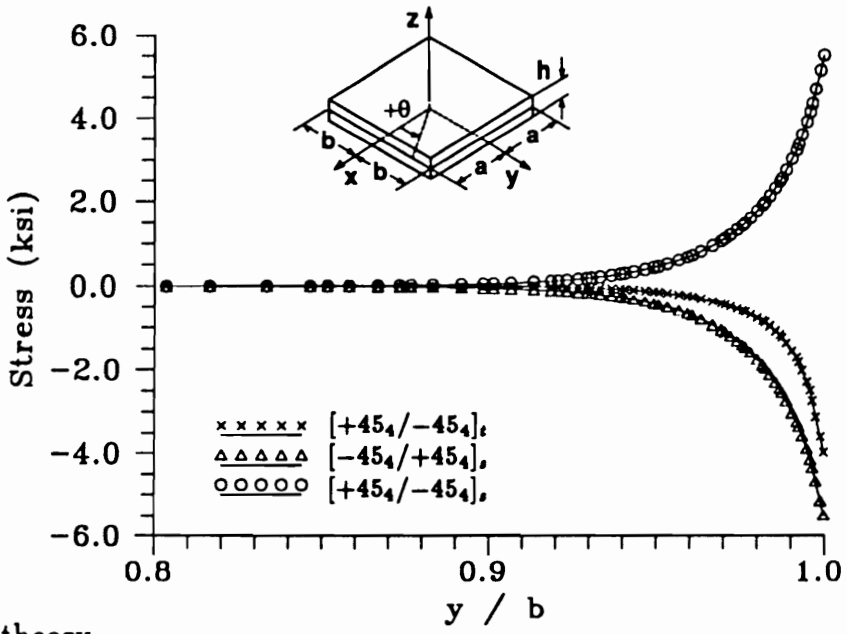

(a) Linear theory

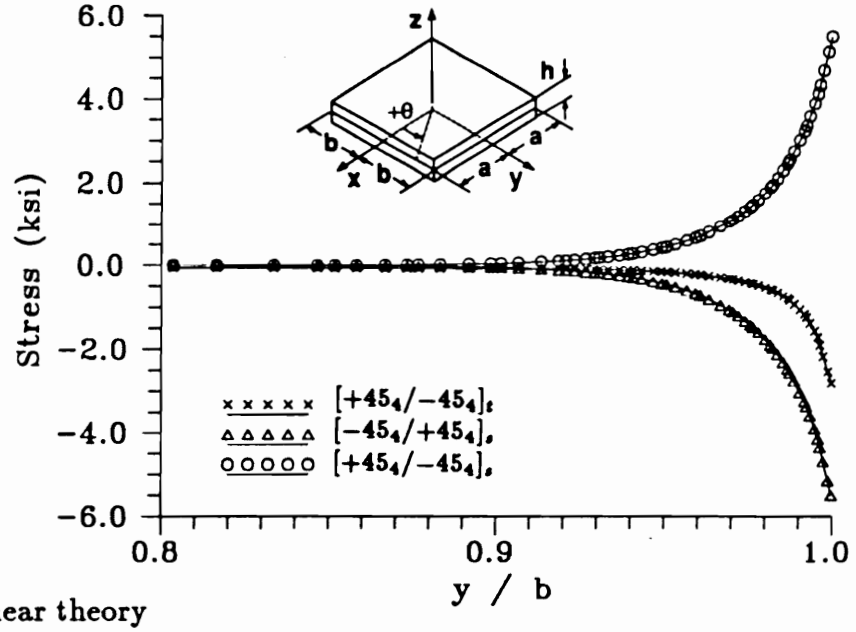

(b) Nonlinear theory

Figure 6.80 τ_{zz} and S_{zz} stress along $x = 0$ at the +45/–45 interface for the 2.0 in. square $+45_4/-45_4$ laminates ($\Delta T = -280°F$, local analysis).

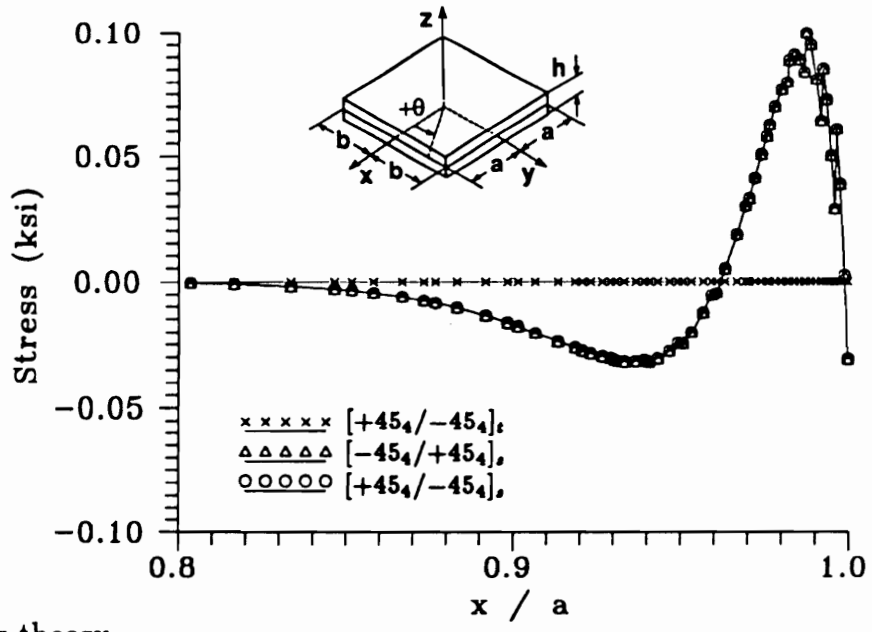

(a) Linear theory

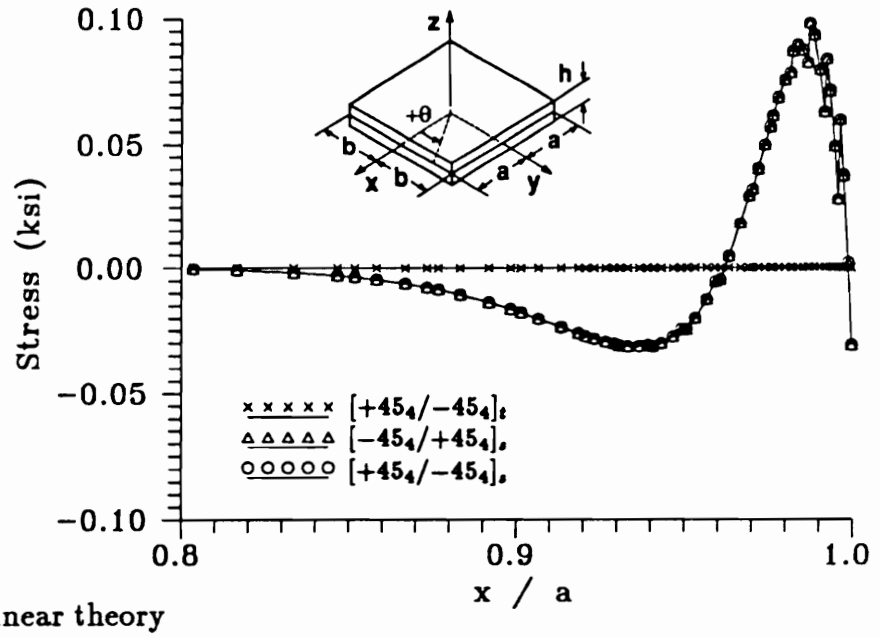

(b) Nonlinear theory

Figure 6.81 τ_{xz} and S_{xz} stress along $y = 0$ at the +45/−45 interface for the 2.0 in. square $+45_4/-45_4$ laminates ($\Delta T = -280°F$, local analysis).

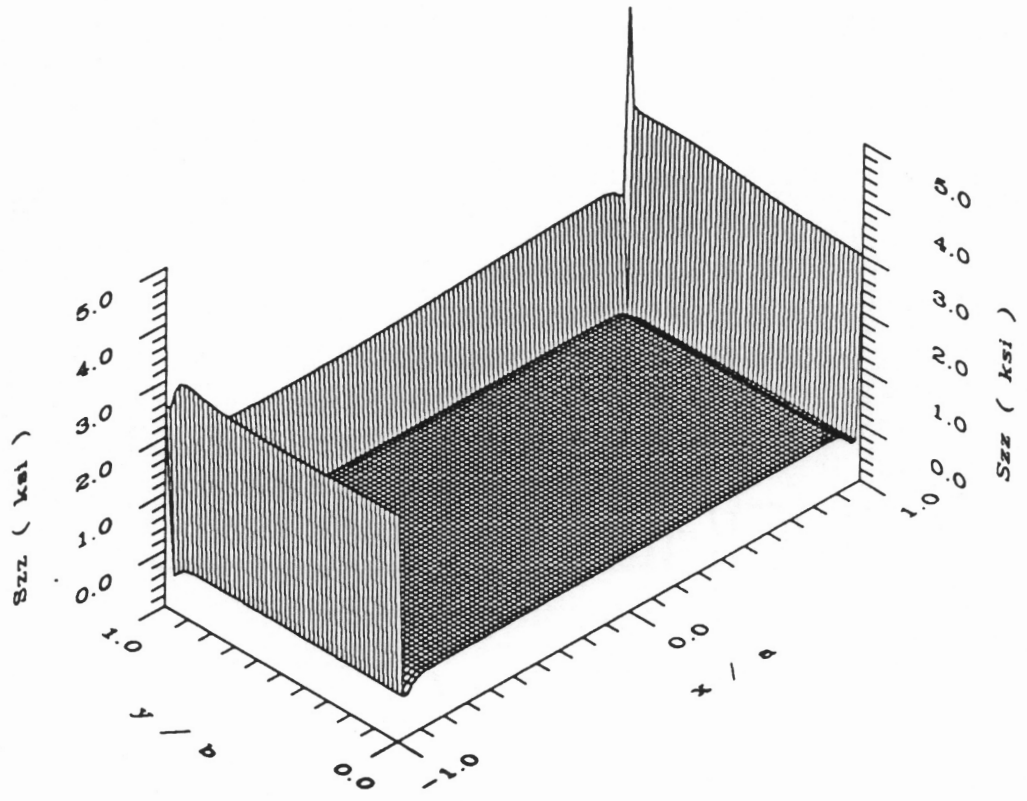

Figure 6.82 S_{zz} stress at the $0/+45$ interface for a 2.0 in. square unsymmetric $[0_4/+45_4]_t$ laminate ($\Delta T = -280°F$).

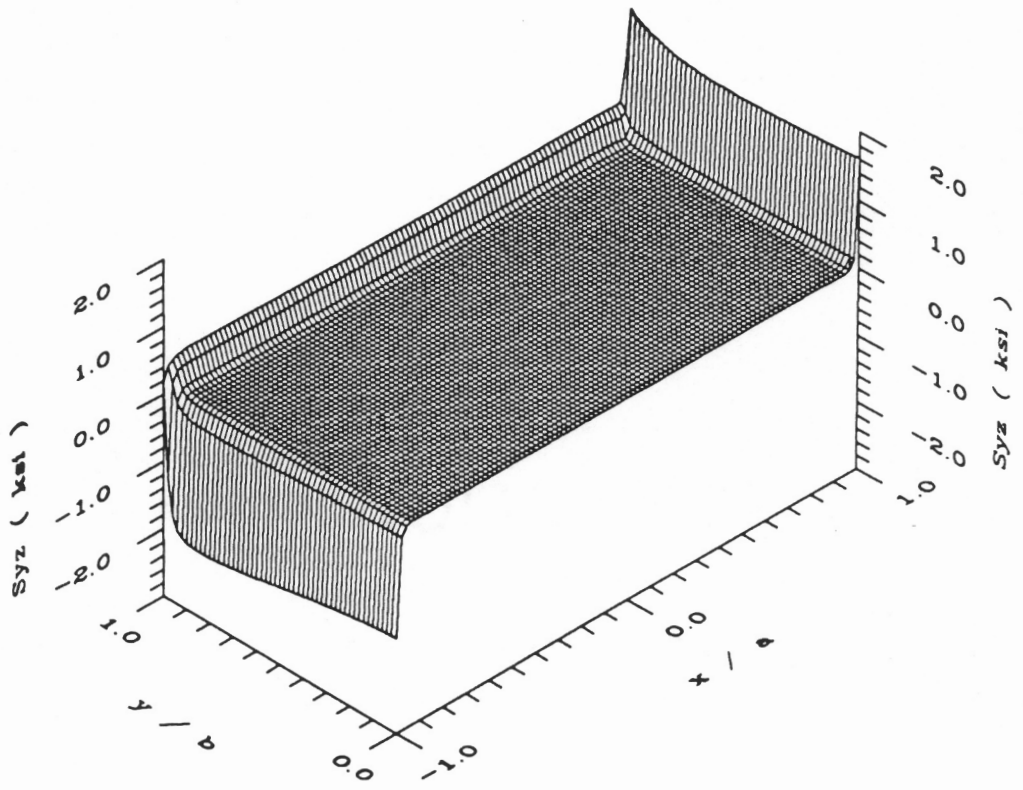

Figure 6.83 S_{yz} stress at the $0/+45$ interface for a 2.0 in. square unsymmetric $[0_4/+45_4]_t$ laminate ($\Delta T = -280°F$).

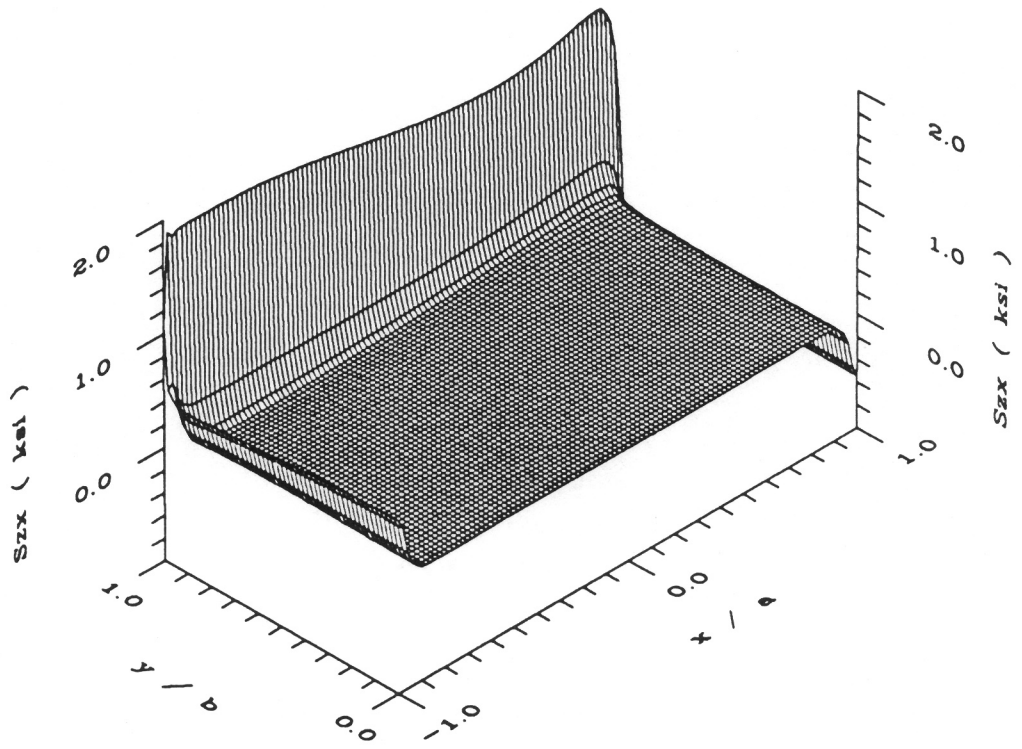

Figure 6.84 S_{zx} stress at the 0/+45 interface for a 2.0 in. square unsymmetric $[0_4/+45_4]_t$ laminate ($\Delta T = -280°F$).

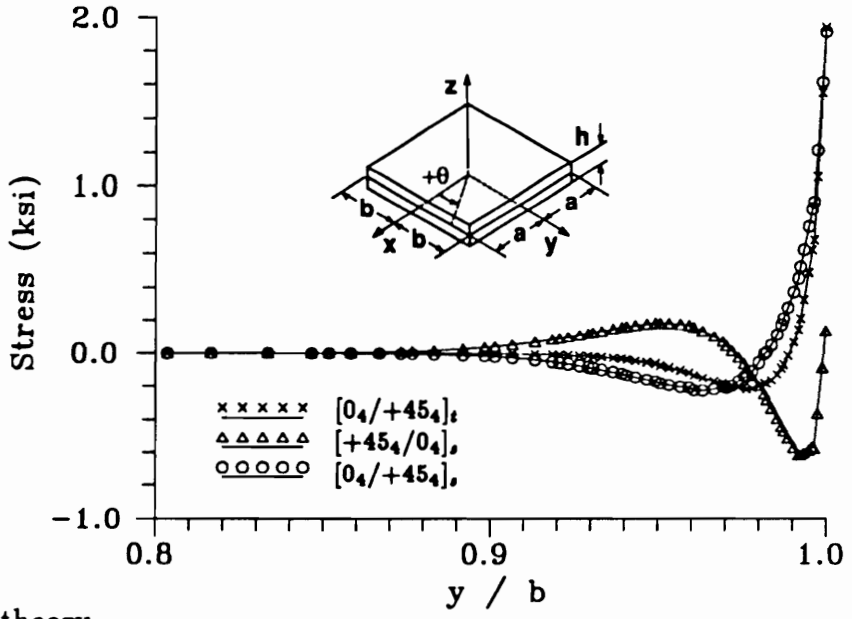

(a) Linear theory

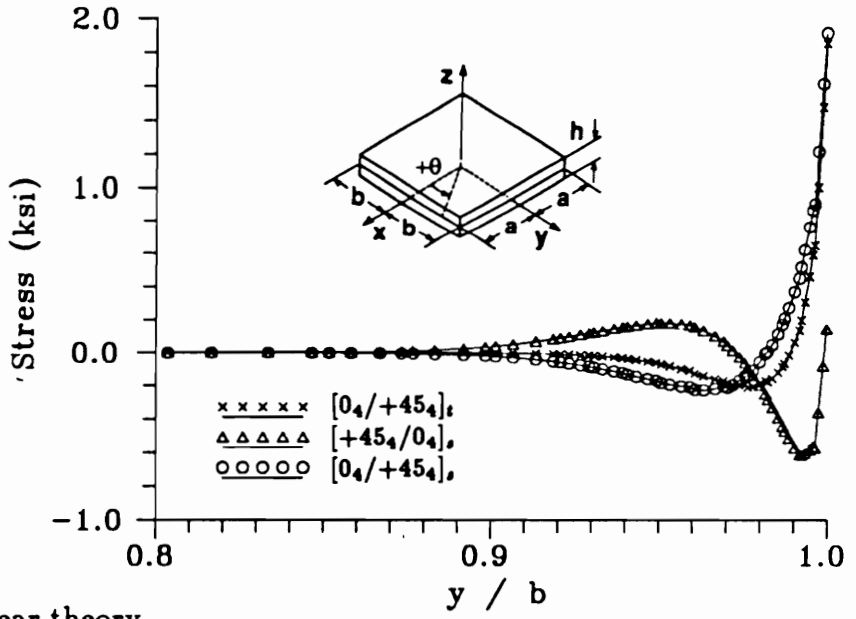

(b) Nonlinear theory

Figure 6.85 σ_{zz} and S_{zz} stress along $x = 0$ at the $0/+45$ interface for the 2.0 in. square $0_4/+45_4$ laminates ($\Delta T = -280°F$, local analysis).

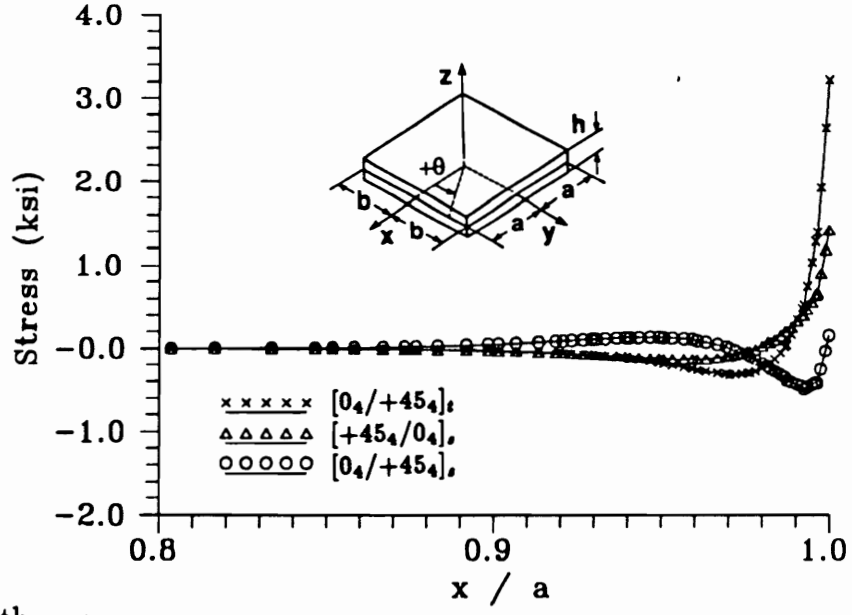

(a) Linear theory

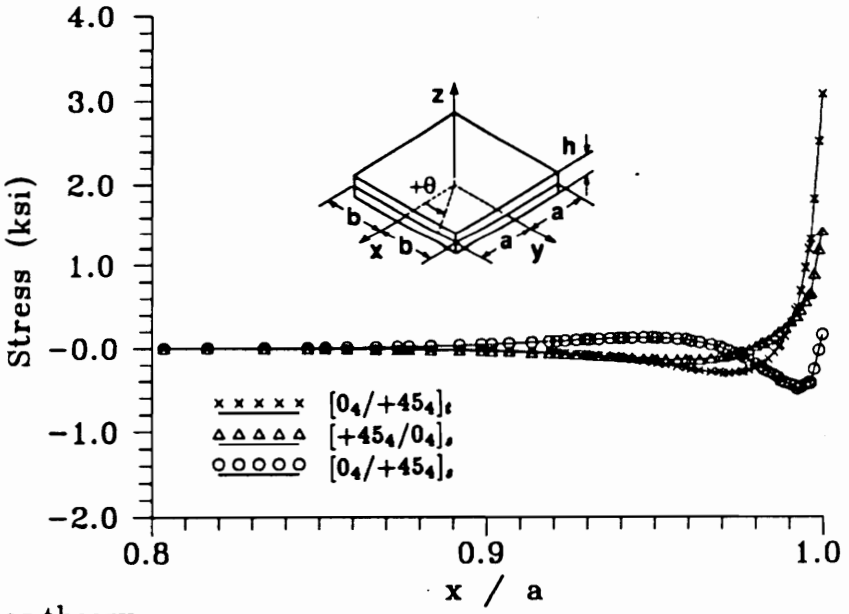

(b) Nonlinear theory

Figure 6.86 σ_{zz} and S_{zz} stress along $y = 0$ at the $0/+45$ interface for the 2.0 in. square $0_4/+45_4$ laminates ($\Delta T = -280°F$, local analysis).

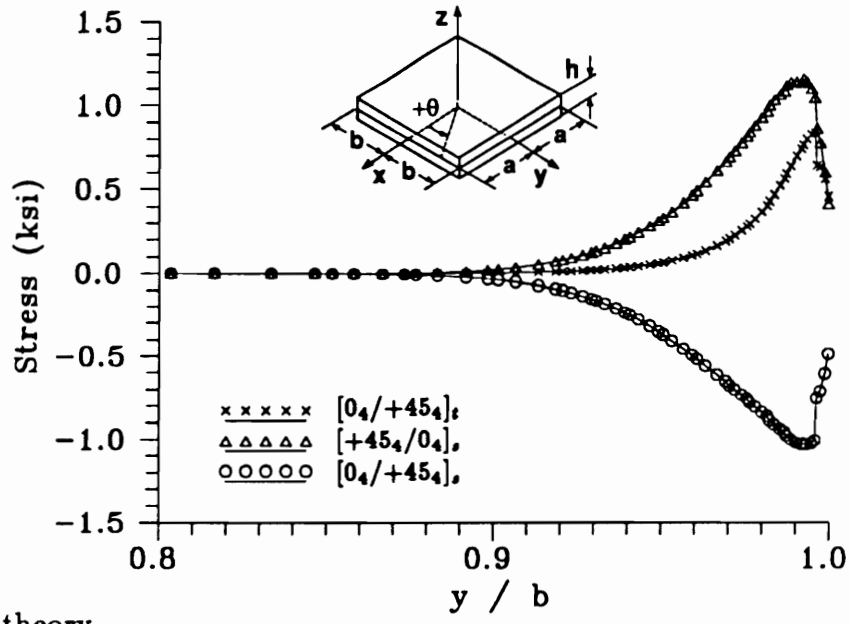

(a) Linear theory

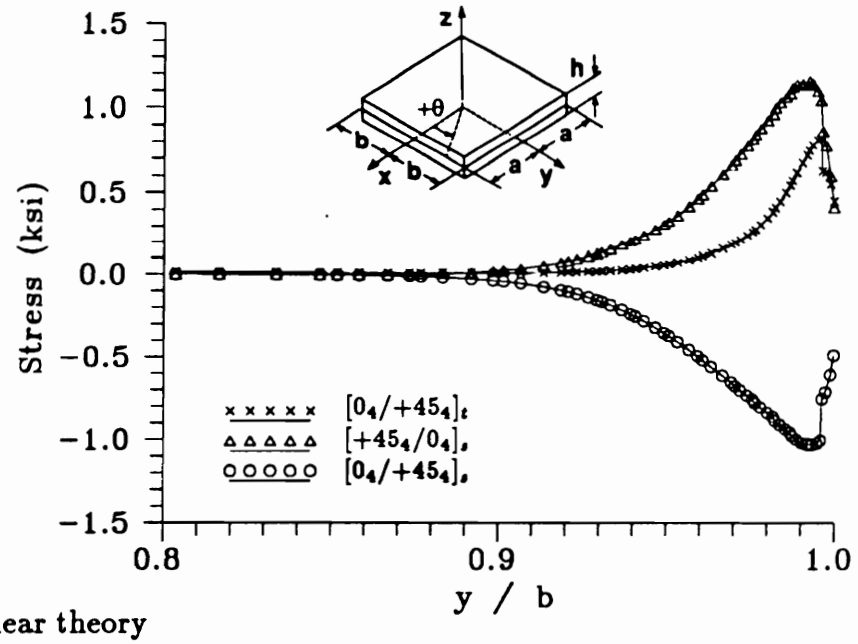

(b) Nonlinear theory

Figure 6.87 τ_{yz} and S_{yz} stress along $x = 0$ at the $0/+45$ interface for the 2.0 in. square $0_4/+45_4$ laminates ($\Delta T = -280°F$, local analysis).

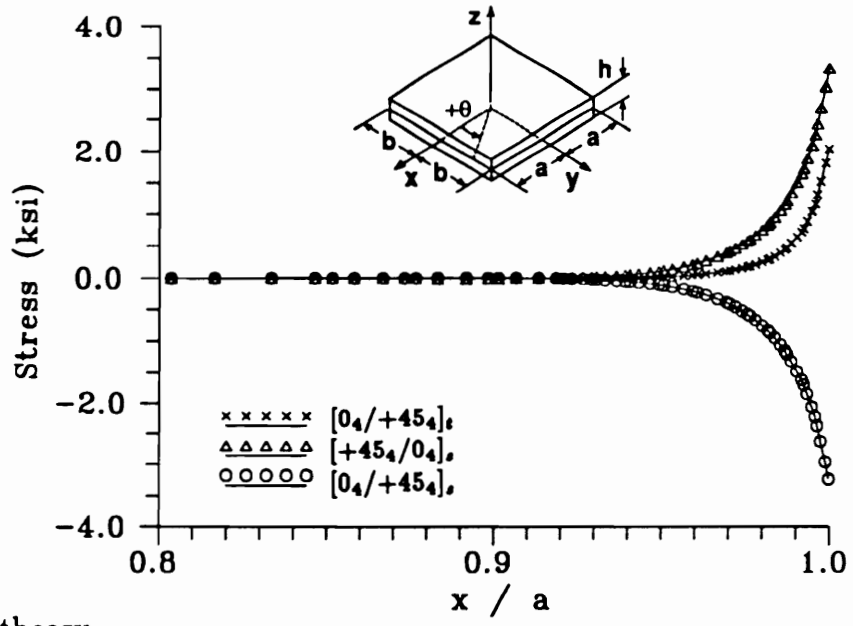

(a) Linear theory

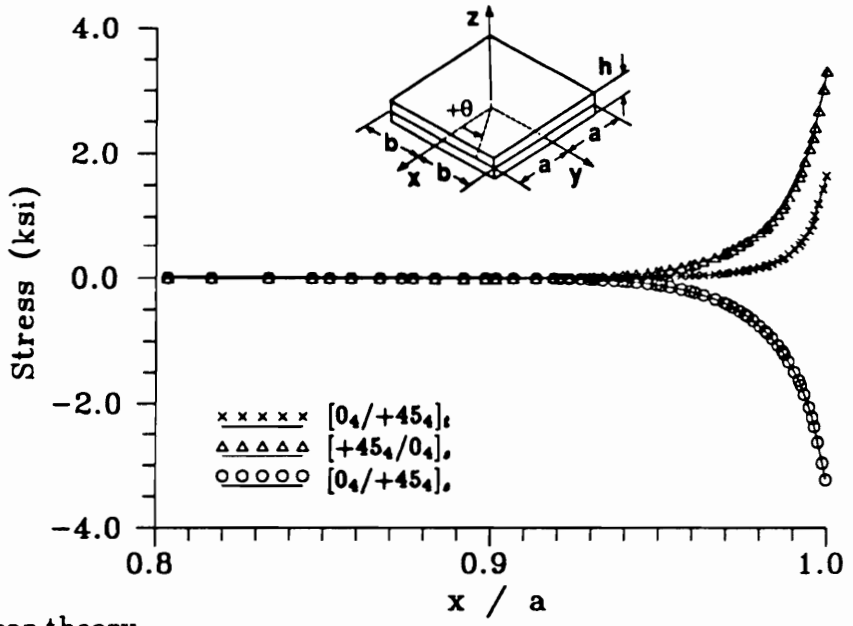

(b) Nonlinear theory

Figure 6.88 τ_{yz} and S_{yz} stress along $y = 0$ at the $0/+45$ interface for the 2.0 in. square $0_4/+45_4$ laminates ($\Delta T = -280°F$, local analysis).

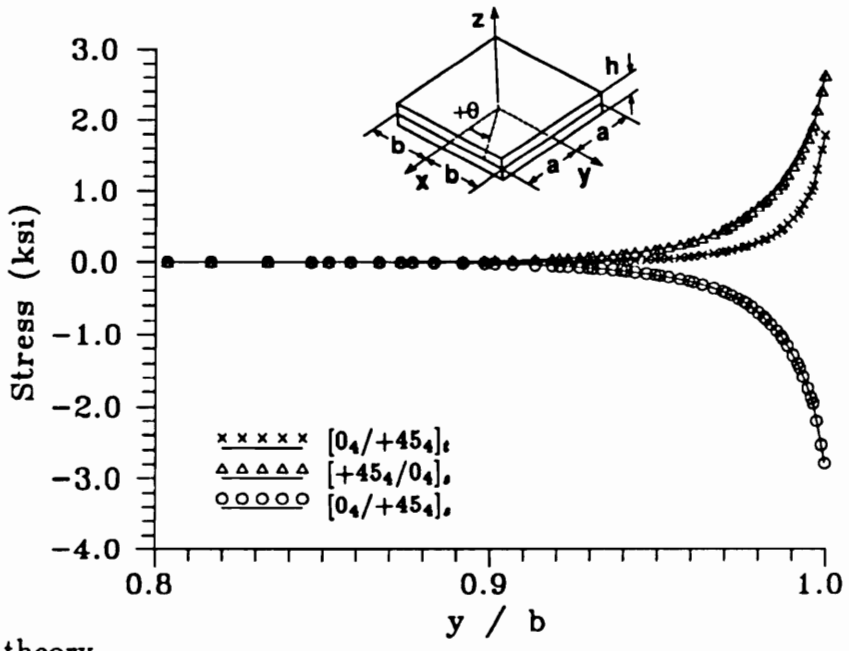

(a) Linear theory

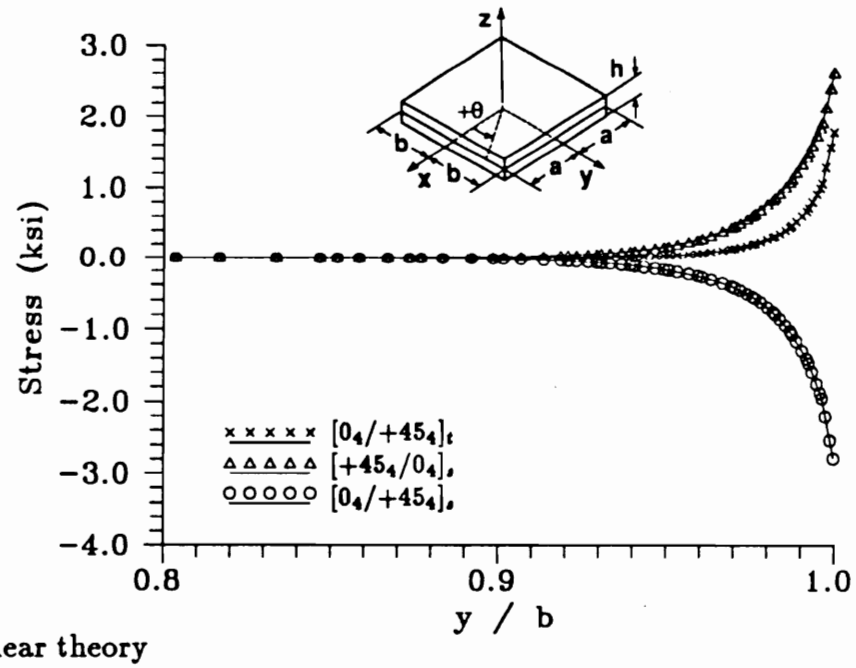

(b) Nonlinear theory

Figure 6.89 τ_{zz} and S_{zz} stress along $x = 0$ at the $0/+45$ interface for the 2.0 in. square $0_4/+45_4$ laminates ($\Delta T = -280°F$, local analysis).

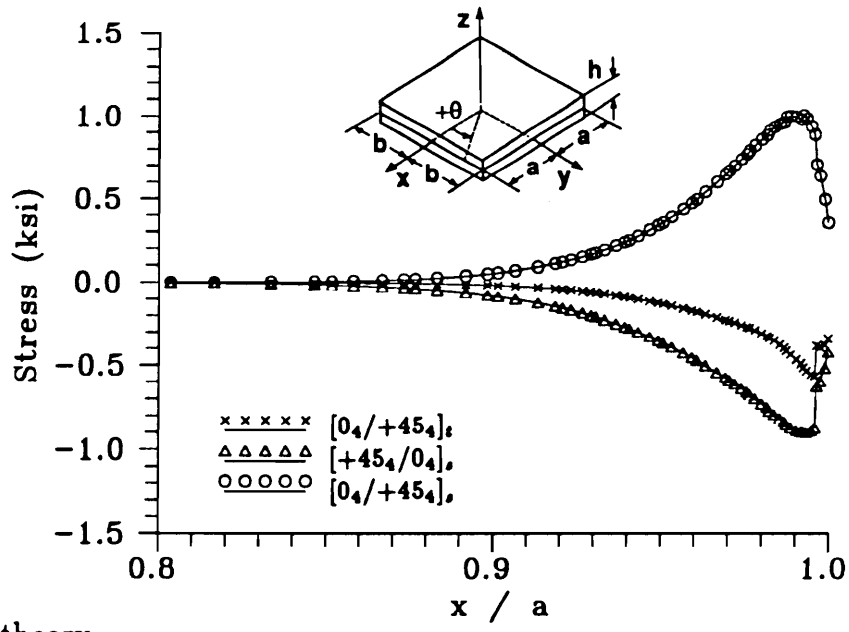

(a) Linear theory

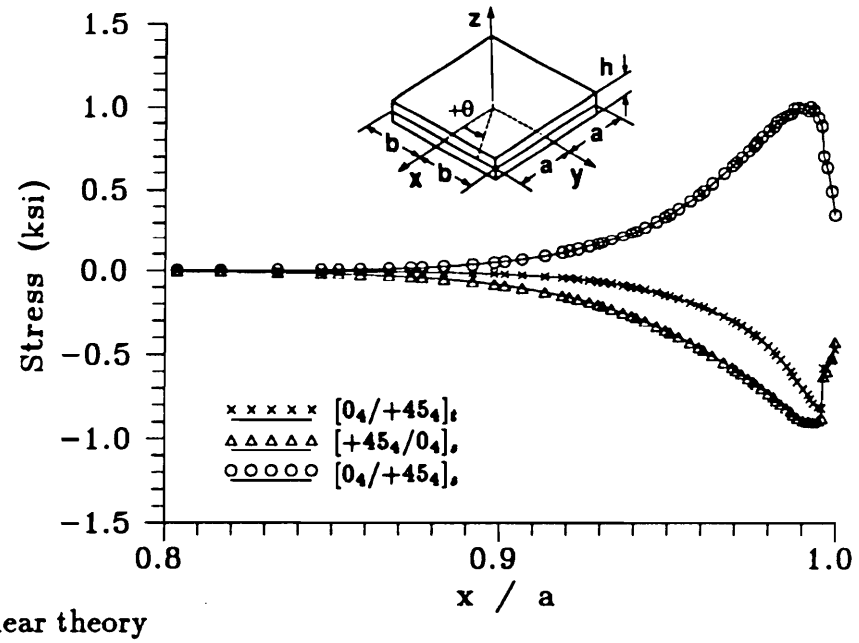

(b) Nonlinear theory

Figure 6.90 τ_{zz} and S_{zz} stress along $y = 0$ at the $0/+45$ interface for the 2.0 in. square $0_4/+45_4$ laminates ($\Delta T = -280°F$, local analysis).

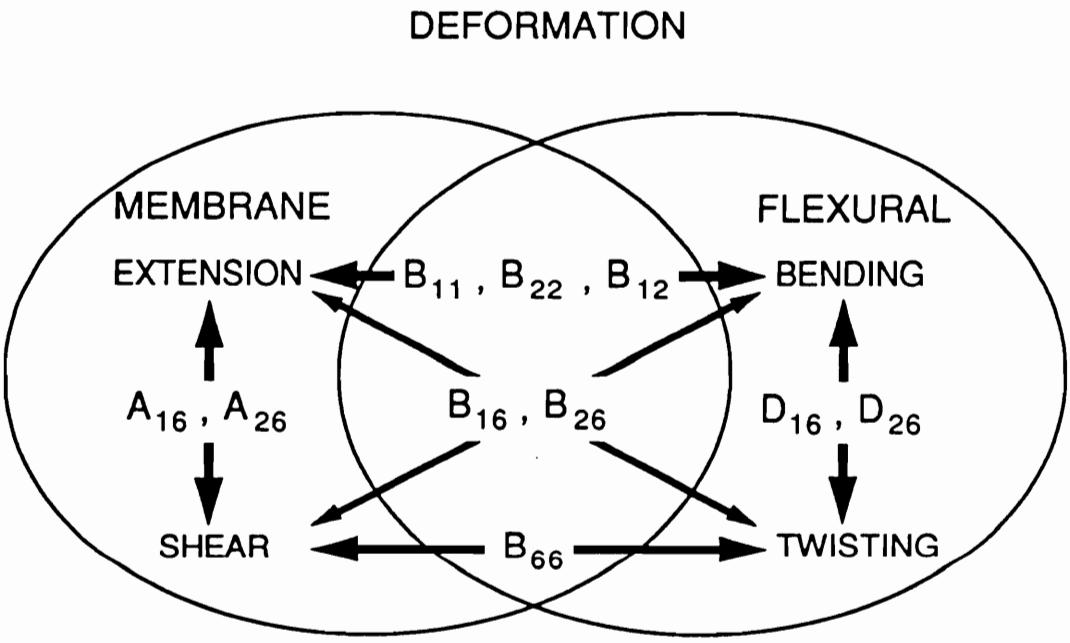

Figure A.1 The deformational coupling relationships of laminated anisotropic plates.

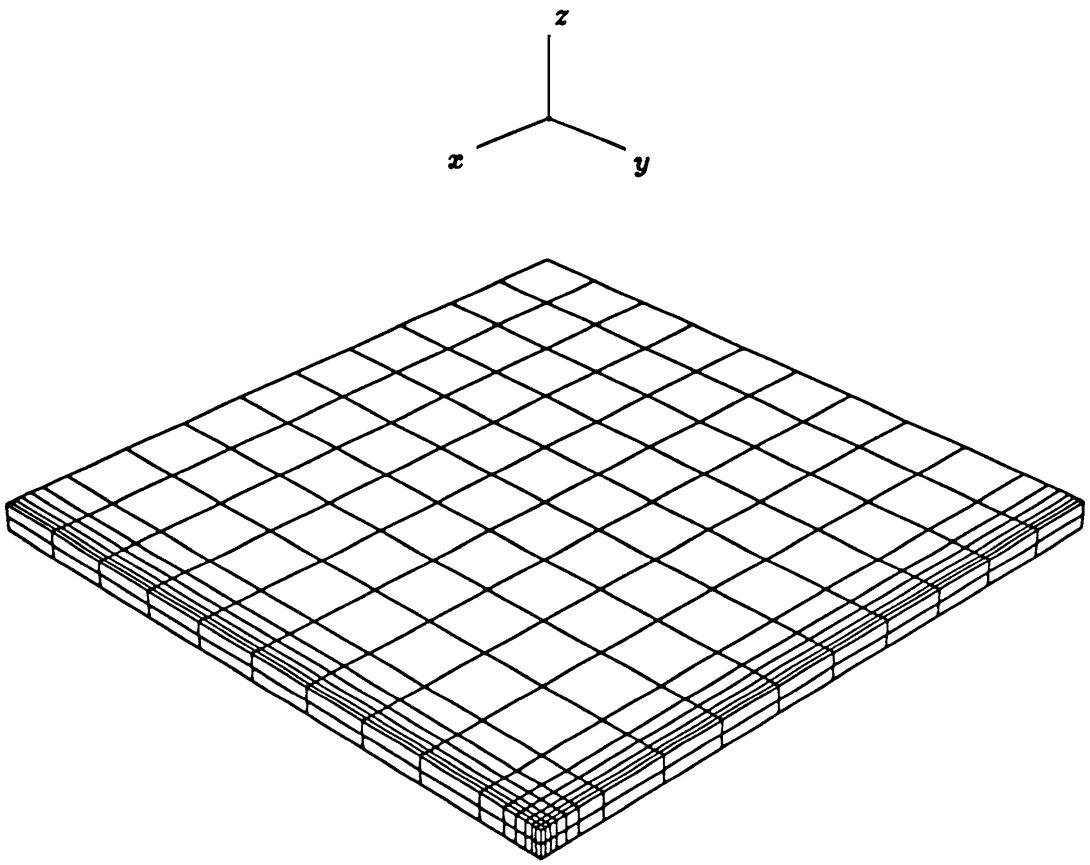

Global finite element model summary:

quarter symmetry model	$+0.00$ in. $\leq x \leq +1.00$ in.
$15 \times 15 \times 2 = 450$ elements	$+0.00$ in. $\leq y \leq +1.00$ in.
13611 equations	-0.02 in. $\leq z \leq +0.02$ in. (unsymmetric)
94.2 megabytes	-0.00 in. $\leq z \leq +0.04$ in. (symmetric)

Figure D.1 Global finite element model used for the analysis of 2.0 in. square symmetric and unsymmetric laminates.

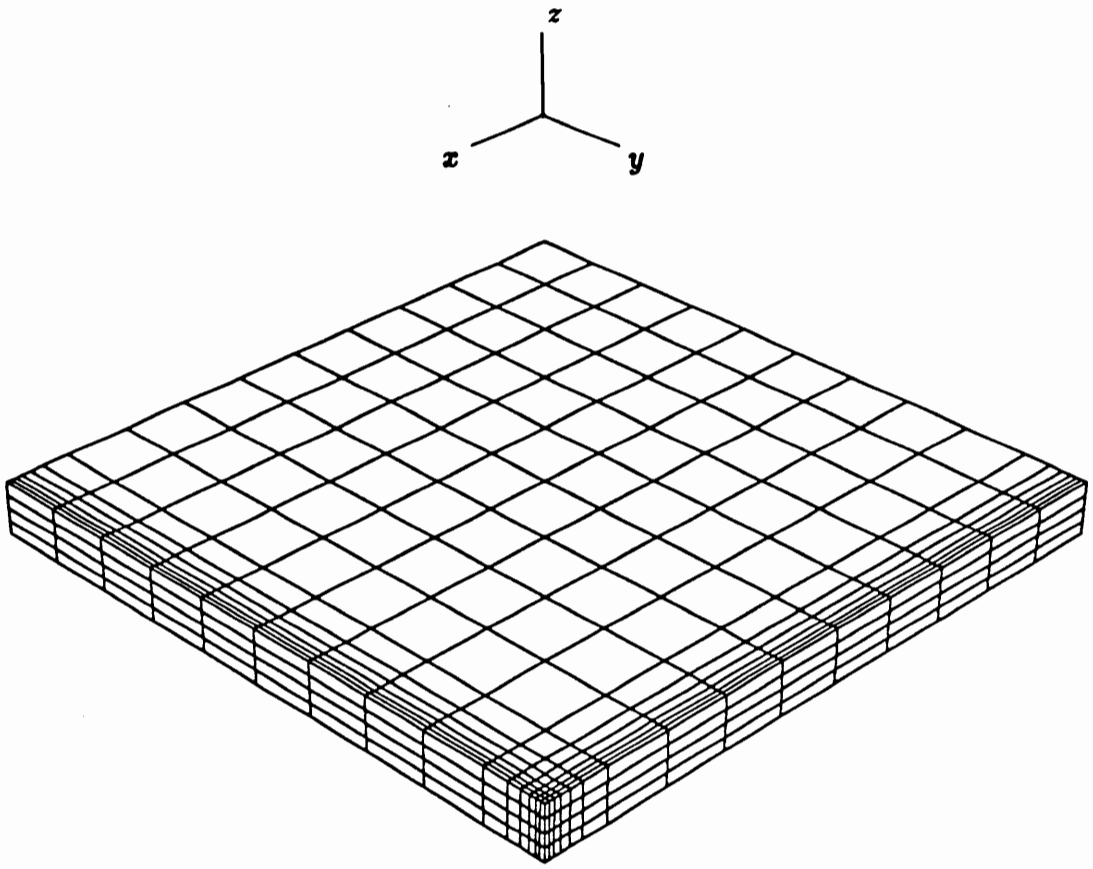

Global finite element model summary:

quarter symmetry model	$+0.00$ in. $\leq x \leq +1.00$ in.
$15 \times 15 \times 4 = 900$ elements	$+0.00$ in. $\leq y \leq +1.00$ in.
23668 equations	-0.04 in. $\leq z \leq +0.04$ in.
269.8 megabytes	symmetric laminate

Figure D.2 Global finite element model used for the geometrically nonlinear analysis of 2.0 in. square symmetric laminates subjected to compressive loading.

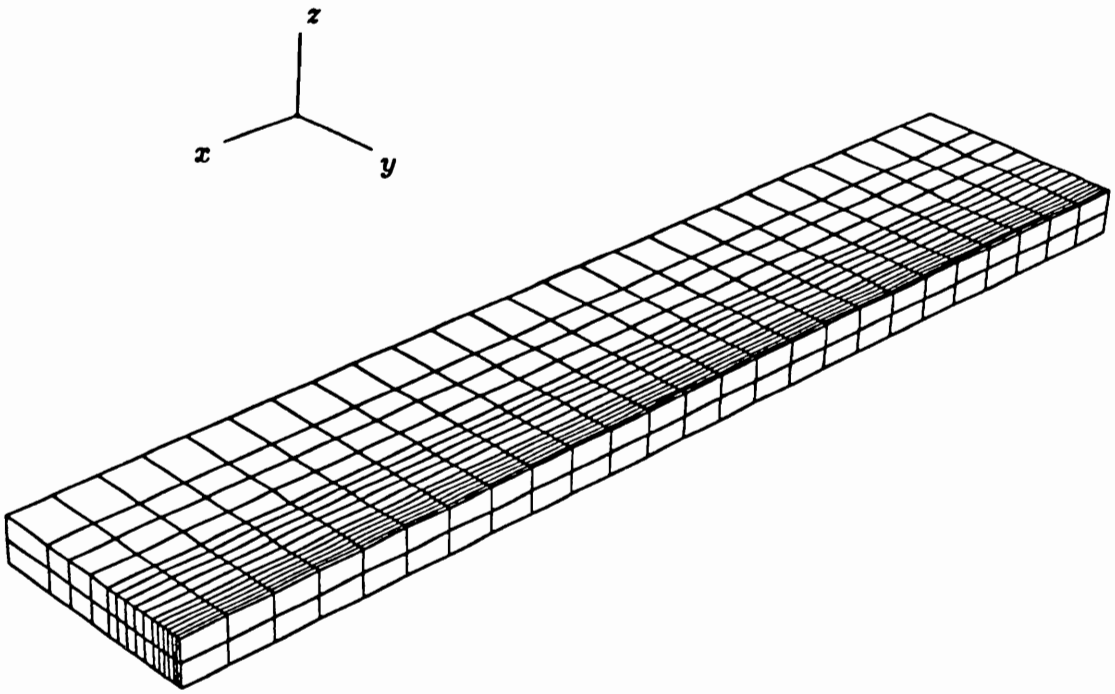

Local finite element model summary:

quarter symmetry model	$+0.00$ in. $\leq x \leq +1.00$ in.
$25 \times 15 \times 2 = 750$ elements	$+0.80$ in. $\leq y \leq +1.00$ in.
22754 equations	-0.02 in. $\leq z \leq +0.02$ in. (unsymmetric)
162.1 megabytes	-0.00 in. $\leq z \leq +0.04$ in. (symmetric)

Figure D.3 Local finite element model used for the analysis of 2.0 in. square symmetric and unsymmetric laminates.

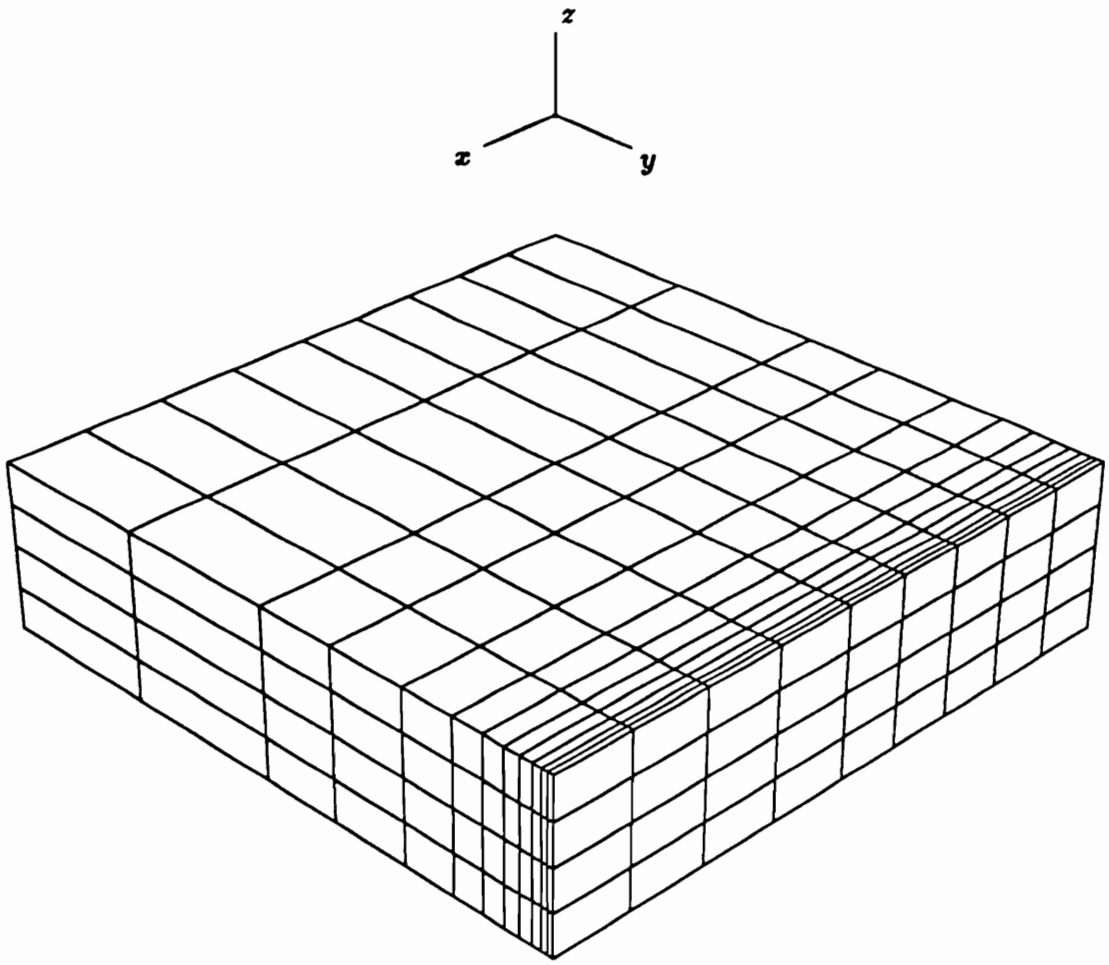

Global finite element model summary:

quarter symmetry model	$+0.00$ in. $\leq x \leq +2.00$ in.
$9 \times 12 \times 4 = 432$ elements	$+0.00$ in. $\leq y \leq +2.00$ in.
11634 equations	-0.25 in. $\leq z \leq +0.25$ in. (unsymmetric)
103.9 megabytes	-0.00 in. $\leq z \leq +0.50$ in. (symmetric)

Figure D.4 Global finite element model used for comparisons with previous results for 4.0 in. square symmetric and unsymmetric laminates.

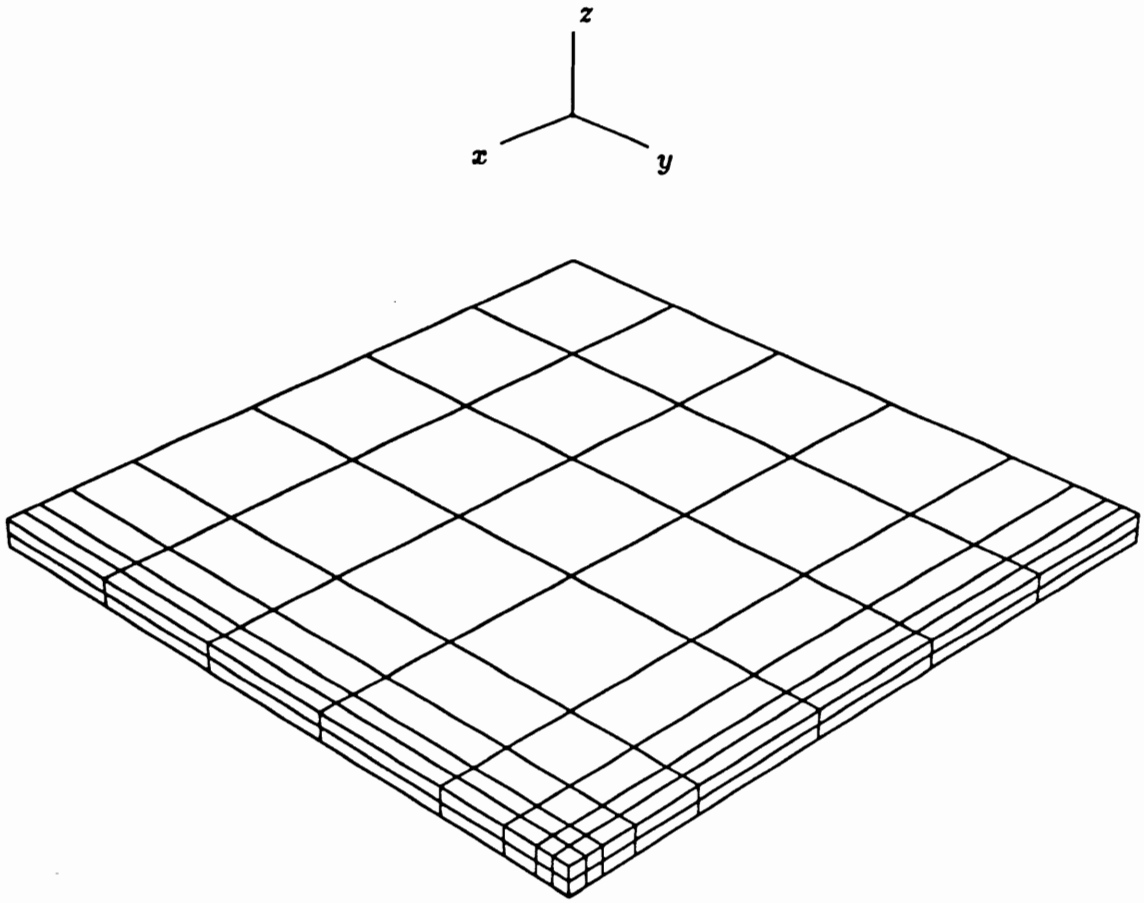

Global finite element model summary:

quarter symmetry model	$+0.00$ in. $\leq x \leq +1.00$ in.
$8 \times 8 \times 2 = 128$ elements	$+0.00$ in. $\leq y \leq +1.00$ in.
4070 equations	-0.02 in. $\leq z \leq +0.02$ in.
16.3 megabytes	unsymmetric laminate

Figure D.5 Global finite element model used for the preliminary analysis of 2.0 in. square unsymmetric laminates.

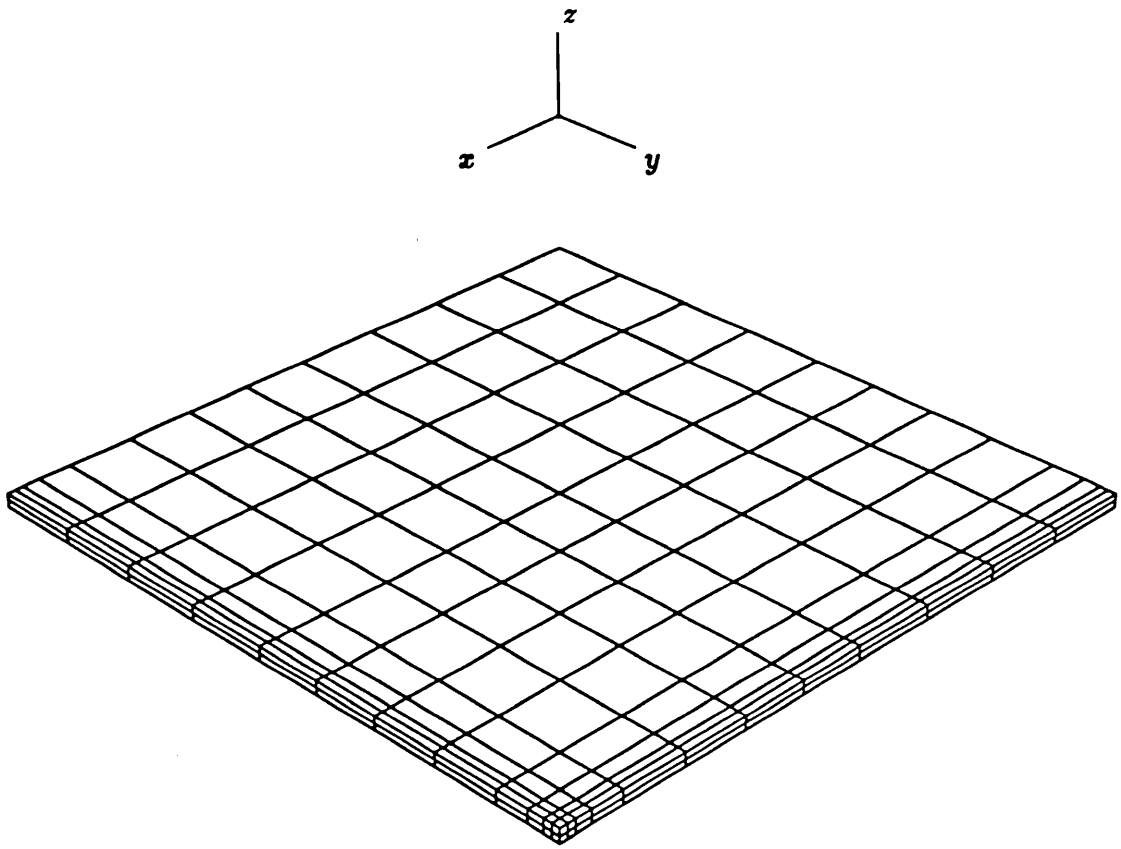

Global finite element model summary:

quarter symmetry model	$+0.00$ in. $\leq x \leq +2.00$ in.
$12 \times 12 \times 2 = 288$ elements	$+0.00$ in. $\leq y \leq +2.00$ in.
8838 equations	-0.02 in. $\leq z \leq +0.02$ in.
49.0 megabytes	unsymmetric laminate

Figure D.6 Global finite element model used for the preliminary analysis of 4.0 in. square unsymmetric laminates.

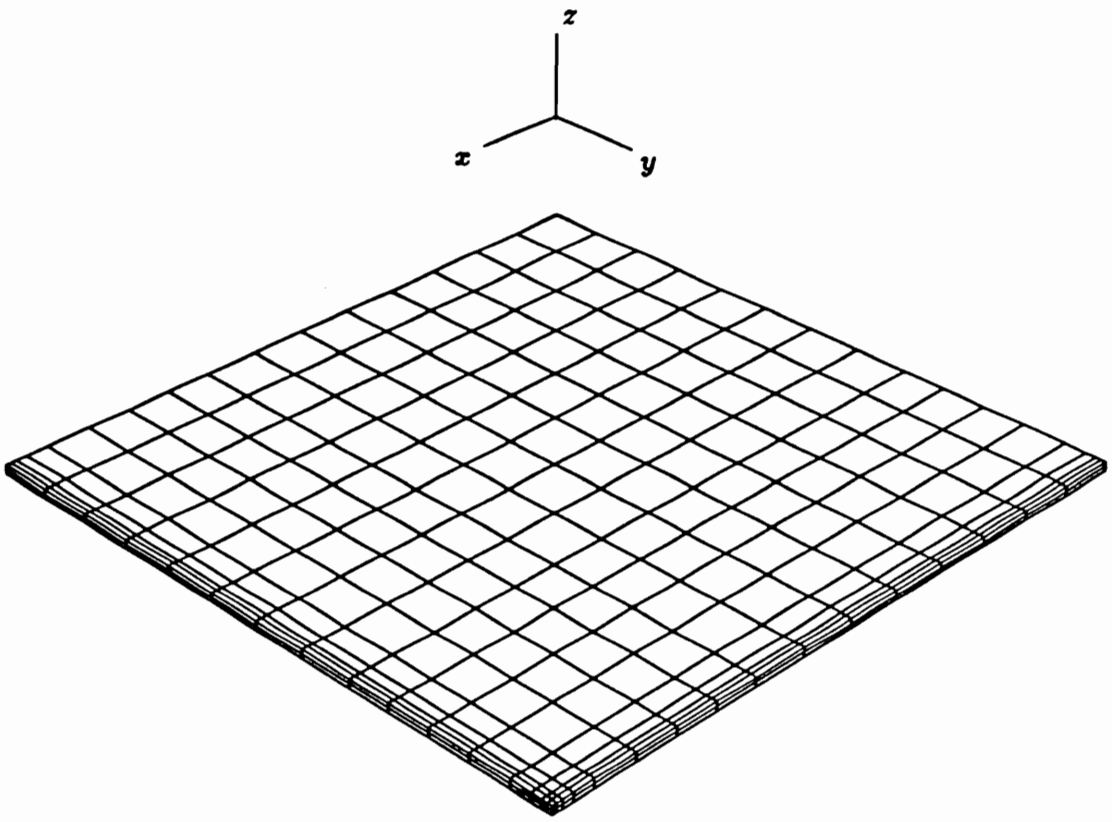

Global finite element model summary:

quarter symmetry model	$+0.00$ in. $\leq x \leq +3.00$ in.
$16 \times 16 \times 2 = 512$ elements	$+0.00$ in. $\leq y \leq +3.00$ in.
15430 equations	-0.02 in. $\leq z \leq +0.02$ in.
113.4 megabytes	unsymmetric laminate

Figure D.7 Global finite element model used for the preliminary analysis of 6.0 in. square unsymmetric laminates.

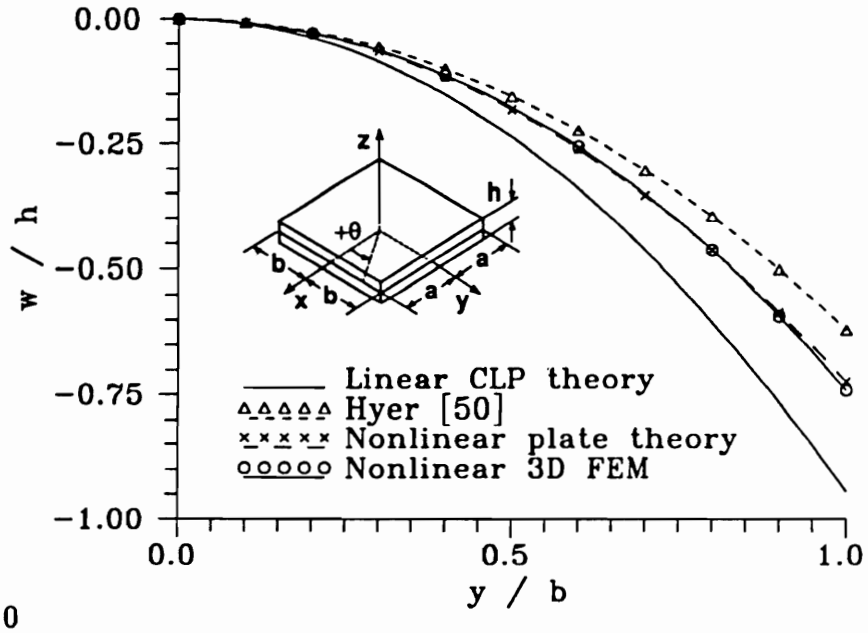

(a.) $x = 0$

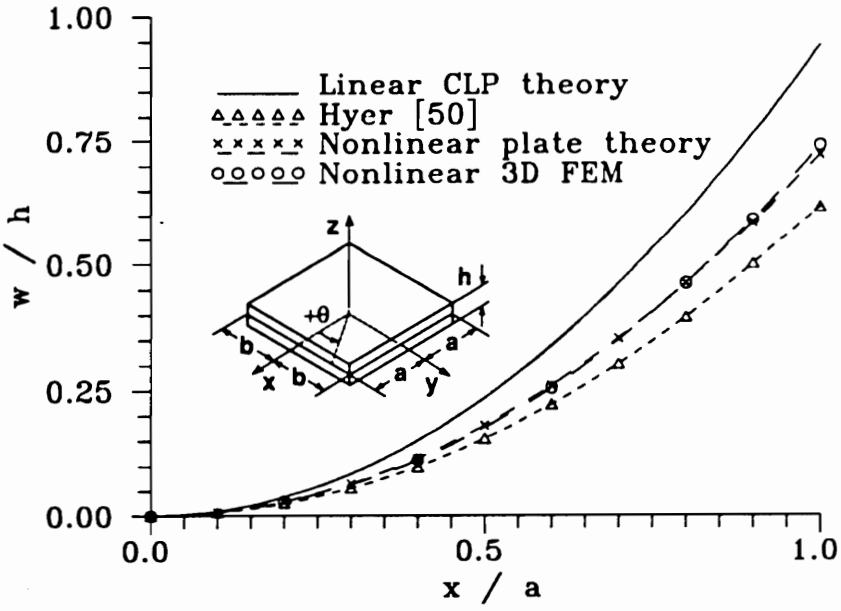

(b.) $y = 0$

Figure E.1 Midplane w/h displacement along $x = 0$ and $y = 0$ for a 2.0 in. square unsymmetric $[0_4/90_4]_t$ laminate ($\Delta T = -280°F$).

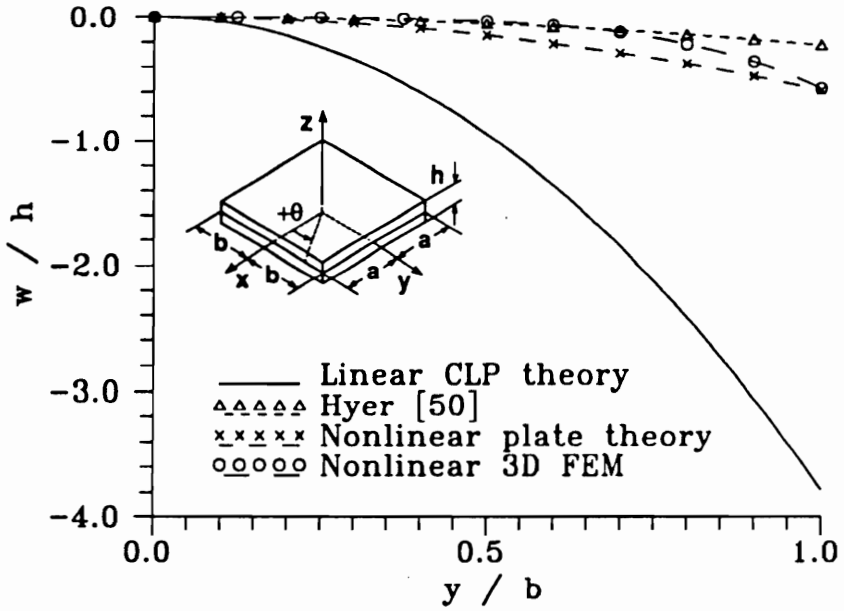

(a.) $x = 0$

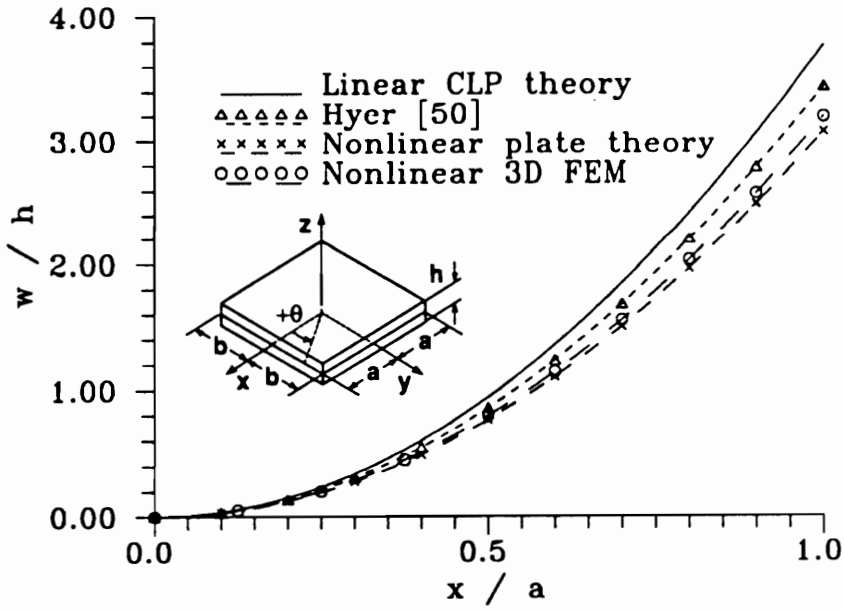

(b.) $y = 0$

Figure E.2 Midplane w/h displacement along $x = 0$ and $y = 0$ for a 4.0 in. square unsymmetric $[0_4/90_4]_t$ laminate ($\Delta T = -280°F$).

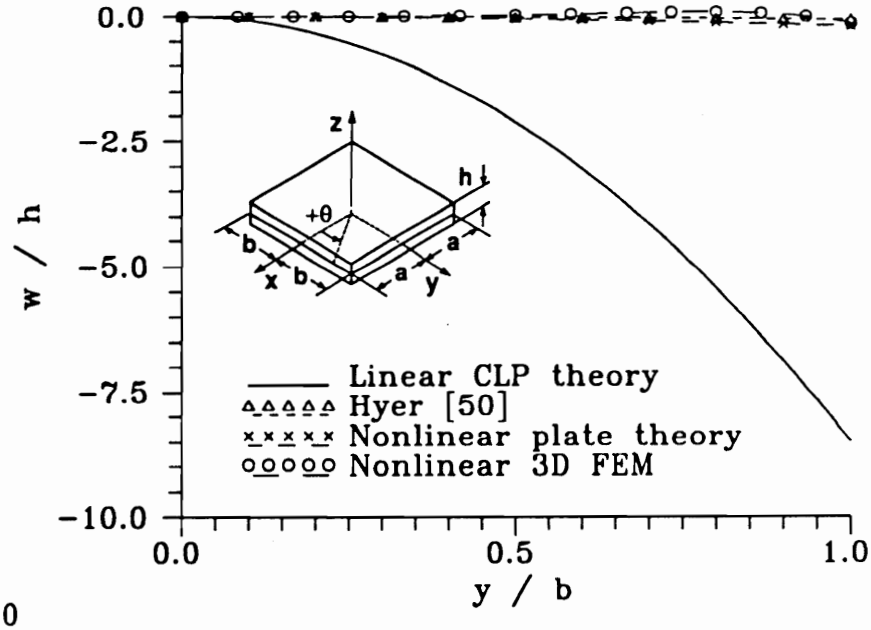

(a.) $x = 0$

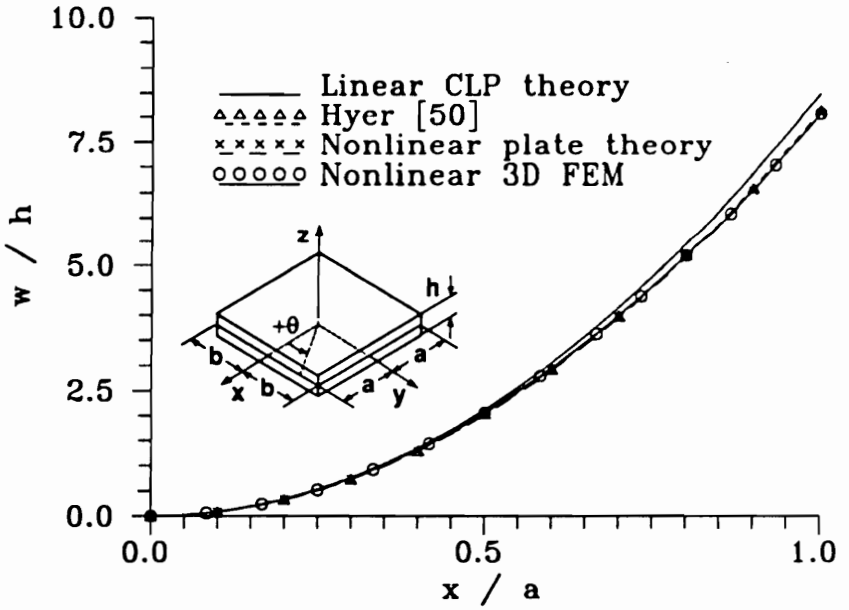

(b.) $y = 0$

Figure E.3 Midplane w/h displacement along $x = 0$ and $y = 0$ for a 6.0 in. square unsymmetric $[0_4/90_4]_t$ laminate ($\Delta T = -280°F$).

VITA

Donald Scott Norwood was born on January 24, 1960 in the Oak Cliff area of Dallas, Texas. He was the first of three children of Donald Loyd Norwood and Joan Evelyn Brown Norwood. He grew up in Dallas and graduated from Bishop Dunne High School in May of 1978. In the fall of 1978, he entered Texas Agricultural and Mechanical University in College Station, Texas where he began his studies in Aerospace Engineering. He earned two degrees in Aerospace Engineering from Texas A and M; a Bachelor of Science degree in December of 1982 and a Master of Science degree in December of 1984. While an undergraduate at Texas A and M, he began working summers as an associate structures engineer at LTV Aerospace and Defense in Dallas. After receiving his Master of Science degree, he joined the Structures Division at LTV Aerospace where he worked in the Structural Mechanics Group. In fall of 1985, he was accepted into the LTV Aerospace Doctoral Fellowship Program. In January of 1986, he entered Virginia Polytechnic Institute and State University in Blacksburg, Virginia to begin work on a Doctor of Philosophy Degree in Engineering Mechanics. In 1986, he joined the NASA-Virginia Tech Composites Program in the Engineering Science and Mechanics Department at Virginia Tech. As a member of the composites research program, he began his research residency in January of 1988 at NASA Langley Research Center in Hampton, Virginia. The current work was sponsored by the Aircraft Structures Branch at NASA Langley and was completed during the research residency. In September of 1990, he will return to work for the Structural Mechanics Group at LTV Aerospace in Dallas.

Donald Scott Norwood